# Spectral Distortions of the Cosmic Microwave Background

Dissertation

der Fakultät für Physik der
Ludwig-Maximilians-Universität München

angefertigt von
Jens Chluba
aus Tralee (Irland)


München, den 31. März 2005

1. Gutachter: Prof. Dr. Rashid Sunyaev, MPA Garching
2. Gutachter: Prof. Dr. Viatcheslav Mukhanov, LMU München

Tag der mündlichen Prüfung: 19. Juli 2005

## *Die Sterne*

*Ich sehe oft um Mitternacht,*
*wenn ich mein Werk getan*
*und niemand mehr im Hause wacht,*
*die Stern am Himmel an.*

*Sie gehn da, hin und her, zerstreut*
*als Lämmer auf der Flur;*
*in Rudeln auch, und aufgereiht*
*wie Perlen an der Schnur;*

*und funkeln alle weit und breit,*
*und funkeln rein und schön;*
*ich seh die große Herrlichkeit,*
*und kann nicht satt mich sehn...*

*Dann saget unterm Himmelszelt*
*mein Herz mir in der Brust;*
*Es gibt was Bessers in der Welt*
*als all ihr Schmerz und Lust.*

Matthias Claudius

# Contents

# List of Figures

# List of Tables

# Abstract

Studying the cosmic microwave background (CMB) has proven to be an immensely rich source of information about the Universe we live in. Many groups were and are intensely working on the interpretation of the large amount of CMB data, which has become available during the last decades and will be obtained with many new projects already observing at present or planned for the near future.

The observations by COBE in the 90's have shown that the CMB is extremely uniform, with angular fluctuations of the temperature on the level of one part in $10^5$ on angular scales larger than 7 degree. On the other hand on these scales no deviations of the CMB energy spectrum from a perfect blackbody were found. But today we do know that there exist spectral distortions of the CMB on arcminute[1] scales due to the scattering of CMB photons off the hot electrons residing inside the deep potential well of clusters of galaxies, which leads to the so called thermal-SZ effect (th-SZ). The th-SZ effect has already been measured for several big cluster and within the next 5 years, many CMB experiments like ACBAR, SZA, PLANCK, SPT, ACT, APEX, AMI and QUIET will perform deep searches for clusters with very high sensitivity. Many tens of thousands of clusters will be detected allowing us to carry out detailed studies of cluster physics and to place constraints on parameters of the Universe.

Due to this great advance in technology one can expect that small deviations from the main SZ cluster signal, e.g. related to relativistic corrections to Compton scattering for high electron temperature, will become observable. Motivated by this promising perspective here we studied the influence of the motion of the Solar System with respect to the CMB rest frame on the SZ cluster signature. This kind of contribution to the SZ signal has been neglected in the literature so far, but as we show here it is of the same order as other corrections under discussion. We found that this motion-induced SZ signal has a very strong *spectral* and *spatial* dependence and due to the great knowledge about the motion-induced CMB dipole it can be predicted with high precision, which makes it easy to account for it in the analysis of future SZ studies.

Here one big problem naturally arises: any experiment trying to observe tiny frequency-dependent signals needs a cross calibration of the different frequency channels. Several different standard methods for calibration issues are known, e.g. based on the annual modulation of the CMB dipole, the microwave flux from planets like Jupiter or the comparison with CMB sky maps obtained by well calibrated experiments like WMAP, each with their own problems and drawbacks. However the achieved level of cross calibration is limited by the knowledge of the calibrator. Today scientists are already speaking about extremely small frequency-dependent features in the CMB temperature power spectrum resulting from the scattering of CMB photons in the fine structure lines of different atomic species during the dark ages. Obtaining these signals can in principle be used to answer some of the interesting questions about the history of chemical enrichment and reionization, but it is likely that the necessary level of cross calibration cannot be reached with the standard methods.

In this context we considered the fact that the superposition of blackbodies with different temperatures is not again a blackbody. We show that in the limit of small temperature difference the superposition leads to a y-type spectral distortion. This kind of distortion arises whenever one in observing the CMB sky with finite angular resolution. We discuss the spectral distortions

[1] 1 arcmin=$1' = 1^\circ/60$; 1 arcsec=$1'' = 1'/60 = 1^\circ/3600$

due to the primordial CMB temperature fluctuations and the motion-induced CMB dipole. Furthermore we considered possible applications for calibration issues. We show that within this context also clusters of galaxies, especially for experiments observing only small parts of the sky, in the future may become standard sources for calibration issues.

Although the observations with COBE/FIRAS have proven that the CMB energy spectrum on large angular scales is extremely close to a pure blackbody one may still expect some deviations due to processes like the damping of acoustic waves, turbulent motion of the matter, the decay of unstable particles or annihilation of matter in the early Universe. Especially possible distortions from very early epochs (redshifts $z \geq \text{few} \times 10^5$) lead to deviations of the CMB brightness temperature at frequencies ($1 - \text{few} \times 10\,\text{GHz}$) well below the range of COBE/FIRAS. Currently people in the USA and especially at the NASA Goddard Space Flight Center are intensely working on experiments to measure the CMB temperature at these frequencies, where the largest distortions could be expected. One can therefore hope that in the near future also new constraints on the CMB energy spectrum will become available.

Therefore in this thesis we also reexamined the thermalization of spectral distortions of the CMB in the early Universe. Due to the large entropy here one of the most important processes is the production of low frequency photons by double Compton scattering. Until now people were only using a description of this emission in the limit of cold electrons and soft initial photons, but especially for the thermalization of large distortions at very high redshifts ($z \geq 10^6$) the inclusion of relativistic corrections to the main processes at work may become necessary. Here we provide two steps towards a solution of this problem. First we discuss in detail the full kinetic equation for the time evolution of the photon field under double Compton scattering in a hot, isotropic thermal plasma, both numerically and analytically. We obtained accurate approximations for the effective double Compton Gaunt factor, which are applicable in a very broad range of physical situations. We then provide a reformulation of the thermalization problem with respect to relativistic corrections and discuss its solution in the limit of small chemical potential distortions at high redshifts. Our results indicate that due to relativistic corrections the thermalization at high redshifts slows down notably and therefore makes the CMB more vulnerable for distortions at epochs $z \geq 10^6$. Here we also report some of our attempts to solve the full problem numerically.

# Chapter 1

# Introduction

## 1.1 General introduction on CMB

Since the serendipitous detection of the cosmic microwave background (CMB[1]) by Penzias and Wilson [96] in 1965 and the interpretation of this signal as the leftover from the hot 'fireball' by Dicke et al. [43] many decades have past. Today the CMB is one of the most important pillars of modern Cosmology and studying its characteristics has proven to be an incredibly rich source of information about the parameters describing our Universe (for reviews see [135, 64]) and particle physics (for review see [71] and references therein). Brave astrophysists may even talk about entering an *era of precision cosmology*, which certainly is strongly motivated by our growing understanding of the CMB, both observationally and theoretically.

The CMB photons detected today originated from the *last scattering surface* (LSS), when the Universe was roughly 380 000 years[2] old and due to its expansion had cooled down sufficiently ($\sim 3000\,\mathrm{K}$) to allow the formation of neutral atoms. Since then these photons have traveled across the whole visible Universe and hardly undergone any interactions with the matter. Still on their way from the LSS they witnessed a huge diversity of astrophysical processes, such as the formation of the first structures by gravitational collapse and the ignition of the first sources, which ended the *dark ages* by reionizing and heating the intergalactic medium and polluting the Universe with the first heavy elements. All these processes and the interactions with the matter before *recombination* and within the LSS left imprints in both the *spatial* (e.g. the acoustic peaks) and the *energy* (e.g. the thermal SZ-effect) distribution of the CMB, mainly due to *gravitational* effects [109] and the Doppler-effect due to *scattering* off moving (not necessarily free) electrons [125]. In this context one usually distinguishes between *primordial* temperature fluctuations (e.g. Sachs-Wolfe effect at large angular scales), which were imprinted onto the LSS already at the end of recombination, and *secondary* anisotropies, which have arisen afterwards and lead to the generation of *new* anisotropies (e.g. integrated Sachs-Wolfe effect and lensing) or the *damping* of primordial anisotropies (e.g. scattering by moving electrons after reionization at $z \lesssim 10 - 30$) [for reviews see 135, 64]. Observing these imprints help understanding the *global parameters* of the Universe, such as the total energy density and the Hubble parameter, baryonic matter, dark matter and dark energy content.

However, in the standard picture the CMB photons were born at much earlier epochs, very close to the big bang, and therefore represent the oldest detectable electromagnetic relics in the Universe, with roughly 410 photons per $\mathrm{cm}^3$ today. Before the end of recombination these photons strongly interacted with the matter in the Universe, which by that time was much hotter and denser than today. Just shortly after the end of inflation, the Universe is thought to be extremely isotropic with only *tiny* fluctuations in the matter density. Conversely, due to the strong coupling between matter and radiation, also the photons were isotropic and at redshifts

[1] A list of acronyms used in this thesis is given at the end.

[2] Corresponding to redshift of $z \sim 1100$.

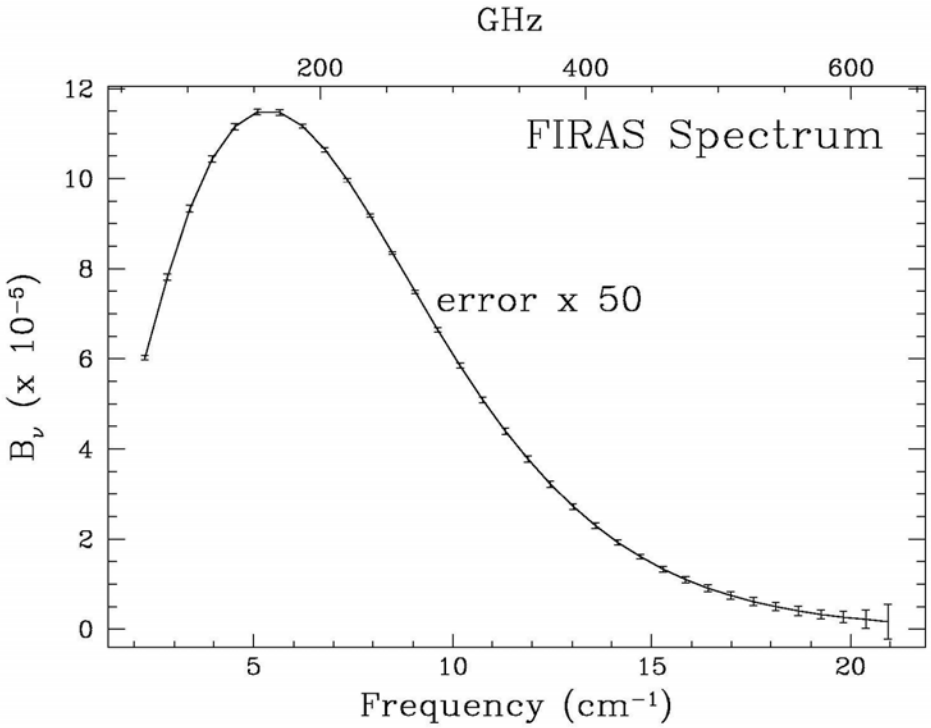


**Figure 1.1:** Uniform CMB spectrum as measured by COBE/FIRAS: the CMB spectrum is extremely close to a perfect black body of temperature $T_0 = 2.725 \pm 0.001$K. Until now no spectral distortions have been detected. The existing limits are $|\mu| < 9 \cdot 10^{-5}$ and $|y| \leq 1.5 \times 10^{-5}$ on possible chemical potential and Compton $y$-distortions [84, 50, 51]. These put severe constraints on possible mechanisms of energy release in the high redshift universe. The Figure was taken from [62].

well before the end of the era of electron-positron annihilation[3] ($z \gtrsim 10^8 - 10^9$) extremely close to a thermal blackbody [43]. The expansion of the Universe, gravitational redshifting and the scattering off slowly moving electrons in the Thomson limit leave the spectrum of the CMB unaltered (all these effects are *achromatic* and affect photons independent of their energy). But still observable *distortions* of the CMB energy spectrum may have emerged after significant release of energy, depending on the exact epoch and by which mechanism this possibly occurred. Studying the details of the (full sky) CMB energy spectrum therefore principally opens a way to investigate the *thermal history* of the Universe far beyond the LSS.

The observations by the COBE satellite have revealed that the energy spectrum of the CMB is extremely close to a perfect blackbody of temperature $T_0 = 2.725 \pm 0.001$K, with *spectral deviations* of no more than $10^{-4}$ [84, 50, 51] (see Fig. 1.1), and *fluctuations* of the radiation *temperature* (after extracting the large CMB dipole [119, 131, 50]) at a level of $\Delta T/T \sim 10^{-5}$ on angular scales smaller than 7° [120, 10]. Nowadays the WMAP spacecraft [11] measured the amplitude of these angular fluctuations of the CMB temperature with extremely high precision on a very broad range of angular scales, from $\theta \sim 12'$ up to the whole sky. The *temperature anisotropies* and the existence of the *acoustic peaks* were predicted already long ago [95, 125], but only now after BOOMERANG, MAXIMA, ARCHEOPS, WMAP and many ground based experiments like CBI, ACBAR, VSA, etc. we do know their precise characteristics, with a precision of better than 1% down to degree angular scales (see Fig. 1.2 and 1.3).

From all this observational evidence, in combinations with other pieces of information about the Universe we live in (e.g. the Hubble Space Telescope Key Project [52] and the matter

[3] Like in the case of recombination the freeze-out of $e^+e^-$-pairs is delayed because of the large entropy of the Universe: CMB photons outnumber the residual baryons by at factor of $\sim 6 \times 10^{10}$.

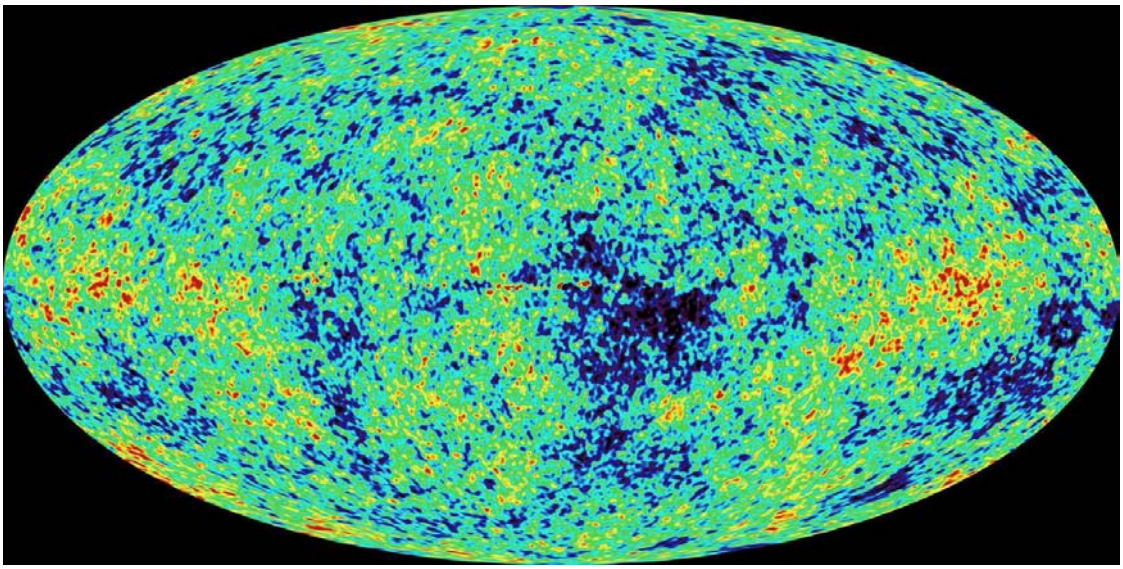

**Figure 1.2:** CMB sky as observed by Wmap: presented is the Wmap Internal Linear Combination CMB temperature map. The temperature fluctuations are consistent with a Gaussian-random field. Slight residuals from foregrounds and our Galaxy may explain some of the irregular features (quadrupole and octupole) close to the galactic plane. The Figure was taken from Wmap homepage.

power spectra as seen in the Lyman-$\alpha$ forest [40]) today a cosmological *concordance model* has emerged and the main parameters have been determined with unprecedented accuracy. Today cosmologists believe that the Universe is $\sim 14$ billion years old and very close to *spatially* flat. It is composed of $\sim 4.4\%$ baryon, $\sim 22\%$ dark matter and $\sim 73\%$ dark energy and currently expanding at a rate of $\sim 1.2 \times 10^{-18}$ s$^{-1}$ or equivalently has a present-day Hubble parameter of $H_0 = 71\,\mathrm{km\ s^{-1}\ Mpc^{-1}}$ (a more complete list of parameters including error bars can be found in Bennett et al. [11]).

However, with respect to the temperature anisotropies scientists have gone an additional step ahead since Cobe: today also $E$-mode (curl-free) polarization has been observed, which naturally follows from Thomson scattering of photons by moving electrons inside the LLS and is of the order of $\sim 10\%$ of the temperature anisotropies at a given scale (for reviews on CMB polarization see [139, 64] and references therein). The first detection was made by Dasi on $1.3 - 0.2^\circ$ angular scales at frequencies in the range $26 - 36\,\mathrm{GHz}$ [79, 78], and later Wmap obtained remarkable results for the temperature-polarization ($TE$) cross-power spectrum at multipoles $l \lesssim 400$ [73] (see Fig. 1.3).

Except for the surprising fact that the Wmap results on polarization indicate a very early time for reionization, $E$-mode polarization can be regarded as complementary information to the $TT$ power spectrum (of course on small scales also interesting contributions due to lensing arise [see 63, and references therein]). On the other hand people are also talking about $B$-mode (divergence-free) polarization, which unlike $E$-mode polarization (in lowest order) cannot be produced by scattering off moving electrons but only by tensor-perturbations (e.g. gravitational waves). Although it is not clear on which level, if at all, $B$-mode polarization can be expected, their detection would qualitatively push CMB science forward into new areas of physics, very close to inflation. Such an observation especially due to foregrounds will be extremely difficult, but scientists are very optimistic and are eagerly waiting for Planck to be launched.

As this short and definitely not comprehensive summary of CMB observations shows, after the Cobe results on the CMB spectrum scientists have focused a lot on the further investigation of the CMB temperature anisotropies, beyond doubt with great success. In this thesis we are mainly concerned with the *spectral distortions* of the CMB due to the interaction with the matter in the Universe. In this context an important effect on the list of secondary anisotropies is the SZ-effect [127, 128], which we will discuss in more detail below (Sect. 1.2.1). It is an

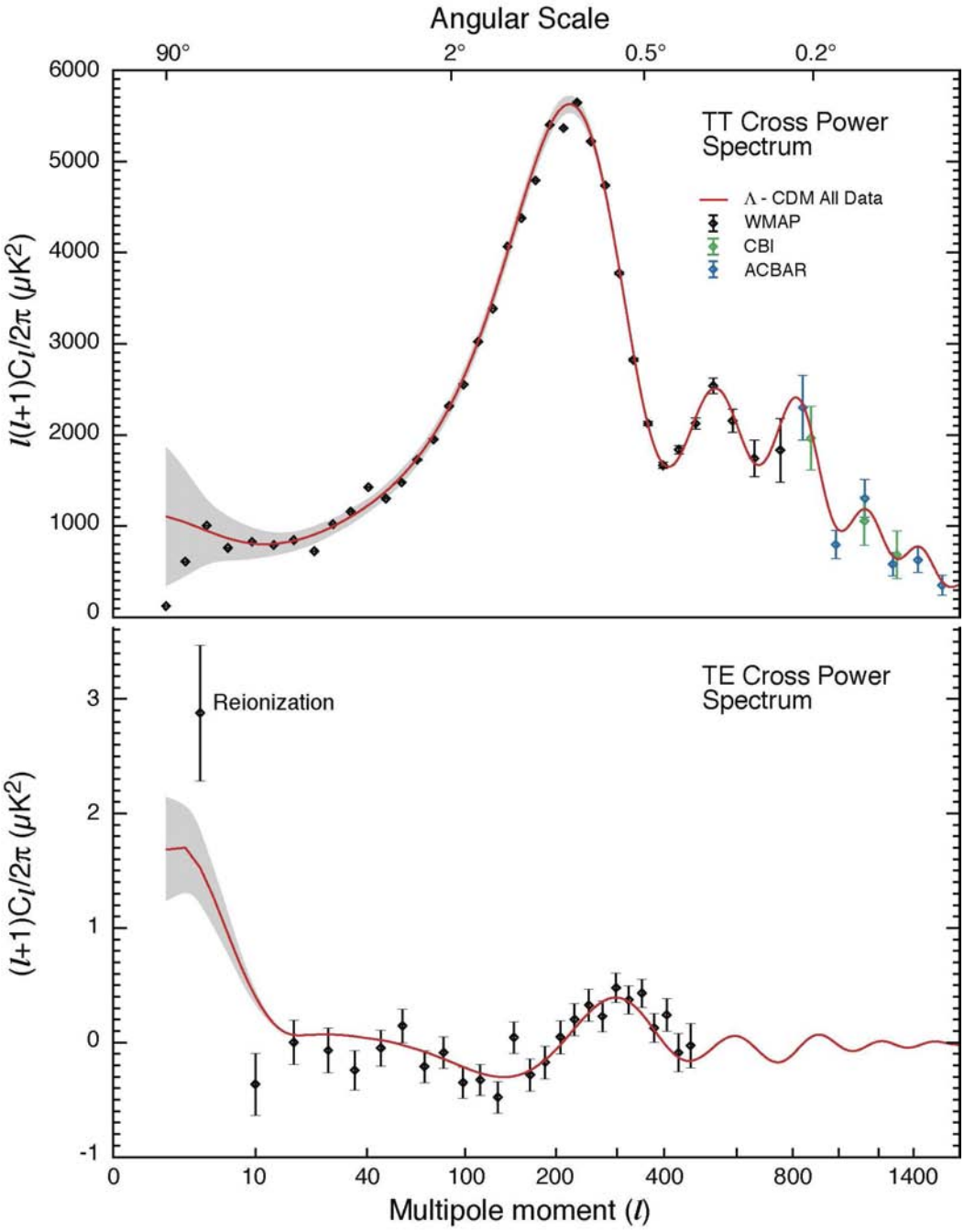


**Figure 1.3:** WMAP $TT$ and $TE$ power spectra: a great consistency of the CMB data with previous CMB observation for the $TT$ power spectrum is found. The position of the first acoustic peak is very sensitive to the geometry of the Universe, which is mainly determined by the total energy density (at least in cases close to spatial flatness). The ratio of the height of the first and second peak is mostly depending on the baryon density. The gray areas indicate the uncertainties due to cosmic variance. The Figure was taken from WMAP homepage.

example, where a significant spectral distortion is associated with an anisotropic distribution on the sky. In contrast to this, for spectral distortions resulting from heating of the CMB photons in the early Universe one can expect that any anisotropy would be of second order.

## 1.2 Spectral distortions of the CMB

The limits on spectral distortion of the CMB obtained with Cobe place severe constraints on possible heating of the photons at high redshifts ($z > 10^3$). But before turning to the very early Universe we give a short introduction on the SZ effect (For reviews see [130, 104, 15, 32]), since we will encounter it many times in the work presented in this thesis.

### 1.2.1 The SZ effect

Considering a beam of electrons moving with velocity $\beta = v/c$ relative to the isotropic CMB, in first order of $\beta \ll 1$ only a change of the thermodynamic temperature (independent of frequency) of the CMB photons is introduced due to the *Doppler* effect (at low redshifts *recoil* is negligible for CMB photons). As mentioned above this is one of the sources for the observed temperature anisotropies of the CMB. Here it is most important that the electron velocity field is *anisotropic*. For isotropic electron distributions (with no global bulk motion relative to the CMB rest frame) in first order of $\beta$ the Doppler boosts average out and no net effect remains (if the photons have no significant quadrupole anisotropy). On the other hand, if the electrons move sufficiently fast ($v \sim 0.1c$) even in the isotropic case a net effect remains in second order of $\beta$. In this situation the change of the brightness temperature strongly depends on frequency.

#### The thermal SZ effect

Electrons with sufficiently large *thermal* velocities for example reside in the deep potential wells of clusters of galaxies. The *Comptonization* of CMB photons by these hot electrons is usually referred to as the *thermal* SZ effect (th-SZ) [141, 127, 128]. Using the Kompaneets equation [75] one can obtain

$$\Delta I_{\rm th}(\nu, \vec{n}) = y \, \frac{x \, e^x}{e^x - 1} \left[ x \, \frac{e^x + 1}{e^x - 1} - 4 \right] I_0(\nu) \tag{1.1}$$

for the change of the CMB brightness due to a cluster of galaxies centered in the direction $\vec{n}$ as seen by an observer resting with respect to the CMB. Here $x = h\nu / k\,T_0$ is the dimensionless frequency, where $T_0$ is the CMB temperature, and $I_0(\nu) = \frac{2h}{c^2} \frac{\nu^3}{e^x - 1}$ denotes the CMB monopole intensity. The Compton $y$-parameter is given by the line of sight integral over the electron pressure

$$y = \int \frac{k\,T_{\rm e}}{m_{\rm e} c^2} \, N_{\rm e} \, \sigma_{\rm T} \, {\rm d}l \,, \tag{1.2}$$

where $\sigma_{\rm T}$ is the Thomson cross section, $N_{\rm e}$ the electron number density and $T_{\rm e}$ the electron temperature. Clusters of galaxies typically have temperatures of a few keV, $\theta_{\rm e} = k\,T_{\rm e}/m_{\rm e}c^2 \sim 0.01$ and Thomson optical depths $\tau = \int N_{\rm e}\,\sigma_{\rm T}\,{\rm d}l \sim 0.01$. Therefore a typical value of the $y$-parameter for clusters is $y \sim 10^{-4}$.

Figure 1.4 shows the spectral dependence of the change in the CMB brightness introduced by the th-SZ as given by equation (1.1). In the Rayleigh-Jeans (RJ) part of the CMB spectrum the th-SZ effect leads to a decrement, in the Wien part to an increment of the intensity. The change of the intensity vanishes close to the *cross-over* frequency at $\nu \sim 217\,{\rm GHz}$. In terms of brightness temperature the th-SZ lead to a temperature decrement $\Delta T/T_0 = -2\,y$ in the RJ region of the spectrum. As this approximation shows the th-SZ typically is one or two orders of magnitude larger than the primordial temperature fluctuations. This implies

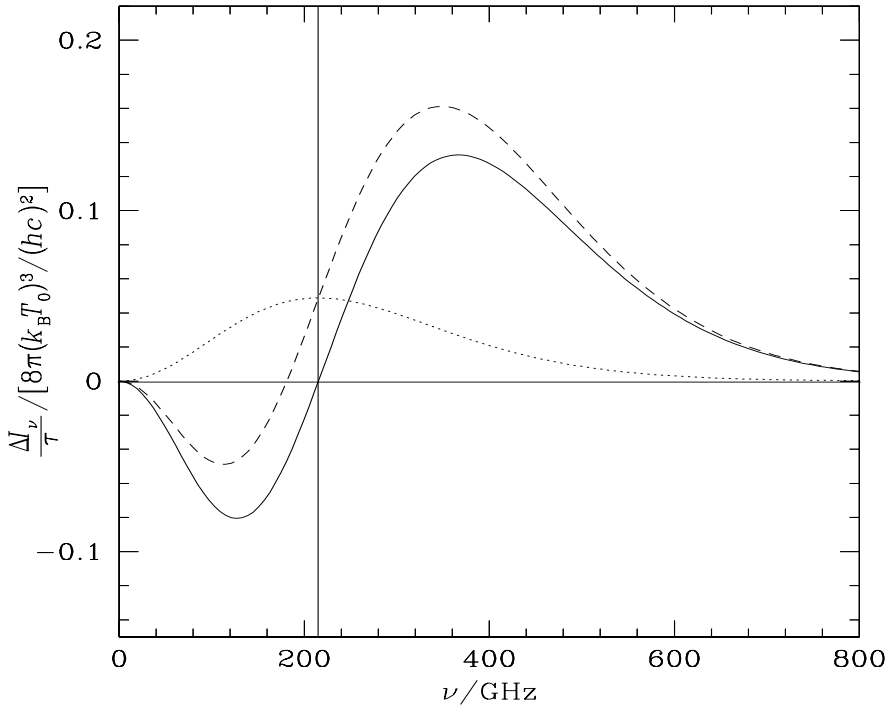


**Figure 1.4:** Change of the CMB brightness due to the thermal and kinetic SZ effect in the non-relativistic limit: the solid line shows the th-SZ for a cluster with electron temperature $k\,T_\mathrm{e} = 10\,\mathrm{keV}$, the dotted line represents the k-SZ for a cluster moving with line of sight velocity $\beta_{\mathrm{c},\parallel} = 0.01$ towards the observer and the dashed line shows the superposition of both effects. For typical clusters the value of the peculiar velocity is a factor of $\sim 10$ smaller, which reduces the importance of the k-SZ to less than $\sim 10\%$ of the th-SZ. The vertical line indicates the location of the cross-over frequency of the th-SZE.

that due to the th-SZ effect clusters of galaxies are (after our own Galaxy) one of the most important and brightest foreground sources for CMB experiments devoted to studying the primordial temperature anisotropies at arcminute angular scales. Given the strong and very peculiar frequency-dependence of the SZ signature, it is possible to extract the contributions due to SZ clusters and thereby open the way for deeper investigations of the primordial temperature anisotropies, which for multipoles $l \gtrsim 3000$ are expected to be weaker than the fluctuations due to clusters of galaxies.

### The kinematic SZ effect

If the cluster of galaxies is moving with bulk velocity $\vec{\beta}_\mathrm{c}$ relative to the CMB rest frame, then similar to the generation of primordial temperature anisotropies a change in the brightness temperature due to the Doppler effect arises. This change is proportional to the line of sight component $\beta_{\mathrm{c},\parallel}$ of the clusters bulk velocity and is usually referred to as the *kinetic* or *kinematic* SZ effect (k-SZ) [129]. The associated change in the CMB brightness as seen by an observer at rest in the CMB rest frame is given by

$$\Delta I_\mathrm{k}(\nu, \vec{n}) = \tau\,\beta_{\mathrm{c},\parallel}\,\frac{x\,e^x}{e^x - 1}\,I_0(\nu)\,. \tag{1.3}$$

Depending on the sign of $\beta_{\mathrm{c},\parallel}$ (positive when the cluster moving towards the observer) the k-SZ effect leads to a decrease or increase of the CMB temperature signal in the direction of the cluster. A typical value for the amplitude of this effect is $\tau\,\beta_\mathrm{c} \sim 10^{-5}$. This implies that the k-SZ effect usually is at least one order of magnitude smaller than the th-SZ. Although single

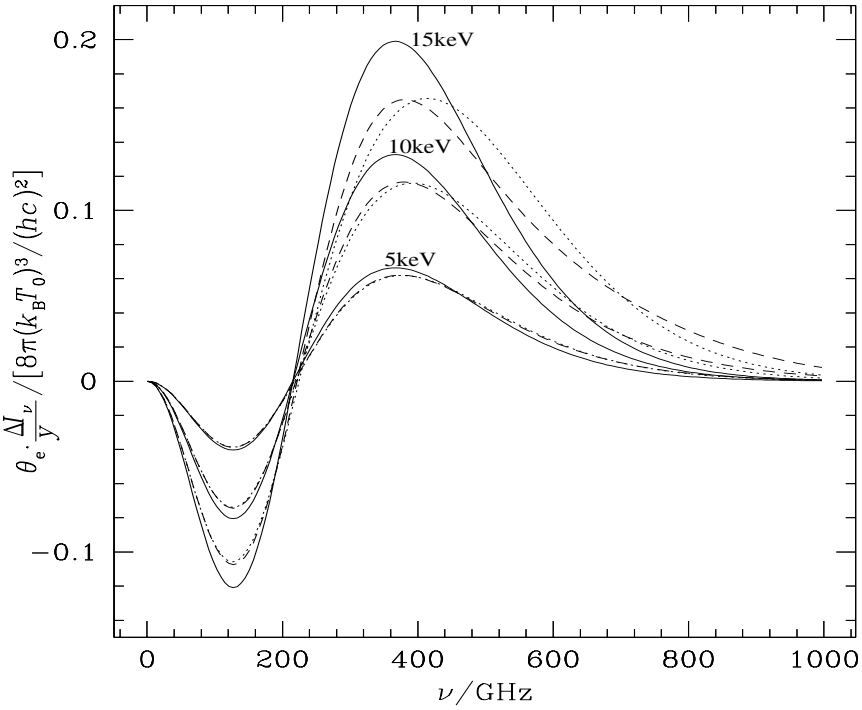


**Figure 1.5:** Change of the CMB brightness due to the thermal SZ effect for hot clusters: the solid curves shows the non-relativistic result for different values of the electron temperature as indicated. The dotted and dashed curves were obtained with the generalized Kompaneets equation including first and second order corrections in the electron temperature $\theta_e$, respectively. At frequencies below the cross-over frequency the first order correction is sufficiently accurate, but at high frequencies the second order corrections lead to significant differences already in the case $k\,T_e = 10\,\mathrm{keV}$.

observations of the th-SZ effect have already been performed for several clusters [32, 103], an accurate measurement of the k-SZ effect is still an experimental challenge.

Figure 1.4 also shows the spectral dependence of the k-SZ (for illustration purposes we chose a rather large value of the peculiar velocity). Here it is most important that unlike the th-SZ effect the k-SZ effect does not vanish at the cross-over frequency. Observing close to this frequency the k-SZ effect will dominate the cluster-induced change in the CMB intensity and therefore in principle offers a way to determine the clusters line of sight peculiar velocity.

### Cosmology with the SZ effect

Once imprinted onto the CMB the temperature change caused by the SZ effect remains unaffected by cosmological dimming. This is due to the fact that at larger redshift the temperature of the CMB monopole is higher by a factor of $(1 + z)$. On the other hand a photon emitted at frequency $\nu$ will reach the observer at $z = 0$ redshifted by $(1 + z)$, implying that the ratio $\nu(z)/T(z)$ does not change with redshift. Therefore one can expect to find clusters up to very high redshifts ($z \geq 1$), where X-ray observations may already be extremely difficult. This offers a powerful tool to probe the formation of large scale structure at early times [76].

Furthermore combining SZ with X-ray observations and knowlegde about the redshift of the cluster one can determine the Hubble constant independent of the usual cosmic distance ladder. This is possible due to the different scalings of the X-ray luminosity ($\propto N_e^2 \sqrt{T_e}$) and the SZ effect ($\propto N_e\, T_e$) with the electron temperature and number density, which allows a direct measurement of the angular diameter distance. This kind of determination has been performed for several clusters yielding values of the Hubble constant comparable with those from other methods [14, 32, 103].

### Relativistic corrections to the SZ effect

If the temperature or peculiar velocity of the SZ cluster are large, higher order corrections to the kinetic equation for Compton scattering have to be taken into account. Starting from the Boltzmann collision integral for Compton scattering one can perform Fokker-Planck type expansions in the dimensionless electron temperature $\theta_{\rm e} = k\,T_{\rm e}/m_{\rm e}c^2$ and velocity $\vec{\beta}_{\rm c}$. These expansions lead to a generalized form of the Kompaneets equation and have been performed by several groups [105, 30, 67, 91, 111] in different orders of $\theta_{\rm e}$ and $\vec{\beta}_{\rm c}$. Using the generalized Kompaneets equation one can easily obtain analytic expression for the relativistic corrections to the SZ effect.

It is important to note that these corrections usually have a strong frequency dependence. Therefore even for temperatures $\theta_{\rm e} \sim 0.01$ corrections of the order of $\sim 10\%$ arise. Furthermore, the convergence of these expansions is very slow. At large frequencies $x \gtrsim 1$ one usually has to take many correction orders into account to obtain an accurate description of the SZ effect. Figure 1.5 illustrates this behaviour. Due to this feature one may even try to detemine the cluster temperature independent of X-ray observations [3], given sufficiently accurate multi-frequency observations of the th-SZ effect.

### Other sources of SZ like contributions

Many groups have worked on the extensions of the SZ effect. Whenever one encounters moving electrons at low redshifts the scattering of CMB photons leads to a SZ like change of the temperature. One obvious possiblity is the motion of the gas inside clusters. Every cluster has grown by mergers of smaller groups and clusters of galaxies. These mergers should induce some large scale motion of the gas inside the cluster, which then will decay in a turbulent cascade to smaller and smaller scales. Indications of turbulent motion of the intracluster gas where found recently in X-ray observations of the Coma cluster [116]. After a recent major merger one simple possiblity is a coherent rotation of the intracluster gas as has been discussed by Chluba & Mannheim [33]. This kind of large scale rotation leads to a small dipolar contribution to the k-SZ effect.

Other interesting possiblities are the SZ by ultra-relativistic electrons [49] in radio bubble inside clusters [99] and the SZ effect for anisotropic electron distributions due to magnetic fields [57]. All the processes mentioned here usually should lead to a change of the CMB temperature which is at least one or two order of magnitude smaller than the main SZ effect as discussed above. Observing these signature is potentially very interesting, but requires a very good understanding of systematics and foregrounds.

## 1.2.2 Spectral distortion due to energy release in the early Universe

In the past, the time evolution of spectral distortions in the non-relativistic case has been discussed in great detail, both numerically and analytically by several people [126, 65, 46, 25, 59]. In this Section we shall give a short overview about the thermalization of CMB spectral distortions after energy release at early epochs.

### Kinetic equilibrium with respect to Compton scattering

Our Universe is characterized by an extremely large entropy: CMB photons outnumber baryons and electrons by at factor of $\sim 6 \times 10^{10}$. This fact makes it exceedingly difficult to distort the CMB spectrum at high redshifts. In the previous Section we have discussed the th-SZ effect associated with the hot electrons inside clusters of galaxies. Here one encounters a situation, in which the electrons due to gravitational collapse were heated up to high temperatures, exceeding the CMB temperature typically by more than eigth orders of magnitude. Due to this huge temperature difference the CMB photons gain energy from the electrons by *inverse Compton* scattering. Using equation (1.1) one can easily show that the change of the photon

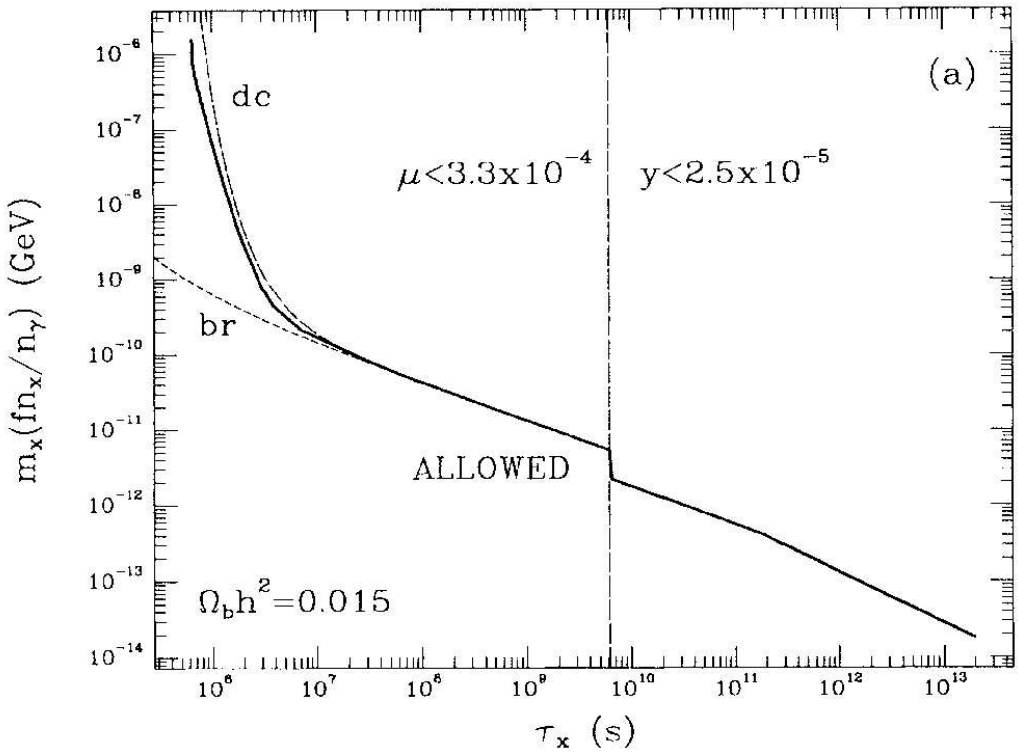


**Figure 1.6:** Limits on the lifetimes of decaying relict particles: here $m_{\rm X}$ is the mass of particle and $n_\gamma$ and $n_{\rm X}$ are the number density of the photons and the particle of species $X$ at the begining of heating, respectively. $f$ is the fraction of the released energy that eventually leads to heating. The solid line shows the numerical result, whereas the other two lines show the analytical estimates of thermalization including double Compton (dc) and Bremsstrahlung (br). The Figure was taken from Hu & Silk [59].

energy density is given by $\delta\rho_\gamma/\rho_\gamma = 4\,y$. Since the $y$-parameter is $y \ll 1$ the photons and electrons could not reach *kinetic equilibrium*: the effects due to Compton scattering vanish when the temperatures of the electrons and photons are equal, i.e. $T_{\rm e} = T_\gamma$, and the photons follow a Bose-Einstein distribution with photon occupation number, $n_{\rm BE} = 1/[e^{x+\mu} - 1]$, where $\mu$ is the constant dimensionless chemical potential. Typically $y \gtrsim 0.25$ is needed to acheive kinetic equilibrium between the electrons and photons. Going to redshifts beyond recombination the integrated Compton $y$-parameter strongly increases and will at some point exceed this value. Heating the electrons (or photons) at higher redshifts by some process will therefore lead to a Bose-Einstein distribution at $z = 0$.

### Inclusion of photon production due to double Compton and Bremsstrahlung

Until now we have not included any process, that can change the number of photons, but without any such process the CMB spectrum cannot be thermalized to a pure blackbody. Since Compton scattering conserves the number of photons, heating only changes the energy density of the photons and in kinetic equilibrium with resect to Compton scattering results in a Bose-Einstein distribution with $\mu > 0$ due to the deficit of photons with respect to a blackbody of the same energy density. In the cosmological context two processes are most important: Bremsstrahlung (BS) and double Compton scattering (DC). In this context it is very important that BS fails to compeat with DC emission at redshifts larger than $z_{\rm dc,bs} \sim {\rm few} \times 10^5$. This again is due to the large entropy of the Universe. Including these processes into the calculation one can distinguish between the following four regimes for the residual CMB spectral distortions arising from a single energy injection, $\delta\rho_\gamma/\rho_\gamma$, at heating redshift $z_{\rm h}$ [25, 62]:

(a) $z_{\rm h} < z_y \sim 6.3 \times 10^3$: Compton scattering is *not able* to establish kinetic equilibrium with the electrons. Photon producing effects (mainly BS) can only restore a Planckian

spectrum at very low frequencies. Heating results in a Compton $y$-distortion at high frequencies like in the case of the th-SZ effect, with $y$-parameter $y \sim \frac{1}{4}\,\delta\rho_\gamma/\rho_\gamma$.

(b) $z_y < z_\mathrm{h} < z_\mathrm{ch} \sim 2.9 \times 10^5$: Compton scattering can establish *partial* kinetic equilibrium with the electrons. Photon produced at low frequencies (mainly BS) upscatter and diminish the spectral distortion at high frequencies. The deviations from a blackbody represent a mixture between a $y$-distortion and a chemical potential distortion.

(c) $z_\mathrm{ch} < z_\mathrm{h} < z_\mathrm{th} \sim 2 \times 10^6$: Compton scattering can establish *full* kinetic equilibrium with the electrons at high redshifts. Low frequency photons (mainly due to DC emission) upscatter and efficiently reduce the spectral distortion at high frequencies. The deviations from a blackbody can be described as a Bose-Einstein distribution with frequency-dependent chemical potential, which is constant at high and vanishes at low frequencies.

(d) $z_\mathrm{th} < z_\mathrm{h}$: Both Compton scattering and photon production processes are extremely efficient and restore any spectral distortion arising after heating.

In general one has to solve the thermalization problem numerically, especially for large injections of energy close to the *thermalization redshift* $z_\mathrm{th}$ and in the redshift regime (b). For the cases (a) and (c) simple analytic approximations were obtained [see e.g. 25, 59] in the limit of small spectral distortions. The COBE/FIRAS instrument placed strict upper limits [50, 51] on a possible chemical potential, $|\mu| < 9 \times 10^{-5}$, and $y$-type, $|y| < 1.5 \times 10^{-5}$, CMB spectral distortions. Nevertheless, the great spectral sensitivity of future CMB experiments like ARCADE [74] and DIMES [72] will tighten these limits even more and therefore tiny deviations from the blackbody spectrum might become measurable.

### Possible sources for energy release

Using these observational limits one can constrain the amount of energy which could have been injected at a given heating redshift. Possible mechanisms of heating include the decay of unstable relict particles [59], particle annihilation [86], heating due to turbulent motion or the dissipation of acoustic waves [126, 45, 60]. In Figure 1.6 as an example we present the limits on the lifetimes of unstable relict particles in the low density universe [59]. For decaying particles with liftimes $t_\mathrm{X} \geq 10^7\,\mathrm{s}$ the CMB provides tight contraints on the possible mass and number density of these particles, whereas for shorter lifetimes the CMB does not give strong limits, since in this case energy release is taking place at redshifts beyond the thermalization redshift for DC scattering. Note that the thermalization redshift for BS is much larger.

It is obvious, that the residual CMB spectral distortions depend on the detailed history of heating. The simplest modification from single heating is to assume two periods of energy release. As Burigana & Salvaterra [26] show, observationally it is quite demanding to distinguish between single or double injection.

## 1.3 In this Thesis

In the previous Sections we have sketched the important parts of the framework for the main subjects of this thesis. We were studying three new ideas within the context of CMB spectral distortions. Due to the different nature of the effects discussed in this thesis we decided that it is better to give a separate short motivation at the beginning of each Chapter, but for overview let us mention some of the underlying ideas.

In Chapter 2 we discuss another relativistic correction to the SZ effect, which has been neglected in the literature so far. This correction is related to the motion of the Solar System with respect to the CMB rest frame. Due to the Doppler effect the motion of the Solar System introduces a spectral distortion of the main CMB cluster signal, which is similar to the first

order temperature correction of the k-SZ. This signal can be easily taken into account in future SZ analysis, since it can be prediced with high accuracy.

The results presented in Chapter 3 are based on the simple idea that the superpostion of blackbodies with different temperatures is not again a blackbody. Therefore any observation of the CMB sky with finite angular resolution will lead to an unavoidable spectral distortion. We show here that in the limit of small fluctuations of the temperature the deviations from a blackbody are given by a $y$-type distortion. We also discuss the possibility to utilize the spectral distortions due to the superposition of blackbodies for calibration purposes, which is one of the most important issues for the future extraction of any small frequency-dependent signal.

Until now the thermalization of CMB spectral distortions in the early Universe has only been discussed using a non-relativistic formulation of the problem. Especially at high redshifts, i.e. for the evolution of chemical potential distortions, relativistic corrections to the main processes at work may start to play an important role. Here we want to provide two important steps towards a solution of this problem.

In Chapter 4 we therefore first study the full kinetic equation for the time evolution of the photon phase space density in hot, isotropic plasma under double Compton scattering, both numerically and analytically. In the context of spectral distortions, until now DC emission was only used in the limit of cold electrons and soft incident photons. Here we derive analytic approximations for the DC Gaunt factor, which are applicable in a very broad range of parameters.

Finally in Chapter 5 we reexamine the formulation of the thermalization problem in a hot thermal plasma (see Sect. 5.1). We then make use of the analytic approximations obtained in Chapter 4 and solve the problem for the thermalization of small chemical potential distortions at high redshifts analytically. These analytic results clearly show, that due to relativistic corrections the thermalization of chemical potential distortions slows down notably. Unfortuneately, although potentially very interesting, a numerical solution of the full thermalization problem turns out to be very difficult and so far our attempts have not lead to conclusive results.

# Chapter 2

# SZ clusters of galaxies: influence of the motion of the Solar System

Within the next 5 years, several CMB experiments like ACBAR, SZA, PLANCK, SPT, ACT, APEX, AMI and QUIET will perform deep searches for clusters with sensitivity limits at the level of $1-10\,\mathrm{mJy}$ and in the future CMB missions such as CMBPOL should reach sensitivities 20-100 times better than those of PLANCK by using currently existing technology [37]. Many tens of thousands of clusters will be detected allowing us to carry out detailed studies of cluster physics and to place constraints on parameters of the Universe like the Hubble parameter and the baryonic matter, dark matter and dark energy content [for reviews see 130, 104, 15, 32].

Motivated by the rapid developments in CMB technology, the purpose of this Chapter is to take into account the changes in the SZ signal that are induced by the motion of the Solar System relative to the CMB rest frame. These changes are connected to the Doppler effect and aberration and exhibit a strong spectral and spatial dependence.

Assuming that the observed CMB dipole is fully motion-induced, its amplitude implies that the Solar System is moving with a velocity of $\beta_\mathrm{o} = v_\mathrm{o}/c = 1.241 \cdot 10^{-3}$ towards the direction $(l, b) = (264.14^\circ \pm 0.15^\circ, 48.26^\circ \pm 0.15^\circ)$ [119, 131, 50]. As will be shown here, in the lowest order of $\beta_\mathrm{o}$ the motion-induced correction to the thermal SZ effect (th-SZ) exhibits an amplitude and spectral dependence, which is similar to the first order $\beta_\mathrm{c}$ correction to the th-SZ, i.e. the SZ signal $\propto \tau\,\beta_\mathrm{c}\,k\,T_\mathrm{e}/m_\mathrm{e}c^2$, where $\tau$ is the Thomson optical depth. On the other hand the observer's frame transformation of the kinetic SZ effect (k-SZ) leads to a much smaller y-type spectral distortion with effective $y$-parameter $\propto \tau\,\beta_\mathrm{c}\,\beta_\mathrm{o}$. Since both the amplitude and direction of the motion of the Solar System are well known the corrections we are discussing here are fully determined and can be easily taken into account in the process of estimation of the key cluster parameters.

Future CMB experiments like PLANCK, SPT and ACT will only partially resolve the central regions for a large fraction of the detected clusters. Below we will consider two cases (i) when future multi-frequency CMB experiments will be able to resolve clusters of galaxies and (ii) when their angular resolution will not allow to study the clusters structures in detail. Therefore here we are not only discussing the change in the *brightness* of the CMB in the direction of a cluster but also the corrections to the *flux* as measured for unresolved clusters due to both the motion-induced change of surface brightness and the apparent change of their *angular dimension*. All these changes are connected to the Doppler effect and aberration, which also influence the primordial temperature fluctuations and polarization as discussed by Challinor & van Leeuwen [31].

Another important consequence of the motion of the Solar System with respect to the CMB rest frame is a dipolar anisotropy induced in the deep *number counts* of sources. This effect was discussed earlier in connection with the distribution of $\gamma$-ray bursts [82, 115] – identical to the Compton-Getting effect [39] for cosmic rays – and radio and IR sources [48, 8, 17]. The motion-induced change in the source number counts strongly depends on the slope of the $\log N$-

$\log F$ curve and the spectral index of the source [48], which makes it possible to distinguish the signals arising from different astrophysical populations. Here we show that a similar effect arises for the number counts of SZ clusters. Due to the very peculiar frequency-dependence of the th-SZ, the number of observed clusters in a direction of the sky can be either decreased or increased depending on the frequency band. The work presented in the Chapter was accepted for publication in *Astronomy and Astrophysics* and was done in collaboration with Gert Hütsi and Rashid Sunyaev [35].

## 2.1 General transformation laws

A photon of frequency $\nu$ propagating along the direction $\boldsymbol{n} = (\phi, \theta)$ in the CMB rest frame $S$ due to *Doppler boosting* and *aberration* is received at a frequency $\nu'$ in the direction $\boldsymbol{n}' = (\phi, \theta')$ by an observer moving with the velocity $\beta_\mathrm{o} = v_\mathrm{o}/c$ along the $z$-axis:

$$\nu = \gamma\nu'(1 - \beta_\mathrm{o}\mu') \qquad\qquad \mu = \frac{\mu' - \beta_\mathrm{o}}{1 - \beta_\mathrm{o}\,\mu'}\,. \tag{2.1}$$

Here $\gamma = 1/\sqrt{1-\beta_\mathrm{o}^2}$ is the Lorentz factor, $\mu = \cos\theta$ and all the primed quantities[1] denote the corresponding variables in the observer's frame $S'$. It was also assumed that the $z'$-axis is aligned with the direction of the motion. For a given spatial and spectral distribution of photons in $S$, in lowest order of $\beta_\mathrm{o}$ the Doppler effect leads to spectral distortions, whereas due to aberration the signal on the sky is only redistributed.

### Transformation of the spectral intensity

The transformation of the spectral intensity (or equivalently the surface brightness) $I(\nu, \vec{n})$ at frequency $\nu$ and in the direction $\vec{n}$ on the sky into the frame $S'$ can be performed using the invariance properties of the occupation number, $n(\nu, \vec{n}) = I(\nu, \vec{n})/\nu^3$:

$$I'(\nu', \vec{n}') = \frac{\nu'^3}{\nu^3}\, I(\nu, \vec{n})\,. \tag{2.2}$$

Here $I'(\nu', \vec{n}')$ is the spectral intensity at frequency $\nu'$ in the direction $\vec{n}'$ as given in the rest frame of the observer. In the lowest order of $\beta_\mathrm{o}$ it is possible to separate the effects of Doppler boosting and aberration:

$$I'(\nu', \vec{n}') \approx I(\nu', \vec{n}') + \Delta I_\mathrm{D}(\nu', \vec{n}') + \Delta I_\mathrm{A}(\nu', \vec{n}')\,. \tag{2.3a}$$

with the Doppler and aberration correction

$$\Delta I'_\mathrm{D}(\nu', \vec{n}') \approx \beta_\mathrm{o}\,\mu'\left[3 - \nu'\partial_{\nu'}\right] I(\nu', \vec{n}') \tag{2.3b}$$

$$\Delta I'_\mathrm{A}(\nu', \vec{n}') \approx \beta_\mathrm{o}\,\sqrt{1-\mu'^2}\,\partial_{\theta'} I(\nu', \vec{n}')\,. \tag{2.3c}$$

Equation (2.3b) only includes the effects due to Doppler boosting, whereas (2.3c) arises solely due to aberration.

With (2.3) it becomes clear that in the first order of $\beta_\mathrm{o}$ any maximum or minimum of the intensity distribution on the sky will suffer only from Doppler boosting. This implies that due to aberration the positions of the central regions of clusters of galaxies will only be redistributed on the sky: in the direction of the motion clusters will appear to be closer to each other while in the opposite direction their angular separation will seem to be bigger.

Another consequence of the observer's motion is that a cluster with angular extension $\Delta \ll 1$ in $S$ will appear to have a size $\Delta' = \Delta[1 - \beta_{\mathrm{o},\parallel}]$ in the observer's frame $S'$. Here $\beta_{\mathrm{o},\parallel} = \beta_\mathrm{o}\,\mu'$

[1] In the following, prime denotes that the corresponding quantity is given in the rest frame of the moving observer.

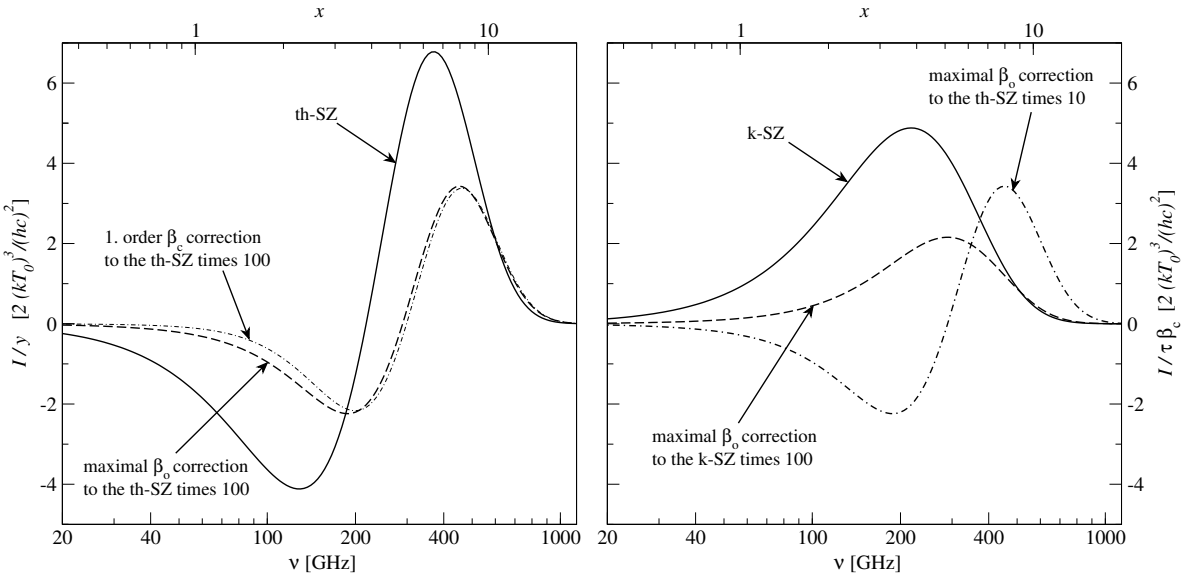


**Figure 2.1:** Frequency dependence of the SZ brightness due to the non-relativistic th- and k-SZ and the corresponding corrections induced by the motion of the Solar System relative to the CMB rest frame for a cluster with electron temperature $k\,T_\mathrm{e} = 5.1\,\mathrm{keV}$, which is moving with $\beta_\mathrm{c} = 10^{-3}$ towards the observer and is located at the maximum of the CMB dipole, i.e. $\beta_{\mathrm{o},\parallel} = 1.241 \cdot 10^{-3}$. The first order $\beta_\mathrm{c}$ correction to the th-SZ (dash-dotted line in the left panel) is shown. Note that for convenience all the velocity corrections are multiplied by a factor as given in the labels.

is the line of sight component of the Solar System's peculiar velocity. Therefore in $S'$ a cluster will look smaller by a factor of $1-\beta_\mathrm{o}$ in the direction of the motion and bigger by $1+\beta_\mathrm{o}$ in the opposite direction. This implies that in the direction of the observer's motion, cluster profiles will seem to be a little steeper and more concentrated.

### Transformation of the measured flux

The spectral flux $F(\nu, \boldsymbol{n}_0)$ from a solid angle area $\mathcal{A}$ in the direction $\boldsymbol{n}_0$ on the sky in $S$ is given by the integral $F(\nu, \boldsymbol{n}_0) = \int_\mathcal{A} I(\nu, \boldsymbol{n})\, \mu_0 \,\mathrm{d}\Omega$, where we defined $\mu_0 = \boldsymbol{n} \cdot \boldsymbol{n}_0$. If one assumes that the angular dimension of $\mathcal{A}$ is small, then using (2.3) in the observer's frame $S'$ the change of the flux due to Doppler boosting and aberration is given by

$$\Delta F'_\mathrm{D}(\nu', \boldsymbol{n}'_0) \approx \beta_{\mathrm{o},\parallel} \left[3 - \nu' \partial_{\nu'}\right] F(\nu', \boldsymbol{n}'_0) \tag{2.4a}$$

$$\Delta F'_\mathrm{A}(\nu', \boldsymbol{n}'_0) \approx \beta_{\mathrm{o},\parallel} \int_\mathcal{A} \theta'^2\, \partial_{\theta'} I(\nu', \boldsymbol{n}')\, \mathrm{d}\theta'\, \mathrm{d}\phi'\,, \tag{2.4b}$$

respectively. Assuming that the area $\mathcal{A}$ contains an unresolved object, that contributes most of the total flux and vanishes at the boundaries of the region, then the term arising due to aberration only can be rewritten as

$$\Delta F'_\mathrm{A}(\nu', \boldsymbol{n}'_0) = -2\,\beta_{\mathrm{o},\parallel}\, F(\nu', \boldsymbol{n}'_0)\,. \tag{2.5}$$

This can be understood considering that in the direction of the motion the solid angle covered by an object is smaller by a factor $[1-\beta_{\mathrm{o},\parallel}]^2 \approx 1 - 2\,\beta_{\mathrm{o},\parallel}$. In this case the total change in the spectral flux $F'(\nu', \boldsymbol{n}'_0)$ is

$$\frac{\Delta F}{F} = \frac{F'(\nu', \boldsymbol{n}'_0) - F(\nu', \boldsymbol{n}'_0)}{F(\nu', \boldsymbol{n}'_0)} = \beta_{\mathrm{o},\parallel} \left[1 - \frac{\partial \ln F}{\partial \ln \nu'}\right]\,. \tag{2.6}$$

For a pure blackbody source of temperature $T$ this leads to $\Delta F/F = \beta_{\mathrm{o},\parallel} \left[\frac{x' e^{x'}}{e^{x'}-1} - 2\right]$, with dimensionless frequency $x' = h\nu'/k\,T$. In the RJ region of the CMB spectrum it therefore follows: $\Delta F/F = -\beta_{\mathrm{o},\parallel}$.

Integrating the flux $F'(\nu', \boldsymbol{n}_0')$ over frequency $\nu'$ it is straightforward to obtain the change of the total bolometric flux $F'_{\rm bol}(\boldsymbol{n}_0') = \int F'(\nu', \boldsymbol{n}_0')\,{\rm d}\nu'$ in the observer's frame $S'$:

$$\frac{\Delta F_{\rm bol}}{F_{\rm bol}} = \frac{F'_{\rm bol}(\boldsymbol{n}_0') - F_{\rm bol}(\boldsymbol{n}_0')}{F_{\rm bol}(\boldsymbol{n}_0')} = 2\,\beta_{\rm o,\parallel}\,. \tag{2.7}$$

This result can also be easily understood considering the transformation law for the total bolometric intensity $I_{\rm bol} = \int I(\nu)\,{\rm d}\nu$, i.e.

$$I'_{\rm bol} = \frac{I_{\rm bol}}{[\gamma(1-\beta_{\rm o}\mu')]^4}\,, \tag{2.8}$$

and the transformation of the solid angle ${\rm d}\Omega' = [\gamma(1-\beta_{\rm o}\mu')]^2\,{\rm d}\Omega$.

### Transformation of the number counts

Defining $\frac{{\rm d}N}{{\rm d}\Omega}(F, \vec{n})$ as the number of objects per solid angle ${\rm d}\Omega$ above a given flux $F$ at some fixed frequency $\nu$ and in some direction $\vec{n}$ on the sky in the CMB rest frame $S$, the corresponding quantity in the observer's frame $S'$ may be written as

$$\frac{{\rm d}N'}{{\rm d}\Omega'}(F', \vec{n}') = \frac{{\rm d}N}{{\rm d}\Omega}(F, \vec{n})\,\frac{{\rm d}\Omega}{{\rm d}\Omega'}\,, \tag{2.9}$$

where $F$ and $\boldsymbol{n}$ are functions of $F'$ and $\boldsymbol{n}'$. Now, assuming isotropy in $S$, in the first order of $\beta_{\rm o,\parallel}$ one may write

$$\frac{{\rm d}N'}{{\rm d}\Omega'}(F', \vec{n}') \approx \frac{{\rm d}N}{{\rm d}\Omega}(F') \times \left[1 + 2\,\beta_{\rm o,\parallel} - \frac{\Delta F}{F}\,\frac{\partial \ln \frac{{\rm d}N}{{\rm d}\Omega}(F')}{\partial \ln F'}\right]\,, \tag{2.10}$$

with $\Delta F = F' - F$. For unresolved objects $\Delta F/F$ is given by equation (2.6). Here we made use of the transformation law for the solid angles and performed a series expansion of $\frac{{\rm d}N}{{\rm d}\Omega}(F)$ around $F'$.

If one assumes $\frac{{\rm d}N}{{\rm d}\Omega}(F) \propto F^{-\lambda}$ and $F(\nu) \propto \nu^{-\alpha}$, it is straightforward to show that for unresolved sources

$$\frac{{\rm d}N'}{{\rm d}\Omega'}(F', \vec{n}') \approx \frac{{\rm d}N}{{\rm d}\Omega}(F')\,\left[1 + \beta_{\rm o,\parallel}(2 + \lambda[1+\alpha])\right]\,. \tag{2.11}$$

This result was obtained earlier by Ellis & Baldwin [48] for the change of the radio source number counts due to the motion of the observer. Depending on the sign of the quantity $\Sigma = 2 + \lambda[1+\alpha]$ there is an increase or decrease in the number counts in a given direction. However, in the case of clusters, $\alpha$ is a strong function of frequency, which makes the situation more complicated.

## 2.2 Transformation of the cluster signal

For an observer at rest in the frame $S$ defined by the CMB the change of the *surface brightness* in the direction $\vec{n}$ towards a cluster of galaxies is given by the sum of the signals due to the th-SZ, $I_{\rm th}(\nu, \vec{n})$ and the k-SZ, $I_{\rm k}(\nu, \vec{n})$:

$$I_{\rm SZ}(\nu, \vec{n}) = I_{\rm th}(\nu, \vec{n}) + I_{\rm k}(\nu, \vec{n})\,. \tag{2.12}$$

In the non-relativistic case these contributions are by equations (1.1) and (1.3), respectively. Here we are only interested in the correction to the intensity in the central region of the cluster, where the spatial derivative of $y$ is small and the effects of aberration may be neglected. In the outer parts of the cluster also changes due to aberration arise.

### Change of the SZ cluster brightness

Using equations (2.3b) and (1.1) and (1.3) one may find

$$\Delta I'_{\rm D,th}(\nu',\vec{n}') = y\, I_0(\nu')\,\frac{x' e^{x'}}{e^{x'}-1}\,\mathcal{C}_{\rm th}(x')\cdot\beta_{\rm o}\,\mu' \tag{2.13a}$$

$$\Delta I'_{\rm D,k}(\nu',\vec{n}') = \tau\,\beta_{\rm c,\parallel}\, I_0(\nu')\,\frac{x' e^{x'}}{e^{x'}-1}\,\mathcal{C}_{\rm k}(x')\cdot\beta_{\rm o}\,\mu' \tag{2.13b}$$

for motion-induced change of the cluster brightness. Here the functions $\mathcal{C}_{\rm th}(\hat{x})$ and $\mathcal{C}_{\rm k}(\hat{x})$ are defined by

$$\mathcal{C}_{\rm th}(\hat{x}) = 4 - 6\,\mathcal{X} + \mathcal{X}^2 + \frac{1}{2}\mathcal{S}^2 \tag{2.14a}$$

$$\mathcal{C}_{\rm k}(\hat{x}) = \mathcal{X} - 1\,, \tag{2.14b}$$

with the notations $\mathcal{X} = x\,\coth(\frac{x}{2})$ and $\mathcal{S} = x/\sinh(\frac{x}{2})$.

In Fig. 2.1 the spectral dependence of $\Delta I'_{\rm D,th}$ and $\Delta I'_{\rm D,k}$ is illustrated. The transformation of the th-SZ leads to a spectral distortion which is very similar to the first order $\beta_{\rm c}$ correction to the th-SZ. In the Rayleigh-Jeans limit $\mathcal{C}_{\rm th}(\hat{x}) \rightarrow -2$ and therefore is 5 times bigger than the $\beta_{\rm c}$ correction to the th-SZ. The maximum/minimum of $\Delta I'_{\rm D,th}$ is at $x = 7.97\,/\,3.31$ and $\Delta I'_{\rm D,th}$ vanishes at $x = 5.10$ ($x = 1$ corresponds to $\nu = 56.8\,{\rm GHz}$). In the direction of the dipole maximum, due to the strong frequency-dependence of $\mathcal{C}_{\rm th}$ the motion-induced correction, $\Delta I'_{\rm D,th}$, reaches percent level with respect to the th-SZ signal close to the crossover frequency $x_{\rm c} = 3.83$ and at frequencies above $x \geq 10.7$. The maximum/minimum of $\Delta I'_{\rm D,th}$ is at $x = 7.97\,/\,3.31$. On the other hand the transformation of the k-SZ leads to a y-type spectral distortion with the corresponding y-parameter $y_{\rm kin} = \tau\,\beta_{\rm c,\parallel}\,\beta_{\rm o}\,\mu' \sim 10^{-8}\,\mu'$. In the Rayleigh-Jeans limit $\mathcal{C}_{\rm k}(\hat{x}) \rightarrow 1$ instead of $-2$ for a pure y-distortion. Again due to the strong frequency-dependence for a cluster located in the dipole maximum the motion-induced correction $\Delta I'_{\rm D,k}$ reaches percent level with respect to the k-SZ signal at frequencies $x \geq 9.1$. The maximum of $\Delta I'_{\rm D,k}$ is at $x = 5.10$. Fig. 2.1 clearly shows that the motion-induced correction to the th-SZ easily reaches the level of a few percent in comparison to the k-SZ (e.g. at $\nu = 400\,{\rm GHz}$ it contributes $\sim 14\%$ to the k-SZ signal for a cluster with $k\,T_{\rm e} = 5.1\,{\rm keV}$ and $\beta_{\rm c} = 10^{-3}$).

### Change of the SZ cluster flux

In order to obtain the motion-induced change of the *flux* for unresolved clusters one has to integrate the surface brightness over the surface of the cluster. In the following we neglect the k-SZ, since its contribution only becomes important close to the crossover frequency. Then it follows that $\Delta F(\nu,\vec{n}) \propto \Delta I(\nu,\vec{n})$, implying that $\mathrm{d}\ln F/\mathrm{d}\ln\nu' = \mathrm{d}\ln I/\mathrm{d}\ln x'$. Comparing equations (2.3b) and (2.13) one can define the effective spectral index of the SZ signal by

$$\alpha = -\frac{\mathrm{d}\ln F(x')}{\mathrm{d}\ln x'} = \frac{\mathcal{C}_{\rm th}(x')}{Y_0(x')} - 3\,, \tag{2.15}$$

with $Y_0(x) = \mathcal{X} - 4$. Using equation (2.15) one can write the CMB central *brightness*, *flux* and *number count* for unresolved clusters as

$$I'_{\rm SZ}(\nu',\vec{n}') = I_{\rm SZ}(\nu',\vec{n}')\,\left[1+\beta_{\rm o}\,\mu'(3+\alpha)\right] \tag{2.16a}$$

$$\Delta F'_{\rm SZ}(\nu',\vec{n}') = \Delta F_{\rm SZ}(\nu',\vec{n}')\,\left[1+\beta_{\rm o}\,\mu'(1+\alpha)\right] \tag{2.16b}$$

$$\frac{\mathrm{d}N'_{\rm SZ}}{\mathrm{d}\Omega'}(F',\vec{n}') = \frac{\mathrm{d}N_{\rm SZ}}{\mathrm{d}\Omega}(F')\,\left[1+\beta_{\rm o}\,\mu'\Sigma\right]\,, \tag{2.16c}$$

with $\Sigma = 2+\lambda(1+\alpha)$ and $\lambda = -\frac{\partial\ln\frac{\mathrm{d}N}{\mathrm{d}\Omega}(F')}{\partial\ln F'}$. Fig. 2.2 shows the change of the central brightness and the flux for an unresolved cluster. It is obvious that only in the RJ region of the CMB spectrum the SZ brightness and flux do follow a power-law. The change of the number counts will be discussed below (see Sect. 2.3.1).

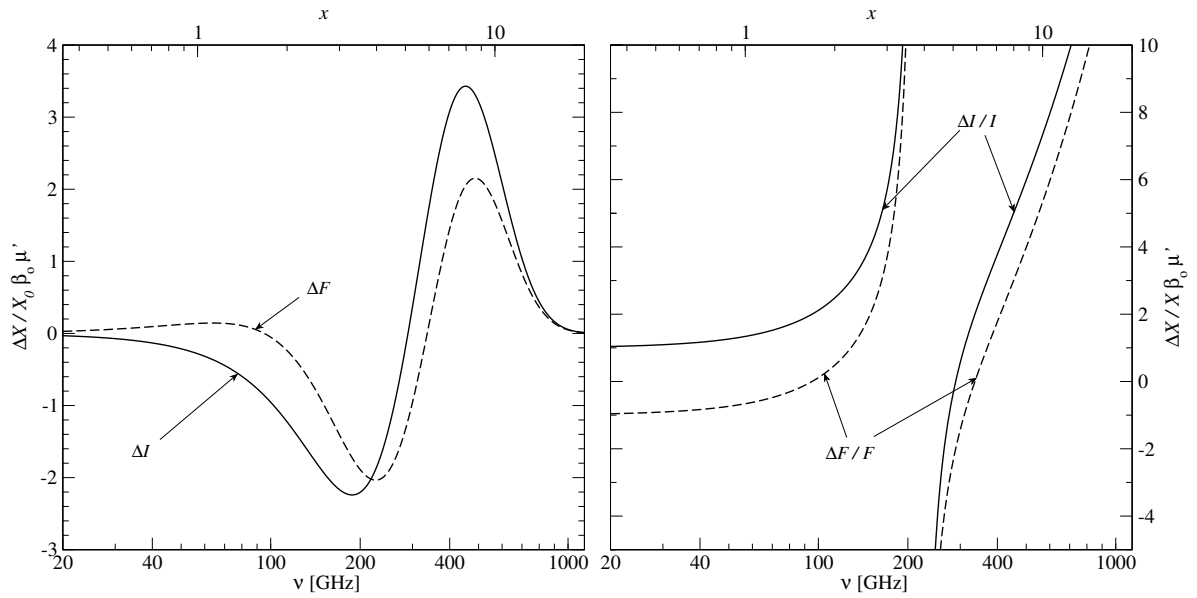


**Figure 2.2:** Motion-induced change of the CMB spectral brightness $\Delta I$ and flux $\Delta F$ for a cluster of galaxies at rest with respect to the CMB. **Left panel**: Absolute change of the cluster brightness (solid line) with $X_0 = 2.70 \times 10^{11}\, y\,\mathrm{mJy/sr}$ and the flux for an unresolved cluster (dashed line) with $X_0 = 7.17\, \langle y/10^{-4}\, r_\mathrm{c}^2 \rangle_\mathrm{cl}\, (r_\mathrm{c}/30'')^2\,\mathrm{mJy}$, where $r_\mathrm{c}$ is the core radius and where $\langle u \rangle_\mathrm{cl} = \int_\mathrm{cl} u\, \mathrm{d}\Omega/4\pi$ denotes the cluster average of the quantity $u$. **Right panel**: Relative change of the brightness (solid line) and flux for an unresolved cluster (dashed line). Here $\Delta I/I = \beta_\mathrm{o}\, \mu'\, (3+\alpha)$ and $\Delta F/F = \beta_\mathrm{o}\, \mu'\, (1+\alpha)$.

## 2.3 Multi-frequency observations of clusters

The observed CMB signal in the direction of a cluster consists of the sum of all the contributions mentioned above, including the relativistic correction to the SZ effect. Given a sufficient frequency coverage and spectral sensitivity one may in principle model the full signal for even one single cluster, but obviously there will be degeneracies which have to be treated, especially if noise and foregrounds are involved. Therefore it is important to make use of the special properties of each contribution to the total signal, such as their spectral features and spatial dependencies.

One obstacle for any multi-frequency observation of clusters is the cross-calibration of different frequency channels. Some method to solve this problem was discussed in Chluba & Sunyaev [34] using the spectral distortions induced by the superposition of blackbodies with different temperatures. In the following we assume that the achieved level of cross-calibration is sufficient. For more information on observational issues in the detection and analysis of the SZ effect see Birkinshaw & Lancaster [16].

The largest CMB signal in the direction of a cluster (after elimination of the CMB dipole) is due to the th-SZ. In order to handle this signal one can make use of the zeros of the spectral functions describing the relativistic corrections. In addition, future X-ray spectroscopy will allow us to accurately determine the mean temperature of the electrons inside clusters. This additional information will place useful constraints on the parameters describing the th-SZ and therefore may allow us to extract the effects connected to the peculiar velocities of the cluster and the observer.

The temperature difference related to the non-relativistic k-SZ is frequency-independent and therefore may be eliminated by multi-frequency observations. As mentioned above (see Fig. 2.1) the motion-induced spectral distortion to the th-SZ has an amplitude and spectral dependence, which is very similar to the effect related to the first order $\beta_\mathrm{c}$ correction to the th-SZ. Therefore it will be difficult to distinguish these two contributions to the SZ signal for one single cluster without prior knowledge about its peculiar velocity. For many clusters on the

other hand one can expect that the signals proportional to $\beta_{\mathrm{c},\parallel}$ average out. This implies that for large cluster samples ($\sim 10^3 - 10^4$) only the signals related to the th-SZ are important.

### 2.3.1 Dipolar asymmetry in the number of observed clusters

Integrating (2.16c) over solid angles leads to the observed number of clusters in a given region of the sky. If one assumes that the observed region is circular with radius $\theta'_{\mathrm{r}}$ centered on the direction $\boldsymbol{n}'_0 = (\phi'_0, \theta'_0)$ then the total observed number of clusters is given by

$$N'_{\mathrm{SZ}}(F') = N_{\mathrm{SZ,eff}}(F') \left[1 + \beta_{\mathrm{o}}\, \mu'_0\, \frac{1+\mu'_{\mathrm{r}}}{2}\, \Sigma\right], \tag{2.17}$$

where $N_{\mathrm{SZ,eff}}(F') = 4\pi\, \frac{\mathrm{d}N_{\mathrm{SZ}}}{\mathrm{d}\Omega}\, \frac{1-\mu'_{\mathrm{r}}}{2}$ is the effective number of clusters inside the observed patch with fluxes above $F'$, $\mu'_{\mathrm{r}} = \cos\theta'_{\mathrm{r}}$ and $\mu'_0 = \cos\theta'_0$. For two equally sized patches in separate directions on the sky the difference in the number of observed clusters will then be

$$\Delta N' = \beta_{\mathrm{o}}\, N_{\mathrm{SZ,eff}}\, \Delta\mu'_0\, \frac{1+\mu'_{\mathrm{r}}}{2}\, \Sigma\,, \tag{2.18}$$

with $\Delta\mu'_0 = \mu'_{0,1} - \mu'_{0,2}$, where $\mu'_{0,i} = \cos\theta'_{0,i}$ for patch $i$. Centering the first patch on the maximum and the second on the minimum of the CMB dipole leads to the maximal change in the number of observed clusters at a given frequency ($\Delta\mu'_0 = 2$). To estimate the significance of this difference we compare $\Delta N'$ to the Poissonian noise in the number of clusters for both patches, which is given by $[N'_{\mathrm{SZ},1} + N'_{\mathrm{SZ},2}]^{1/2} \approx \sqrt{2}\, N^{1/2}_{\mathrm{SZ,eff}}$. To obtain a certain signal to noise level $q$ the inequality

$$\beta_{\mathrm{o}}\, |\Sigma|\, \Delta\mu'_0\, [1+\mu'_{\mathrm{r}}]\, \sqrt{1-\mu'_{\mathrm{r}}} \geq \frac{4\,q}{\sqrt{N_{\mathrm{SZ,f}}}} \tag{2.19}$$

has to be fulfilled. We defined $N_{\mathrm{SZ,f}} = 4\pi\, \frac{\mathrm{d}N_{\mathrm{SZ}}}{\mathrm{d}\Omega}$ as the number of clusters on the whole sky above a given flux level $F'$. Here two effects are competing: the smaller the radius of each patch, the smaller the number of observed clusters above a given flux but the larger the effective $\langle\beta_{\mathrm{o},\parallel}\rangle$. The optimal radius is $\theta_{\mathrm{r}} \sim 70^\circ$ but for a given $q$ and sensitivity the size in principle can be smaller.

### 2.3.2 Estimates for the dipolar asymmetry in the cluster number counts

In this section we present results for the SZ cluster number counts using a simple Press-Schechter [98] prescription for the mass function of halos as modified by Sheth et al. [117] to include the effects of ellipsoidal collapse. For simplicity we assume that all the clusters remain unresolved.

Since here we are interested in unresolved objects we only need to specify the cluster mass-temperature relation and baryonic fraction. For the former we apply the frequently used scaling relation and normalization as given by Bryan & Norman [24], whereas for the latter we simply assume a universal value of $\Omega_{\mathrm{b}}/\Omega_{\mathrm{m}}$, which is rather close to the local values as derived from X-ray data [e.g. 88] independent of cluster mass and redshift. We note that these two assumptions are the biggest source of uncertainty in our calculations and the use of them is only justified given the lack of current knowledge about the detailed evolution of the baryonic component in the Universe. In spite of these gross simplifications our results on cluster number counts agree very well with those obtained in state-of-the-art hydrodynamical simulations by Springel et al. [123] and White et al. [136] as demonstrated in Fig. 2.3. Here the counts are calculated for the ΛCDM concordance model [121] assuming an observing frequency of 150 GHz. The first set of simulations included only adiabatic gas physics, whereas for the second also gas cooling and feedback from supernovae and galactic winds were taken into account. We also plot the

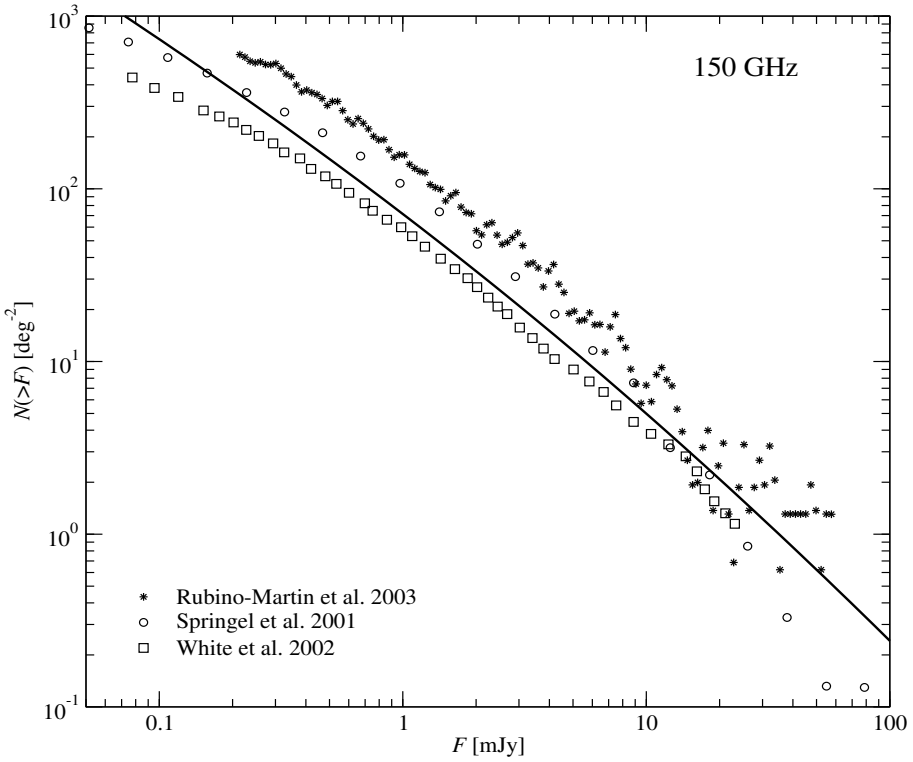


**Figure 2.3:** $\log N$-$\log F$: Number of unresolved clusters per square degree with flux level above $F$ at observing frequency $\nu = 150\,\mathrm{GHz}$. The solid line shows the modified Press-Schechter prescription as used in this work.

results obtained by Rubiño-Martín & Sunyaev [107] using Monte-Carlo simulations based on a Press-Schechter approach. In the estimates presented below we will use the curve given by the solid line in Fig.2.3, which in the most interesting range of lower flux limits (1 mJy -10 mJy) has an effective power-law slope in the range $\lambda \sim 1.10 - 1.25$.

In Fig. 2.4 we compare the motion-induced dipolar asymmetry in number counts as a function of the observing frequency using the optimal patch radius $\theta_\mathrm{r} = 70^\circ$ for both sides of the sky with the $1\sigma$ Poisson noise level for the two lower flux limits of 1 mJy and 10 mJy. In addition we mark the regions where we expect an increase of the number of negative sources and a decrease/increase of the number of positive sources, respectively, if one is observing only in the direction of the maximum of the CMB dipole. It is important to note that the motion-induced change in the cluster number counts vanishes at frequencies $\nu \sim$ 300 GHz. The exact value of this frequency depends both on the slope of the number count curve and the spectral index.

Fig. 2.5 presents the sensitivity limits where the motion-induced signal is equal to the $3\sigma$ and $5\sigma$ Poissonian noise levels for different observing frequencies. One can see that the most promising frequencies for a detection of the motion-induced asymmetries are around the crossover frequency (i.e.$\sim$ 217 GHz) and in the range $\nu \sim 400 - 500\,\mathrm{GHz}$. Clearly, for a proper modeling near the crossover frequency one has to take into account the contribution from the k-SZ, which has been neglected so far. It is evident that the k-SZ is contributing symmetrically to channels around 217 GHz in the sense that the number of positive and negative sources is approximately equal. On the other hand in the range $\nu \sim 400 - 500\,\mathrm{GHz}$ other astrophysical sources start to contribute to the source counts (see Sect. 2.3.3).

### 2.3.3 Source count contribution from non-SZ populations

In the range $\nu \sim 400 - 500\,\mathrm{GHz}$, which is the most promising for a detection of the motion-induced number count asymmetry, other foreground sources begin to play a role, e.g. dusty

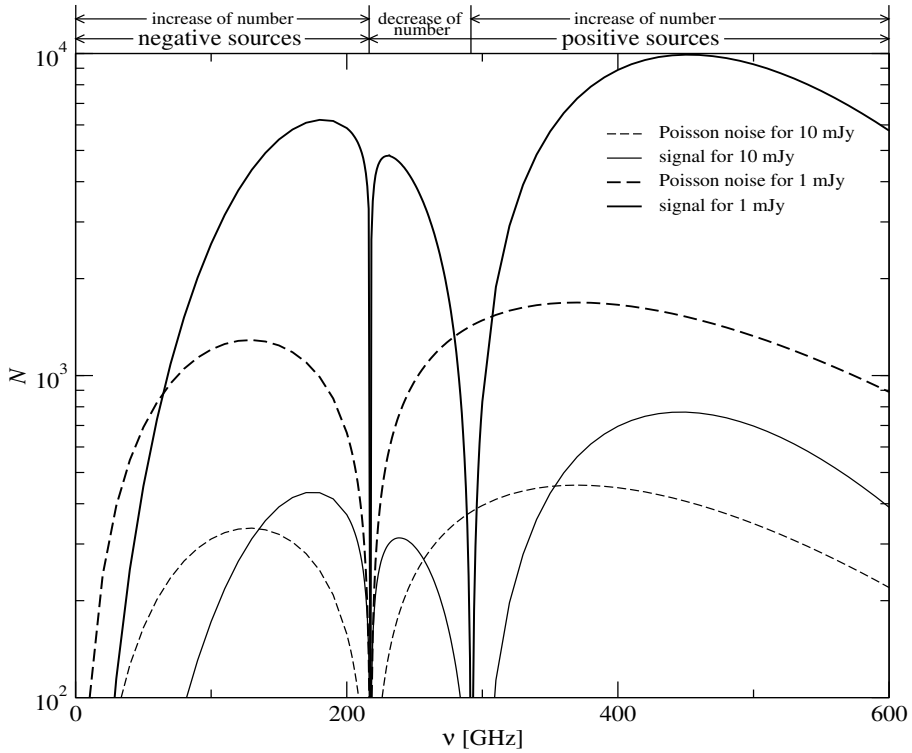


**Figure 2.4:** Motion-induced dipolar asymmetry in number counts (solid lines) as a function of the observing frequency using the optimal patch radius $\theta_r = 70°$ for both patches, where the first is centered on the maximum, the second on the minimum of the CMB dipole. For comparison we give the corresponding $1\sigma$ Poissonian noise level (dashed curves). In addition we mark the regions where we expect an increase of the number of negative sources and a decrease/increase of the number of positive sources, respectively, if one is observing only in the direction of the maximum of the CMB dipole.

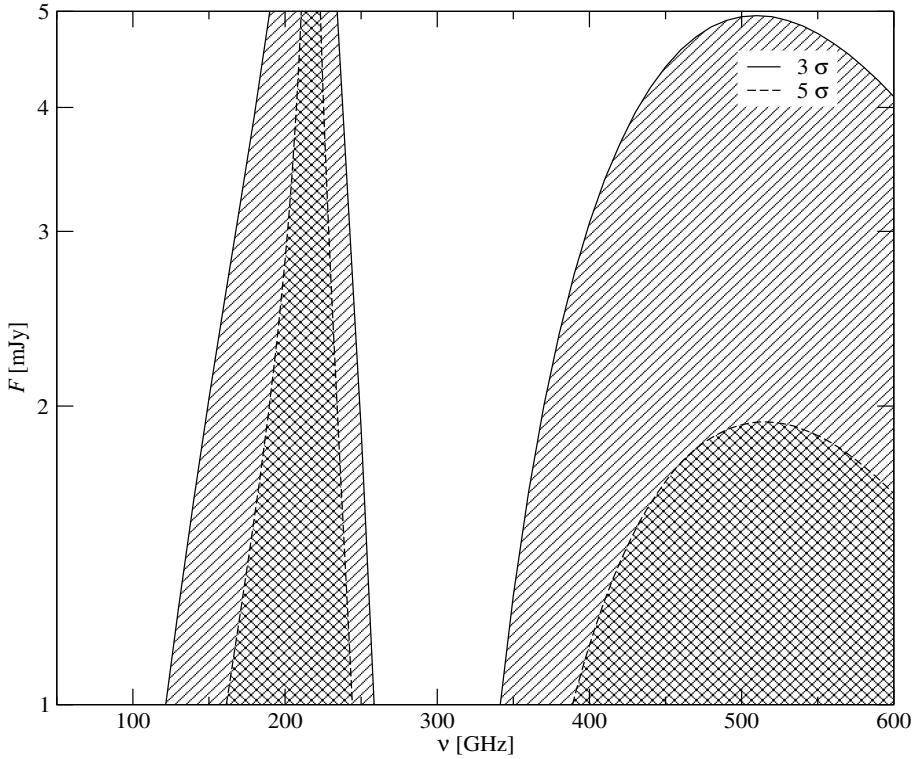


**Figure 2.5:** Required sensitivities for a $3\sigma$ and $5\sigma$-detection of the motion-induced dipolar asymmetry in number counts as a function of frequency. The shaded areas indicate regions where a detection above $3\,\sigma$ and $5\,\sigma$ level is possible, respectively.

high redshift galaxies [18]. In the microwave band these galaxies have an extremely peculiar spectrum $F(\nu) \propto \nu^{-\alpha_{\rm d}}$, with $\alpha_{\rm d}$ ranging from $-3$ to $-4$. Using formula (2.10) it is easy to show that the observed properties of this population will also be influenced by the motion of the Solar System, but in a completely different way than clusters: in the direction of our motion relative to the CMB rest frame their brightness and fluxes decrease when for clusters they increase. This implies that in the frequency range $\nu \sim 400 - 500\,{\rm GHz}$ the motion-induced dipolar asymmetry in the number counts for these sources has the opposite sign in comparison to clusters, i.e. $\Delta N'_{\rm d} < 0$ when $\Delta N'_{\rm cl} > 0$. Detailed multi-frequency observations should allow us to distinguish the source count contributions of these two classes of objects, but nevertheless it is interesting that they have a different sign of the motion-induced flux dipole.

## 2.4 Summary and discussion

We derived the changes to the SZ cluster brightness, flux and number counts induced by the motion of the Solar System with respect to the CMB rest frame. Since both the amplitude and direction of this motion are known with high precision it is easy to take these changes into account in the analysis and interpretation of future SZ data.

The corrections to the SZ cluster brightness and flux have a similar spectral dependence and amplitude as the first order velocity correction to the th-SZ (see Fig. 2.1). Since the motion-induced cluster signal can contribute $\sim 10\%$ of the k-SZ it might be necessary to take it into account in future high precision CMB surveys, dedicated to accurately measuring the line of sight component of the cluster peculiar motions.

The dipolar asymmetry induced in the SZ cluster number counts in contrast to the counts of more conventional sources can change polarity depending on the observational frequency (see Sect. 2.3.3). This behavior is due to the very specific frequency dependence of the SZ effect. Our estimates show that frequencies around the crossover frequency $\sim 217$ GHz and in the range $\sim 400 - 500$ GHz are most promising for a detection of this motion-induced number count asymmetry (see Fig. 2.5).

# Chapter 3

# Spectral distortion of the CMB and the superposition of blackbodies

The CMB angular temperature fluctuations observed by COBE and WMAP enable us to place a lower limit on the spectral distortions of the CMB at any angular scale. These distortions are connected with the simple fact that the superposition of blackbodies with different temperatures in general is not a blackbody. In this Chapter we show that in the limit of small temperature fluctuations the superposition of blackbodies leads to a y-type spectral distortion.

It is commonly assumed that the spectrum in one direction of the sky is Planckian and that only the temperature changes from point to point. This follows from the nature of the main effects leading to the appearance of these fluctuations, i.e. the Sachs-Wolfe-effect [109] and the Doppler effect due to Thomson scattering off moving electrons [125] at redshift $\sim 1100$. However, as will be demonstrated below, there are spectral distortions in the second order of $\Delta T/T$. These distortions are inevitable when the CMB is observed with finite angular resolution or when regions on the sky containing blackbodies with different temperatures are averaged or compared with each other.

The CMB missions mentioned in the introduction have shown that there are fluctuations of the radiation temperature on the level of $\Delta T \sim \mu$K$-$mK over a broad range of angular scales. Any experiment trying to extend the great success of the COBE/FIRAS instrument, will only have a finite angular resolution and would therefore observe a superposition of several Planck spectra with different temperatures corresponding to the maxima and minima on the CMB sky as measured with WMAP. One may distinguish two basic observational strategies: (i) *absolute* measurements, where the beam flux in some direction on the sky is compared to an internal calibrator (COBE/FIRAS) and (ii) *differential* measurements, where the beam flux in one direction on the sky is compared to the beam flux in another direction (COBE/DMR or WMAP). In the first strategy one observes a sum of blackbodies (SB) due to the average over the beam temperature distribution, whereas in the second two sums of blackbodies are compared with each other. Under these circumstances we will in general speak about the superposition of blackbodies, i.e. the sum and difference of blackbodies with different temperatures.

Any experiment trying to extent the great success of the COBE/FIRAS instrument, which placed strict upper limits [50, 51] on a possible chemical potential [126], $|\mu| < 9 \cdot 10^{-5}$, and y-type [141], $|y| < 1.5 \cdot 10^{-5}$, CMB spectral distortion, will only have a finite angular resolution and would therefore observe a superposition of several Planck spectra with different temperatures corresponding to the maxima and minima on the CMB sky as measured with WMAP. It is known [142] that in the case of a Gaussian temperature distribution this will lead to a spectral distortion indistinguishable from a y-distortion, with a corresponding y-parameter which is proportional to the dispersion of the temperature distribution. Since the temperature fluctuations of the CMB indeed are Gaussian, this implies that the corresponding spectral distortions averaged over large parts of the sky should be of y-type. But here we are interested in the case of measurements with an angular resolution of a few arcminutes to degrees. In this

situation, we deal with the limited statistics of finite regions with different mean temperatures and therefore it is not obvious what type of spectral distortion would be induced in each small patch of the sky. As mentioned above, a similar situation arises when we compare the signals from two regions on the sky, i.e. the difference of the intensities as is usually done in differential observations. Below it will be shown that for any observation of the CMB temperature fluctuations, there will be *unavoidable spectral distortions* due to the difference in the temperature of the radiation we measure and compare and that these distortions will be *indistinguishable from a y-type-distortion*. The biggest distortions arise due to the CMB dipole.

The unprecedented high sensitivity of future or proposed space missions like PLANCK and CMBPOL or ground based instruments under construction like APEX, the South Pole Telescope (SPT), the Atacama Cosmology Telescope (ACT) and QUEST at DASI (QUAD) will offer ways to investigate tiny secondary CMB angular and spectral fluctuations and should therefore add a lot to the success of previous missions. One target will be the measurement of the SZ effect from clusters, proto clusters or groups of galaxies and superclusters [127] or signatures from the first stars in the universe [92]. In the future CMB experiments will be so sensitive that it will be possible to investigate in detail the imprints of reionization and the traces of energy release in the early universe.

Basu et al. [9] proposed a method to constrain the ionization history of the universe and the history of heavy element production using the properties of resonant scattering of CMB photons in the fine structure lines of oxygen, carbon and nitrogen atoms and ions produced by the first generation of stars. The strong frequency dependence of this effect permits one to extract the undisturbed angular dependence of the frequency-independent primary temperature fluctuations and thereby avoid cosmic variance. By comparing the signals in different frequency channels it is possible to investigate the contributions of the lines of different ions at different redshifts and therefore to examine different scenarios of element production and ionization histories in the low density regions of the universe, with overdensities less than $\lesssim 10^4$. The sensitivities of PLANCK and ACT should be sufficient to detect the signals imprinted by the effects of resonant scattering, but the crucial point for the successful measurement of *any* small frequency-dependent signal is the *cross calibration* of the different frequency channels down to the limits set by the sensitivity of the experiments. Full sky missions like COBE/DMR or WMAP normally use the CMB dipole and its annual modulation to check the calibration of their instruments down to a level of $\mu$K, whereas experiments with partial sky coverage like BOOMERANG directly use the CMB dipole for calibration issues [13]. But both methods permit one to cross calibrate different frequency channels only to a first approximation assuming that the dipole has a Planckian spectrum and the same amplitude at all frequencies. Unfortunately, this precision of the cross calibration will likely not be sufficient to detect the signals from the dark ages as discussed by Basu et al. [9].

It is known that the motion system relative to the CMB restframe in addition to the dipole generates (in the second order of $v/c$) a small monopole and quadrupole contribution to the CMB brightness of the sky in the restframe of the observer [129, 12, 23]. Sunyaev & Zeldovich [129], when they were discussing the radiation field inside a cluster of galaxies moving relative to the CMB restframe, have shown that the corresponding dipole-induced quadrupole has a non Planckian spectrum, which was then later derived by Sazonov & Sunyaev [112]. Kamionkowski & Knox [70] later applied this solution to the case of our motion relative to the CMB restframe and proposed to use the dipole-induced quadrupole for calibration purposes.

The solution of Sazonov & Sunyaev [112] is valid in the case of narrow beam observations. In this Chapter we choose an independent approach, which is based on the superposition of blackbody spectra with different temperatures, to look for the maximal and minimal spectral distortion obtainable from CMB maps. Our method allows us to calculate the value of the y-parameter for the dipole-induced monopole and quadrupole for a beam with finite width or equivalently for any average of the signal over extended regions on the sky. Most importantly we show that the difference of the sky brightness in the direction of the maximum and minimum

of the CMB dipole, corresponding to the maximal difference of the radiation temperature on the CMB sky, leads to a y-type distortion with an associated y-parameter of $y_{\rm opt} = 3.1 \cdot 10^{-6}$. We propose here to use this spectral distortion arising due to the CMB dipole to cross calibrate the frequency channels of a CMB experiment in principle down to the level of a few tens of nK. We discuss different observing strategies in order to maximize the inferred spectral distortion (Sect. 3.6).

In this Chapter, we first give a short summary of the basic equations necessary in the following derivations and define some of the terminology used (Sect. 3.1). We then discuss the underlying theory for small spectral distortions (Sect. 3.2) and show that in this limit even the distortions arising due to the superposition of two blackbodies (Sect. 3.3) with close temperatures are well described by a y-type solution. Furthermore, we discuss in detail the spectral distortion due to the superposition of Planck spectra with different temperatures arising from to the CMB dipole (Sect. 3.4) and from the higher multipoles (Sect. 3.5) using generated CMB sky maps for the WMAP best fit model. We discuss the spectral distortions arising in differential measurements of the CMB temperature fluctuation (Sect. 3.6) and how to possibly use the spectral distortions induced by the CMB dipole to cross calibrate the frequency channels of CMB experiments (Sect. 3.7). We end this work with a discussion of the consequences of the obtained results for some of the highly demanding tasks which may be addressed by future CMB projects (Sect. 3.8) and finally conclude in Sect. 3.9. The results of this work have been published in Chluba & Sunyaev [34].

## 3.1 Basic ingredients

### 3.1.1 Compton y-distortion

In the non relativistic limit, the Comptonization of the CMB photons by hot, isotropic, thermal electrons with Compton y-parameter $y = \int \frac{k T_{\rm e}}{m_{\rm e} c^2}\, \sigma_{\rm T}\, N_{\rm e}\, {\rm d}l$, where $T_{\rm e}$ is the temperature of the electron gas, $\sigma_{\rm T}$ is the Thomson cross section and $N_{\rm e}$ is the electron number density, leads to a y-distortion [141]:

$$\frac{\Delta I}{I_0} = y\, \frac{x\, e^x}{e^x - 1} \cdot \left[ x\, \frac{e^x + 1}{e^x - 1} - 4 \right] \tag{3.1}$$

for $y \ll 1$. Here $x = h\nu/k\,T_0$ is the dimensionless frequency, $\nu$ is the photon frequency, $T_0$ is the temperature of the incoming radiation and $\Delta I = I - I_0$ denotes the difference between the observed intensity $I$ and undisturbed CMB blackbody spectrum $I_0 = B_\nu(T_0)$, with

$$B_\nu(T) = \frac{2\,h}{c^2}\, \frac{\nu^3}{e^{h\nu/k\,T} - 1}\,. \tag{3.2}$$

In the Rayleigh Jeans (RJ) limit, i.e. $x \ll 1$, equation (3.1) simplifies to $\Delta T/T_0|_{\rm RJ} = -2\,y$. Since in this limit a blackbody of temperature $T$ is approximately given by $B_{\nu,{\rm RJ}} = \frac{2}{c^2}\,\nu^2\,k\,T$, it is convenient to compare the Comptonized spectrum to a blackbody of temperature $T_{\rm RJ} = T_0\,[1 - 2\,y]$, making the relative difference (3.1) vanish at small $\nu$:

$$\frac{\Delta I}{\bar{I}} = y\, \frac{\hat{x}\, e^{\hat{x}}}{e^{\hat{x}} - 1} \cdot \left[ \hat{x}\, \frac{e^{\hat{x}} + 1}{e^{\hat{x}} - 1} - 2 \right]\,. \tag{3.3}$$

Here we now defined $\hat{x} = h\nu/k\,T_{\rm RJ}$ and $\bar{I} = B_\nu(T_{\rm RJ})$ is a blackbody of temperature $T_{\rm RJ}$. The corresponding difference in the radiation temperature can be written as

$$\frac{\Delta T}{T} = y \cdot g_y(\hat{x}) \equiv y \cdot \left[ \hat{x}\, \frac{e^{\hat{x}} + 1}{e^{\hat{x}} - 1} - 2 \right]\,. \tag{3.4}$$

Here we wish to emphasize again, the most important difference to the standard y-distortion is the fact that $\Delta T/T$ vanishes at low frequencies.

Equation (3.4) shows that the most important characteristic of a y-distortion is given by the function

$$g(\hat{x}) = \hat{x}\,\frac{e^{\hat{x}}+1}{e^{\hat{x}}-1} \equiv \hat{x}\coth\frac{\hat{x}}{2} \tag{3.5}$$

Whenever the function $g(\hat{x})$ characterizes the frequency-dependent part of the relative temperature difference we may speak about a *y-type* spectral distortion.

### 3.1.2 Relation between temperature and intensity

To obtain the relative difference in temperature (3.4) corresponding to a y-distortion from the relative difference in intensity (3.3) the relation

$$\frac{\Delta T}{T} = \frac{\Delta I}{I}\,\frac{\mathrm{d}\ln T}{\mathrm{d}\ln I} = \frac{e^{\hat{x}}-1}{\hat{x}\,e^{\hat{x}}}\,\frac{\Delta I}{I} \tag{3.6}$$

was implicitly used. In CMB measurement this relation is commonly applied to *relate* intensity differences to temperature differences, assuming that the difference in intensity obeys $\frac{\Delta I}{I} \ll 1$ or equivalently $\frac{\Delta T}{T} \ll 1$. The sensitivity of future CMB experiments will be extremely high in a broad range of frequencies and angular scales. Therefore it is important to understand what corrections arise in next order of $\frac{\Delta I}{I}$ and $\frac{\Delta T}{T}$ and what kind of distortions are introduced by using relation (3.6). For this we consider the simplest case, when we are comparing two pure blackbodies with different temperatures $T$ and $T'$ and corresponding intensities $I = B_\nu(T)$ and $I' = B_\nu(T')$. Then using (3.2) the relative difference in intensities can be written as

$$\frac{\Delta I}{I} = \frac{I'-I}{I} = \frac{e^{\hat{x}}-1}{e^{\hat{x}/(1+\Delta)}-1} - 1\,, \tag{3.7}$$

where we defined $\hat{x} = h\nu/k\,T$ and $\Delta = (T'-T)/T$.

Now, using the Taylor expansion up to the second order in $\Delta$ from equation (3.7) we obtain

$$\frac{\Delta I}{I} \approx \frac{\hat{x}\,e^{\hat{x}}}{e^{\hat{x}}-1}\cdot\left[\Delta + g_y(\hat{x})\cdot\frac{\Delta^2}{2}\right] + \mathcal{O}(\Delta^3)\,, \tag{3.8}$$

where $g_y(\hat{x})$ is defined by equation (3.4). Now we apply the relation (3.6) to *infer* the relative temperature difference

$$\frac{\Delta T(\hat{x})}{T} = \Delta + g_y(\hat{x})\cdot\frac{\Delta^2}{2} + \mathcal{O}(\Delta^3)\,. \tag{3.9}$$

This result clearly shows that in the second order of $\Delta$ a y-distortion with y-parameter $y = \Delta^2/2$ is introduced. This distortion vanishes at low frequencies ($\hat{x} \to 0$) and increases like $g_y(\hat{x}) \sim \hat{x}$ in the Wien region ($\hat{x} \gg 1$). Writing $\Delta + g_y(\hat{x})\cdot\Delta^2/2 = \Delta\cdot[1 + g_y(\hat{x})\cdot\Delta/2]$ this implies that for *any* given $\Delta$ there is a critical frequency $\hat{x}_y$ which fulfills

$$g_y(\hat{x}_y) = \frac{2\,\epsilon}{|\Delta|} \tag{3.10}$$

and above which the contribution of the y-distortion relative to the first order term becomes bigger than $\epsilon$. The value of $\epsilon$ is directly related to the sensitivity of the experiments. In Fig. 3.1 $\hat{x}_y$ has been calculated for different $\epsilon$. At frequencies lower than $\hat{x}_y$ the relation (3.6) is exact within the sensitivity of the experiment, whereas for $\hat{x} > \hat{x}_y$ the second order correction has to be taken into account. In the regime $\hat{x}_y \gtrsim 4$ for estimates the simple approximation $\hat{x}_y = 2\,\epsilon/|\Delta| + 2$ may be used.

To give an example, the biggest temperature fluctuation on the whole CMB sky is due to the CMB dipole. Comparing the maximum and the minimum of the dipole corresponds to

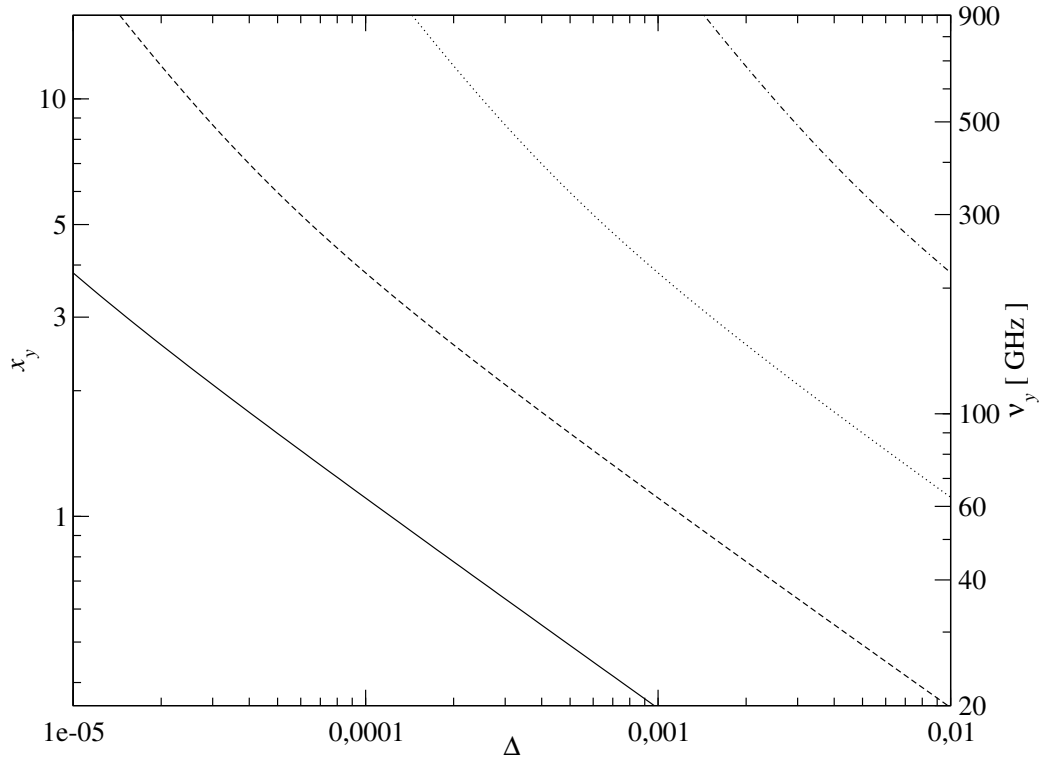


**Figure 3.1:** $\hat{x}_y$ as a function of $\Delta$ for different values of $\epsilon$ according to equation (3.10): For $\epsilon = 10^{-5}$ (solid), $\epsilon = 10^{-4}$ (dashed), $\epsilon = 10^{-3}$ (dotted) and $\epsilon = 10^{-2}$ (dashed-dotted). The right ordinate corresponds to $\nu_y = k\,T_0 \cdot \hat{x}_y/h$, with $T_0 = 2.725\,\mathrm{K}$.

$\Delta \sim 2.48{\cdot}10^{-3}$. If some CMB experiment is able to accurately measure temperature fluctuations on the level of $\mu$K, contributions of $\epsilon \sim 10^{-4}$ relative to the dipole signal can be distinguished leading to $\hat{x}_{y,\mathrm{d}} \sim 1$. This estimate shows that at high frequencies spectral distortions introduced by the usage of the relation (3.6) for the dipole anisotropy should be taken into account in future CMB missions like Planck and Act. In Sect. 3.4 we will discuss these distortions due to the dipole in more detail.

The temperature difference should not be larger than a few percent of the temperature of the reference blackbody, otherwise corrections due to higher orders in $\Delta$ will become important and lead to additional distortions (see Sect. 3.2). Fortunately, the temperature differences on the CMB sky are sufficiently small to neglect these corrections.

Equation (3.9) also shows that in general the inferred temperature difference is frequency-dependent. At frequencies below $\hat{x}_y$ the *inferred* temperature difference is close to the *true* temperature difference $\Delta$ and frequency-independent within the sensitivity of the experiment. In this case, we will speak about a *temperature* distortion or fluctuation, emphasizing that it is frequency-independent. It is possible to eliminate the temperature distortion using multi-frequency measurements. For $\hat{x} > \hat{x}_y$ frequency- dependent terms become important, which we will henceforth call *spectral* distortions.

## 3.2 Small spectral distortions due to the superposition of blackbodies

When the CMB sky is observed with finite angular resolution or equivalently if the brightness of parts of the sky (not necessarily connected) are averaged one is dealing with the sum and more generally with the superposition of blackbodies. Here we develop a general formalism to calculate the spectral distortions arising for arbitrary temperature distribution functions

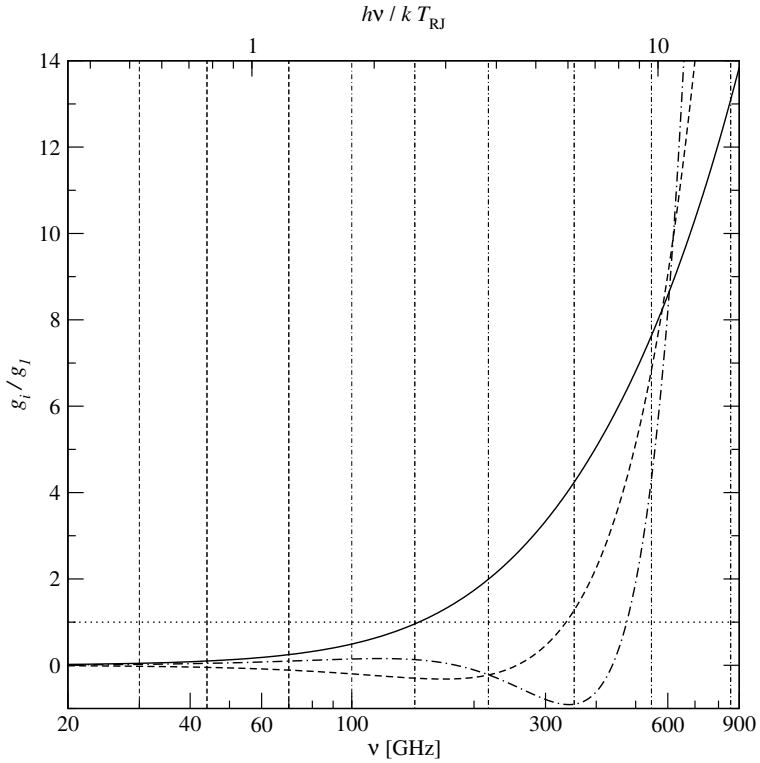


**Figure 3.2:** Frequency dependence of $g_i/g_1 \equiv \Delta T_i/T_{\rm RJ}\,\delta^i$: Dotted line $\Delta T_1/T_{\rm RJ}\,\delta$, which is equivalent to a temperature distortion, solid line $g_y(\hat{x}) = 2\Delta T_2/T_{\rm RJ}\,\delta^2$, which is equivalent to a y-distortion $\Delta T/y\,T_0$ as given by equation (3.4), dashed line $\Delta T_3/T_{\rm RJ}\,\delta^3$ and dashed-dotted line $\Delta T_4/T_{\rm RJ}\,\delta^4$. The function $g_y(\hat{x})$ becomes larger than unity for $\nu \geq 146.2$ GHz or $\hat{x} \geq 2.57$, larger than 5 for $\nu \geq 396.7\,$GHz or $\hat{x} \geq 6.99$ and larger than 10 for $\nu \geq 681.3\,$GHz or $\hat{x} \geq 12$. For $\nu = 100$ GHz or $\hat{x} = 1.76$ it follows $g_y = 0.5$. Also shown as vertical lines are the PLANCK LFI (dashed) and HFI (dash-dotted) frequency channels.

in the limit of small temperature fluctuations and derive criteria for the applicability of this approximation. We first discuss the basic equations necessary to describe the spectrum of the sum of blackbodies (SB) as compared to some arbitrary *reference* blackbody (Sect. 3.2.1) and then generalize these results to the superposition of blackbodies (Sect. 3.2.2).

### 3.2.1 Sum of blackbodies

Following the paper of [142] we express the total spectrum resulting for the SB with different temperatures $T$ as:

$$I(\nu) = \int R(T)\, B_\nu(T)\, \mathrm{d}T\,. \tag{3.11}$$

Here $R(T)$ denotes the normalized ($\int R\,\mathrm{d}T = 1$, $R \geq 0$) temperature distribution function, which will be used below to model the *beam* of some CMB experiment, and $B_\nu(T)$ is a Planck spectrum of temperature $T$ as given by equation (3.2). Now we want to compare the spectrum $I(\nu)$ to a *reference* blackbody of temperature $T_{\rm ref}$. Defining $\delta = (T - T_{\rm ref})/T_{\rm ref}$ and inserting $T = T_{\rm ref}\,(1+\delta)$ into equation (3.2), $B_\nu$ may be rewritten as

$$B_\nu(\delta) = A\,T_{\rm ref}^3\,\frac{\hat{x}^3}{e^{\hat{x}/(1+\delta)} - 1} \tag{3.12}$$

where $\hat{x} = h\nu/k\,T_{\rm ref}$ is the dimensionless frequency and $A = 2k^{\,3}/h^2\,c^2$. CMB temperature fluctuations are of the order $\Delta T/T \sim 10^{-5} - 10^{-3}$. Therefore we are interested in the case

when $|\delta| \ll 1$. This allows us to perform a Taylor expansion of equation (3.12):

$$B_\nu(\delta) = B_\nu|_{\delta=0} - \delta\cdot\hat{x}\,\frac{\partial B_\nu}{\partial\xi}\bigg|_{\delta=0} + \frac{\delta^2}{2}\cdot\hat{x}\,\left[\hat{x}\,\frac{\partial^2 B_\nu}{\partial\xi^2} + 2\,\frac{\partial B_\nu}{\partial\xi}\right]_{\delta=0} - \frac{\delta^3}{6}\cdot\hat{x}\,\left[\hat{x}^2\,\frac{\partial^3 B_\nu}{\partial\xi^3} + 6\,\hat{x}\,\frac{\partial^2 B_\nu}{\partial\xi^2} + 6\,\frac{\partial B_\nu}{\partial\xi}\right]_{\delta=0} + \frac{\delta^4}{24}\cdot\hat{x}\,\left[\hat{x}^3\,\frac{\partial^4 B_\nu}{\partial\xi^4} + 12\,\hat{x}^2\,\frac{\partial^3 B_\nu}{\partial\xi^3} + 36\,\hat{x}\,\frac{\partial^2 B_\nu}{\partial\xi^2} + 24\,\frac{\partial B_\nu}{\partial\xi}\right]_{\delta=0}, \tag{3.13}$$

where here $\xi = \hat{x}/(1+\delta)$ was defined. Keeping only terms up to fourth order in $\delta$ this simplifies to:

$$B_\nu(\delta) = I_{\rm ref}\sum_{k=0}^{4} g_k(\hat{x})\,\delta^k\,. \tag{3.14}$$

Here we used the abbreviation $I_{\rm ref} = B_\nu(\delta = 0)$ for the reference blackbody spectrum of temperature $T_{\rm ref}$ and defined the functions $g_k(\hat{x})$ as

$$g_0(\hat{x}) = 1 \tag{3.15a}$$

$$g_1(\hat{x}) = \frac{\hat{x}\,e^{\hat{x}}}{e^{\hat{x}}-1} \tag{3.15b}$$

$$g_2(\hat{x}) = \frac{g_1}{2}\left[\hat{x}\,\frac{e^{\hat{x}}+1}{e^{\hat{x}}-1} - 2\right] \equiv \frac{g_1}{2}\cdot g_y(\hat{x}) \tag{3.15c}$$

$$g_3(\hat{x}) = g_1\left[\frac{\hat{x}^2}{6}\,\frac{\cosh\hat{x}+2}{\cosh\hat{x}-1} - \frac{2g_2}{g_1} - 1\right] \tag{3.15d}$$

$$g_4(\hat{x}) = g_1\left[\frac{\hat{x}^3}{24}\,\frac{6\coth\frac{\hat{x}}{2} + \sinh\hat{x}}{\cosh\hat{x}-1} - 3\,\frac{g_2+g_3}{g_1} - 1\right] \tag{3.15e}$$

where $g_y(\hat{x})$ is defined by equation (3.4). In Fig. 3.2 the frequency dependence of the functions $g_i(\hat{x})$ is illustrated. Deviations from a blackbody spectrum become most important in the Wien region and vanish in the RJ region of the CMB spectrum.

Inserting equation (3.14) into (3.11) the relative difference $\Delta I/I_{\rm ref} = (I - I_{\rm ref})/I_{\rm ref}$ between the SB spectrum and the reference blackbody $I_{\rm ref}$ can be derived

$$\frac{\Delta I}{I_{\rm ref}} \approx \sum_{k=1}^{4} g_k(\hat{x})\,\left\langle\delta^k\right\rangle\,, \tag{3.16}$$

where we introduced the abbreviation $\left\langle\delta^k\right\rangle = \int R\,\delta^k\,{\rm d}T$ for the $k$-th moment of the temperature distribution. To find the corresponding difference in temperatures from (3.16) one may use the relation (3.6). As mentioned before the *inferred* temperature difference in general will be frequency-dependent.

In equation (3.16) the term proportional to the first moment, $\left\langle\delta^1\right\rangle$, corresponds to a temperature distortion which introduces a frequency-independent shift in the measured temperature difference. It is possible to eliminate this contribution by multi-frequency measurements, since it does not change with frequency. The term proportional to the second moment is indistinguishable from a Compton y-distortion as given by equation (3.3) with y-parameter

$$y_{\rm S} = \frac{\left\langle\delta^2\right\rangle}{2}\,. \tag{3.17}$$

Higher moments lead to additional spectral distortions making the total spectral distortion differ from a pure y-distortion. As will be shown below for the CMB these higher order corrections can be neglected.

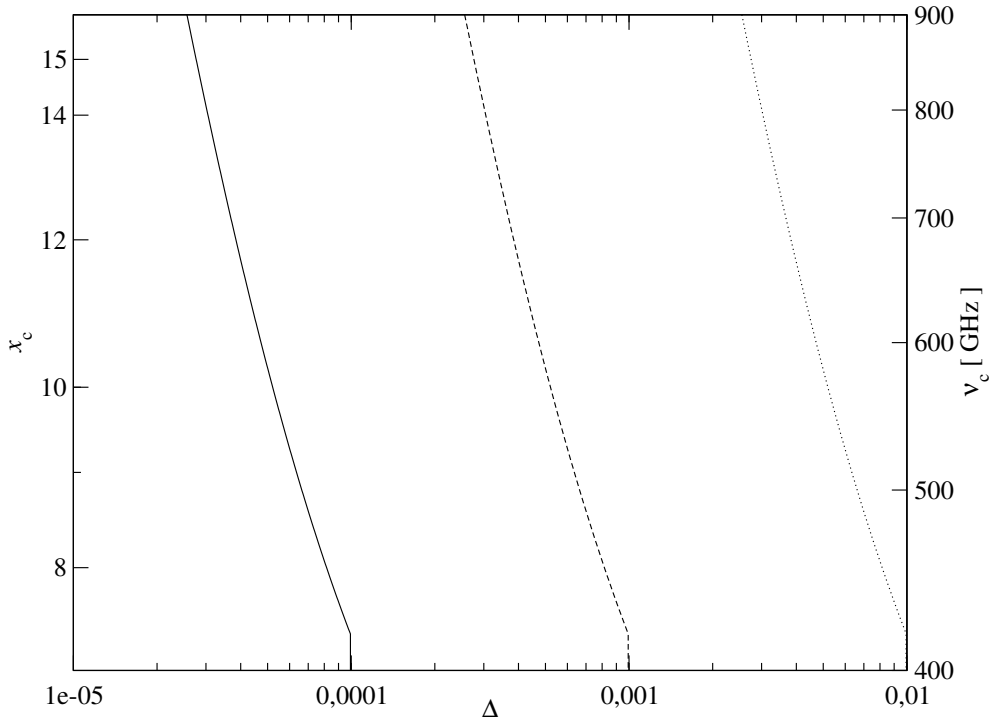


**Figure 3.3:** $\hat{x}_\mathrm{c}$ as a function of $\Delta$ for different values of $\epsilon$ according to equation (3.21) assuming that $\langle \delta^k \rangle = \Delta^k$: For $\epsilon = 10^{-4}$ (solid), $\epsilon = 10^{-3}$ (dashed) and $\epsilon = 10^{-2}$ (dotted). The right ordinate corresponds to $\nu_\mathrm{c} = k\,T_0 \cdot \hat{x}_\mathrm{c}/h$, with $T_0 = 2.725\,\mathrm{K}$.

## Limiting cases for $\frac{\Delta T}{T_\mathrm{ref}}$

In the RJ limit ($\hat{x} \ll 1$), starting from (3.11) and using relation (3.6) one can find

$$\left.\frac{\Delta T}{T_\mathrm{ref}}\right|_\mathrm{RJ} \overset{\hat{x}\ll 1}{\approx} \langle\delta\rangle + \frac{\hat{x}^2}{12}\left\langle\frac{\delta^2}{1+\delta}\right\rangle \tag{3.18a}$$

$$\overset{\hat{x}\ll 1 \wedge \delta \ll 1}{\approx} \langle\delta\rangle + \frac{\hat{x}^2}{12}\Big[\langle\delta^2\rangle - \langle\delta^3\rangle + \langle\delta^4\rangle\Big]. \tag{3.18b}$$

This result shows that for $\hat{x} \to 0$ the functions $g_2$, $g_3$, and $g_4$ all vanish like $\sim x^2$, reflecting the fact that the sum of RJ spectra is again a RJ spectrum and that no spectral distortions are expected for $\hat{x} \ll 1$. In the first step we have only assumed that $\hat{x} \ll 1$. Therefore, up to the second order in $\hat{x}$ equation (3.18a) describes the SB for any $\delta$ to very high accuracy. For $\delta \gg 1$ equation (3.18a) takes the form $\Delta T/T_\mathrm{ref}|_\mathrm{RJ} \approx \langle\delta\rangle \cdot [1 + \frac{\hat{x}^2}{12}]$. For the approximation (3.18b) we have in addition to $\hat{x} \ll 1$ assumed that $\delta \ll 1$. In this limit the same result can be obtained starting from equation (3.16).

In the Wien region of the CMB spectrum ($\hat{x} \gg 1$) again starting from (3.11) and using relation (3.6) one can deduce

$$\left.\frac{\Delta T}{T_\mathrm{ref}}\right|_\mathrm{W} \overset{\hat{x}\gg 1}{\approx} \frac{1}{x}\cdot\left[\left\langle\exp\left(x\cdot\frac{\delta}{1+\delta}\right)\right\rangle - 1\right] \tag{3.19a}$$

$$\overset{\hat{x}\gg 1 \wedge x\cdot\delta \ll 1}{\approx} \langle\delta\rangle - \langle\delta^2\rangle + \langle\delta^3\rangle - \langle\delta^4\rangle + \frac{\hat{x}}{2}\left[\langle\delta^2\rangle + \frac{\hat{x}}{3}\,\langle\delta^3\rangle + \frac{\hat{x}^2}{12}\,\langle\delta^4\rangle\right]. \tag{3.19b}$$

Equation (3.19a) is valid for $\hat{x} \gg 1$ and arbitrary $\delta$, whereas (3.19b) only is applicable for $\hat{x} \gg 1$ and $x \cdot \delta \ll 1$. Result (3.19b) can be also obtained starting from equation (3.16).

### When do higher order moments become important?

Using multi-frequency observations it is possible to eliminate the temperature distortion ($\propto \langle\delta\rangle$). In this case, the leading term in the signal corresponds to the y-distortion. Here we are interested in the question when higher order moments start to contribute significantly to the total spectral distortions. In the RJ region using equation (3.18b) one can find that for

$$\epsilon \cdot \left\langle \delta^2 \right\rangle > |\left\langle \delta^3 \right\rangle - \left\langle \delta^4 \right\rangle| \tag{3.20}$$

the relative contributions of the higher moments to the y-distortion is less than $\epsilon$. This equation shows that in general corrections due to the higher moments will be of the order of $\sim |\left\langle \delta^3 \right\rangle| / \left\langle \delta^2 \right\rangle$. For temperature distributions which are symmetric around the reference temperature all the odd moments vanish. In this case the corrections typically will be of the order of $\sim \left\langle \delta^4 \right\rangle / \left\langle \delta^2 \right\rangle$. If we consider the simple case, when we compare two pure blackbodies with temperatures $T_1$ and $T_2$ and use $T_{\rm ref} = T_1$ then the moments are given as $\left\langle \delta^k \right\rangle = \Delta^k$, with $\Delta = (T_2 - T_1)/T_1$. From this we can conclude that the relative contribution of the third moment to the spectral distortion will be $\lesssim |\Delta|$. Therefore, in the RJ region of the spectrum even for $\Delta \sim 10^{-2}$ higher order moments will lead to corrections $\lesssim 1\%$ to the y-distortion. For the CMB with $\Delta \sim 10^{-5} - 10^{-3}$ these corrections can be safely neglected.

In the Wien region the situation is a bit more complicated. Given some value of $\epsilon$ one can find the frequency $\hat{x}_{\rm c}$ above which the relative contribution of higher order moments will become important. To find $\hat{x}_{\rm c}$ one has to solve the non-linear equation

$$\epsilon = \frac{g_3(\hat{x}_{\rm c}) \left\langle \delta^3 \right\rangle + g_4(\hat{x}_{\rm c}) \left\langle \delta^4 \right\rangle}{g_2(\hat{x}_{\rm c}) \left\langle \delta^2 \right\rangle} \tag{3.21}$$

or an equivalent equation directly using (3.11). In Fig. 3.3 $\hat{x}_{\rm c}$ has been calculated for different $\epsilon$ and $\Delta$ again considering the simple case, when we compare two pure blackbodies with temperatures $T_1$ and $T_2$ and use $T_{\rm ref} = T_1$. Higher order moments contribute 1% to the total spectral distortion above $\hat{x}_{\rm c} = 10$ for $\Delta \sim 5 \cdot 10^{-3}$, which is roughly 5 times the dipole amplitude. For $|\Delta| \lesssim 3 \cdot 10^{-3}$ corrections are less than 1% even in the highest Planck frequency channels. In the limit $\hat{x}_{\rm c} \gtrsim 6$ for estimates of the critical frequency above which higher order correction become bigger than $\epsilon$ one may use

$$\hat{x}_{\rm c} = \min \left[ 3\,\epsilon\, \frac{\left\langle \delta^2 \right\rangle}{|\left\langle \delta^3 \right\rangle|} + 4, \sqrt{12\,\epsilon\, \frac{\left\langle \delta^2 \right\rangle}{\left\langle \delta^4 \right\rangle}} + 5 \right] . \tag{3.22}$$

In summary, the above discussion shows that as long as $|\Delta| < \epsilon$ the spectral distortion for $\hat{x} < \hat{x}_{\rm c}$ is given by a pure y-distortion. In this case the biggest deviations from a y-distortion are expected in the Wien region of the CMB spectrum, where the sensitivity of the Planck mission and other future experiments is high. But even for the dipole anisotropy these corrections should be less than 1%. If $|\Delta| \sim \epsilon$ deviations in the RJ become important and higher order corrections have to be taken into account. Given the amplitude of the temperature fluctuations on the CMB sky, $\Delta \sim 10^{-5} - 10^{-3}$, corrections to the y-distortion due to higher moments will be less than 1% in the highest Planck frequency channels even for the dipole amplitude and certainly less than 0.1% for the higher multipoles. Therefore we can safely describe the spectral distortions arising due to the superposition of blackbodies with slightly different temperatures by y-distortions. In what follows below we assume that higher order corrections are negligible.

### Beam spectral distortion

In the RJ limit the sum of blackbodies (SB) is again a blackbody with temperature $T_{\rm RJ} = \int R\,T\,{\rm d}T$. The RJ temperature $T_{\rm RJ}$ can be directly measured at sufficiently low frequencies and hence it is convenient to compare the SB to a *reference* blackbody of temperature $T_{\rm RJ}$. This makes any distortion due to the SB vanish at low $\nu$.

In the following, we will call $\langle \delta^k \rangle$ *beam* moment, when $\delta = (T - T_{\rm RJ})/T_{\rm RJ}$ is defined as the relative difference between the temperature $T$ of a given blackbody inside the beam and the RJ temperature of the SB, i.e. the beam RJ temperature $T_{\rm RJ}$. For this choice of reference blackbody the temperature distortion vanishes and we obtain

$$\frac{\Delta I}{\bar{I}} \approx g_2(\hat{x}) \, \langle \delta^2 \rangle \, , \tag{3.23}$$

where $\hat{x} = h\nu/k\,T_{\rm RJ}$ and we introduced $\bar{I} = B_\nu(T_{\rm RJ})$. We should mention again that the beam spectral distortion arising due to the SB with different temperatures can be approximated by a pure y-distortion with y-parameter $y_{\rm S}$ as given by (3.17), if only the second moment of the temperature distribution, $\langle \delta^2 \rangle$, is important. In general higher moments have to be taken into account leading to additional spectral distortions.

It is important to note that for any given temperature distribution the minimal distortion arising due to the sum of Plancks corresponds to a y-distortion with y-parameter $y_{\rm S}$. Therefore by calculating the second beam moment it is possible to place a lower limit on the distortions arising from any average over not necessarily connected regions of the CMB sky.

### Sum of two Planck spectra with different weights

For the sum of two Planck spectra with temperatures $T_1$ and $T_2$ of relative weights $w_1$ and $w_2 = 1 - w_1$ the RJ temperature is given by $\bar{T} = w_1\,T_1 + w_2\,T_2$. For the first five beam moments one may obtain:

$$\langle \delta^0 \rangle = 1, \qquad \langle \delta^1 \rangle = 0 \tag{3.24a}$$

$$\langle \delta^2 \rangle = w_1\,w_2 \cdot \left[\frac{\Delta T}{\bar{T}}\right]^2 \tag{3.24b}$$

$$\langle \delta^3 \rangle = w_1\,w_2\,(1 - 2\,w_1) \cdot \left[\frac{\Delta T}{\bar{T}}\right]^3 \tag{3.24c}$$

$$\langle \delta^4 \rangle = w_1\,w_2\,(1 - 3\,w_1\,w_2) \cdot \left[\frac{\Delta T}{\bar{T}}\right]^4 . \tag{3.24d}$$

Here $\Delta T = T_1 - T_2 \neq 0$ was defined. Making use of equation (3.22), in general ($w_1 \neq w_2 \neq 0$) the spectral distortion significantly deviates from a y-distortion by a fraction $\epsilon$ at frequencies

$$\hat{x} \geq \min\left[\frac{3\,\epsilon}{|1 - 2\,w_1|}, \sqrt{\frac{12\,\epsilon}{1 - 3\,w_1\,w_2}}\right] \cdot \frac{\bar{T}}{|\Delta T|} \tag{3.25}$$

If one of the weights $w_1$ or $w_2$ vanishes then, as expected, there is no distortion. In the case $w_1 \equiv w_2$, all the odd moments vanish and the even moments are given by $\langle \delta^n \rangle = [\Delta T/(T_1 + T_2)]^n$. Then the critical frequency $\hat{x}_{\rm c} = 2 \cdot \sqrt{3} \cdot 10^{-1}\,(T_1 + T_2)/|\Delta T|$ above which the spectral distortion deviates significantly from a y-distortion becomes 10 only if $|\Delta T| \approx 0.069\,\bar{T}$. This implies that for non Gaussian temperature distributions deviations from a y-distortion will only be important if the temperature difference becomes of the order of a few % of the RJ temperature. This is clearly not the case for the CMB in the observed universe. Even the dipole anisotropy leads to a y-distortion up to very high frequencies and we can safely neglect the contributions of moments of the temperature distribution with $k > 2$.

### Difference to an arbitrary reference blackbody

Here we want to derive the equations describing the comparison of the spectrum of the SB with an arbitrary reference blackbody. This example can be applied for *absolute* measurements of the CMB. Starting again from equation (3.16) and using the results obtained for the beam

spectral distortions, one can rewrite the moments of $\delta_{\rm ref} = (T - T_{\rm ref})/T_{\rm ref}$ in terms of the *beam* moments, $\langle \delta^k \rangle$ and $\Delta_{\rm RJ} = (T_{\rm RJ} - T_{\rm ref})/T_{\rm ref}$, with $\delta = (T - T_{\rm RJ})/T_{\rm RJ}$:

$$\langle \delta^1_{\rm ref} \rangle = \Delta_{\rm RJ} \tag{3.26a}$$

$$\langle \delta^2_{\rm ref} \rangle = \langle \delta^2 \rangle + \Delta^2_{\rm RJ} + \mathcal{O}\left(\langle \delta^2 \rangle \cdot \Delta_{\rm RJ}\right) . \tag{3.26b}$$

Using formula (3.16), one can directly infer the relative difference between the spectrum of the SB and the *chosen* reference blackbody $I_{\rm ref} = B_\nu(T_{\rm ref})$:

$$\frac{I - I_{\rm ref}}{I_{\rm ref}} = g_1(\hat{x}_{\rm ref})\, \Delta_{\rm RJ} + g_2(\hat{x}_{\rm ref})\, \left[\Delta^2_{\rm RJ} + \langle \delta^2 \rangle\right] , \tag{3.27}$$

where $\hat{x}_{\rm ref} = h\nu/k\,T_{\rm ref}$ and we assumed that the contributions of $\langle \delta^2 \rangle \cdot \Delta_{\rm RJ}$ and any higher moments of both $\delta$ and $\Delta_{\rm RJ}$ are negligible. Note that $g_2(\hat{x}_{\rm ref}) = g_2(\hat{x}) \cdot [1 + \mathcal{O}(\Delta_{\rm RJ})]$ and therefore $g_2(\hat{x}_{\rm ref}) \langle \delta^2 \rangle \equiv \Delta I/\bar{I}$, where $\Delta I/\bar{I}$ is given by equation (3.23).

Equation (3.27) shows that the spectral distortion of the SB spectrum with respect to the some reference blackbody $I_{\rm ref}$ has the following three contributions:

(i) A temperature distortion $\propto \Delta_{\rm RJ}$. This distortion vanishes if the SB is compared to a blackbody with temperature $T_{\rm ref} = T_{\rm RJ}$. Since the y-distortion vanishes in the RJ region of the CMB spectrum $\Delta_{\rm RJ}$ can be directly measured at low frequencies.

(ii) A y-distortion $\propto \Delta^2_{\rm RJ}$ due to the dispersion of the RJ temperature of the SB with respect to the chosen reference temperature. This contribution also vanishes if the chosen reference blackbody has temperature $T_{\rm ref} = T_{\rm RJ}$.

(iii) A y-distortion $\propto \langle \delta^2 \rangle$ due to the dispersion of the temperature $T$ with respect to the RJ temperature of the SB. Only if the temperature distribution function is a Dirac $\delta$-function, i.e. when all the blackbodies inside the beam have the same temperature or equivalently when the angular resolution of the experiment is *infinite*, this term vanishes. For the SB it sets the minimal value of the y-parameter for a given temperature distribution function.

Equation (3.27) represents the most general case for the comparison of the SB with any reference blackbody in the limit of small temperature fluctuations around the temperature of the reference blackbody. It implies that in this limit the y-distortion arising due to the comparison of the SB spectrum with some chosen reference blackbody with temperature $T_{\rm ref}$ is completely determined by the second beam moment and the beam RJ temperature.

### 3.2.2 Superposition of Planck spectra

Using the results obtained so far, it is possible to generalized the sum of Planck spectra to the superposition of Planck spectra. This case applies for *differential* measurements of the CMB, where we directly compare two identical beams with intensities $I_1$ and $I_2$ and measure the intensity difference $\Delta I = I_2 - I_1$. If we want to apply the relation (3.6) to relate $\Delta I \leftrightarrow \Delta T$ then we have to fix the *reference* temperature $T_{\rm ref}$ and thereby define the reference blackbody $I_{\rm ref}$. During the discussion in Sect. 3.1.2 we used $T_{\rm ref} = T$ (cf. equation (3.7)) but in principle one is free to choose any temperature for which the limit of small spectral distortions is justified, since $\Delta I = I_2 - I_1 = I_2 - I_{\rm ref} + I_{\rm ref} - I_1$. In the case of the CMB, one will usually set $T_{\rm ref}$ equal to the whole sky mean temperature $T_0$, but as will be shown below the *inferred* y-distortion strongly depends on this choice.

Defining $\Delta_i = (T_i - T_{\rm ref})/T_{\rm ref}$, where $T_i$ are the temperatures of the blackbodies inside the beam $i$, and applying formula (3.16) one may obtain

$$\frac{I_2 - I_1}{I_{\rm ref}} = g_1(\hat{x})\, \left[\Delta_{{\rm sup},12} + g_y(\hat{x}) \cdot y_{{\rm sup},12}\right] , \tag{3.28}$$

with $\hat{x} = h\,\nu/k\,T_{\rm ref}$ and

$$\Delta_{\rm sup,12} = \langle\Delta_2\rangle_{\rm b,2} - \langle\Delta_1\rangle_{\rm b,1} = \frac{\bar{T}_{\rm b,2} - \bar{T}_{\rm b,1}}{T_{\rm ref}} \tag{3.29a}$$

$$y_{\rm sup,12} = \frac{1}{2}\left[\left\langle\Delta_2^2\right\rangle_{\rm b,2} - \left\langle\Delta_1^2\right\rangle_{\rm b,1}\right], \tag{3.29b}$$

where $\langle X\rangle_{{\rm b},i}$ denotes the corresponding beam averages and we defined the beam RJ temperatures $\bar{T}_{{\rm b},i} = \langle T_i\rangle_{{\rm b},i}$. In equation (3.28) we have neglected the contributions of any higher moments of $\Delta_i$. Here the temperature distortion is directly related to the relative difference of the RJ temperatures.

The y-parameter $y_{\rm sup,12}$ can be rewritten using the beam moments $\left\langle\delta_i^2\right\rangle_{{\rm b},i}$, with $\delta_i = (T_i - \bar{T}_{{\rm b},i})/\bar{T}_{{\rm b},i}$ and defining $\Delta_{{\rm ref},i} = \langle\Delta_i\rangle_{{\rm b},i} = (\bar{T}_{{\rm b},i} - T_{\rm ref})/T_{\rm ref}$:

$$y_{\rm sup,12} = \frac{1}{2}\left[\left\langle\delta_2^2\right\rangle_{\rm b,2} - \left\langle\delta_1^2\right\rangle_{\rm b,1}\right] + \frac{1}{2}\left[\Delta_{\rm ref,2}^2 - \Delta_{\rm ref,1}^2\right] + \mathcal{O}(\left\langle\delta_i^2\right\rangle_{{\rm b},i}\cdot\Delta_{{\rm ref},i})\,. \tag{3.30}$$

The difference of the beam moments $\left\langle\delta_i^2\right\rangle_{{\rm b},i}$ does not depend on the chosen reference temperature $T_{\rm ref}$ and therefore always leads to the same contribution

$$y_{\rm b} = \frac{1}{2}\left[\left\langle\delta_2^2\right\rangle_{\rm b,2} - \left\langle\delta_1^2\right\rangle_{\rm b,1}\right] \tag{3.31}$$

to the inferred y-parameter. In the limit of high angular resolution it vanishes. For the second term in (3.30) ($\propto \Delta_{\rm ref,2}^2 - \Delta_{\rm ref,1}^2$) one finds

$$y_{12}(T_{\rm ref}) = \frac{1}{2}\left[\Delta_{\rm ref,2}^2 - \Delta_{\rm ref,1}^2\right] = \Delta_{\rm sup,12}\cdot\Delta_{\rm RJ}\,, \tag{3.32}$$

with $\Delta_{\rm RJ} = (T_{\rm RJ} - T_{\rm ref})/T_{\rm ref}$ and $T_{\rm RJ} = (\bar{T}_{\rm b,1} + \bar{T}_{\rm b,2})/2$. This contribution to the total inferred y-parameter, $y_{\rm sup,12}(T_{\rm ref}) = y_{\rm b} + y_{12}(T_{\rm ref})$, depends on the choice of $T_{\rm ref}$. Here it becomes clear that setting $T_{\rm ref} \equiv T_{\rm RJ}$, i.e. to the average RJ temperature of the sum of *both* beams, only the difference of the second *beam* moments leads to a y-distortion. Let us note here that equation (3.27) is a special case of (3.28), where beam 1 has no contribution of the beam moment $\left\langle\delta_1^2\right\rangle_{\rm b,1}$, i.e. where the beam spectrum is a blackbody with temperature $\bar{T}_{\rm b,1}$, and where $T_{\rm ref} = \bar{T}_{\rm b,1}$.

### Dependence on the reference temperature

Here we want to clarify some aspects of the dependence of the inferred y-parameter on the chosen reference temperature. If we assume that $y_{\rm b} \ll 1$ and $\bar{T}_{\rm b,2} > \bar{T}_{\rm b,1}$, we can find the reference temperature at which the total y-distortion vanishes:

$$T_{y=0} = \frac{\bar{T}_{\rm b,1} + \bar{T}_{\rm b,2}}{2}\left[1 + \frac{\bar{T}_{\rm b,1} + \bar{T}_{\rm b,2}}{\bar{T}_{\rm b,2} - \bar{T}_{\rm b,1}}\cdot\frac{y_{\rm b}}{2}\right]. \tag{3.33}$$

In the limit of high angular resolution ($y_{\rm b} = 0$) we find that $T_{y=0} = T_{\rm RJ}$. One encounters this situation in differential measurements of the CMB brightness between two points on the sky. For $\bar{T}_{\rm b,2} > \bar{T}_{\rm b,1}$ and $y_{\rm b} > 0$ the reference temperature at which the y-distortion vanishes is always positive and also the temperature distortion corresponding to the first term in equation (3.28) is positive. Then for the inferred y-distortion the following three regimes can be defined: (i) for $T_{\rm ref} < T_{y=0}$ the inferred y-distortion is positive, (ii) for $T_{\rm ref} = T_{y=0}$ per definition there is no y-distortion up to the first order in $y_{\rm b}$ and (iii) for $T_{\rm ref} > T_{y=0}$ the inferred y-distortion is negative even though $\bar{T}_{\rm b,2} > \bar{T}_{\rm b,1}$. This shows that for the superposition of Planck spectra it is in general not sufficient to choose the beam intensity with higher RJ temperature as $I_2$ in order to obtain a positive y-parameter.

Now we are interested in the change of $\Delta_{\rm sup,12}$ and $y_{\rm sup,12}$, if we change from one reference temperature $T_{\rm ref}$ to another $T'_{\rm ref}$. For $T'_{\rm ref}$ one can again write down an equation similar to (3.28), where now $\Delta_i = (T_i - T_{\rm ref})/T_{\rm ref}$ is replaced by $\Delta'_i = (T_i - T'_{\rm ref})/T'_{\rm ref}$ and $\hat{x} = h\nu/k\,T_{\rm ref}$ by $\hat{x}' = h\nu/k\,T'_{\rm ref}$. Using (3.29) and (3.30), we can write

$$\Delta'_{\rm sup,12} = \frac{T_2 - T_1}{T'_{\rm ref}} = \Delta_{\rm sup,12}\cdot[1+\Delta_{\rm r}] \tag{3.34a}$$

$$\begin{aligned} y'_{\rm sup,12} &= y'_{\rm b} + y'_{12}(T'_{\rm ref}) \overset{y'_{\rm b}\equiv y_{\rm b}}{\underset{\downarrow}{=}} y_{\rm b} + \Delta'_{\rm sup,12}\cdot\Delta'_{\rm RJ} \\ &= y_{\rm b} + \Delta_{\rm sup,12}\cdot[1+\Delta_{\rm r}]\cdot[\Delta_{\rm RJ}\,(1+\Delta_{\rm r}) + \Delta_{\rm r}] \qquad (3.34b) \\ &\approx y_{\rm b} + y_{12} + \Delta_{\rm sup,12}\cdot\Delta_{\rm r}\,, \qquad (3.34c) \end{aligned}$$

with $\Delta_{\rm r} = (T_{\rm ref} - T'_{\rm ref})/T'_{\rm ref}$ and where prime denotes that the reference temperature $T'_{\rm ref}$ was used. The difference of y-parameters is given by $\Delta y = y'_{\rm sup,12} - y_{\rm sup,12} = \Delta_{\rm sup,12}\cdot\Delta_{\rm r}$. For $T_{\rm ref} = T_{\rm RJ}$ the contribution $y_{12} = 0$. Therfore we can write the inferred y-parameter for any reference temperature as:

$$y(T_{\rm ref}) \approx y_{\rm b} + \frac{\bar{T}_{\rm b,2} - \bar{T}_{\rm b,1}}{\bar{T}_{\rm b,1} + \bar{T}_{\rm b,2}}\cdot\frac{\bar{T}_{\rm b,1} + \bar{T}_{\rm b,2} - 2\,T_{\rm ref}}{T_{\rm ref}}\,. \tag{3.35}$$

This result describes all the cases discussed previously: If we want to discuss the beam distortions we have to set the reference temperature to $T_{\rm RJ}$ making $y \approx y_{\rm b}$. If we are discussing the y-parameter for the comparison of the SB with some reference blackbody we have $\bar{T}_{\rm b,1} = T_{\rm ref}$ resulting in $y \approx y_{\rm b} + \Delta^2_{\rm RJ}/2$. This implies that in the limit of small spectral distortions the y-parameter for the superposition of Planck spectra is completely determined by the second beam moments and the beam RJ temperatures.

## 3.3 Superposition of two Planck spectra

In order to illustrate the main results obtained in the previous Sect. we now discuss the spectral distortions arising due to the sum and difference of two pure blackbodies with different temperatures $T_1$ and $T_2$ and the corresponding intensities $I_1 = B_\nu(T_1)$ and $I_2 = B_\nu(T_2)$ in the presence of a reference blackbody $I_{\rm ref} = B_\nu(T_{\rm ref})$ with temperature $T_{\rm ref}$. In principle one can directly apply the results obtained in Sect. 3.2 and easily derive the equations describing this situation, but in order to check the derivations of the previous Sect. we here choose an approach starting from the expansion (3.8) taking only the first order corrections into account. Since the CMB temperature fluctuations are very small this approximation is sufficient.

The results obtained for the sum of two blackbodies apply to the case of an *absolute* measurement of the CMB sky, where the beam contains only blackbodies with two equally weighted temperatures. In the limit of narrow beams the results obtained for the difference of two blackbodies can be directly used to discuss the effects arising in *differential* measurements. In Sect. 3.7 we will use some of the result of this Sect. in the discussion about cross calibration issues.

### 3.3.1 Sum of two Planck spectra

We want to describe the difference $\Delta I_{\rm S} = I_{\rm S} - I_{\rm ref}$, as a function of frequency. Here we defined the sum of the two blackbodies by $I_{\rm S} = (I_1 + I_2)/2$. The easiest is to first calculate the difference $\Delta I_i = I_i - I_{\rm ref}$ since $\Delta I_{\rm S} \equiv (\Delta I_1 + \Delta I_2)/2$. If we define $\Delta_i = (T_i - T_{\rm ref})/T_{\rm ref}$ and $\hat{x} = h\nu/k\,T_{\rm ref}$ we can make use of equation (3.8) and write the relative difference of $I_{\rm S}$ and $I_{\rm ref}$ as

$$\frac{I_{\rm S} - I_{\rm ref}}{I_{\rm ref}} \approx \frac{\hat{x}\,e^{\hat{x}}}{e^{\hat{x}}-1}\cdot\left[\frac{\Delta_1+\Delta_2}{2} + g_y(\hat{x})\cdot\frac{y_1+y_2}{2}\right]\,. \tag{3.36}$$

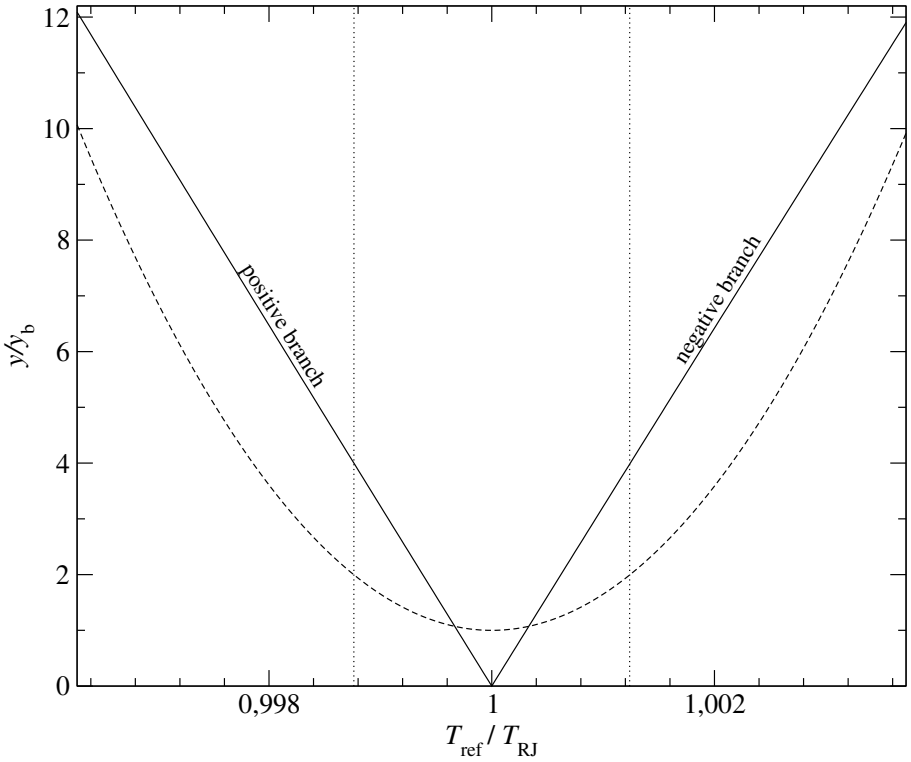


**Figure 3.4:** Dependence of the inferred y-parameter on the chosen reference temperature $T_{\mathrm{ref}}$ for two blackbodies with temperatures $T_1 = 2.72162\,\mathrm{K}$ and $T_2 = 2.72838\,\mathrm{K}$, corresponding to the minimum and maximum of the CMB dipole. In this case the mean RJ temperature is $T_{\mathrm{RJ}} = (T_1 + T_2)/2 = 2.725\,\mathrm{K}$ and $y_{\mathrm{b}} = 7.7 \cdot 10^{-7}$. — Sum of two blackbodies: total y-parameter as given by (3.37b) (dashed line). — Difference of two blackbodies: the absolute value $|y_{\mathrm{dif}}|$ of the inferred y-parameter as given in equation (3.40b) (solid line). The dotted vertical lines show the location of $T_{\mathrm{ref}} = T_1$ and $T_{\mathrm{ref}} = T_2$ respectively.

Here we abbreviated the y-parameters as $y_i = \Delta_i^2/2$. Defining the RJ temperature $T_{\mathrm{RJ}} = (T_1 + T_2)/2$ of the sum of the two blackbodies, the sum of the first order terms and the y-parameters may be rewritten like

$$\Delta_{\mathrm{RJ}} = \frac{\Delta_1 + \Delta_2}{2} = \frac{T_{\mathrm{RJ}} - T_{\mathrm{ref}}}{T_{\mathrm{ref}}} \tag{3.37a}$$

$$y_{\mathrm{sum}} = \frac{y_1 + y_2}{2} \approx \frac{1}{2}\left[\Delta_{\mathrm{RJ}}^2 + \left(\frac{T_1 - T_2}{T_1 + T_2}\right)^2\right] . \tag{3.37b}$$

From this it can be seen that if the reference temperature is set to $T_{\mathrm{RJ}}$ the temperature distortion corresponding to the first term in (3.36) vanishes ($\Delta_{\mathrm{RJ}} = 0$) and only a minimal y-distortion with y-parameter

$$y_{\mathrm{b}} = \frac{1}{2}\left[\frac{T_1 - T_2}{T_1 + T_2}\right]^2 \tag{3.38}$$

is left. At low frequencies ($\hat{x} < \hat{x}_y$) this reflects the fact that the sum of RJ spectra is again a RJ spectrum. Comparing (3.37) to (3.26) one may conclude that $y_{\mathrm{b}}$ corresponds to the contribution of the second beam moment $\langle \delta^2 \rangle$ to the y-parameter. Comparing (3.38) to (3.24b) with $w_1 = w_2 = \frac{1}{2}$ confirms this conclusion.

The dependence of the inferred y-parameter on the chosen reference temperature is illustrated in Figure 3.4. As mentioned above the y-parameter reaches a minimum for $T_{\mathrm{ref}} = T_{\mathrm{RJ}}$. It is important to note that the minimal value of the y-parameter $y_{\mathrm{b}}$ does not depend on the reference temperature $T_{\mathrm{ref}}$ but only on the second beam moment of the temperature distribution function. Changing $T_{\mathrm{ref}}$ from $T_{\mathrm{RJ}} \rightarrow T_i$ the inferred y-parameter monotonically increases

being a factor of $\sim 2$ larger than $y_\mathrm{b}$ for $T_\mathrm{ref} = T_i$. This can be understood as follows: If we set $T_\mathrm{ref} = T_i$ we obtain $y_\mathrm{sum} = (T_1 - T_2)^2/4\,T_i^2 \approx (T_1 - T_2)^2/4\,T_1^2 + \mathcal{O}(\Delta T^3/T_1^3)$, with $\Delta T = T_1 - T_2$. Therefore the ratio $y_\mathrm{sum}/y_\mathrm{d} \approx (T_1 + T_2)^2/2\,T_1^2 \approx 2$.

Outside the region $T_1 \leq T_\mathrm{ref} \leq T_2$ the inferred y-parameter increases further. It is in principle possible to gain large factors in the inferred y-parameter by going very far away from the RJ temperature of the SB, but at some point next order corrections will become important and therefore limit $T_\mathrm{ref}$ to the region where the approximation of small spectral distortions is still valid. For the CMB the most natural choices of the reference temperature are the whole sky mean temperature $T_0$ and the maximum or minimum of the CMB dipole. For the SB the inferred y-parameter varies from $y \sim 7.7 \cdot 10^{-7}$ for $T_\mathrm{ref} = T_0$ to $y \sim 1.5 \cdot 10^{-6}$ for $T_\mathrm{ref} = T_1$. The behavior of the inferred y-parameter shows that in order to minimize the arising spectral distortion for *absolute* measurements it is important to use an internal calibrator with temperature close to the beam RJ temperature $T_\mathrm{RJ}$.

In the limit $T_1 \rightarrow T_2$ we are in principle comparing one pure Planck spectrum with a reference blackbody. This case applies for an *absolute* measurement of the CMB sky in the limit of very narrow beams. In this case it follows that $y_\mathrm{b} \rightarrow 0$ and in addition $y_\mathrm{sum} \rightarrow 0$ for $T_\mathrm{ref} = T_\mathrm{RJ}$. Except for some changes in scales the behavior of the curve shown in Fig. 3.4 is unaffected.

### 3.3.2 Difference of two Planck spectra

Since $\Delta I = I_2 - I_1 \equiv \Delta I_2 - \Delta I_1$, where $\Delta I_i = I_i - I_\mathrm{ref}$, applying equation (3.8) one can easily find

$$\frac{I_2 - I_1}{I_\mathrm{ref}} \approx \frac{\hat{x}\, e^{\hat{x}}}{e^{\hat{x}} - 1} \cdot \Big[\Delta_2 - \Delta_1 + g_y(\hat{x}) \cdot (y_2 - y_1)\Big]\,. \tag{3.39}$$

Again it is possible to simplify the difference of the first order terms and the y-parameters leading to

$$\Delta_{12} = \Delta_2 - \Delta_1 = \frac{T_2 - T_1}{T_\mathrm{ref}} \tag{3.40a}$$

$$y_\mathrm{dif} = y_2 - y_1 = \Delta_{12} \cdot \Delta_\mathrm{RJ}\,, \tag{3.40b}$$

where $\Delta_\mathrm{RJ} = (T_\mathrm{RJ} - T_\mathrm{ref})/T_\mathrm{ref}$ and $T_\mathrm{RJ} = (T_1 + T_2)/2$. For the difference of two Plancks the temperature distortion does not vanish for any choice of the reference temperature (see equation (3.40a)), whereas the y-distortion changes sign at $T_\mathrm{ref} = T_\mathrm{RJ}$. As mentioned earlier, this shows that for the difference of two Planck spectra in order to obtain a positive y-parameter it is in general not sufficient to choose the intensity with higher RJ temperature as $I_2$. Comparing (3.40) to (3.29a) and (3.32) and keeping in mind that both beam moments $\langle \delta_i^2 \rangle_{\mathrm{b},i} = 0$ shows the equivalence of both approaches. In Figure 3.4 the dependence of the absolute value of the inferred y-parameter on the chosen reference temperature is shown. At $T_\mathrm{ref} = T_i$ the inferred y-parameter for the difference of two blackbodies is 2 times larger than in the case of the sum, $(|y_\mathrm{dif}|/y_\mathrm{sum})|_{T_i} \sim 2$.

As in the case of the sum of two Plancks for $T_\mathrm{ref}$ outside the region $T_1 \leq T_\mathrm{ref} \leq T_2$ the inferred y-parameter increases strongly. Again there is a limit set by the approximations of small spectral distortions. The behavior of the inferred y-parameter shows that in order to minimize the spectral distortion arising in differential measurements it is important to choose a reference temperature close to the RJ temperature of the observed region.

## 3.4 Spectral distortions due to the CMB dipole

The largest temperature fluctuation on the observed CMB sky is connected with the CMB dipole. Its amplitude has been accurately measured by Cobe/Firas [51]: $\Delta T_\mathrm{d} = 3.381 \pm$

0.007mK, corresponding to $\Delta T/T \sim 0.2\,\%$ on very large angular scales. Assuming that it is only due to the motion of the solar system with respect to the CMB rest frame it implies a velocity of $v = 372 \pm 1$ km/s in the direction $(l, b) = (264.14^\circ \pm 0.15^\circ, 48.26^\circ \pm 0.15^\circ)$. In order to understand the spectral distortions arising due to the dipole, we start with the direction dependent temperature of the CMB, neglecting any intrinsic anisotropy:

$$T(\mu) = \frac{T_0}{\gamma[1 - \beta\,\mu]} \tag{3.41a}$$

$$\overset{\beta\ll 1}{\approx} T_0 \left[1 - \frac{\beta^2}{6} + \beta\,\mu + \beta^2\left(\mu^2 - \frac{1}{3}\right)\right]. \tag{3.41b}$$

Here we introduced the abbreviation $\mu = \cos\theta$, with $\theta$ being the angle between the direction of $v$ and the location on the sky. $T_0$ denotes the intrinsic CMB temperature, $\beta = v/c$ is the velocity in units of the speed of light and $\gamma = 1/\sqrt{1-\beta^2}$ is the corresponding Lorentz factor. The whole sky mean RJ temperature is given by

$$\bar{T}_\mathrm{f} = \frac{T_0}{2\gamma\beta}\,\ln\left[\frac{1+\beta}{1-\beta}\right] \overset{\beta\ll 1}{\approx} T_0\left[1 - \frac{\beta^2}{6}\right], \tag{3.42}$$

where 'f' denotes full sky average temperature. Equation (3.42) implies that due to the motion of the solar system relative to the CMB rest frame the observed whole sky mean RJ temperature is $\Delta T = 0.70\,\mu$K less than the intrinsic temperature $T_0$. The measured value of the whole sky mean temperature as given by the COBE/FIRAS experiment [51] is $T_0 = 2.725 \pm 0.001\,\mathrm{K}$. Therefore this difference is still $\sim 1000$ times smaller than the current error bars and far from being measured.

Below we now discuss the spectral distortions arising due to the CMB dipole in the context of finite angular resolution. Since only the second moment of the temperature distribution is important, we will use the second order expansion of $T(\mu)$ in $\beta$ as given in equation (3.41b). In the last part of this section we show that starting with equation (3.41a) all the results of this section can also be directly obtained by expansion of the blackbody $B_\nu(T(\mu))$ in terms of small $\beta$. This shows the equivalence of both approaches. Nevertheless, the big advantage of the treatment developed in Sect. 3.2 is that it can be applied to general temperature distributions and that the source of the y-distortion can be directly related to the second moment of the temperature distribution.

### 3.4.1 Whole sky beam spectral distortion

Defining $\delta = [T(\mu) - \bar{T}_\mathrm{f}]/\bar{T}_\mathrm{f}$, where $\bar{T}_\mathrm{f}$ is given by equation (3.42), the full sky moments can be calculated by the integrals $\langle\delta^k\rangle_\mathrm{f} = \frac{1}{2}\int_{-1}^{1}\delta(\mu)^k\,\mathrm{d}\mu$. The first three moments may be found as

$$\langle\delta^0\rangle_\mathrm{f} = 1, \qquad \langle\delta^1\rangle_\mathrm{f} = 0 \tag{3.43a}$$

$$\langle\delta^2\rangle_\mathrm{f} = \frac{4\beta^2\gamma^2}{\Xi^2} - 1 \overset{\beta\ll 1}{\approx} \frac{\beta^2}{3} + \mathcal{O}(\beta^4), \tag{3.43b}$$

where $\Xi = \ln\left[\frac{1+\beta}{1-\beta}\right]$. With $\beta_\mathrm{d} = \Delta T_\mathrm{d}/T_0 = 1.241\cdot 10^{-3}$ one finds: $\langle\delta^2\rangle_\mathrm{f} = 5.1\cdot 10^{-7}$. This implies a full sky y-distortion with

$$y_\mathrm{d} = \frac{\beta_\mathrm{d}^2}{6} \approx 2.6\cdot 10^{-7}, \tag{3.44}$$

which is currently $\sim 60$ times below the COBE/FIRAS upper limit. This distortion translates into a temperature difference of $\Delta T = 0.7\cdot g_y(\hat{x})\,\mu$K. The exact behavior of $g_y(\hat{x})$ is shown in Fig. 3.2. We have checked that deviations from a y-distortion will become important only at extremely high frequencies ($\hat{x} \geq 360$).

Here we want to note that this full sky distortions arises due to the existence of the dipole anisotropy. In absolute measurements of the CMB $y_\mathrm{d}$ places a lower limit on the full sky y-parameter (see Sect. 3.2.1).

### 3.4.2 Beam spectral distortion due to the CMB dipole

Here we are interested in the angular pattern of the y-distortion induced by the SB over the dipole for an observation with a finite angular resolution and in particular in the location of the maximal y-distortion, when we compare the beam flux at different frequencies to a reference blackbody with beam RJ temperature. To model the beam we use a simple top-hat filter function

$$W(\theta') = \begin{cases} 1 & \text{for } \theta' \leq \theta_\mathrm{r}, \\ 0 & \text{else}, \end{cases} \tag{3.45}$$

where the $z'$-axis is along the beam direction[1] and $\theta_\mathrm{r}$ is the radius of the top-hat in spherical coordinates.

The $k$th moment of some variable $X$ over the beam is then given by the integral

$$\left\langle X^k \right\rangle_\mathrm{r} = \frac{1}{2\,\pi\,(1-\mu_\mathrm{r})} \int\limits_0^{2\,\pi} \int\limits_{\mu_\mathrm{r}}^{1} X^k \,\mathrm{d}\mu' \,\mathrm{d}\phi' \,, \tag{3.46}$$

where 'r' denotes beam average for a top-hat of radius $\theta_\mathrm{r}$ and $\mu_\mathrm{r} = \cos\theta_\mathrm{r}$. Defining $\mu_0 = \cos\theta_0$ and using

$$\mu = \mu_0 \cdot \mu' + \cos(\phi' - \phi_0)\, \sin(\theta_0)\sqrt{1-\mu'^2} \,, \tag{3.47}$$

one can calculate the beam averages of the dipole and quadrupole anisotropy

$$\langle \mu \rangle_\mathrm{r} = \zeta_+ \,\mu_0 \tag{3.48a}$$

$$\left\langle \mu^2 - \frac{1}{3} \right\rangle_\mathrm{r} = \mu_\mathrm{r}\,\zeta_+ \left( \mu_0^2 - \frac{1}{3} \right) \,, \tag{3.48b}$$

where we introduced the abbreviation $\zeta_\pm = \frac{1\pm\mu_\mathrm{r}}{2}$. These equation will be very useful in all the following discussion.

Using formula (3.41b) and equations (3.46) and (3.48) the mean RJ temperature inside the beam in some direction $(\phi_0, \theta_0)$ relative to the dipole axis is given as

$$\bar{T}_\mathrm{r} = T_0 \,\left[ 1 - \frac{\beta^2}{6} + \beta\,\zeta_+\,\mu_0 + \,\beta^2\,\mu_\mathrm{r}\,\zeta_+ \left( \mu_0^2 - \frac{1}{3} \right) \right] \,. \tag{3.49}$$

The position of the maximum and minimum is, as expected, at $\theta_0 = 0$ and $\theta_0 = \pi$ respectively.

Now the second moment of $\delta = [T(\mu) - \bar{T}_\mathrm{r}]/\bar{T}_\mathrm{r}$ inside the beam can be derived as:

$$\left\langle \delta^2 \right\rangle_\mathrm{r} \overset{\beta_\mathrm{d} \ll 1}{\approx} \frac{\beta_\mathrm{d}^2}{3} \cdot \left[ 1 + \zeta_+ - 3\,\zeta_+ \left( \mu_0^2 - \frac{1}{3} \right) \right] \zeta_- \,, \tag{3.50}$$

where up to second order in $\beta$ only the CMB dipole contributes and we have set $\beta \equiv \beta_\mathrm{d}$. The corresponding y-parameter

$$y_\mathrm{r} = y_\mathrm{d} \cdot \left[ 1 + \zeta_+ - 3\,\zeta_+ \left( \mu_0^2 - \frac{1}{3} \right) \right] \zeta_- \,, \tag{3.51}$$

[1] Prime denotes coordinates with respect to the system $S'$ where the $z'$-axis is defined by the direction of the beam.

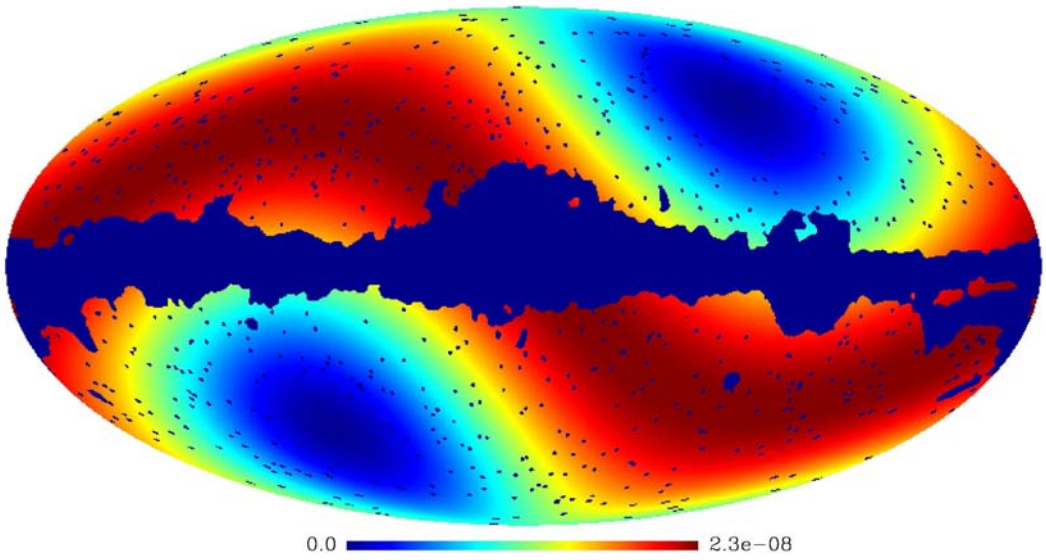


**Figure 3.5:** Angular distribution of $y_\mathrm{r}$ as given by equation (3.51) for $\theta_\mathrm{r} = 20°$. The maximal spectral distortion is expected to appear in a ring perpendicular to the dipole axis and in this case has a value $y_\mathrm{r,max} = 2.3 \cdot 10^{-8}$. The minimal y-parameter has a value of $y = 2.4 \cdot 10^{-10}$ and is located around the maximum and minimum of the dipole. The galactic plane was cut out using the kp0-mask of the WMAP data base.

has a monopole and quadrupole angular dependence. As expected it vanishes for high angular resolution ($\zeta_- \to 0$). In Fig. 3.5 the angular distribution of $y_\mathrm{r}$ for $\theta_\mathrm{r} = 20°$ is illustrated. The maximum lies in a broad ring perpendicular to the dipole axis, which even without taking the galaxy into account covers a large fraction of the sky. In the shown case, the maximal value of the y-parameter is approximately $y_\mathrm{r,max} \sim y_\mathrm{d}/10$.

Using equation (3.50) the position of the maximum can be found: $\theta_\mathrm{0,max} = \frac{\pi}{2}$. This suggests that the location of the maximal distortion is where the derivative of the temperature distribution is extremal. The maximal y-parameter is given as

$$y_\mathrm{r,max} = y_\mathrm{d} \cdot [1 - \mu_\mathrm{r}\, \zeta_+] \; . \tag{3.52}$$

The dependence of $y_\mathrm{r,max}$ on the beam radius is shown in Fig. 3.6. For beam radii larger than $\theta_\mathrm{r} = 90°$ it follows that $y_\mathrm{r,max} \geq y_\mathrm{d}$ and at $\theta_\mathrm{r} = 120°$ it is 9/8 times $y_\mathrm{d}$. The maximal y-parameter, $y_\mathrm{r,max}$, is a steep function of beam radius: It has values $y_\mathrm{d}/2$, $y_\mathrm{d}/3$ and $y_\mathrm{d}/10$ for $\theta_\mathrm{r} = 51.83°$, $\theta_\mathrm{r} = 40.68°$ and $\theta_\mathrm{r} = 21.29°$ respectively and vanishes like $\sim 3\,\theta_\mathrm{r}^2/4$ for high angular resolution. For $\theta_\mathrm{r} = 5°$ it is $\sim 6 \cdot 10^{-3} \times y_\mathrm{d}$. This implies that the beam spectral distortions resulting from the dipole are lower than $\Delta T/T \sim 10^{-9}$ for experiments with resolution better than $\sim 10°$. As will be shown later, on this level contributions from the higher multipoles will start to become important (Sect. 3.5).

### 3.4.3 Distortion with respect to any $T_\mathrm{ref}$

We have seen in Sect. 3.2.1 that the inferred y-parameter for the comparison of the SB with some reference blackbody with temperature $T_\mathrm{ref}$ has one contribution from the second beam moment $\langle \delta^2 \rangle$ and another due to the dispersion $\Delta^2_\mathrm{RJ}$ of the beam RJ temperature relative to the temperature of the chosen reference blackbody (cf. equation (3.26b)). Therefore one can immediately write down the relative difference of the beam intensity and the intensity of the chosen reference blackbody making use of (3.26), (3.27), (3.49) and (3.50). In the limit $\theta_\mathrm{r} \to 0$ we can apply the results obtained in Sect. 3.3.1 for the sum of two blackbodies, if we set $T_1 = T_2$. Here we want to discuss the case $T_\mathrm{ref} = T_0$ in more detail. For this choice the residual

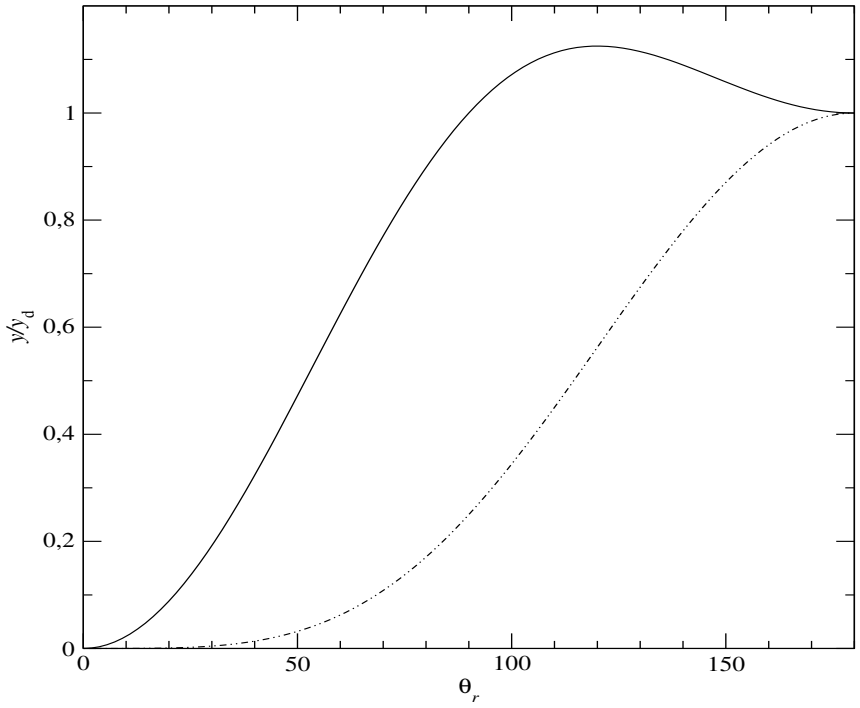


**Figure 3.6:** Dependence of the y-parameter in units of $y_\mathrm{d} = 2.6 \cdot 10^{-7}$ on the beam radius $\theta_\mathrm{r}$ in degree for a circular beam: $y_\mathrm{r}$ for $\mu_0 = \pm 1$ as given by equation (3.51) (dash-dot-dotted), $y_\mathrm{r,max}$ according to equation (3.52) (solid). For values $-1 < \mu_0 < 1$ the curves lie between these two extremes.

full sky y-distortion (which may be obtained by averaging the intensity data over the whole sky) is minimal.

### Distortion with respect to $T_0$

Now, instead of comparing the spectrum of the SB to a blackbody with beam RJ temperature $\bar{T}_\mathrm{r}$ we compare to a blackbody of temperature $T_0$. Then the spectral distortion follows from equation (3.27) and in addition to the beam moment (3.50) the first two moments of $\Delta = (\bar{T}_\mathrm{r} - T_0)/T_0$ have to be calculated:

$$\Delta^1 = -\frac{\beta_\mathrm{d}^2}{6} + \beta_\mathrm{d}\,\zeta_+\,\mu_0 + \beta_\mathrm{d}^2\,\mu_\mathrm{r}\,\zeta_+\left(\mu_0^2 - \frac{1}{3}\right) \tag{3.53a}$$

$$\Delta^2 = \frac{\beta_\mathrm{d}^2}{3}\,\zeta_+^2 + \beta_\mathrm{d}^2\,\zeta_+^2\left(\mu_0^2 - \frac{1}{3}\right) . \tag{3.53b}$$

The spectral distortion arising from the SB can now be characterized as follows: (i) At low frequencies the y-distortion vanishes. The motion of the solar system with respect to the CMB rest frame induces a temperature dipole ($\sim \beta_\mathrm{d}$) and a temperature monopole and quadrupole ($\sim \beta_\mathrm{d}^2$) all resulting from the $\Delta^1$-term:

$$\left.\frac{\Delta T}{T_0}\right|_\mathrm{t} = -\frac{\beta_\mathrm{d}^2}{6} + \beta_\mathrm{d}\,\zeta_+\,\mu_0 + \beta_\mathrm{d}^2\,\mu_\mathrm{r}\,\zeta_+\left(\mu_0^2 - \frac{1}{3}\right) . \tag{3.54}$$

In the limit of high angular resolution ($\zeta_+, \mu_\mathrm{r} \to 1$) this is equivalent to the expansion (3.41b). (ii) A y-distortion is induced which is proportional to the sum $\Delta^2 + \langle\delta^2\rangle_\mathrm{r}$:

$$\left.\frac{\Delta T}{T_0}\right|_\mathrm{y} = \frac{g_2(\hat{x})}{g_1(\hat{x})}\left[\frac{\beta_\mathrm{d}^2}{3} + \beta_\mathrm{d}^2\,\mu_\mathrm{r}\,\zeta_+\left(\mu_0^2 - \frac{1}{3}\right)\right] . \tag{3.55}$$

It has a monopole and quadrupole angular dependence and only arises due to the CMB dipole. The sum of both contributions mentioned above can be rewritten as

$$\left.\frac{\Delta T}{T_0}\right|_{\rm tot} = \Delta - \Delta^2 - \left\langle\delta^2\right\rangle_{\rm r} + \frac{g(\hat{x})}{2}\,\left[\Delta^2 + \left\langle\delta^2\right\rangle_{\rm r}\right] \tag{3.56a}$$

$$= -\frac{\beta_{\rm d}^2}{2} + \beta_{\rm d}\,\zeta_+\,\mu_0 + \frac{g(\hat{x})}{2}\,\left[\frac{\beta_{\rm d}^2}{3} + \beta_{\rm d}^2\,\mu_{\rm r}\,\zeta_+\left(\mu_0^2 - \frac{1}{3}\right)\right]\,, \tag{3.56b}$$

where we used the definition (3.5) for $g(\hat{x})$. Rewriting the function $g_2(\hat{x})$ in terms of $g(\hat{x})$ lead to exact cancellation of the motion-induced temperature quadrupole and changes the temperature monopole by $\beta_{\rm d}^2/3$ (cf. $\Delta - \Delta^2 - \left\langle\delta^2\right\rangle_{\rm r}$-term in equation (3.56a)).

In the picture of the SB it is easily understandable that there is no difference in the resulting spectral distortion whether the dipole anisotropy is intrinsic or due to motion. Therefore, as was noted earlier by Kamionkowski & Knox [70], it is impossible to distinguish the intrinsic dipole from a motion-induced dipole by measurement of the frequency-dependent temperature quadrupole.

### Expansion of $\Delta I/I_0$ for small $\beta$

Here we want to show that the results (3.50) and (3.56) can also be directly obtained starting with the expansion of the blackbody spectrum with temperature $T(\mu)$ for small velocity $\beta$ and thereby prove the equivalence and correctness of both approaches. For this, inserting (3.41a) into the blackbody spectrum (3.2), by Taylor expansion up to second order of $\beta$ one may find

$$\frac{\Delta I}{I_0} = \beta^2\,g_1(\hat{x})\,\left[\frac{g(\hat{x})}{3} - \frac{1}{2}\right] + \beta\,g_1(\hat{x})\,\mu + \beta^2\,g_1(\hat{x})\,g(\hat{x})\left(\mu^2 - \frac{1}{3}\right)\,. \tag{3.57}$$

This equation has been obtained earlier by Sazonov & Sunyaev [112] for a cluster of galaxies moving with respect to the CMB and was later applied by Kamionkowski & Knox [70] to discuss aspects of the observed CMB dipole and quadrupole. It is valid for a measurement of the CMB temperature with high angular resolution, where the y-parameter due to the second beam moment is negligible ($y \sim 10^{-9}$ for $10^\circ$ angular resolution).

First we want to calculate the SB in a circular beam and compare it to the blackbody $I_0$ of temperature $T_0$, i.e. we want to derive $\langle\Delta I/I_0\rangle_{\rm r}$. Using equation (3.46) and since only $\mu$ and $\mu^2$ depend on $\mu'$ and $\phi'$ this integration with (3.48) immediately leads to equation (3.56).

Next we want to derive the spectral distortion relative to the reference blackbody with beam RJ temperature starting with (3.57). For this we rearrange (3.57) in terms of $g_1(\hat{x})$ and $g_2(\hat{x})$ leading to

$$I(\hat{x}) = I_0(\hat{x}) \cdot [1 + g_1(\hat{x}) \cdot \delta_0 + g_2(\hat{x}) \cdot \delta_0^2]\,, \tag{3.58}$$

with $\delta_0 = -\frac{\beta^2}{6} + \beta\,\mu + \beta^2\left(\mu^2 - \frac{1}{3}\right)$. In the RJ limit $g_1 \rightarrow 1$ and $g_2 \rightarrow 0$. This immediately leads from equation (3.58) to $T_{\rm RJ} = \langle T_0 \cdot [1 + \delta_0]\rangle_{\rm r} = T_0 \cdot [1 + \Delta]$, where $\Delta$ is given by equation (3.53a). Now we replace $\hat{x} = h\,\nu/k\,T_0 = (h\,\nu/k\,T_{\rm RJ}) \cdot T_{\rm RJ}/T_0 = \hat{x}_* \cdot [1 + \Delta]$ in equation (3.58) and expand in second order of $\Delta$ obtaining:

$$I(\hat{x}_*) = I_*(\hat{x}_*) \cdot \left[1 + g_1(\hat{x}_*) \cdot (\delta_0 - \Delta + \Delta^2 - \delta_0\Delta) + g_2(\hat{x}_*) \cdot (\delta_0^2 + \Delta^2 - 2\,\delta_0\Delta)\right]\,, \tag{3.59}$$

with $I_*(\hat{x}_*) = B_\nu(T_{\rm RJ})$. Since only $\delta_0$ depends on $\mu'$ and $\phi'$ we may perform the beam averages using equations (3.46) and (3.48). This is equivalent to replacing $\delta_0 \rightarrow \Delta$ and $\delta_0^2 \rightarrow \left\langle\delta_0^2\right\rangle_{\rm r}$ in equation (3.59). Therefore this leads to

$$\frac{I - I_*}{I_*} = g_2(\hat{x}_*) \cdot [\left\langle\delta_0^2\right\rangle_{\rm r} - \Delta^2]\,. \tag{3.60}$$

Inserting equation (3.53b) and

$$\left\langle \delta_0^2 \right\rangle_{\rm r} = \frac{\beta^2}{3} + \beta^2\,\mu_{\rm r}\,\zeta_+\left(\mu_0^2 - \frac{1}{3}\right) \tag{3.61}$$

one may obtain $\left\langle \delta_0^2 \right\rangle_{\rm r} - \Delta^2 \equiv \left\langle \delta^2 \right\rangle_{\rm r}$, where $\left\langle \delta^2 \right\rangle_{\rm r}$ is given by equation (3.50) and we made use of the identities

$$1 - \zeta_+^2 = [1 + \zeta_+]\,\zeta_- \tag{3.62a}$$

$$\mu_{\rm r} - \zeta_+ = -\zeta_- \,. \tag{3.62b}$$

Let us note here that since only $\delta_0$ depends on $\mu'$ and $\phi'$ we may have calculated the beam average already from equation (3.58). After expansing in terms of $\Delta$ this would have directly lead to the result (3.60) without the intermediate step (3.59). This finally shows the complete equivalence of both approaches.

## 3.5 Spectral distortions due to higher multipoles

The largest temperature anisotropy on the CMB sky is connected with the CMB dipole which was discussed in detail above (Sect. 3.4). In what follows here we are only concerned with spectral distortions arising from multipoles with $l \geq 2$. As has been shown above, the spectral distortions induced by the CMB dipole are indistinguishable from a y-distortion. Since the typical amplitude of the temperature fluctuations for $l \geq 2$ is a factor of $\sim 100$ less than the dipole anisotropy ($\Delta T/T \sim 10^{-5}$), the spectral distortion arising from higher multipoles will also be indistinguishable from a y-distortion.

### Calculations using a realization of the CMB sky

In order to investigate the spectral distortions arising from the multipoles $l \geq 2$, we use one realization of the CMB sky computed with the Synfast code of the Healpix distribution[2] given the theoretical $C_l$s for the temperature anisotropies computed with the Cmbfast code[3] for the WMAP best fit model [11]. Here we are only interested in the distortions arising from the primordial CMB anisotropies. Future experiments will have $\sim$arcmin resolution. Therefore we perform our analysis in the domain, $l \leq 3000$, corresponding to angular scales with dimensions $\theta \gtrsim 3.6'$.

Using the generated CMB maps we extract the temperature distribution function $R(T)$ inside a circular beam of given radius $\theta_{\rm r}$ in different directions on the sky. We then calculate the spectrum and the spectral distortion inside the beam using equation (3.11) and setting the reference temperature to the beam RJ temperature $T_{\rm RJ} = \int R\,T\,{\rm d}T$. As expected, we found that the spectral distortions are indistinguishable from a y-distortion with y-parameter given by equation (3.17). As discussed above this follows from the fact that the temperature fluctuations for $l \geq 2$ are extremely small ($\sim 10^{-5}$).

In Fig. 3.7 the probability density $p(y)$ for a given aperture is shown. It is defined such that $p(y)\,dy$ gives the probability to find a value of the y-parameter in a random direction on the sky between $y$ and $y + dy$ for a given beam radius. As expected, the average value $\langle y \rangle$ increases with aperture radius, while the width of $p(y)$ decreases. For $\theta_{\rm r} \gtrsim 1$ the average beam y-parameter varies only slowly. In the limit of a whole sky measurement, the y-parameter converges to $y_{\rm h} = 8.33 \cdot 10^{-10}$, which corresponds to the whole sky rms dispersion $\Delta T \sim 111\,\mu$K of the used realization of the CMB sky. For $\theta_{\rm r} \lesssim 1$ the beam y-parameter falls off very fast. As Fig. 3.7 suggests, for $\theta_{\rm r} \lesssim 2 - 5^\circ$ the distortions arising due to the dipole are negligible in comparison to the distortions arising due to higher multipoles.

[2] http://www.eso.org/science/healpix/
[3] http://www.cmbfast.org/

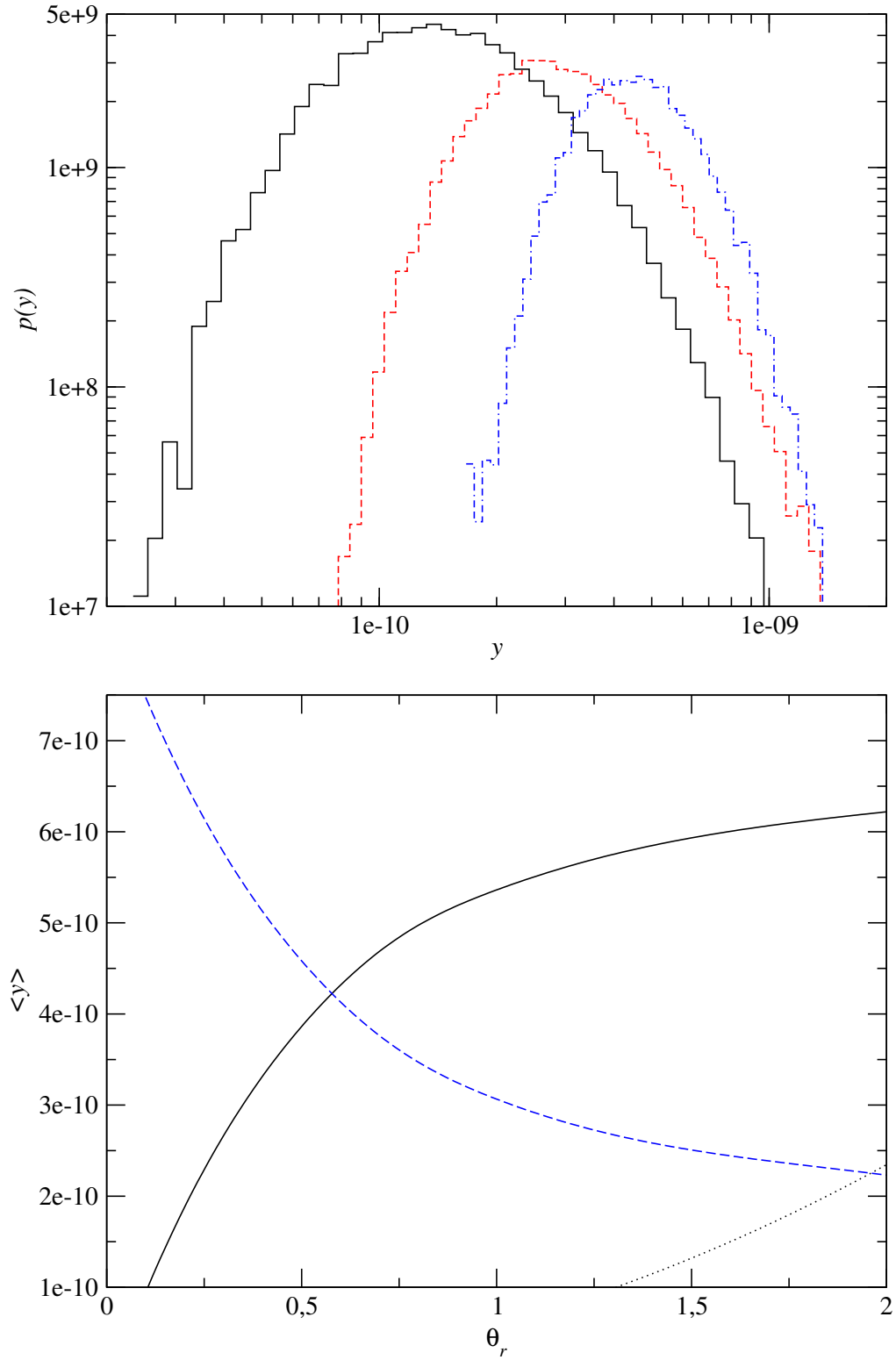


**Figure 3.7:** Top: Probability density $p(y)$ for different aperture radii: $\theta_\mathrm{r} = 0.25°$ (solid), $\theta_\mathrm{r} = 0.5°$ (dashed) and $\theta_\mathrm{r} = 1.0°$ (dashed-dotted). — Bottom: Dependence of the average y-parameter on the aperture radius $\theta_\mathrm{r}$ in degrees: for the *beam* spectral distortion (solid) and for the y-parameter resulting from the dispersion of the beam RJ temperatures in different directions on the sky relative to $T_0$ (dashed). Also shown is the maximal beam spectral distortion arising due to the dipole, $y_{\mathrm{r,max}}$ (dotted), according to equation (3.52).

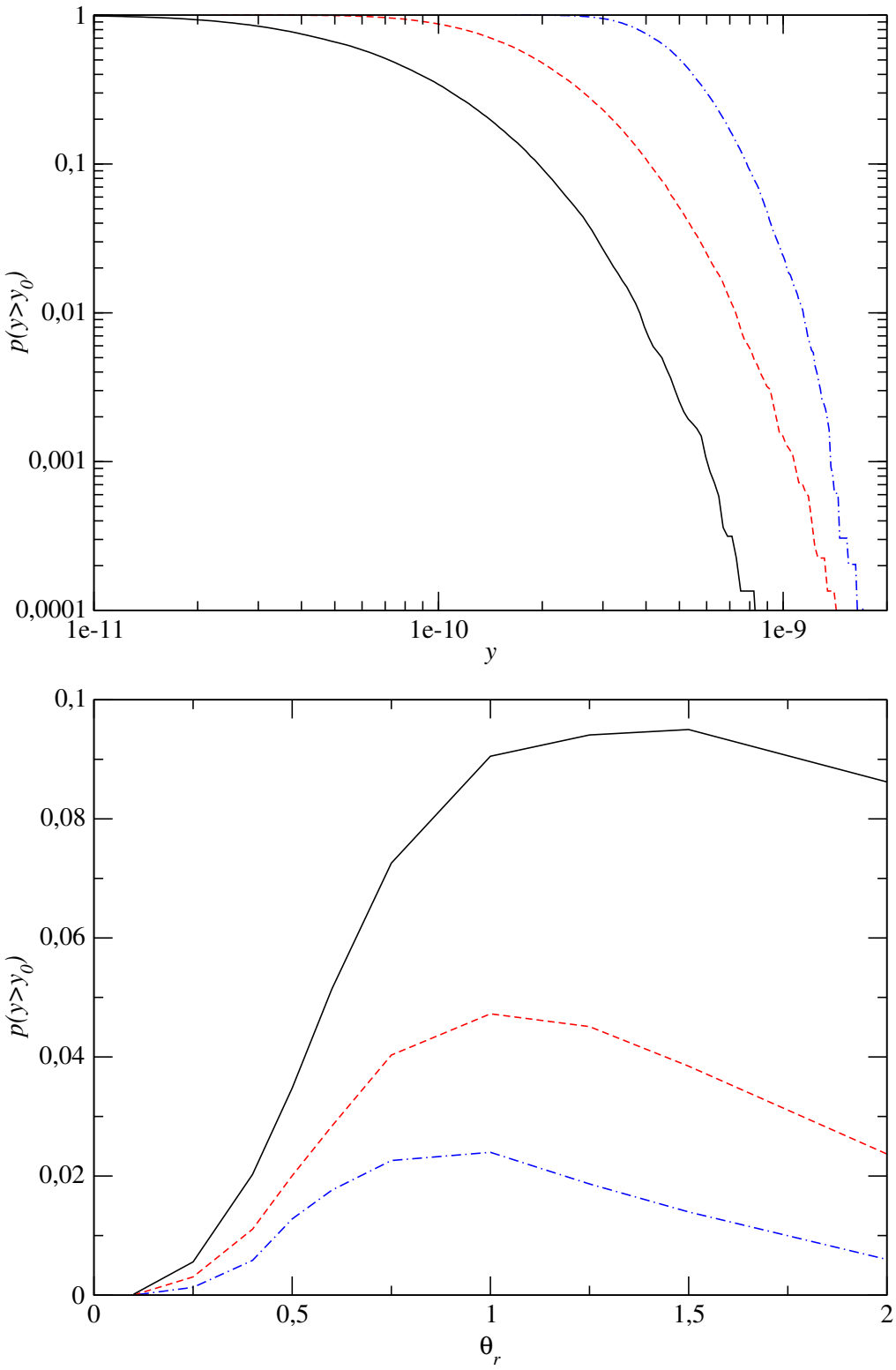


**Figure 3.8:** Top: Cumulative probability $p(y \geq y_0)$ for different aperture radii $\theta_\mathrm{r} = 0.1°$ (solid), $\theta_\mathrm{r} = 0.25°$ (dashed) and $\theta_\mathrm{r} = 1.0°$ (dashed-dotted). – Bottom: Dependence of the cumulative probability $p(y \geq y_0)$ on the aperture $\theta_\mathrm{r}$ for $y_0 = 8 \cdot 10^{-10}$ (solid), $y_0 = 9 \cdot 10^{-10}$ (dashed) and $y_0 = 10^{-9}$ (dashed-dotted).

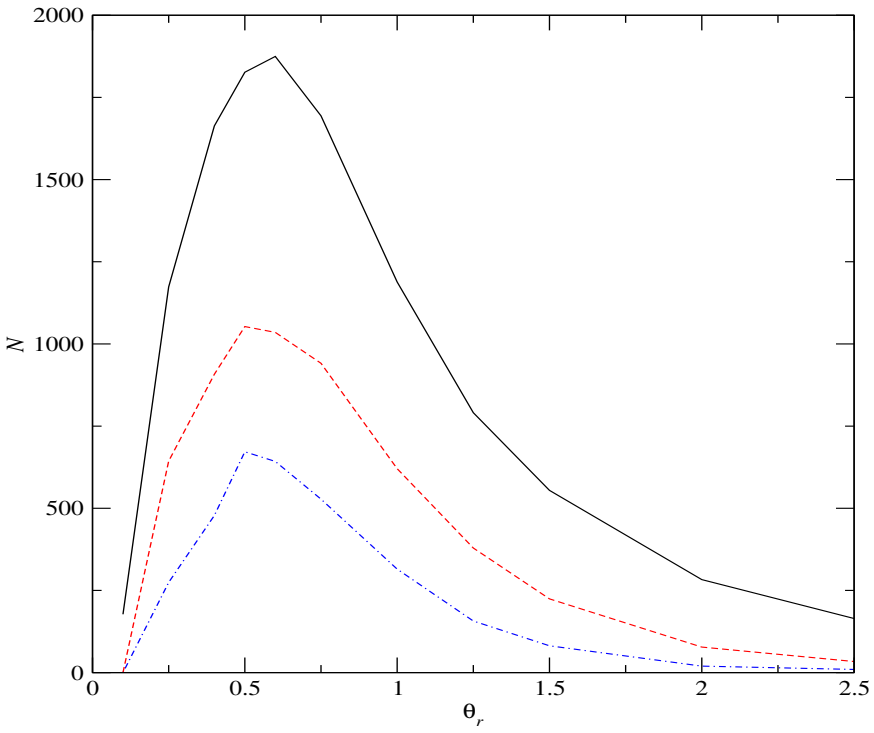


**Figure 3.9:** Number of regions on the sky with $y \geq y_0$ for different aperture radii $\theta_\mathrm{r}$ in degree: for $y_0 = 8 \cdot 10^{-10}$ (solid), $y_0 = 9 \cdot 10^{-10}$ (dashed) and $y_0 = 10^{-9}$ (dashed-dotted).

Figure 3.7 also shows the y-parameter resulting from the dispersion of the beam RJ temperatures in different directions on the sky relative to $T_0$. It drops with increasing beam radius, because the average beam RJ temperature becomes closer to $T_0$ for bigger beam radius. Looking at the sum of the *beam* distortion and the distortion due to the dispersion of the beam RJ temperatures shows that the averaged whole sky distortion is independent of the angular resolution.

In Fig. 3.8 the cumulative probability of finding a spectral distortion with $y \geq y_0$ is shown for different apertures. Fixing the value $y_0$, there is a maximum probability of 2.4% to measure $y \geq 10^{-9}$ for an aperture radius $\theta_\mathrm{r} \sim 1^\circ$ during the mapping or scanning of extended regions of the sky. This corresponds to $\sim$ 500 sources on the whole sky. In Fig. 3.9 the dependence of the number of sources with $y$ above $y_0$ for a given radius $\theta_\mathrm{r}$ is illustrated. It peaks around $\theta_\mathrm{r} \sim 0.5$ degree, corresponding to the first acoustic peak. The maxima of the y-distortion do not coincide with the maxima of $\Delta T/T$, but that they both should have similar statistical properties. We expect that the maxima of the y-parameter are there, where the derivatives of the averaged temperature field are large.

### The motion-induced CMB octupole

In section 3.4 we discussed spectral distortions due to the motion of the solar system relative to the CMB rest frame up to the second order in $\beta_\mathrm{d}$. On the level of $y \sim 10^{-10} - 10^{-9}$ third order corrections $\propto \beta_\mathrm{d}^3$ should also start to contribute. In this order of $\beta_\mathrm{d}$ not only the motion-induced dipole and quadrupole lead to spectral distortions but also terms connected to the products of the intrinsic dipole and quadrupole with the motion-induced dipole and quadrupole. Here we now only discuss the motion-induced CMB third order terms.

Expanding (3.41a) up to third order in $\beta_\mathrm{d}$ and calculating the beam averaged RJ temper-

ature for the top-hat beam using (3.46) leads to

$$\bar{T}_{\mathrm{r,oct}} = \bar{T}_{\mathrm{r}} + T_0\,\beta_{\mathrm{d}}^3\,\zeta_+\,\left[\frac{1}{10}\,\mu_0 + (1-5\,\zeta_+\,\zeta_-)\,\mu_0\left(\mu_0^2-\frac{3}{5}\right)\right], \tag{3.63}$$

where $\bar{T}_{\mathrm{r}}$ is given by (3.49). In addition to the motion-induced octupole in third order of $\beta_{\mathrm{d}}$ there also is a correction to the CMB dipole. Now we can also recalculate the second beam moment leading to a y-parameter of

$$y_{\mathrm{r,oct}} = y_{\mathrm{d}}\,\beta_{\mathrm{d}}\cdot\left[\mu_0\left(1+\frac{7}{5}\,\mu_{\mathrm{r}}\right) - 6\,\mu_0\left(\mu_0^2-\frac{3}{5}\right)\right]\zeta_+\,\zeta_-\,, \tag{3.64}$$

for the third order in $\beta_{\mathrm{d}}$. The total motion-induced y-parameter is then given by the sum $y = y_{\mathrm{r}} + y_{\mathrm{r,oct}}$, where $y_{\mathrm{r}}$ is given by (3.51). As before in the limit $\theta_{\mathrm{r}} \rightarrow 0$ the y-parameter $y_{\mathrm{r,oct}}$ vanishes. It has a dipole and octupole angular dependence and reaches a maximal value of $y_{\mathrm{r,oct}} \sim 9.6\cdot 10^{-11}$ in the $\mu_0, \theta_{\mathrm{r}}$-plane. Therefore one may completely neglect the contribution of the second beam moment to the y-parameter. If we consider the third beam moment we find

$$\left\langle\delta^3\right\rangle_{\mathrm{r}} = 6\,y_{\mathrm{d}}\,\beta_{\mathrm{d}}\cdot\left[-\frac{2}{5}\,\mu_0 + \mu_0\left(\mu_0^2-\frac{3}{5}\right)\right]\zeta_+\,\zeta_-^2\,. \tag{3.65}$$

It reaches a maximal value of $\left\langle\delta^3\right\rangle_{\mathrm{r}}/6 \sim 1.8\cdot 10^{-11}$. Due the strong dependence on $\theta_{\mathrm{r}}$ we may therefore also neglect any contribution of the third beam moment.

## 3.6 Spectral distortions induced in differential measurements of the CMB sky

In Sect. 3.4 we discussed the spectral distortion arising due to the CMB dipole *inside* a single circular beam in comparison to a *reference* blackbody with temperature $T_0$. In this chapter we address the spectral distortion arising in *differential* measurements of the CMB fluctuations, where two beam intensities $I_1$ and $I_2$ are directly compared with each other and the intensity difference $\Delta I = I_2 - I_1$ is measured. Since in Sect. 3.5 we have shown that y-distortion arising due to higher multipoles have corresponding y-parameters $y \leq 10^{-9}$, here we are only taking distortions arising due to the CMB dipole into account. If we assume that the both beams are circular and have the same radius $\theta_{\mathrm{r}}$ (see Fig. 3.10), we may define the beam RJ temperatures as $\bar{T}_{\mathrm{r},1}$ and $\bar{T}_{\mathrm{r},2}$, where $\bar{T}_{\mathrm{r},i}$ of each beam is given by equation (3.49). Now, defining the reference blackbody $I_* = B_\nu(T_*)$ with temperature $T_{\mathrm{ref}} = T_*$ using equations (3.6) and (3.28) we find for the inferred temperature difference at frequency $\hat{x}_* = h\nu/k\,T_{\mathrm{ref}}$

$$\frac{\Delta T(\hat{x}_*)}{T_*} = \Delta_{\mathrm{r,12}} + y_{\mathrm{r,12}}\cdot g_y(\hat{x}_*)\,, \tag{3.66}$$

where we have introduced the abbreviations

$$\Delta_{\mathrm{r,12}} = \frac{\bar{T}_{\mathrm{r},2}-\bar{T}_{\mathrm{r},1}}{T_*} \tag{3.67a}$$

$$y_{\mathrm{r,12}} = y_{\mathrm{b,r}} + y_{\mathrm{ref}} \tag{3.67b}$$

$$y_{\mathrm{ref}} = \frac{\bar{T}_{\mathrm{r},2}-\bar{T}_{\mathrm{r},1}}{\bar{T}_{\mathrm{r},1}+\bar{T}_{\mathrm{r},2}}\cdot\frac{\bar{T}_{\mathrm{r},1}+\bar{T}_{\mathrm{r},2}-2\,T_*}{T_*}\,. \tag{3.67c}$$

Using equation (3.51), the difference of the beam y-parameters $y_{\mathrm{b,r}} = y_{\mathrm{r}}(\mu_2) - y_{\mathrm{r}}(\mu_1)$ can be written as

$$y_{\mathrm{b,r}} = -3\,y_{\mathrm{d}}\,\Delta\mu\,[2\,\mu_1+\Delta\mu]\,\zeta_+\,\zeta_-\,, \tag{3.68}$$

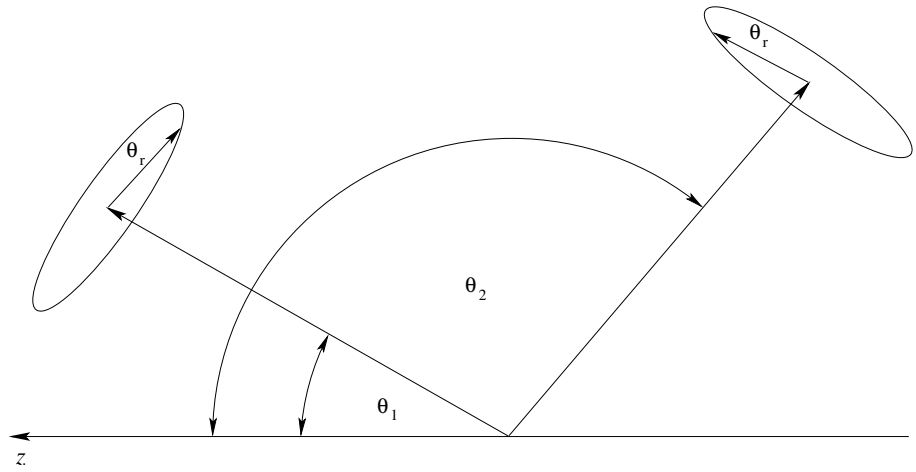


**Figure 3.10:** Illustration of a differential observing strategy: The maximum of the dipole lies in the direction of the $z$-axis. Both observed patches have the same radius $\theta_\mathrm{r}$ and the observed intensity difference is $\Delta I = I_2 - I_1$.

where $\mu_i = \cos\theta_i$, $\Delta\mu = \mu_2 - \mu_1$ and $\theta_i$ is the angle between the dipole axis and the beam $i$. Here it is important to note that in the case $\Delta\mu = 2$, i.e. when we are comparing the maximum and minimum of the CMB dipole $y_\mathrm{b,r} \equiv 0$, since both beams have the same shape and size. In this case we are directly dealing with the difference of two blackbodies with temperatures $\bar{T}_{\mathrm{r},i}$ and we may apply the results obtained earlier in Sect. 3.3.

Now one can write for the relative temperature difference of the two beams at two frequency $\hat{x}_{*,1}$ and $\hat{x}_{*,2}$, with $\hat{x}_{*,2} > \hat{x}_{*,1}$ and $\hat{x}_{*,i} = h\nu_i/k\,T_*$ as

$$\Delta\Delta = \frac{\Delta T(\hat{x}_{*,2}) - \Delta T(\hat{x}_{*,1})}{T_*} = y_{\mathrm{r},12} \cdot [g_y(\hat{x}_{*,2}) - g_y(\hat{x}_{*,1})]\,. \tag{3.69}$$

If we assume that $\hat{x}_{*,1} \ll 1$, i.e. for a measurement in the RJ region of the CMB spectrum, then we can approximate $g_y(\hat{x}_{*,1}) \approx \hat{x}_{*,1}^2/6$. For estimates we will assume that $g_y(\hat{x}_{*,1}) = 0$.

On the CMB sky the most natural choices for the reference temperature is the full sky mean temperature $T_0$ and the temperature of the maximum or the minimum of the CMB dipole anisotropy, whereas the last two are equivalent. Below we now discuss the dependence of the inferred y-parameter on the angle between the beams for these two choices of the reference temperature. In the limit $\theta_\mathrm{r} \to 0$ we can apply the results obtained in Sect. 3.3.2 for the difference of two blackbodies.

**Case $T_* = T_0$**

In this case, making use of equation (3.49) and (3.67c) one may find

$$y_{\mathrm{ref},0} = 3\,y_\mathrm{d}\,\Delta\mu\,[2\,\mu_1 + \Delta\mu]\,\zeta_+^2 + \mathcal{O}(\beta_\mathrm{d}^3)\,. \tag{3.70}$$

Using the beam y-parameter $y_\mathrm{b,r}$ as given in equation (3.68) we find for the corresponding total inferred y-parameter

$$y_{\mathcal{A},0} = 3\,y_\mathrm{d}\,|\mu_\mathrm{r}\,\zeta_+\,\Delta\mu \cdot [2\,\mu_1 + \Delta\mu]| + \mathcal{O}(\beta_\mathrm{d}^3)\,. \tag{3.71}$$

The largest values of the y-parameter in the $\mu_1, \Delta\mu$-plane are obtained for the combinations $(\mu_1, \Delta\mu) = (0, 1)$, $(0, -1)$, $(1, -1)$, $(-1, 1)$. In these optimal cases it follows

$$y_{\mathcal{A},0,\mathrm{opt}} = 3\,y_\mathrm{d}\,\zeta_+\,|\mu_\mathrm{r}| + \mathcal{O}(\beta_\mathrm{d}^3)\,. \tag{3.72}$$

The dependence of $y_{\mathcal{A},0,\mathrm{opt}}$ on the radius of the beam is shown in Fig. 3.11. The distortion does not vanish for high angular resolution ($\theta_\mathrm{r} \to 0$) and the maximum is 3 times bigger than $y_\mathrm{d}$.

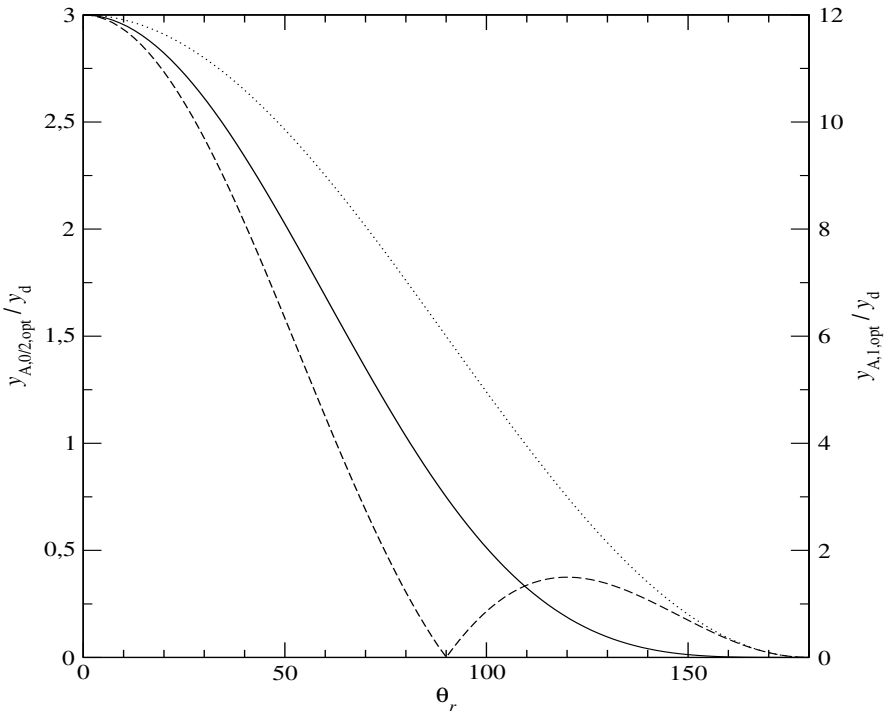


**Figure 3.11:** Dependence of the y-parameter in units of $y_\mathrm{d} = 2.6 \cdot 10^{-7}$ on the beam radius $\theta_\mathrm{r}$ in degree for differential measurements: $y_{\mathcal{A},0,\mathrm{opt}}$ as given by equation (3.72) (dashed/left ordinate), $y_{\mathcal{A},1,\mathrm{opt}}$ as given by equation (3.75) (solid/right ordinate) and $y_{\mathcal{A},2,\mathrm{opt}}$ as given by equation (3.76) (dotted/left ordinate) .

The corresponding absolute temperature difference in some of the Planck frequency channels are given in Table 3.1. For $\theta_\mathrm{r} = \pi/2$ the y-distortion vanishes.

Let us note here that in the case $\Delta\mu = 2$, i.e. when we are directly comparing the maximum and the minimum of the CMB dipole, the spectral distortion vanishes. This can be understood as follows: As was argued in Sect. 3.2.2, if the chosen reference temperature is equal to $T_{y=0}$ as given by equation (3.33) the total y-parameter is zero. For $\mu_1 = -1$ and $\mu_2 = 1$ the beam moments $\left\langle \delta_i^2 \right\rangle_{\mathrm{r},i}$ are both equal and therefore do not contribute to the total inferred y-parameter (3.67b). In this case we obtain $T_{y=0} = T_\mathrm{RJ} = (\bar{T}_{\mathrm{r},1} + \bar{T}_{\mathrm{r},2})/2 = T_0 + \mathcal{O}(\beta_\mathrm{d}^2)$. Therefore, consistent in the second order of $\beta_\mathrm{d}$ the total inferred y-parameter vanishes. This conclusion can also be directly drawn from equation (3.35).

**Case $T_* = \bar{T}_{\mathrm{r},1}$**

In this case, again making use of equation (3.49) and (3.67c) one may find

$$y_{\mathrm{ref},1} = 3\, y_\mathrm{d}\, \Delta\mu^2\, \zeta_+^2 + \mathcal{O}(\beta_\mathrm{d}^3)\,. \tag{3.73}$$

Now using equation (3.68) we may write the total inferred y-parameter as

$$y_{\mathcal{A},1} = 3\, y_\mathrm{d} \zeta_+ \, |\Delta\mu \cdot [\mu_\mathrm{r}\, \mu_2 - \mu_1]| + \mathcal{O}(\beta_\mathrm{d}^3)\,. \tag{3.74}$$

The largest values of the y-parameter in the $\mu_1, \Delta\mu$-plane are obtained for the combinations $(\mu_1, \Delta\mu) = (1, -2)$ and $(-1, 2)$. In these optimal cases the y-parameter is

$$y_{\mathcal{A},1,\mathrm{opt}} = 12\, y_\mathrm{d}\, \zeta_+^2 + \mathcal{O}(\beta_\mathrm{d}^3)\,. \tag{3.75}$$

For high resolution ($\zeta_+ \to 1$) we can obtain $y_{\mathcal{A},1,\mathrm{opt}}$ directly as the difference of two Planck spectra with temperature corresponding to the maximum $T_2$ and the minimum $T_1$ of the dipole

using (3.40b) with $T_{\rm ref} = T_1$. In this case we directly get $\frac{1}{2}\,[(T_2 - T_1)/T_1]^2 = 2\,\beta_{\rm d}^2 = 12\,y_{\rm d}$. As will be discussed later this way of comparing the maximum and minimum of the CMB dipole should open a way to cross calibrate the frequency channels in future experiments with full sky coverage to very high precision (Sect. 3.7).

The dependence of $y_{\mathcal{A},1,\rm opt}$ on the beam radius is shown in Fig. 3.6. As in the previous case, the y-distortion does not vanish for high resolution ($\theta_{\rm r} \rightarrow 0$) and in the maximum it is even 12 times bigger than $y_{\rm d}$, corresponding to $y_{\rm opt} = 3.1 \cdot 10^{-6}$. This is only $\sim 5$ times below the current upper limit on the mean y-parameter given by COBE/FIRAS. The corresponding absolute temperature difference in some of the PLANCK frequency channels are given in Table 3.1.

Another case may be interesting for CMB missions with partial sky coverage, but which have access to the maximum or the minimum of the dipole ($\mu_1 = \pm 1$) and a region in the directions perpendicular to the dipole axis ($\mu_2 = 0$): Using (3.74) with $(\mu_1, \Delta\mu) = (\pm 1, \mp 1)$ one obtains

$$y_{\mathcal{A},2,\rm opt} = 3\,y_{\rm d}\,\zeta_+ + \mathcal{O}(\beta_{\rm d}^3)\,. \tag{3.76}$$

In this case the amplitude is comparable to $y_{\mathcal{A},0}$, but the dependence on the beam radius $\theta_{\rm r}$ is much weaker (see Fig. 3.6).

## 3.7 Cross Calibration of frequency channels

The cross calibration of the different frequency channels of CMB experiments is crucial for the detection of any frequency-dependent signal. As has been mentioned earlier usually the dipole and its annual modulation due to the motion of the earth around the sun is used for calibration issues. The amplitude of the dipole is known with a precision of $\sim 0.3\%$ on a level of $\Delta T \sim$ mK. But the sensitivities of future experiments will be significantly higher than previous missions and request a possibility for cross calibration down to the level of tens of nK.

In this Sect. we now discuss two alternative ways to cross calibrate the frequency channels of future CMB experiments. Most importantly we show that making use of the superposition of blackbodies and the spectral distortions induced by the CMB dipole should open a way to cross calibrate down to the level necessary to detect signals from the dark ages as proposed by Basu et al. [9].

### 3.7.1 Calibration using clusters of galaxies

It is obvious that the brightest relaxed clusters of galaxies on the sky open additional way to cross calibrate the different frequency channels of future CMB experiments like PLANCK and ground based experiments like ACT. The CMB signal of the majority of rich clusters has a very distinct y-type spectrum due to the thermal SZE. Multi-frequency measurements allow one to determine their y-parameters and thereby open a way to use them as sources for cross calibration. This cross calibration will then enable us to detect the effects of relativistic correction for very hot clusters and thereby to measure the temperatures of clusters independent of X-ray observations.

Clusters such as Coma, where existing X-ray data provide excellent measurements of the electron densities and temperatures inside the cluster and where we know the contamination of the CMB brightness by radio-sources and the dust in galaxies very well, even may be used for absolute calibration of CMB experiments. For the Coma cluster today X-ray data allow us to predict the CMB surface brightness with precision of the order of a few percent.

Due to the redshift independence of the SZ signal, distant clusters have similar surface brightness but much smaller angular diameters. Therefore they are good sources for calibration issues for experiments covering only limited parts of the sky and having high angular resolution like ACT (for example ACT is planing to investigate 200 square degree of the sky [77]).

One disadvantage of clusters for cross calibration purposes is that they are too bright: Typically clusters have y-parameter of the order of $\sim 10^{-5} - 10^{-4}$ and therefore are only a few times weaker than the temperature signal of the CMB dipole ($\sim 3\,\mathrm{mK}$). In comparison to the level of calibration and cross calibration achieved directly using the dipole this is not much of an improvement.

In addition planets or galactic and extragalactic radio-sources might serve for cross calibration purposes, if we know their spectral features with very high precision. Quasars and Active Galactic Nuclei are not good candidates for this issue, since they are highly variable in the spectral band of interest.

### 3.7.2 Cross calibration using the superposition of blackbodies

All the sources mentioned in Sect. 3.7.1 do not allow us to cross calibrate down to the level of the sensitivity of future CMB experiments and do not enable us to detect signals from the dark ages as predicted by Basu et al. [9]. Therefore here we want to discuss a method to cross calibrate the frequency channel using the spectral distortions induced by the CMB dipole (see Sect. 3.4). These spectral distortions can be predicted with very high accuracy on a level of $\sim \mu$K. This is $\sim 1000$ times lower than the dipole signal and should therefore allow us the cross calibration to a very high precision.

Each CMB experiment measures the fluctuations of the CMB intensity on the sky. Due to the nature of the physical processes producing these fluctuations at each point they are related to the fluctuations of the radiation temperature. In a map-making procedure the measured fluctuations in the intensity are translated into the fluctuations in the radiation temperature. Usually the aim of any map-making procedure is to reduce statistic and systematic error in order to obtain a clean signal from these CMB temperature fluctuations. As has been discussed in Sects. 3.2 the superposition of blackbodies with slightly different temperature in the second order induces y-distortions in the *inferred* temperature differences. The amplitude of these distortions depends on the temperature difference and the chosen reference temperature. In Sects. 3.4 and 3.6 it has been shown that due to the two basic observing strategies, *absolute* and *differential* measurements, the dipole can induce y-distortions with y-parameters up to $y \sim 10^{-6}$. It was also shown in Sect. 3.5 that contributions from higher multipoles are much smaller ($y \sim 10^{-11} - 10^{-9}$).

The y-distortions induced by the dipole can contaminate the maps produced in the map-making procedure on a level higher than the sensitivity of the experiment. Therefore it is important to chose the map-making procedure such that spectral distortions are minimized. The discussion in Sects. 3.3 has shown that for this purpose in *absolute* measurements of the CMB sky it is the best to choose the temperature of the reference blackbody close to the beam RJ temperature. This implies that for CMB experiment the best choice for the temperature of the internal calibrator is the full sky mean temperature $T_0$. In order to minimize the spectral distortions arising due to the superposition of blackbodies in *differential* measurements the best choice for the reference temperature used to relate the intensity difference maps to the temperature difference maps is the RJ temperature of the combined temperature distribution of both beams. This optimal reference temperature will be time dependent due to the various scanning strategies and orientations of the spinning axis relative to the dipole during observations.

The purpose of this Sect. is not to discuss the details about map-making procedures but to show that there are ways to manipulate these CMB maps in order to make the spectral distortions arising due to the superposition of blackbodies become useful for cross calibration purposes. As the discussion in Sect. 3.3 has shown, for this issue it is better to move $T_{\mathrm{ref}}$ as far as possible away from $T_0$. The optimal choice of $T_{\mathrm{ref}}$ depends on the sensitivity of the experiment and on the observing strategy: For *absolute* measurements $T_{\mathrm{ref}}$ should be as close as possible to $T_0$ in order to minimize the induced y-distortions but on the other hand it should be chosen such that the induced y-distortion due to the CMB dipole is still measurable

**Table 3.1:** y-distortion: $\Delta T = T_{\rm ref} \cdot y$ in $\mu$K for $y$ as given in the left column in some of the PLANCK spectral channels. Here $y_{\rm d} = 2.6 \cdot 10^{-7}$, $y_{\rm opt,0} = 3\, y_{\rm d}$ and $y_{\rm opt} = 12\, y_{\rm d}$.

| | Center of channels [GHz] | | | | | | |
|---|---|---|---|---|---|---|---|
| $\nu_{\rm c}$ | 30 | 44 | 70 | 100 | 143 | 217 | 353 |
| $y_{\rm d}$ | 0.03 | 0.07 | 0.17 | 0.34 | 0.67 | 1.39 | 2.97 |
| $y_{\rm opt,0}$ | 0.10 | 0.21 | 0.52 | 1.03 | 2.01 | 4.18 | 8.90 |
| $y_{\rm opt}$ | 0.39 | 0.83 | 2.07 | 4.13 | 8.05 | 16.71 | 35.56 |

within the sensitivity of the experiment. But in principle there is no strong constraint, since the induced y-distortions can again eliminated afterwards. For *differential* measurements it is possible to chose the optimal reference temperature for calibration issues independent of the best map-making reference temperature, but here it is important to compare regions on the sky with maximal temperature difference, i.e. with maximal angular separation in the observed field. Below we now separately discuss CMB experiments using *differential* measurements with full and partial sky coverage in more detail.

### Full sky CMB surveys

For full sky missions like PLANCK the regions with maximal temperature difference are located around the extrema of the CMB dipole. Using equation (3.74) we see that they correspond to $\Delta\mu = 2$ and the resulting maximal spectral distortion is characterized by $y_{\rm opt} = 12\, y_{\rm d} = 3.1{\cdot}10^{-6}$, if we set $T_{\rm ref} = \bar{T}_{\rm r,1}$ or $T_{\rm ref} = \bar{T}_{\rm r,2}$, i.e. to the maximum or minimum of the temperature on the CMB sky arising due to the dipole.

One attractive procedure to compare the maximum and minimum of the CMB dipole is to take the CMB intensity maps of each spectral channel and to calculate the difference between each map and the map obtained by remapping the value of the intensity $I(\boldsymbol{n})$ at position $\boldsymbol{n}$ to the value $I(-\boldsymbol{n})$ at position $-\boldsymbol{n}$, i.e rotating the initial map by 180 degrees around any axis, which is perpendicular to the CMB dipole axis and is crossing the origin or equivalently setting $\mu_2 = -\mu_1$ in equation (3.66).

Afterwards these artificial intensity maps for each spectral channel are converted into temperature maps using equation (3.6) and setting the reference temperature at each point to $T_*(\boldsymbol{n}) = \bar{T}_{\rm r,1}(\boldsymbol{n})$ of the intrinsic map. Neglecting the contributions from intrinsic multipoles with $l \geq 2$, the difference map in some frequency channel $\hat{x}_* = h\nu/k\,\bar{T}_{\rm r,1}$ will be given by

$$\frac{\Delta T(\hat{x}_*, \vec{n})}{\bar{T}_{\rm r,1}(\vec{n})} = -2\,\beta_{\rm d}\,\zeta_+\,\mu + 2\,\beta_{\rm d}^2\,\zeta_+^2\,\mu^2 + 12\,y_{\rm d}\,\zeta_+^2\,\mu^2 \cdot g_y(\hat{x}_*)\,, \tag{3.77}$$

where we used the definition (3.4) for $g_y(\hat{x})$. This shows that the artificial maps will contain a frequency-independent temperature dipole component with twice the initial dipole amplitude and a monopole and quadrupole y-distortion resulting from the second term in (3.77). The maxima of the spectral distortion will coincide with the extrema of the CMB dipole.

Now, using the artificial map of the lowest frequency channel as a reference and taking the differences between this reference map and the artificial maps in higher spectral channels we can eliminate the frequency-independent term corresponding to twice the dipole in equation (3.77). This then opens a way to cross calibrate all the channels to very high precision, since the quadrupole component in these artificial maps will be larger in higher spectral channels, following the behavior of $g_y$ with $\hat{x}$.

The signal will include both statistical and systematic errors for the average temperature of the sky and the dipole amplitude $\beta_{\rm d}$. All uncertainties are mainly influencing the frequency-

independent dipole term but for the frequency-dependent monopole and quadrupole they will become important only in next order:

$$\begin{aligned}\bar{T}_1 \cdot \beta_\mathrm{d}^2 &= \bar{T}_{1,0}\,\beta_{\mathrm{d},0}^2\,(1 \pm \Delta_T) \cdot (1 \pm \Delta_\beta)^2 \\ &= \bar{T}_{1,0}\,\beta_{\mathrm{d},0}^2\,[1 \pm 2\,\Delta_\beta \pm \Delta_T] + \mathcal{O}(\Delta_\beta \cdot \Delta_T)\,, \end{aligned} \tag{3.78}$$

where $\bar{T}_{1,0}$ is the correct value of the temperature at a given point on the sky, $\beta_{\mathrm{d},0}$ is the correct dipole amplitude and $\Delta_T$ and $\Delta_\beta$ are their corresponding relative uncertainties. This implies that all the corrections to the frequency-dependent terms are at least 1000 times smaller than the signal we are discussing here. On this level correction due to higher order moments might become important, but their contributions will be less than 1%. This means that y-distortion on a level of $10\,\mu$K can be predicted with $\sim 100\,$nK precision.

Applying the procedure as described above we are adding signals that have statistically independent noise. Therefore the statistical noise of the artificial maps should be a factor of $2/\sqrt{2} = \sqrt{2}$ stronger than the initial maps. On the other hand we are increasing the amplitude of the y-distortion quadrupole by a factor of 12, resulting in strong gain.

The maxima of the quadrupole component in the artificial maps will be rather broad and correspond to thousands of square degrees on the sky, allowing us to average the signal and thereby increasing the sensitivity. For a circular beam average the formula (3.77) will be applicable. The statistical sensitivity of the Planck experiment will permit us to find these spectral distortions in the artificial maps down to the level necessary to detect the effects of reionization as discussed by Basu et al. [9]. Applying the above procedure to the 33 GHz and 93 GHz frequency channels of Wmap will lead to a maximal temperature difference of $\Delta T = 3.6\,\mu$K, whereas the maximal difference will be $\Delta T = 35.6\,\mu$K for the 353 GHz channel of Planck (see Table 3.1). Nevertheless, even in the case of Wmap the very high precision of the experiment might permit the detection of this quadrupole and thereby open the way to cross calibrate its different spectral channels.

For Cobe/Firas the proposed method permits us to check the precision of the internal calibration. The internal calibrator was measured and tested with some finite precision and there is the possibility that the internal calibration may be better than the precision at which it was tested. The proposed method has distinct spectral and angular properties, making it possible to improve the cross calibration of the spectral channels and possibly this will open a way to further improve the great results this experiment already gave us.

### CMB surveys with partial sky coverage

Surveys with partial sky coverage may not simultaneously have access to regions around the maximum and the minimum of the dipole. Therefore here one should choose two regions in the accessible field of view such that the mean temperature difference between these regions is as large a possible. The dependence of the signal on the separation angle has been discussed in detail in Sect. 3.6.

Before cross calibration all the bright sources detected such as bright clusters of galaxies and point sources inside the chosen areas should be extracted. Typically the expected amount of SZ sources will be of the order of a few tens per square degrees with corresponding angular extensions less than $1'$ [see 32, 107]. Afterwards the difference of the signals in the two patches can be taken and compared to the signals in the other spectral channels.

For example choosing one area centered on the minimum or maximum of the CMB dipole as a reference ($T_* = \bar{T}_{\mathrm{r},1}$) and choosing the second area in the ring perpendicular to the dipole axis the maximal y-parameter is $y = 3\,y_\mathrm{d}\,\zeta_+ = 7.7 \cdot 10^{-7}\,\zeta_+$ (cf. equation (3.76)). If we instead set $T_* = T_0$ we obtain the same maximal y-parameter but a stronger dependence on the beam radius or size of the regions we average (cf. equation (3.72)). This small example shows that for any experiment with partial sky coverage a separate analysis of the optimal choice of the reference temperature and the regions on the sky has to be done.

## 3.8 Other sources of spectral distortions

Injection of energy into the CMB prior to recombination leads to spectral distortions of the background radiation. Given the WMAP best fit parameters, before redshift $z_{\rm th} \sim 2 \cdot 10^6$ all distortions are efficiently wiped out, whereas energy injection in the redshift range $z_{\rm th} > z > z_\mu$, with $z_\mu \sim 1.4 \cdot 10^5$, leads to a $\mu$-distortion and injection in the range $z_\mu > z > z_{\rm rec}$ to a y-distortion, with $z_{\rm rec} \sim 1090$ [126, 66, 25, 59].

As was shown by [118] photon diffusion and thermal viscosity lead to the dissipation of small scale density perturbations before recombination. This damping of acoustic waves will contribute to a $\mu$- and y-distortion because it was leading to (i) energy release [126, 45, 60] and (ii) mixing of photons from regions having different temperatures [142].

Now, the WMAP data implies that the initial spectrum of perturbations is close to a scale-invariant Harrison-Zeldovich spectrum with spectral index $n = 1.03 \pm 0.04$ [11]. Different estimates for the spectral distortions arising from the dissipation of acoustic waves in the early universe give a chemical potential of the order of $\mu_{\rm dis} \sim 2 \cdot 10^{-7}$ and y-distortions with $y_{\rm dis} \sim 10^{-7}$ [45, 60].

Another contribution to the y-distortion arises from the epoch of reionization [141, 61] and from the sum of the SZE of clusters of galaxies [83]. The WMAP results for the TE power spectrum point towards an early reionization of the universe with corresponding optical depth $\tau_{\rm re} = 0.17 \pm 0.04$ [73, 121]. Here two main effects are important: (i) The photoionized gas typically has temperatures $T$ of the order of $\sim 10^4\,{\rm K}$. Therefore the diffuse gas after reionization will produce a y-distortion in the CMB spectrum with

$$y_{\rm re} \sim \int \frac{k\,T}{m_{\rm e}\,c^2}\,{\rm d}\tau \sim 3 \cdot 10^{-7}\,\frac{\tau_{\rm re}}{0.17}\,\frac{T}{10^4\,{\rm K}}\,.$$

(ii) The motion of the matter induces a y-distortion on the whole sky due to the second order Doppler effect, with corresponding y-parameter [61], $y_v = \frac{1}{3}\int \sigma_{\rm T}\,N_{\rm e}\,c\,\langle v^2\rangle\,{\rm d}t$, where $\langle v^2\rangle$ is the velocity dispersion over the whole sky in units of the speed of light. For a CDM model it is of the order of

$$y_v \sim 2 \cdot 10^{-8}\left(\left[\frac{z_{\rm re}}{10}\right]^{1/2} - 1\right)\frac{\langle v^2\rangle}{10^{-5}}\,\frac{\Omega_{\rm b}h^2}{0.0224}\,.$$

Since the reionization optical depth is very small, this is one order of magnitude smaller than $y_{\rm re}$. If secondary ionization was patchy this will in addition lead to angular fluctuations [110].

All the effects mentioned in this section lead to y-distortions with corresponding y-parameter in the range $y \sim 10^{-8} - 10^{-7}$. As has been shown in Sects. 3.4 and 3.6 the y-distortions arising due to the CMB dipole are of the same order. For example the CMB dipole induces a full sky y-distortion with $y_{\rm d} = 2.6 \cdot 10^{-7}$. Therefore, to measure any of the effects discussed above it is necessary to take spectral distortions associated with the CMB dipole into account. But since the angular distribution and the amplitude of these distortions can be accurately predicted they can be easily extracted. As has been shown in Sect. 3.5 spectral distortions arising from higher multipoles typically have $y \sim 10^{-11} - 10^{-9}$ and therefore do not play an important role in this context. But even for these distortions the locations and amplitudes can be accurately predicted with measured CMB maps and therefore offer the possibility to eliminate these distortions from the maps.

## 3.9 Summary

We have discussed in detail the spectral distortions arising due to the superposition of blackbodies with different temperatures in the limit of small temperature fluctuations. The superposition leads to y-distortion with y-parameter $y_{\rm S} = \langle\delta^2\rangle/2$, where $\langle\delta^2\rangle$ denotes the second moment of the temperature distribution function, if the difference in temperatures is less than a few

percent of the mean RJ temperature. We have shown that in this limit even comparing to pure blackbodies leads to a y-distortion.

The results of this derivation were then applied to measurements of the CMB temperature anisotropies with finite angular resolution and in particular to the CMB dipole and its associated spectral distortions, but in principle the method developed here can be applied whenever one is dealing with the superposition of blackbodies with similar temperatures. We have shown that taking the difference of the CMB intensities in the direction of the maximum and the minimum of the CMB dipole leads to a y-distortion with y-parameter $y_{\rm opt} = 3.1 \cdot 10^{-6}$. This value is 12 times higher than the y-type monopole, $y_{\rm d} = 2.6 \cdot 10^{-7}$. Since the amplitude of this distortion can be calculated with the same precision as the CMB dipole, i.e. 0.3% today [51], it may open a way to use it for calibration issues.

We discussed another possibility to check the zero levels of different frequency channels by observing the difference of the brightness in the direction of the dipole maximum and in the direction perpendicular to the dipole axis: The dipole-induced spectral distortion in this case is 4 times weaker than for the difference of the maximum and minimum and corresponds to $y \sim 7.7 \cdot 10^{-7}$. Nevertheless, it is still 3 times stronger than the dipole-induced whole sky y-distortion with y-parameter $y_{\rm d}$.

The value of $y_{\rm opt}$ is only 5 times lower than the upper limit on the whole sky y-parameter obtained by the COBE/FIRAS experiment [51] and is orders of magnitudes above the sensitivity of PLANCK and CMBPOL in each of their spectral channels. Therefore this signal might become useful for both cross calibration and even absolute calibration of different frequency channels of these experiments to very high precision, in order to permit detection of the small signals of reionization as for example discussed by Basu et al. [9], and to study frequency-dependent foregrounds with much higher sensitivity. We should emphasize that on this level we are only dealing with the distortions arising from the CMB dipole as a result of the comparison of Planck spectra with different temperatures close to the maximum and minimum of the CMB dipole, i.e. due to the superposition of blackbodies. The distortions are introduced due to the processing of the data and become most important in the high frequency channels.

The development of the CMB experimental technology is repeating with a 20 year delay the progress that was made in the astronomical observations with X-ray grazing incidence mirrors and CCD detectors. Due to the big efforts of many spacecraft teams, the X-ray background today is resolved to more than 85 % [106]. During the next decade, CMB observers will be able to pick up all rich clusters of galaxies and all bright y-distorted features connected with supernovae in the early universe, groups of galaxies and even down to patchy reionization in the CMB maps. Deep source counts may permit the separation of their contribution to the y-parameter and in principle might bring us close to the level of the y-distortions mentioned in Sect. 3.8. As has been argued, at this stage the contributions to the y-parameter arising from the superposition of Planck spectra with different temperatures corresponding to the observed CMB temperature fluctuations will be the easiest to separate. Again, the main contribution will arise from the CMB dipole. On the full sky the corresponding y-parameter will be $y_{\rm d} = 2.6 \cdot 10^{-7}$. But even the distortions arising from the primordial temperature fluctuations with multipoles $l \geq 2$ can lead to distortions of the order of $y \sim 10^{-9}$ in significant parts of the sky. In the future this type of spectral distortion can be taken into account making it possible to enter the era of high precision CMB spectral measurements.

The main obstacle for measuring and utilizing the effects connected with the superposition of blackbodies for calibration issues will be the lack of knowledge about both the spectral and spacial distribution of foregrounds. Given the fast progress in experimental technology and the increasing amount of data available there may still be a way to separate all these signals in the future. In any case, for upcoming CMB experiments spectral distortions arising due to the superposition of blackbodies, the effects of foregrounds and correlated noise should be taken into account simultaneously and self-consistently.

# Chapter 4

# The double Compton process in mildly relativistic thermal plasmas

In this Chapter the kinetic equation of double Compton emission in an isotropic, mildly relativistic thermal plasma for arbitrary incoming photon distributions is discussed both numerically and analytically. With this work we shall obtain the necessary tools to include the effects of relativistic corrections on the production of photons in the context of the thermalization of cosmic microwave background (CMB) spectral distortions in the very early universe.

Here temperature corrections up to forth order for the lowest order in the emitted photon energy are considered. We give two kinds of analytic approximations to the double Compton emission coefficient at low frequencies: (i) a *direct* Taylor series expansion in fourth order of temperature and (ii) an *inverse* approximation, which utilizes only the first order temperature correction. We derive these analytic expressions for the double Compton emission coefficient of incoming monochromatic photons, Planck, Bose-Einstein and Wien spectra and compare them with the results obtained by a numerical integration of the full Boltzmann collision term using a Monte-Carlo-method. We show here that combining the *direct* and *inverse* formula an agreement of better than 5 % in a very broad range of temperatures and under various physical conditions can be achieved.

Furthermore we show that the double Compton emissivity strongly depends on the ratio of the energies of the incoming photon and electron: For hard photons and non-relativistic electrons the emission is strongly suppressed as compared to the case of similar photon and electron energy, whereas in the opposite situation, i.e. relativistic electrons and soft initial photons, emission is enhanced. For photons and electrons close to thermodynamic equilibrium the double Compton emissivity increases less rapid with temperature as compared to the non-relativistic calculation. Given the importance of double Compton scattering for the thermalization of cosmic microwave background spectral distortions after energy release in the early universe ($z > 10^6$) this fact hints to the possibility that the thermalization at high redshifts is less efficient. We will discuss possible consequences of relativistic corrections in this context in Chapter 5. The results of the work presented here will be submitted in the near future [36].

## 4.1 The current understanding of the double Compton process

Double Compton (DC) scattering is the process of the form $e + \gamma_0 \leftrightarrow e' + \gamma_1 + \gamma_2$. It corresponds to the lowest order correction to Compton scattering, with two photons in the outgoing channel and like thermal Bremsstrahlung (BS) exhibits an *infrared divergence* at low frequencies.

The full DC scattering squared matrix element and differential cross sections for various limiting cases were first derived by Mandl & Skyrme [81] and may also be found in Jauch & Rohrlich [69]. Before the existence of the DC scattering effect was postulated by Heitler & Nordheim [56] and the expression for the differential cross section in the limit when one of the

emitted photons is very soft was found by Eliezer [47]. Experimental evidence for the existence of the effect was obtained by Boekelheide [19] and also Cavanagh [27]. Afterwards the results of Mandl & Skyrme [81] were confirmed experimentally [134] and even the absolute amplitude of the DC cross section was measured accurately [87].

The kinetic equation for DC emission and absorption in an *isotropic, cold* plasma and for low energy initial photons, i.e. small $\omega_0 = h\nu_0/m_\mathrm{e}c^2$, where $\nu_0$ is the frequency of the initial photon $\gamma_0$, was first derived by Lightman [80] and independently by Thorne [133] using the *soft photon limit*. In this approximation it is assumed that one of the outgoing photons ($\gamma_1$ or $\gamma_2$) is *soft* as compared to the other. Under these assumptions the emissivity of DC increases like $\propto \omega_0^2$ with photon energy [see 69, Eq. 11-45].

In equilibrium, i.e for thermal electrons of temperature $T_\mathrm{e}$ and Planckian photons with temperature $T_\gamma \equiv T_\mathrm{e}$, DC emission is completely balanced by its inverse process, DC absorption. Including DC and BS emission this equilibrium is reached very fast at low frequencies but the action of Compton scattering is necessary and very important for the high frequency evolution of the photon spectrum. It was also realized by Lightman [80] and later again by Pozdnyakov et al. [101] and Svensson [132] that DC emission in comparison to thermal BS becomes the main source of soft photons in low density plasmas: let $n_\mathrm{i}$ be the ion and $n_\gamma$ the photon number density, then the DC emission dominates over BS when the following criterion is fulfilled: $n_\mathrm{i} \lesssim 10\, n_\gamma \left(k\,T_\mathrm{e}/m_\mathrm{e}c^2\right)^{5/2}$. For this estimate the initial photons were assumed to follow a Wien distribution and have the same temperature as the electrons. Due to the large entropy ($n_\mathrm{i}/n_\gamma \sim 10^{-10}$) of the universe, at early stages ($z \gtrsim 5\cdot 10^5$) DC emission becomes very important for the thermalization of CMB spectral distortions and especially the evolution of chemical potential distortions after energy release [126, 46, 25, 59]. We will discuss possible implications of the result obtained here for the thermalization in the next Chapter.

Again assuming cold electrons and soft incident photons but making *a priori* no assumption about the emitted photon energy Gould [54] obtained an analytic correction factor for the DC emission coefficient of monoenergetic initial photons. In his limit the *recoil* effect is negligible (i.e. the scattered electrons will carry away momentum but only a tiny amount of energy). Here we show that for increasing energy of the incident photon the recoil effect becomes especially important in the high frequency part of the DC emission spectrum. Furthermore, we show that the low frequency emissivity strongly decreases for larger $\omega_0$.

In both approaches mentioned above the electrons were initially at rest, implying that no *Doppler boosting* is taking place. As we discuss here, increasing the temperature of the electrons boosting becomes important leading to *Doppler broadening* at high and an enhancement of the DC emission at low frequencies. Previously, temperature corrections to the low frequency DC emissivity in a mildly relativistic plasma for incoming Wien spectra, again in the soft photon limit, were given by Svensson [132]. It was shown that in the mildly relativistic case the low frequency DC emissivity increases significantly slower with temperature. Here we now discuss temperature corrections to the DC emissivity for arbitrary incoming photon distributions and derive analytic expressions, which are applicable in a wide range of photon and electron energies including induced effects.

In addition, until now the evolution of the high frequency initial photon was not discussed in the literature: due to DC scattering the initial photon is redistributed in energy and therefore a small correction to the Compton process arises. Here we now take into account the full evolution equation of the photon phase space density under DC scattering. We also in detail discuss numerically the DC emission for monochromatic incident photons and derive analytic approximations for the low frequency DC emissivity. Using these results we discuss the case of more general incoming photon distributions and derive analytic expressions for the *effective DC Gaunt factor*. Using these we show that the redistribution of high frequency photons by DC scattering, at least in the cosmological context, is not important. Therefore we then focus on the analytic description of the low frequency emission for incoming photons with Planck, Bose-Einstein and Wien spectra. Note that in the following we use $h = c = k = 1$ throughout.

## 4.2 The kinetic equation for DC scattering

### 4.2.1 General definitions

DC emission is a result of the scattering event between an electron and a photon with an additional photon in the outgoing channel:

$$e(P) + \gamma(K_0) \longrightarrow e(P') + \gamma(K_1) + \gamma(K_2)\,.$$

Here $P = (E, \boldsymbol{p})$, $P' = (E', \boldsymbol{p}')$ and $K_i = (\nu_i, \boldsymbol{k}_i)$ denote the corresponding particle four-momenta[1]. In the following we will call $\gamma(K_0)$ the *initial*, $\gamma(K_1)$ the *scattered* and $\gamma(K_2)$ the *emitted* photon. It is important to bear in mind that this nomenclature for the photons in the outgoing channel is arbitrary since they are indistinguishable. It is only motivated by the classical picture, in which the trajectory of the initial photon can be followed, and when it is scattered without changing its energy significantly. In this case the emitted photon is very soft as compared to the initial one and it is possible to distinguish then at least energetically. Quantum-mechanically it is also possible that $\nu_2 \geq \nu_1$ meaning that the two photons in principle can exchange their roles, i.e. the *emitted* photon, at least energetically, can substitute the *scattered* and vice versa. Note that the emission integral as given below takes both photons into account and therefore has to be regarded as a *two*-photon emission spectrum.

#### Reaction channels

In thermodynamic equilibrium DC emission is balanced by the inverse process, DC absorption. The time evolution of the phase space density of the photon phase space density under DC emission and absorption can be described by the Boltzmann equation (see Cercignani & Kremer [29] as reference about the relativistic Boltzmann equation). If we consider the time evolution of the photon phase space density at frequency $\nu_2$, i.e. we focus on the photon $\gamma_2(K_2)$, four reactions lead to a change of the occupation number $n(\nu_2)$:

$$\gamma_0 + e \rightarrow \gamma_1 + \gamma_2 + e' \tag{4.1a}$$
$$\gamma_0 + e \leftarrow \gamma_1 + \gamma_2 + e' \tag{4.1b}$$
$$\gamma_2 + e \rightarrow \gamma_0 + \gamma_1 + e' \tag{4.1c}$$
$$\gamma_2 + e \leftarrow \gamma_0 + \gamma_1 + e'\,. \tag{4.1d}$$

The first is the *emission* of a photon $\gamma_2$ in the outgoing channel due to the collision of the initial photon $\gamma_0$ with an electron. The second is the *destruction* or *absorption* of one photon $\gamma_2$ by a collision with an electron and another photon $\gamma_1$. These two reactions where taken into account in the derivation of the DC kinetic equation by Lightman [80] and Thorne [133].

The third reaction can be considered as the *scattering* of the photon $\gamma_2$ *out* of the phase space volume and the last reaction is the *creation* of one photon $\gamma_2$ out of two. These two reactions are proportional to the total DC scattering cross section. They effectively lead to a *redistribution* of photon in energy rather than a production of new photons. Since for the reactions (4.1a) and (4.1b) in both directions two possibilities exist (exchange of the roles of $\gamma_1$ and $\gamma_2$) the relative amplitude of these with respect to the others is a factor of 2 bigger. As mentioned by Mork [89] this leads to a factor of $\frac{1}{2}$ in the total DC cross section, which has to be taken into account in the full Boltzmann equation.

[1] Henceforth bold font denotes 3-vectors.

### Statement of the Boltzmann equation

Now one can write down the full kinetic equation for the phase space evolution of the photon field at frequency $\nu_2$ as

$$\left.\frac{\partial n_2}{\partial t}\right|_{\rm DC} = \frac{(2\pi)^4}{2\nu_2}\int \mathrm{d}\Pi\,\mathrm{d}\Gamma_0\,\mathrm{d}\Pi'\,\mathrm{d}\Gamma_1 \times \left\{\delta^4(P+K_0-P'-K_1-K_2)\cdot|\mathcal{M}|^2_{\gamma_0\gamma_1\gamma_2}\,F_{\gamma_0\gamma_1\gamma_2} - \frac{1}{2}\delta^4(P+K_2-P'-K_1-K_0)\cdot|\mathcal{M}|^2_{\gamma_2\gamma_1\gamma_0}\,F_{\gamma_2\gamma_1\gamma_0}\right\}. \tag{4.2}$$

Here the particle phase space volumes have the form

$$\mathrm{d}\Pi = \frac{\mathrm{d}^3p}{(2\pi)^3 2E} \qquad \mathrm{d}\Pi' = \frac{\mathrm{d}^3p'}{(2\pi)^3 2E'} \qquad \mathrm{d}\Gamma_i = \frac{\mathrm{d}^3k_i}{(2\pi)^3 2\nu_i} \tag{4.3}$$

for the electrons and photons correspondingly. The squared matrix element $|\mathcal{M}|^2 = e^6\,X$ follows from quantum electrodynamics. Here $e$ is the electron charge and $X$ is defined in the Appendix D.1. In the above notation $|\mathcal{M}|^2_{\gamma_0\gamma_1\gamma_2}$ and $|\mathcal{M}|^2_{\gamma_2\gamma_1\gamma_0}$ indicate that the roles of the photons $\gamma_0$ and $\gamma_2$ were exchanged in the evaluation of $|\mathcal{M}|^2$.

Assuming that Fermi blocking is negligible, the statistical factor $F_{\gamma_i\gamma_1\gamma_j}$, with $i \neq j$, is given by

$$F_{\gamma_i\gamma_1\gamma_j} = f\,n_i[1+n_1][1+n_j] - f'\,n_1\,n_j[1+n_i]\,, \tag{4.4}$$

where the abbreviations $f = f(\boldsymbol{p})$, $f' = f(\boldsymbol{p}')$ for the electron and $n_i = n(\boldsymbol{k}_i)$ for the photon phase space densities were introduced. In equation (4.2) the term $\propto F_{\gamma_0\gamma_1\gamma_2}$ corresponds to the reactions (4.1a) and (4.1b) and the term $\propto F_{\gamma_2\gamma_1\gamma_0}$ accounts for the channels (4.1c) and (4.1d). Note again the factor of $\frac{1}{2}$ in the second term of the integrand of (4.2).

In the following we assume that all the phase space densities are *isotropic* implying that they only depend on the energy of the corresponding particle. Furthermore we also assume that the electrons are non-degenerate, justifying that Fermi blocking was neglected above. In this case, the electron phase space density may be described by a relativistic Maxwell-Boltzmann distribution

$$f(E) = \frac{N_\mathrm{e}}{4\pi\,m_\mathrm{e}^3\,K_2(1/\theta_\mathrm{e})\,\theta_\mathrm{e}}\,e^{-E/m_\mathrm{e}\theta_\mathrm{e}}\,, \tag{4.5}$$

where $N_\mathrm{e}$ is the electron number density, such that $N_\mathrm{e} = \int f(E)\,\mathrm{d}^3p$, and $K_2(1/\theta_\mathrm{e})$ is a modified Bessel function of second kind [1], with $\theta_\mathrm{e} = T_\mathrm{e}/m_\mathrm{e}$. In the low temperature limit, $\theta_\mathrm{e} \ll 1$, the relativistic Maxwell Boltzmann distribution (4.5) can be handled by the expression given in the Appendix A, which is useful for both analytic and numerical purposes.

To further reduce the Boltzmann collision integral (4.2) one can make use of the $\delta$-functions, which assure energy and momentum conservation. We first integrate over the momenta of the scattered electrons $\mathrm{d}^3p'$, leading to the substitution

$$\boldsymbol{p}' = \boldsymbol{p} + \boldsymbol{k}_0 - \boldsymbol{k}_1 - \boldsymbol{k}_2 \tag{4.6a}$$

in the whole integrand of the Boltzmann equation (4.2). Note that for the second term of the integrand in equation (4.2) the 3-momenta $\boldsymbol{k}_0 \leftrightarrow \boldsymbol{k}_2$ have to be exchanged. Equation (4.6a) corresponds to the condition for *momentum conservation* and is complemented by the *energy conservation* equation, which as an example can be expressed like

$$\nu_1 = \frac{P\cdot K_0 - P\cdot K_2 - K_0\cdot K_2}{(P+K_0-K_2)\cdot\hat{K}_1}\,. \tag{4.6b}$$

A similar equation can be obtained for the energy of the emitted photon $K_2$ by the replacement $K_2 \rightarrow K_1$. Depending on the physical situation, equation (4.6b) can be used to eliminate one additional variable in Boltzmann collision integral (4.2).

Below we now discuss two possible ways of preceeding, one leading to a description of the DC scattering process with standard textbook scattering cross sections, the other leading to the *conditional DC emission kernel*, $\mathcal{P}(\nu_0 \to \nu_2 \,|\, \nu_1)$, which describes the DC emission spectrum in an isotropic plasma for monochromatic initial photons and thermal electrons, with fixed energy, $\nu_1$, of the scattered photons. It turns out that especially for the understanding of DC scattering the kernel approach provides very useful and interesting insights into the physics of DC scattering, but for analytic derivation the standard approach is significantly simpler.

### 4.2.2 Standard approach

After carrying out the integration over the scattered electron momenta, $\mathrm{d}^3p'$, the standard textbook procedure is to further simplify the Boltzmann collision term by integrating over the frequency of the scattered photon, $\mathrm{d}\nu_1$, in the interval $[0, \infty)$. This then, in addition to relation (4.6a), leads to the substitution (4.6b) in the whole integrand of (4.2). Now, the Boltzmann equation for the phase space evolution of the photons can be cast into the form

$$\left.\frac{\partial n_2}{\partial t}\right|_{\mathrm{DC}} = \frac{1}{\nu_2^2} \int \mathrm{d}^3p \int \mathrm{d}^3k_0 \int \mathrm{d}\Omega_1 \left\{ g_{\o 0}\, \frac{\mathrm{d}\sigma_{\mathrm{DC}}^{\gamma_0\gamma_1\gamma_2}}{\mathrm{d}\Lambda}\, F_{\gamma_0\gamma_1\gamma_2} - \frac{g_{\o 2}}{2}\, \frac{\nu_2^2}{\nu_0^2}\, \frac{\mathrm{d}\sigma_{\mathrm{DC}}^{\gamma_2\gamma_1\gamma_0}}{\mathrm{d}\Lambda}\, F_{\gamma_2\gamma_1\gamma_0} \right\}, \quad (4.7)$$

where $\mathrm{d}^3k_0$ and $\mathrm{d}\Omega_1$ denote the integration over the initial photon momenta and solid angles of the scattered photons, respectively. The differential DC scattering cross section in this case is given by [see 69, Eq. 11-38]

$$\frac{\mathrm{d}\sigma_{\mathrm{DC}}^{\gamma_i\gamma_1\gamma_j}}{\mathrm{d}\Lambda} = \frac{\alpha\, r_0^2}{(4\pi)^2}\, \frac{\nu_1\, \nu_j}{g_{\o i\gamma}\, \nu_i}\, \frac{X}{(P + K_i - K_j)\cdot \hat{K}_1}\,. \quad (4.8)$$

Here we defined the *Møller relative speed* of the incident electron and photon as $g_{\o i} = \hat{P}\cdot\hat{K}_i = 1 - \beta\,\mu_{\mathrm{e}i}$, with the dimensionless electron velocity $\beta = |\boldsymbol{v}|/c = |\hat{\boldsymbol{p}}| = |\boldsymbol{p}|/E$ and the directional cosine $\mu_{\mathrm{e}0} = \hat{\boldsymbol{p}}\cdot\hat{\boldsymbol{k}}_0$. Note that in the following an additional hat above 3- and 4- vectors indicates that they are normalized to the time like coordinate of the corresponding 4-vector. Furthermore $\alpha = e^2/4\pi \approx 1/137$ is the fine structure constant, $r_0 = \alpha/m_{\mathrm{e}}$ is the classical electron radius and $\gamma = E/m_{\mathrm{e}} = 1/\sqrt{1-\beta^2}$ denotes the Lorentz-factor of the initial electron. One also has to bear in mind that the invariant matrix element has to be evaluated accordingly, i.e. $X(K_0, K_1, K_2) \neq X(K_2, K_1, K_0)$.

In general the Boltzmann collision integral (4.7) has to be performed numerically, but in the limit of small temperatures and energies of the initial and emitted photons it is possible to derive various useful analytic approximations, which we will discuss below.

### 4.2.3 Kernel approach

In order to obtain the conditional DC emission kernel, $\mathcal{P}(\nu_0 \to \nu_2 \,|\, \nu_1)$, we align the $z$-axis of the coordinate system with the direction of the emitted photon $K_2$ and in addition to $\mathrm{d}^3p'$ integrate over the directional cosine $\mathrm{d}\mu_{12}$ of the scattered photons. In the following we use the notations $\mu_{ij} = \hat{\boldsymbol{k}}_i\cdot\hat{\boldsymbol{k}}_j$ and $\phi_{ij}$ for the directional cosines and azimuthal angles between the photons $i$ and $j$, respectively. In the same manner we introduce abbreviations for quantities involving the initial electron and photon $i$, i.e. $\mu_{\mathrm{e}i} = \hat{\boldsymbol{p}}\cdot\hat{\boldsymbol{k}}_i$ and $\phi_{\mathrm{e}i}$ for the directional cosines and azimuthal angles between these particles, respectively.

With these comments the full kinetic equation for the evolution of the isotropic photon phase space density, $n(\nu)$, under DC scattering off relativistic, Maxwellian electrons can be

cast into the form

$$\begin{aligned}\left.\frac{\partial n_2}{\partial t}\right|_{\rm DC} &= \int \frac{\nu_0^2}{\nu_2^2}\, n_0[1+n_1][1+n_2]\,\mathcal{P}(\nu_0 \to \nu_2\,|\,\nu_1)\,{\rm d}\nu_0\,{\rm d}\nu_1 \\ &\quad - \int n_1\, n_2[1+n_0]\,\mathcal{P}(\nu_0 \leftarrow \nu_2\,|\,\nu_1)\,{\rm d}\nu_0\,{\rm d}\nu_1 \\ &\quad - \frac{1}{2}\int n_2[1+n_0][1+n_1]\,\mathcal{P}(\nu_2 \to \nu_0\,|\,\nu_1)\,{\rm d}\nu_0\,{\rm d}\nu_1 \\ &\quad + \frac{1}{2}\int \frac{\nu_0^2}{\nu_2^2}\, n_1\, n_0[1+n_2]\,\mathcal{P}(\nu_2 \leftarrow \nu_0\,|\,\nu_1)\,{\rm d}\nu_0\,{\rm d}\nu_1\,, \end{aligned} \tag{4.9}$$

where the abbreviation $n_i = n(\nu_i)$ for the isotropic photon phase space density was used. Here the *conditional DC emission kernel* is given by

$$\mathcal{P}(\nu_i \to \nu_j\,|\,\nu_1) = \iiint {\rm d}^3p\ {\rm d}\Omega_0\,{\rm d}\phi_{12}\, g_{\o i}\frac{{\rm d}\sigma_{\rm DC}^{\gamma_i\gamma_1\gamma_j}}{{\rm d}\Lambda_1}\, f\,, \tag{4.10}$$

where ${\rm d}^3p$ and ${\rm d}\Omega_0$ denote the integration over the momenta of the incident electrons and the solid angle of the initial photons, respectively. In addition we defined the differential DC scattering cross section as

$$\frac{{\rm d}\sigma_{\rm DC}^{\gamma_i\gamma_1\gamma_j}}{{\rm d}\Lambda_1} = \frac{\alpha\, r_0^2}{(4\pi)^2}\,\frac{\nu_j}{g_{\o i\gamma}\,\nu_i}\sum_{k=1}^{2}\frac{\Theta(1-|\mu_{12}^k|)\,X}{|\alpha_1+\alpha_2\,\frac{\mu_{12}^k}{\sqrt{1-(\mu_{12}^k)^2}}|}\,, \tag{4.11a}$$

where $\Theta(x)$ is the Heaviside step function, which is unity for non-negative argument but zero otherwise. Note that here the invariant matrix element $X$ has to be evaluated at $\mu_{12} = \mu_{12}^k$ and also the sequence of photons has to be preserved. Furthermore we introduced the abbreviations

$$\mu_{12}^{1,2} = \frac{-\alpha_1\alpha_3 \pm \alpha_2\,\sqrt{\alpha_1^2+\alpha_2^2-\alpha_3^2}}{\alpha_1^2+\alpha_2^2} \tag{4.11b}$$

$$\alpha_1 = \omega_2 - \omega_0\,\mu_{02} - \gamma\beta\,\mu_{\rm e2} \tag{4.11c}$$

$$\alpha_2 = \omega_0\cos(\phi_{02}-\phi_{12})\sqrt{1-\mu_{02}^2} + \gamma\beta\,\cos(\phi_{\rm e2}-\phi_{12})\sqrt{1-\mu_{\rm e2}^2} \tag{4.11d}$$

$$\alpha_3 = \gamma + \omega_0 - \omega_2 - \frac{\gamma\,[\omega_0\lambda_0 - \omega_2\lambda_2] - \omega_0\omega_2\alpha_{02}}{\omega_1}\,, \tag{4.11e}$$

with the dimensionless photon energy $\omega_i = \nu_i/m_{\rm e}$, the electron and photon scalars $\lambda_i = \hat{P}\cdot\hat{K}_i = 1-\beta\mu_{{\rm e}i}$ and $\alpha_{ij} = \hat{K}_i\cdot\hat{K}_j = 1-\mu_{ij}$. Equation (4.11b) follows as a solution of the energy conservation equation (4.6b). The corresponding expression in the case when the photons $\gamma_0$ and $\gamma_2$ are exchanged can be directly deduced from (4.11b) – (4.11e).

### Detailed balance relation

In thermal equilibrium the photon phase space density does not change under DC scattering. Therefore, making use of the *detailed balance* principle equation (4.9) leads to the relation

$$\mathcal{P}(\nu_i \leftarrow \nu_j\,|\,\nu_1) = \frac{\nu_i^2}{\nu_j^2}\, e^{x_{\rm e,j}}\, e^{\Delta x_{\rm e,i}} \times \mathcal{P}(\nu_i \to \nu_j\,|\,\nu_1)\,, \tag{4.12}$$

where we defined $x_{{\rm e},k} = \frac{\omega_k}{\theta_{\rm e}}$ and $\Delta x_{{\rm e},i} = x_{{\rm e},1} - x_{{\rm e},i}$.

The relation (4.12) may be used to rewrite the Boltzmann equation (4.9) as

$$\begin{aligned}\left.\frac{\partial n_2}{\partial t}\right|_{\rm DC} &= \int \frac{\nu_0^2}{\nu_2^2}\,\mathcal{P}(\nu_0 \to \nu_2\,|\,\nu_1)\,[1+n_0][1+n_1][1+n_2] \\ &\quad\times\left\{\frac{n_0}{1+n_0} - e^{x_{\rm e,2}}\,e^{\Delta x_{\rm e,0}}\frac{n_1}{1+n_1}\,\frac{n_2}{1+n_2}\right\}\mathrm{d}\nu_0\,\mathrm{d}\nu_1 \\ &\quad - \frac{1}{2}\int \mathcal{P}(\nu_2 \to \nu_0\,|\,\nu_1)\,[1+n_0][1+n_1][1+n_2] \\ &\quad\times\left\{\frac{n_2}{1+n_2} - e^{x_{\rm e,0}}\,e^{\Delta x_{\rm e,2}}\frac{n_0}{1+n_0}\,\frac{n_1}{1+n_1}\right\}\mathrm{d}\nu_0\,\mathrm{d}\nu_1\,. \end{aligned} \tag{4.13}$$

In this form it is more suitable for numerical applications. If induced terms are not important the second term in each curly bracket is negligible and in addition one can drop the factors $[1+n_0][1+n_1][1+n_2]$.

### Interpretation of the kernel

If we consider *isotropic* and *monochromatic* initial photons with phase space density, $n(\nu) = N_0\,\delta(\nu-\nu_0)/\nu_0^2$, where $\nu_0$ is the frequency of the initial photons and $N_0$ is their corresponding isotropic number density, which is assumed to obey $N_0 \ll \nu_0^2$ such that induced terms can be neglected, the Boltzmann equation (4.9) can be written as

$$\left.\frac{\partial n_2}{\partial t}\right|^{\rm m}_{\rm DC} = \frac{N_0}{\nu_2^2}\int \mathcal{P}(\nu_0 \to \nu_2\,|\,\nu_1)\,\mathrm{d}\nu_1 - \frac{N_0}{2}\,\frac{\delta(\nu_2-\nu_0)}{\nu_0^2}\int \mathcal{P}(\nu_2 \to \nu_0'\,|\,\nu_1)\,\mathrm{d}\nu_0'\,\mathrm{d}\nu_1\,. \tag{4.14}$$

In this case for all frequencies $\nu_2 \neq \nu_0$ only the DC emission integral contributes to the phase space evolution of the photons. Here a interpretation of the DC kernel can be directly given: fixing the frequency $\nu_1$ of the scattered photon $\mathcal{P}(\nu_0 \to \nu_2\,|\,\nu_1)$ is proportional to the total number of photons emitted per unit time into the frequency interval $(\nu_2, \nu_2 + \mathrm{d}\nu_2)$. Tuning the frequency $\nu_2$ one obtains the DC emission spectrum of *all* the initial photons for which the scattered photons have frequency $\nu_1$. This in addition implies that the integral of $\mathcal{P}(\nu_0 \to \nu_2\,|\,\nu_1)$ over $\mathrm{d}\nu_2$ is proportional to the total number of photons scattered per unit time into the frequency interval $(\nu_1, \nu_1 + \mathrm{d}\nu_1)$, i.e.

$$\left.\frac{\partial n_1}{\partial t}\right|^{\rm m}_{\rm DC} = \frac{N_0}{\nu_1^2}\int \mathcal{P}(\nu_0 \to \nu_2\,|\,\nu_1)\,\mathrm{d}\nu_2\,. \tag{4.15}$$

Here it is important to note that in general

$$\mathcal{P}(\nu_0 \to \nu_2\,|\,\nu_1) \neq \mathcal{P}(\nu_0 \to \nu_1\,|\,\nu_2)\,. \tag{4.16}$$

Although the matrix element $X$ is fully symmetric under exchange of the photons $K_1$ and $K_2$ both the scattering cross section (4.11a) and the DC kernel have lost this symmetry.

For $\nu_2 \equiv \nu_0$ also the second term in (4.14) contributes. Its origin can be understood in the following way: multiplying (4.14) by $\nu_2^2$ and integrating over $\mathrm{d}\nu_2$ leads to

$$\left.\frac{\partial N_2}{\partial t}\right|^{\rm m}_{\rm DC} = N_0\int \mathcal{P}(\nu_0 \to \nu_2\,|\,\nu_1)\,\mathrm{d}\nu_1\,\mathrm{d}\nu_2 - \frac{N_0}{2}\int \mathcal{P}(\nu_0 \to \nu_0'\,|\,\nu_1)\,\mathrm{d}\nu_0'\,\mathrm{d}\nu_1\,. \tag{4.17}$$

The two integrals appearing here are identical and correspond to the *total DC scattering cross section*, $\sigma_{\rm dc}$, for this case. Therefore the total change of the number of photons produced in the outgoing channel is given by $\partial_t N_2|^{\rm m}_{\rm DC,tot} = \sigma_{\rm dc} N_0$. Only half of these photons were newly *created* the other half has been *scattered* out of their initial phase space volume, reducing the occupation number at $\nu_0$ by $\sigma_{\rm dc} N_0/2\nu_0^2$.

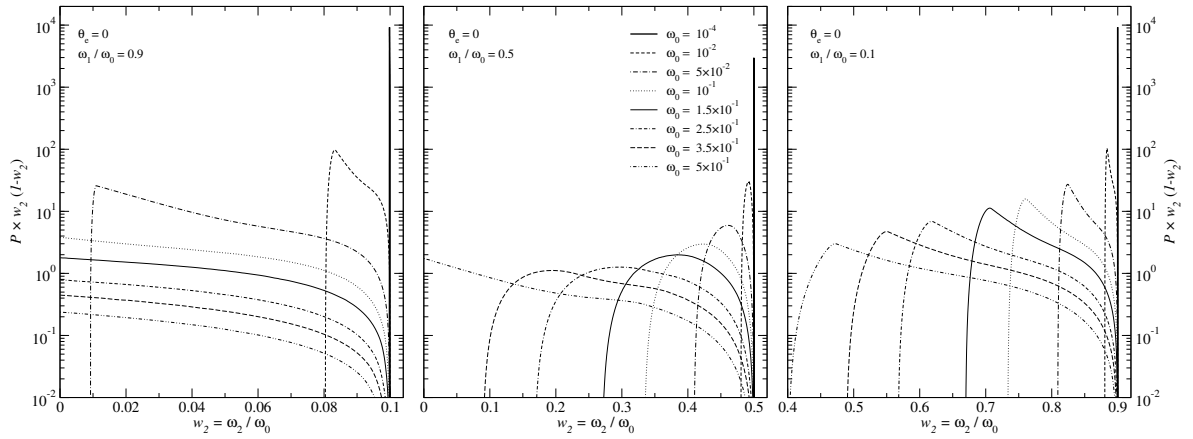


**Figure 4.1:** The conditional DC emission kernel, $\mathcal{P}(\nu_0 \to \nu_2 \,|\, \nu_1)$, for cold electrons ($\theta_\mathrm{e} = 0$) as a function of $w_2 = \omega_2/\omega_0$ for three energies of the scattered photon, $\omega_1/\omega_0 = 0.1$, 0.5 and 0.9, and different energies $\omega_0$ of the initial photon, as indicated respectively. The *infrared* divergencies for $w_2 \to 0$ and $w_2 \to 1$ have been scaled out. Also the range of $w_2$ in each plot was chosen for convenience.

## 4.3 The DC emission kernel $\mathcal{P}(\nu_0 \to \nu_2 \,|\, \nu_1)$ for thermal electrons

In this Section we will discuss the properties of the conditional DC kernel in detail numerically for some illustrative cases. A brief description of the numerical approach we use to solve the multidimensional Boltzmann integrals is given in the Appendix D.2. We also make attempts to understand some of the general features of the DC kernel analytically and by comparison with Compton scattering.

### 4.3.1 The DC kernel for cold electrons

Figure 4.1 shows some of the numerical results for the conditional DC emission kernel in the case of cold electrons as a function of the emitted photon frequency. Here we focus our discussion on three representative choices for the frequency of the scattered photon, i.e. $\omega_1/\omega_0 = 0.1$, 0.5 and 0.9, and different energies of the initial photon. We have scaled out the *infrared* divergencies for $w_2 \to 0$ and $w_2 \to 1$. This property of DC emission will be discussed in detail later (Sect. 4.4.5).

Since the electrons are initially at rest each photon in the outgoing channel can only have energies less than $\nu_0$ ($\nu_1 < \nu_0$ and $\nu_2 < \nu_0$). For $\nu_0 \ll m_\mathrm{e}$ the *recoil* is negligible (i.e. the scattered electrons will carry away momentum but only a tiny amount of energy) implying that the sum of the energies of the emitted and scattered photon for one single event obeys $\nu_0 = \nu_1 + \nu_2 - \mathcal{O}(\nu_0/m_\mathrm{e})$. As can be seen in Fig. 4.1, for soft initial photons (i.e. $\omega_0 = 10^{-4}$) the kernel is very close to a $\delta$-function. It will be shown below that the width of the kernel in this case is $\Delta_\mathcal{P} \approx 2\,\omega_0$ (see Eq. (4.19)).

On the other hand the width of the kernel increases strongly for higher energies of the initial photon, i.e. when the recoil becomes significant. The characteristic height of the kernel in each case is $\sim 1/\omega_0$. For $\omega_1/\omega_0 = 0.5$ in the chosen coordinates the kernel is rather symmetric around a central frequency even for initial photons with energy $\omega_0 \leq 0.15$, whereas in the other two cases, $\omega_1/\omega_0 = 0.1$ and $\omega_1/\omega_0 = 0.9$, the kernel is strongly asymmetric with a maximum closer to its lower boundary. Note that possibly due to the larger number of degrees of freedom for DC scattering in contrast to the case of Compton scattering there is no cusp.

#### Simple analytic considerations

Using the energy conservation equation for the photon $K_2$ one can deduce its allowed maximal and minimal frequency for a given scattered photon energy, $\nu_1$, depending on the energy of the initial photon. Similar to the case of Compton scattering, the maximal energy follows when

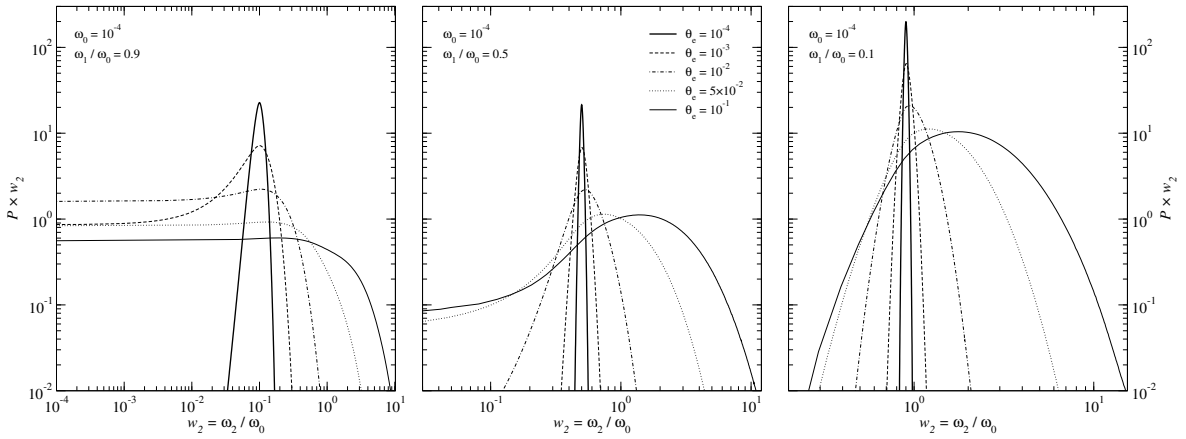


**Figure 4.2:** The conditional DC emission kernel, $\mathcal{P}(\nu_0 \to \nu_2 \,|\, \nu_1)$, for soft initial photons with $\omega_0 = 10^{-4}$ as a function of $w_2 = \omega_2/\omega_0$ for three energies of the scattered photon, $\omega_1/\omega_0 = 0.1$, 0.5 and 0.9, and different electron temperatures $\theta_\mathrm{e}$, as indicated respectively. The *infrared* divergence for $w_2 \to 0$ has been scaled out. Also the range of $w_2$ in each plot is chosen for convenience.

both photons in the outgoing channel are propagating in the same direction as the initial photon (*forward scattering*). Here the momentum transfer to the scattered electron is zero and due to energy conservation it follows $\nu_{2,\mathrm{max}} \equiv \nu_0 - \nu_1$. On the other hand the maximal momentum is transfered to the electron, when both photons are propagating in the direction opposite to the initial photon (*backward scattering*). With these energetic considerations one may conclude that the energy of the emitted photon lies within the frequency range

$$\max(0,\, 1 - w_1 - \Delta_\mathcal{P}) \le w_2 \le 1 - w_1\,, \tag{4.18}$$

where here we introduced the abbreviation $w_i = \omega_i/\omega_0$ and defined the total width of the DC kernel as

$$\Delta_\mathcal{P} = \frac{2\,\omega_0}{1 + 2\,\omega_0} \overset{\omega_0 \ll 1}{\approx} 2\,\omega_0\,. \tag{4.19}$$

This equation also describes the width of the Compton kernel in the case of cold electrons and therefore again shows the close connection between DC and Compton scattering. But here one should stress that there is one additional constraint for the width of the DC kernel, which follows from the fact that its lower boundary has to be non-negative. In the the case of Compton scattering the energy of the scattered photon is limited to the range $1-\Delta_\mathcal{P} \le w_1 \le 1$. Since $\Delta_\mathcal{P} \le 1$ no further restrictions to the Compton kernel are necessary. In the case of DC scattering, it follows from equation (4.18) that for a given frequency of the scattered photon, there is a critical frequency, $\omega_{0,\mathcal{P},\mathrm{crit}}$, for the initial photon, at which the lower boundary of the DC kernel vanishes. This frequency is given by

$$\omega_{0,\mathcal{P},\mathrm{crit}} = \frac{1 - w_1}{2\,w_1}\,. \tag{4.20}$$

For $w_1 \ll 1$ the initial photon energy can be arbitrarily large and still the lower boundary of the DC kernel is non-negative, just like for Compton scattering. This case is equivalent to the *soft photon limit*, with the photon $K_1$ playing the role of the emitted soft photon. If we consider the cases $w_1 = 0.5$ and 0.9 we find $\omega_{0,\mathcal{P},\mathrm{crit}} = 0.5$ and $\omega_{0,\mathcal{P},\mathrm{crit}} = 1/18 \approx 0.055$, respectively. A comparison with Fig. 4.1 shows that all these properties of the DC kernel for cold electrons discussed here are recovered very well.

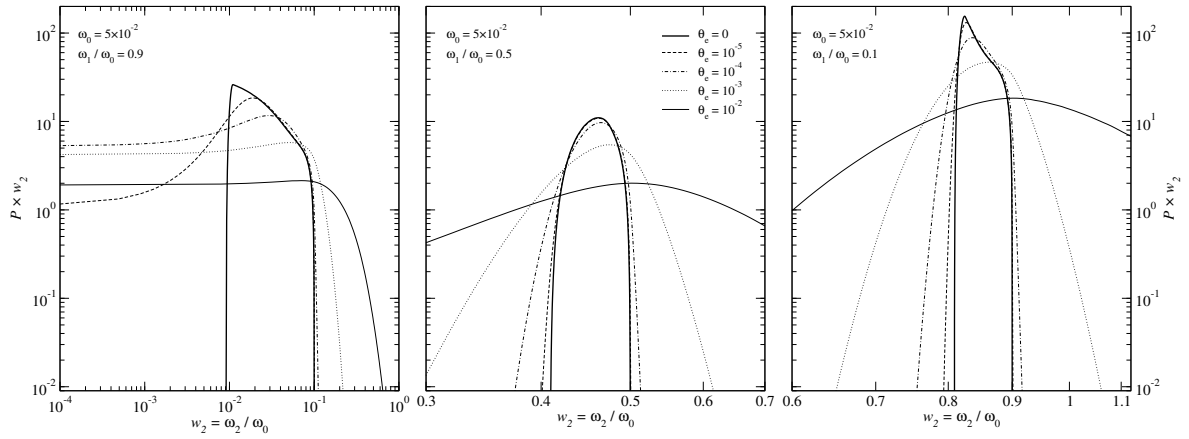


**Figure 4.3:** The conditional DC emission kernel, $\mathcal{P}(\nu_0 \to \nu_2 \,|\, \nu_1)$, for initial photons with $\omega_0 = 5 \times 10^{-2}$ as a function of $w_2 = \omega_2/\omega_0$ for three energies of the scattered photon, $\omega_1/\omega_0 = 0.1$, 0.5 and 0.9, and different electron temperatures $\theta_\mathrm{e}$, as indicated respectively. The *infrared* divergence for $w_2 \to 0$ has been scaled out. Also the range of $w_2$ in each plot is chosen for convenience.

### 4.3.2 The DC kernel for thermal electrons

Figure 4.2 shows some of the numerical results for the conditional DC emission kernel in the case of soft initial photons as a function of the emitted photon frequency. Again we focus our discussion on three representative choices for the frequency of the scattered photon, i.e. $\omega_1/\omega_0 = 0.1$, 0.5 and 0.9, and now vary the temperature $\theta_\mathrm{e}$ of the electron gas. For the cases shown the *recoil* is negligible and the spectra are dominated by *Doppler broadening*. The emitted photons now are no longer restricted to frequencies $\nu_2 \leq \nu_0 - \nu_1$, since the initial electrons can transfer energy to the photon field. Due to the similarity of this effect with *inverse* Compton scattering one may call it *inverse* DC scattering.

In Fig. 4.3 we show a sequence of kernels illustrating the transition between recoil and Doppler domination. Here one may see that the broadening due to the Doppler effect is much stronger than due to recoil. Therefore, like in the case of Compton scattering, the transition from recoil to Doppler dominated spectra is very rapid.

### 4.3.3 Mean photon energy and dispersion of the DC kernel

In order to further compare the properties of the DC kernel with the Compton kernel we here introduce the mean photon energy and the dispersion of the kernel. Since the normalization of the DC kernel is a strong function of photon energy (e.g. due to the infrared divergence), it is convenient to define a *normalized* kernel distribution function. Therefore here we introduce the kernel normalization, $\mathcal{N}_\mathcal{P}$, mean photon energy, $\bar{w}_\mathcal{P}$, and dispersion, $\sigma_\mathcal{P}$, as

$$\mathcal{N}_\mathcal{P} = \int \mathcal{P}(\nu_0 \to \nu_2 \,|\, \nu_1)\, \mathrm{d}\nu_2 \tag{4.21a}$$

$$\bar{w}_\mathcal{P} = \frac{1}{\mathcal{N}_\mathcal{P}} \int w_2\, \mathcal{P}(\nu_0 \to \nu_2 \,|\, \nu_1)\, \mathrm{d}\nu_2 \tag{4.21b}$$

$$\sigma^2_\mathcal{P} = \frac{1}{\mathcal{N}_\mathcal{P}} \int [w_2 - \bar{w}_\mathcal{P}]^2\, \mathcal{P}(\nu_0 \to \nu_2 \,|\, \nu_1)\, \mathrm{d}\nu_2\,, \tag{4.21c}$$

where all these quantities are functions of the electron temperature $\theta_\mathrm{e}$, the initial photon frequency $\nu_0$ and the scattered photon frequency $\nu_1$. Furthermore we have expressed the mean photon energy and the dispersion in units of $\nu_0$.

Here we focus on the DC kernel for low frequency scattered photons, since there one expects the biggest correspondence to Compton scattering. Numerically we calculated the mean and

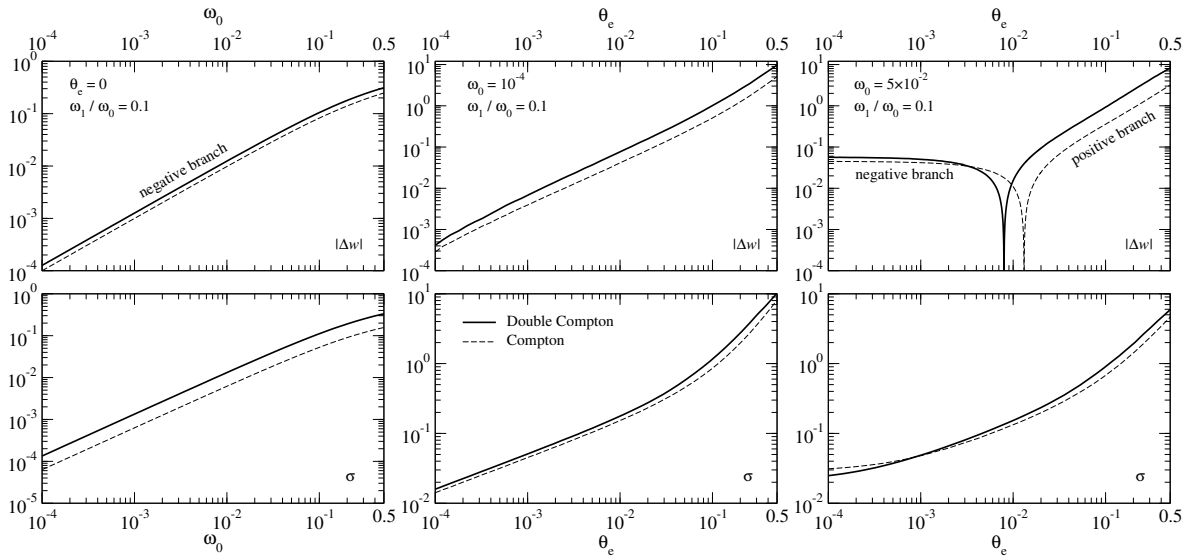


**Figure 4.4:** Properties of the conditional DC emission kernel for soft scattered photons( $\omega_1/\omega_0 = 0.1$). Shown are the mean energy change (upper panels) $\Delta w = \bar{w}_{\mathcal{P}} - (1 - w_1)$ and the dispersion (lower panels) $\sigma_{\mathcal{P}}$ in comparison to the corresponding Compton scattering quantities, $\Delta w_{\rm CS} = \bar{w}_{\mathcal{P},\rm CS} - 1$ and $\sigma_{\rm CS}$. The left panel shows the numerical results for cold electrons as a function of the initial photon energy. The middle and right panels are given for soft ($\omega_0 = 10^{-4}$) and intermediate ($\omega_0 = 5 \times 10^{-2}$) initial photons as a function of electron temperature, respectively. Note that for the mean energy change absolute values are presented.

dispersion for $\omega_1 = 0.1\,\omega_0$. We have also done integrations for $\omega_1 = 0.01\,\omega_0$ and $\omega_1 = 0.5\,\omega_0$, which all show a very similar dependence on the chosen parameters, but were numerically more demanding.

For cold electrons it is possible to give the exact expressions for the normalization, mean and dispersion of the Compton kernel (see Appendix C.1.1). In the case of non-zero temperature various approximations exist for mildly relativistic electrons and photons, which of those we used here are summarized in the Appendix C. In the case of even higher temperatures and photon energies we performed a numerical evaluation of the Boltzmann-integrals for Compton scattering using the same numerical procedures as for DC scattering substituting the cross sections and variables accordingly.

Some of the properties of the conditional DC emission kernel for low frequency scattered photons are shown in Fig. 4.4 in comparison to the corresponding Compton scattering quantities. The presented results again directly show the close link between DC and Compton scattering in the *soft photon limit*. Except for some factors of the order of 1-2 the characteristics of both kernels are very similar. Comparing the dispersions for cold and thermal electrons, again one can see that the broadening due to the Doppler effect is much stronger than for the recoil. Similarly the mean gain of energy due to Doppler boosting is larger. In general the gain of energy and broadening seem to be slightly stronger for DC in comparison to Compton scattering. Going to $\omega_1 = 0.01\,\omega_0$ did not affect the curves very much. However, one may expect that higher order moments would reveal differences between the shapes of the kernels of DC and Compton scattering.

## 4.4 DC emission for monochromatic photons and thermal electrons

We will discuss the full kinetic equation for the time evolution of the photon phase space density under DC scattering for different physical conditions below, but in this Section we focus our analysis only on the emission process for *isotropic, monochromatic* photons, with

phase space density $n(\nu) = N_0\,\delta(\nu-\nu_0)/\nu_0^2$, and *isotropic thermal* electrons of temperature $T_\mathrm{e}$ in the incoming channel. In this case, using the DC differential cross section (4.8) the change of the phase space density due to DC emission can be written as

$$\left.\frac{\partial n_2}{\partial t}\right|_{\mathrm{em}}^{\mathrm{m}} = \frac{N_0}{\nu_2^2}\int \mathrm{d}^3p \int \mathrm{d}\Omega_0 \int \mathrm{d}\Omega_1\, g_{\o 0}\frac{\mathrm{d}\sigma_{\mathrm{DC}}^{\gamma_0\gamma_1\gamma_2}}{\mathrm{d}\Lambda}\, f\,. \tag{4.22}$$

Note that here we again have neglected induced effects, i.e. we assumed $N_0 \ll \nu_0^2$ and that the electrons are non-degenerate.

### 4.4.1 Cold electrons and soft initial photons

In this Sect. we now first summarize some of the analytic approximation for cold electrons and soft initial photons and then present numerical results for this case.

#### Lightman-approximation

The expression obtained by Lightman [80] can be deduced from the Boltzmann emission integral (4.22) by performing a series expansion of the DC differential cross section (4.8) in lowest orders of $\nu_0 \ll m_\mathrm{e}$ and $\nu_2 \ll m_\mathrm{e}$ and setting $\beta = 0$, i.e. assuming that the electrons are initially at rest. In this limit $f(p) = N_\mathrm{e}\,\delta(p)/4\pi\,p^2$ and the integration over $\mathrm{d}^3p$ can be carried out immediately. The series expansion in lowest order of $\nu_2 \ll m_\mathrm{e}$ is equivalent to using the *soft photon approximation* for the DC differential cross section, i.e. assuming in addition that $\nu_2 \ll \nu_0$. It follows:

$$\left.\frac{\mathrm{d}\sigma_{\mathrm{DC}}^{\gamma_0\gamma_1\gamma_2}}{\mathrm{d}\Lambda}\right|_{\mathrm{L}} \approx \frac{\alpha}{4\pi^2}\,r_0^2\,\frac{\omega_0^2}{\nu_2}\,[1+\mu_{01}^2]\left[1-\mu_{01}-\frac{\Delta\mu^2}{2}\right], \tag{4.23}$$

with $\Delta\mu = \mu_{02}-\mu_{12}$. Now, after aligning the $z$-axis with the direction of the emitted photon all the integrations can be easily performed analytically. Making use of the identity $\mu_{01} = \mu_{02}\,\mu_{12} + \cos(\phi_{02}-\phi_{12})\sqrt{1-\mu_{02}^2}\sqrt{1-\mu_{12}^2}$, where $\phi_{02}$ and $\phi_{12}$ denote the azimuthal angles of the initial and the scattered photon, respectively, this then leads to the *Lightman*-approximation for DC emission spectrum of cold electrons and soft, monochromatic initial photons

$$\left.\frac{\partial n_2}{\partial t}\right|_{\mathrm{em,L}}^{\mathrm{m}} = \frac{4\alpha}{3\pi}\,N_\mathrm{e}\,N_0\,\sigma_\mathrm{T}\,\frac{\omega_0^2}{\nu_2^3}\,, \tag{4.24}$$

with the *Thomson* scattering cross section $\sigma_\mathrm{T} = 8\pi\,r_0^2/3$.

The expression (4.24) is the DC scattering equivalent of the *Kramers*-equation for thermal Bremsstrahlung. The characteristics of equation (4.24) can be summarized as follows: the DC emission spectrum increases $\propto \omega_0^2$ and, as mentioned earlier, exhibits a *infrared* divergence typical for first order radiative corrections to quantumelectrodynamical processes. It is usually assumed that under physical conditions emission and absorption balance each other below some lower frequency, $\nu_{2,\mathrm{min}}$, and that energy conservation in addition introduces some high frequency cutoff, $\nu_{2,\mathrm{max}}$. Therefore the photon production rate increases logarithmically,

$$\left.\frac{\partial N_2}{\partial t}\right|_{\mathrm{em,L}}^{\mathrm{m}} = \frac{4\alpha}{3\pi}\,N_\mathrm{e}\,N_0\,\sigma_\mathrm{T}\,\omega_0^2 \times \ln\left(\frac{\nu_{2,\mathrm{max}}}{\nu_{2,\mathrm{min}}}\right), \tag{4.25}$$

with the ratio of the upper to the lower frequency cutoff of the DC emission spectrum.

As will be discussed below, the Lightman-approximation only describes the very low frequency part of the DC emission spectrum ($\nu_2/\nu_0 \leq 10^{-4}-10^{-3}$) for cold electrons and soft initial photons ($\nu_0/m_\mathrm{e} \leq 10^{-3}$). For initial photons with slightly higher energies relativistic corrections lead to a significant suppression of the emission at low frequencies relative to the non-relativistic case (see Fig. 4.5 and the discussion in Sect. 4.4.2).

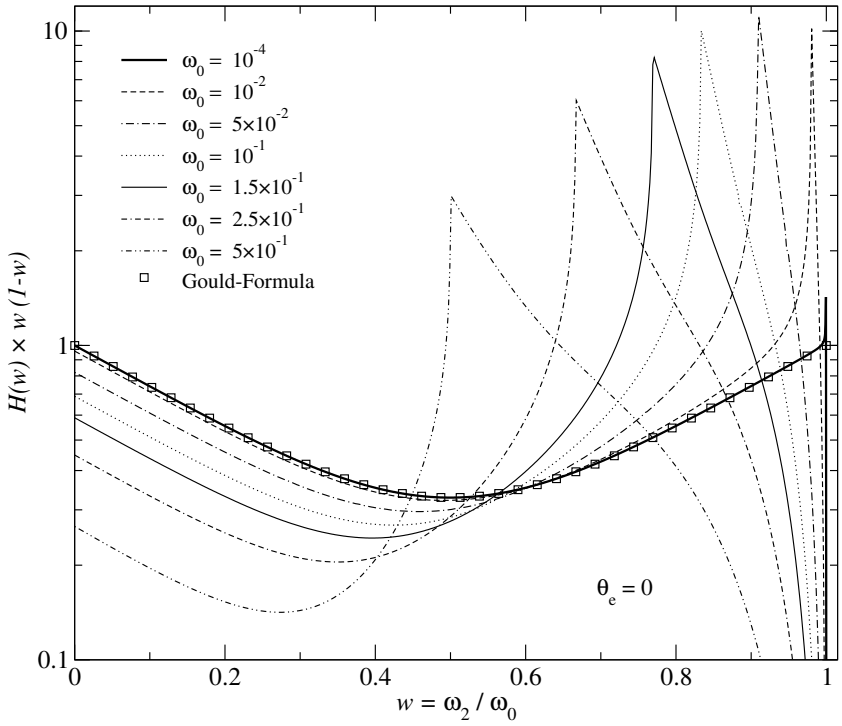


**Figure 4.5:** Two-photon DC emission spectrum for cold electrons. Shown is the ratio $H(w)$ as given by (4.28) for different initial photon energies. The divergencies at $w = 0$ and $w = 1$ have been separated out. All the spectra are given for a fixed lower energy cutoff $w_{\rm min} = 10^{-4}$.

## Gould-formula

The result obtained by Gould [54] can be derived in a similar manner as the Lightman-approximation (4.24), but without performing a series expansion of (4.8) in terms of $\nu_2$, i.e. making *a priory* no assumption about the energy of the emitted photon or equivalently going beyond the *soft photon approximation*. This increases the complexity of the expression for the differential cross section significantly and the intermediate step is therefore omitted here. The integrations then lead to the *Gould*-formula for DC emission spectrum of cold electrons and low energy, monochromatic initial photons

$$\left.\frac{\partial n_2}{\partial t}\right|^{\rm m}_{\rm em,G} = w\, H_{\rm G}(w) \times \left.\frac{\partial n_2}{\partial t}\right|^{\rm m}_{\rm em,L}\,, \tag{4.26}$$

with $w \equiv w_2 = \nu_2/\nu_0$ and

$$H_{\rm G}(w) = \frac{1 - 3w[1-w] + \frac{3}{2}w^2[1-w]^2 - w^3[1-w]^3}{w[1-w]}\,. \tag{4.27}$$

A interpretation of $H_{\rm G}(w)$ can be given as follows: multiplying $\partial_t n_2|^{\rm m}_{\rm em,G}$ by $\nu_2^2$ and dividing by $N_0$ one obtains the relative change of the number of photons due to DC emission per $\mathrm{d}w$ and per $\mathrm{d}t$, i.e. $H_{\rm G}(w)$ is proportional to the relative photon production rate, $\Delta\dot{N}^{\rm m}_{\rm em,G}/N_0 \propto H_{\rm G}(w)\,\mathrm{d}w$.

In order to compare the numerical results for different initial conditions it is convenient to define the ratio

$$H(w) = \frac{1}{w}\,\frac{\partial_t n_2|^{\rm m}_{\rm em}}{\partial_t n_2|^{\rm m}_{\rm em,L}}\,, \tag{4.28}$$

where $\partial_t n_2|^{\rm m}_{\rm em}$ is given by the full Boltzmann emission integral (4.22) and $\partial_t n_2|^{\rm m}_{\rm em,L}$ is the Lightman-approximation (4.24). With this particular definition of $H(w)$ one can rewrite the

full Boltzmann emission integral, $\partial n_2/\partial t|_{\rm em}$ and the associated total change of the photon number density, $\partial N_2/\partial t|_{\rm em}$, like

$$\left.\frac{\partial n_2}{\partial t}\right|^{\rm m}_{\rm em} = \frac{4\alpha}{3\pi}\, N_{\rm e}\, N_0\, \sigma_{\rm T}\, \frac{\omega_0}{\nu_2^2} \times H(w) \tag{4.29a}$$

$$\left.\frac{\partial N_2}{\partial t}\right|^{\rm m}_{\rm em} = \frac{4\alpha}{3\pi}\, N_{\rm e}\, N_0\, \sigma_{\rm T}\, \omega_0^2 \times \int_{w_{\rm min}}^{w_{\rm max}} H(w)\, {\rm d}w\,. \tag{4.29b}$$

The interpretation of $H(w)$ is similar to the one of $H_{\rm G}(w)$. It can be regarded as the DC scattering equivalent of the *Gaunt*-factor for thermal Bremsstrahlung.

In Figure 4.5 the dependence of $H(w)$ on $w$ for several frequencies, $\omega_0$, of the initial photon in a cold plasma is presented. Here we first focus the discussion on the thick solid line, which corresponds to numerical result for the Gould-factor, $H_{\rm G}(w)$, and return to the other cases in Sect. 4.4.2. As can be seen, the analytic prediction (4.27) only deviates at frequencies very close to $w = 1$ from the full numerical result. This point will also be addressed in Sect. 4.4.2.

As was noted by Gould [54] the function $H_{\rm G}(w)$ is symmetric in $w \leftrightarrow 1 - w$. This aspects of DC emission in a cold plasma and for low energy initial photons deserves the following comment: since the electrons are initially at rest each photon in the outgoing channel can only have energies less than $\nu_0$ (namely $\nu_1 < \nu_0$ and $\nu_2 < \nu_0$). As we have seen in Sect. 4.3.1 for $\nu_0 \ll m_{\rm e}$ the *recoil* is negligible and the DC kernel is very close to a $\delta$-function. Therefore the number of DC photons at $\nu_2$ is approximately equal to the number of DC photons at $\nu_1 = \nu_0 - \nu_2$, or equivalently $H_{\rm G}(w) \cong H_{\rm G}(1-w)$. Therefore in a cold plasma for very soft initial photons one can expect a complete symmetry of the DC emission spectrum around $w = 1/2$. Deviations from this symmetry arise due to both increasing importance of recoil and Doppler broadening.

The total change of the number of emitted photons between $w_{\rm min}$ and $1 - w_{\rm min}$ can be directly calculated analytically form (4.26). Assuming that $w_{\rm min} \ll 1$ with equation (4.29b) one obtains the approximation

$$\left.\frac{\partial N_2}{\partial t}\right|^{\rm m}_{\rm em,G} \approx \frac{8\alpha}{3\pi}\, N_{\rm e}\, N_0\, \sigma_{\rm T}\, \omega_0^2 \times \left[\ln\left(\frac{1-w_{\rm min}}{w_{\rm min}}\right) - \frac{167}{120} + 3\, w_{\rm min}\right]. \tag{4.30}$$

Here it is important to note that this results includes the total number of photons in the outgoing channel, whereas the number of newly *created* photons is $\frac{1}{2}\,\partial_t N_2|^{\rm m}_{\rm em,G}$.

Comparing (4.30) with the corresponding result in the Lightman-approximation, Eq. (4.25), shows that the logarithmic term of (4.30) is a factor of 2 larger. This is because in the Lightman-approach the divergence at $w = 1$ is not taken into account, implying that only the created photons are counted. The other terms in equation (4.30) are a result of quantumelectrodynamical corrections represented by the factor (4.27).

It should be mentioned that in both the Lightman and Gould approach no energy is transfered to the electrons, since the recoil is neglected. Therefore all the energy of the initial photons is transfered to the DC emission spectrum and no heating or cooling of the electrons can occur. However, in general this will certainly not be true.

### 4.4.2 Cold electrons and arbitrary initial photons

Here we now want to discuss in detail the properties of the DC emission spectrum for photons with arbitrary initial energies. As was mentioned in the previous Section, in a cold plasma and for very soft initial photons the DC emission spectrum is symmetric around $w = 1/2$. Figure 4.5 shows, that this symmetry is broken once the *recoil* of the electron becomes important, i.e. for increasing energy of the initial photon. Despite this asymmetry, a numerical calculation has shown that the total number of photons below and above $w = 1/2$, namely $N_<$ and $N_>$, respectively, is still approximately equal, even for high energy ($\omega_0 \sim 0.1$) initial photons. The

difference in the number of photon $\Delta N = N_< - N_>$ is mostly determined by photons in the the range $\Delta w \sim 2\,\Delta_{\mathcal{P}}$ around $w = 1/2$. On the other hand the largest contributions to the total number of photons for a cold plasma come from $w \sim 0$ and $w \sim 1$. Therefore only when the width of the DC kernel at $w = 1/2$ becomes of the order of $\Delta_{\mathcal{P}} \sim 1/2$ the asymmetry in the number of photon can be significant.

Furthermore, for initial photons with energies larger than $\omega_0 \sim 10^{-3}$ relativistic corrections lead to a notable suppression of the DC emission at low frequencies relative to the non-relativistic case. Since in the *soft photon limit* the DC differential cross section factorizes into the differential Compton scattering cross section and an angular dependent correction factor [cf. 69, Eq. 11-41], this behavior should most likely reflects the decrease of the total Compton scattering cross section for high energy photons [cf. 69, Eq. 11-24].

The high frequency part of the DC emission spectrum is rather complex. The cusp present in all the spectra (even for soft initial photons) arises due to the low frequency cutoff, $\nu_{2,\mathrm{min}}$, below which one assumes efficient absorption of the emitted photons. At high frequencies $\nu_2$ the scattered photon is not allowed to have energies less than this cutoff (see comment in the Appendix D.2). For increasing energy of the initial photon the position of the cusp moves towards lower frequencies. This reflects the increase in the importance of the electron recoil. All the spectra approach zero very fast for energies close to $\nu_0$, since there the access able phase space volume is very small.

### Analytic estimation of the position of the cusp

If we consider the energy conservation equation of the scattered photon (4.6b) for initially resting electrons and make use of the positivity of $(P + K_0 - K_2) \cdot K_1$, one may find that the condition $\nu_1 \geq 0$ implies $1 - w(1 + \omega_0\,\alpha_{02}) \geq 0$. Therefore the scattering angle of the photon $K_2$ has to obey $\mu_{02} \geq 1 - \frac{1-w}{\omega_0\,w}$. Since $\mu_{02} \in [-1, 1]$ this condition results in the two cases

$$\mu_{02} \in \begin{cases} [-1, 1] & \text{for} \quad w \leq \frac{1}{1+2\omega_0} \\ [1 - \frac{1-w}{\omega_0\,w}, 1] & \text{for} \quad \frac{1}{1+2\omega_0} \leq w \leq 1 \end{cases} . \tag{4.31}$$

Therefore, in the limit $\nu_{2,\mathrm{min}} \ll m_\mathrm{e}$ one may expect that the position of the cusp is close to

$$w_\mathrm{cusp} \approx \frac{1}{1 + 2\omega_0} , \tag{4.32}$$

i.e. where the allowed phase space changes radically due to the restriction of the scattering angles. Comparing with the numerical results presented in Fig. 4.5 shows the correctness of this presumption (e.g. for $\omega_0 = 10^{-2}$, $10^{-1}$, $1.5 \times 10^{-1}$ and $5 \times 10^{-1}$ it follows that $w_\mathrm{cusp} \approx 0.98$, 0.83, 0.77 and 0.5, respectively). Note that for larger values of the low frequency cutoff, $\nu_{2,\mathrm{min}}$, the estimate (4.32) will not be valid anymore.

### Analytic approximations for the DC emission spectrum

Comparing the curves for different values of $\omega_0$ shows that at low frequencies all have a similar shape and only the amplitude changes. Therefore it seems worth trying to find an analytic approximation describing the DC emission for energetic initial photon in the *soft photon limit* and then combining it with the Gould-factor, $H_\mathrm{G}(w)$. This *Ansatz* turns out to be very useful also for the other cases addressed in this Chapter.

We start by expanding the DC differential cross section (4.8) in lowest order of $\omega_2 = \nu_2/m_\mathrm{e}$ and setting $\beta = 0$. Furthermore we expand the resulting expression up to 4. order in $\omega_0$ to take into account higher order corrections in the energy of the initial photon. Carrying out all the integrations of the Boltzmann emission integral (4.22) then lead to

$$\left.\frac{\partial n_2}{\partial t}\right|^\mathrm{m}_\mathrm{em,s} = G^0_\mathrm{m}(\omega_0) \times \left.\frac{\partial n_2}{\partial t}\right|^\mathrm{m}_\mathrm{em,L} , \tag{4.33}$$

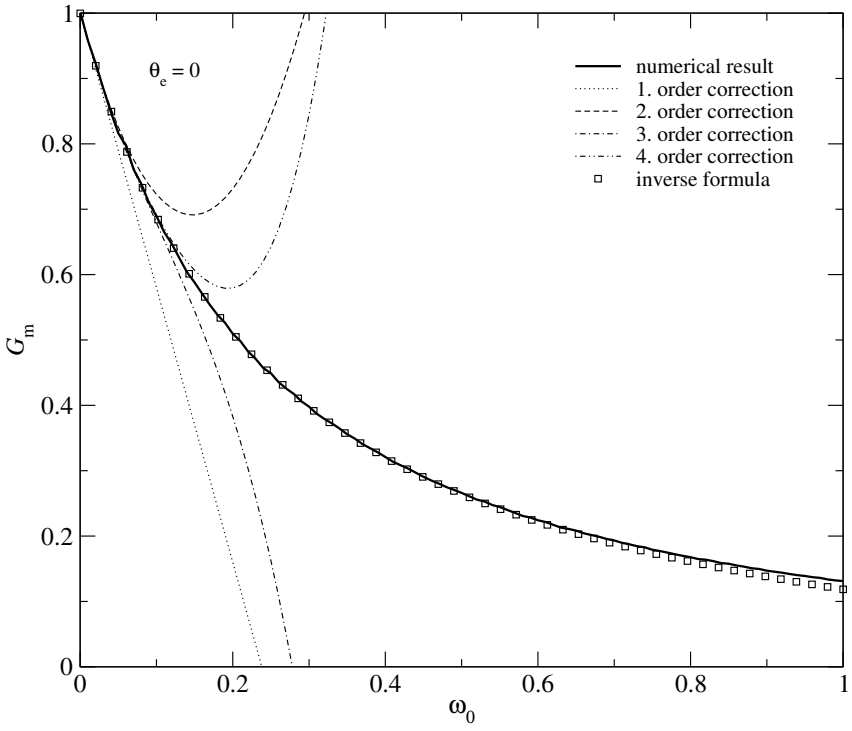


**Figure 4.6:** DC correction factor $G^0_{\rm m}$ for cold electrons and monochromatic initial photons as a function of $\omega_0$. Also shown are the *direct* expansion (4.34), up to different orders in $\omega_0$, and the *inverse* approximation (4.35), as indicated respectively.

where the correction factor $G^0_{\rm m}(\omega_0)$ following from the *direct* series expansion is given by

$$G^0_{\rm m}(\omega_0) = 1 - \frac{21}{5}\,\omega_0 + \frac{357}{25}\,\omega_0^2 - \frac{7618}{175}\,\omega_0^3 + \frac{21498}{175}\,\omega_0^4\,. \tag{4.34}$$

In order to distinguish the DC correction factor in the *soft photon limit* from $H(w)$, which applies for the full spectral range, we here introduced the new letter $G$.

Figure 4.6 shows the numerical result for $G^0_{\rm m}(\omega_0)$ in comparison to the analytic approximation (4.34), taking into account the corrections up to different orders in $\omega_0$. The approximation converges only very slowly and in the highest order considered here breaks down close to $\omega_0 \sim 0.15$. Due to this behavior of the asymptotic expansion there is no significant improvement expected when going to higher orders in $\omega_0$, but the monotonic decrease of the emission coefficient suggest that a functional form $G^0_{\rm m} = [1 + \sum_{k=1}^{4} a_k\,\omega_0^k]^{-1}$ could lead to a better performance. Determining the coefficients $a_i$ by comparison with the direct expansion (4.34) one may obtain an *inverse* approximation for the DC correction factor

$$G^{0,\rm inv}_{\rm m}(\omega_0) = \frac{1}{1 + \frac{21}{5}\,\omega_0 + \frac{84}{25}\,\omega_0^2 - \frac{2041}{875}\,\omega_0^3 + \frac{9663}{4375}\,\omega_0^4}\,. \tag{4.35}$$

As Fig. 4.6 clearly shows, $G^{0,\rm inv}_{\rm m}(\omega_0)$ provides an excellent description of the numerical result even up to relativistic energies of the initial photon.

Combining (4.35) with the Gould-formula (4.27) leads to the approximation

$$H^0_{\rm em}(\omega_0, \omega_2) = H_{\rm G}(w) \times G^{0,\rm inv}_{\rm m}(\omega_0) \tag{4.36}$$

for the ratio $H$ as defined by equation (4.28). In order to test the performance of this approximation, we have numerically determined the lowest frequency, $\omega_{2,\rm crit}$, at which the approximation for $H$ deviates by $\epsilon$ percent from the full numerical result. In Fig. 4.7 the results for $\omega_{2,\rm crit}$ are

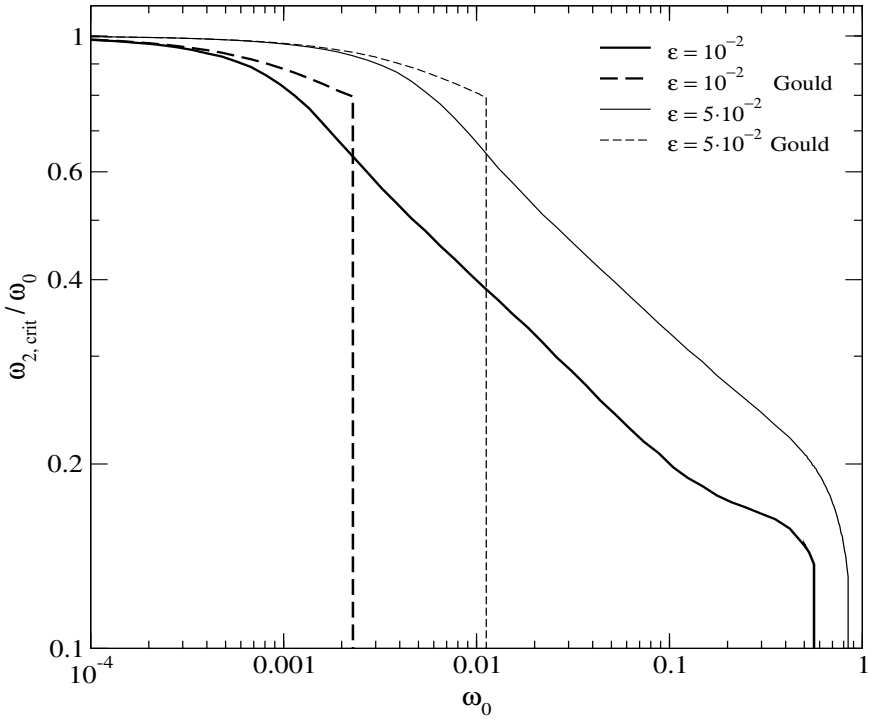


**Figure 4.7:** Critical frequency $\omega_{2,\mathrm{crit}}$ above which the analytic approximation $H^0_{\mathrm{em}}$ as given by equation (4.36) deviates more than $\epsilon$ percent from the full numerical result for $H$. Also shown are the results for the Gould-formula (4.27). All the curves were calculated for cold electrons and a fixed lower energy cutoff $w_{\mathrm{min}} = 10^{-4}$.

presented for the Gould-formula $H_{\mathrm{G}}$ and $H^0_{\mathrm{em}}$. Our calculation clearly shows that the approximation (4.36) has a significantly better performance than the Gould-formula for large values of $\omega_0$. Although for small $\omega_0$ the Gould-formula dominates slightly it breaks down very abruptly at higher energies of the initial photon. We did not consider the Lightman-approximation, since it breaks down at extremely low frequencies ($\omega_2 \lesssim \omega_0 \times 10^{-3}$).

### Change of the number density due to DC emission

In addition to the direct comparison with the DC emission spectrum one can consider the total change of the photon number density due to DC scattering. Since the number of newly created photons is mainly determined by the low frequency part of the DC emission spectrum, one can expect to obtain a good description of the photon production rate using the analytic formulae given above. Equation (4.29b) with the approximation (4.36) yields

$$\left.\frac{\partial N_2}{\partial t}\right|^{\mathrm{m,0}}_{\mathrm{em}} = G^{0,\mathrm{inv}}_{\mathrm{m}}(\omega_0) \times \left.\frac{\partial N_2}{\partial t}\right|^{\mathrm{m}}_{\mathrm{em,G}}, \tag{4.37}$$

where we made use of the result obtained for the Gould-formula, i.e. Eq. (4.30). In Fig. 4.8 the total photon production rate, $\frac{1}{2}\,\partial N_2/\partial t|^{\mathrm{m}}_{\mathrm{em}}$ as given by equation (4.29b), for a cold plasma is shown as a function of $\omega_0$ in comparison with the Lightman-approximation (4.25), the Gould-formula (4.30) and the approximation (4.37). The formula (4.37) agrees extremely well with the full numerical result even up to relativistic energies of the initial photon. The Lightman-approximation overestimates the number of produced photons by $\gtrsim 15\%$ even for low energy initial photons. For $\omega_0 \leq 10^{-2}$ the Gould-formula is accurate within $\lesssim 5\%$ but at higher energies the suppression of the DC emission becomes significant. Also the logarithmic dependence of the total change in the number of photon for soft initial photons on the assumed lower energy cutoff $w_{\mathrm{min}}$ is evident.

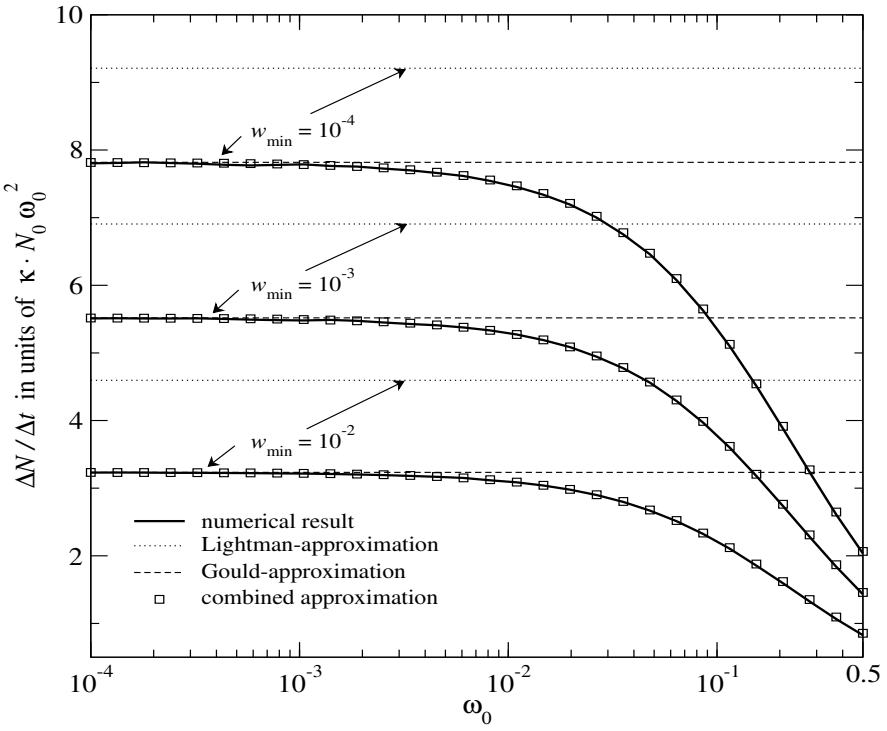


**Figure 4.8:** Total photon production rate, $\frac{1}{2}\,\partial N_2/\partial t|^{\rm m}_{\rm em}$, for cold electrons as a function of $\omega_0$ in comparison with the Lightman-approximation (4.25), the Gould-formula (4.30) and the combined approximation (4.37). All the curves are given in units of $\kappa\, N_0\, \omega_0^2$, with $\kappa = \frac{4\alpha}{3\pi}\, N_{\rm e}\, \sigma_{\rm T}$, and have been calculated for a fixed lower energy cutoff, $w_{\rm min}$, as labeled respectively.

### 4.4.3 Thermal electrons and low energy initial photons

In this Sect. we now discuss the results for the DC emission spectrum in the case of thermal electrons and soft photons. The main differences in comparison to the previous discussion arise because the electrons in the incoming channel can now also transfer energy to the photons in the outgoing channel. Especially in the high frequency part of the spectrum this effect becomes apparent (see Fig. 4.9).

As Fig. 4.9 shows at low frequencies the DC emission increases with temperature. A part of this increase is connected with the Doppler booting of the initial photon by a factor of $\gamma$. Since the DC emission rate is proportional to $\omega_0^2$ this increases the DC emissivity by the thermally averaged squared Lorentz-factor, $\left\langle \gamma^2 \right\rangle$. As will be shown below the full increase of the DC emissivity is given by $2\left\langle \gamma^2 \right\rangle - 1$.

At high frequencies the emission spectrum due to inverse DC scattering extends beyond $\nu_0$. For photons emitted at high frequencies the scattered photons are soft again implying that the DC cross section factorizes into the Compton scattering cross section and some modification factor. Therefore the high frequency part of the DC emission spectrum looks similar to a *comptonized* line spectrum, where the average gain in the energy of the photon and the dispersion of the spectrum increase with the electron temperature.

#### Analytic approximations for the DC emission spectrum

In order to improve the modeling of the DC emission spectrum we again return to the soft photon limit. Expanding the DC differential cross section (4.8) in the lowest orders of $\nu_0 \ll m_{\rm e}$

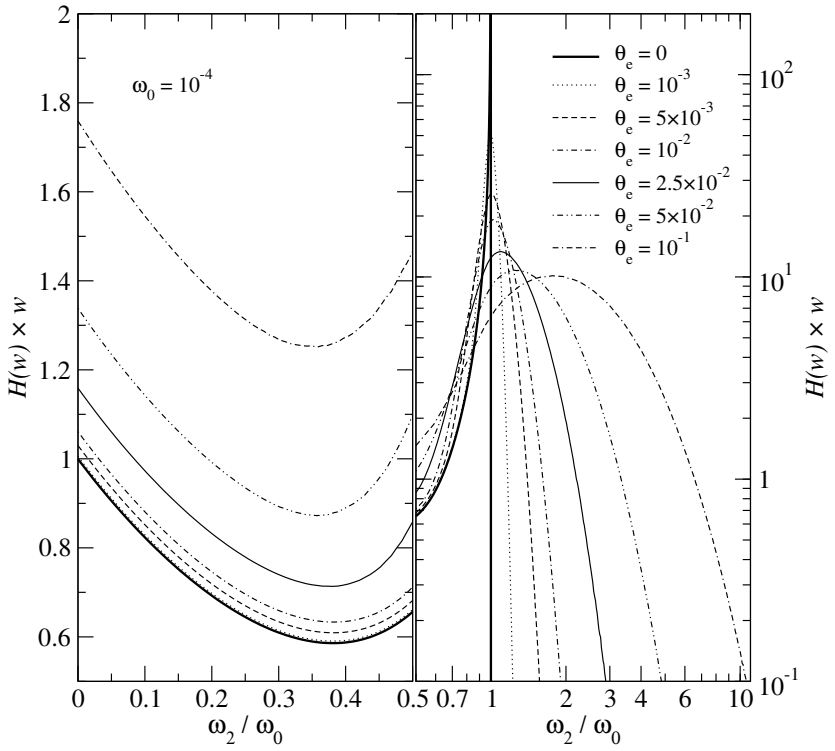


**Figure 4.9:** Two-photon DC emission spectrum for soft initial photons ($\omega_0 = 10^{-4}$) and electrons with different temperatures. Note that here only the divergency at $w = 0$ has been separated out. All the spectra are given for a fixed lower energy cutoff $w_{\rm min} = 10^{-4}$.

and $\nu_2 \ll m_{\rm e}$ one obtains

$$\left.\frac{{\rm d}\sigma_{\rm DC}^{\gamma_0\gamma_1\gamma_2}}{{\rm d}\Lambda}\right|_{\rm s}^{\rm nr} \approx \frac{\alpha}{2\pi^2}\,\frac{r_0^2}{g_{\o 0}}\,\frac{\omega_0^2}{\nu_2}\left[\gamma^2\lambda_0\lambda_1(\gamma^2\lambda_0\lambda_1-\alpha_{01})+\frac{\alpha_{01}^2}{2}\right]\frac{\gamma^2\lambda_0\lambda_1\lambda_2^2\alpha_{01}-\frac{1}{2}(\lambda_1\alpha_{02}-\lambda_0\alpha_{12})^2}{\gamma^{10}\lambda_0\lambda_1^6\lambda_2^4}\,. \tag{4.38}$$

Now we perform all the angular integrations of the Boltzmann emission integral (4.22) but assume monoenergetic electrons, with velocity $\beta_0$. This then leads to

$$\left.\frac{\partial n_2}{\partial t}\right|_{\rm em,s}^{\rm m,nr} = \frac{1+\beta_0^2}{1-\beta_0^2}\times\left.\frac{\partial n_2}{\partial t}\right|_{\rm em,L}^{\rm m}\,. \tag{4.39}$$

From this the correction factor for thermal electrons with temperature $\theta_{\rm e}$ can be found by averaging over the relativistic Maxwell-Boltzmann distribution (4.5):

$$\begin{aligned} G_{\rm m,nr}(\theta_{\rm e}) &= \int_0^\infty \frac{1+\beta_0^2}{1-\beta_0^2}\,f(E_0)\,p_0^2\,{\rm d}p_0 \equiv 2\left\langle\gamma_0^2\right\rangle - 1 \\ &= \frac{[1+24\,\theta_{\rm e}^2]\,K_0(1/\theta_{\rm e})+8\,\theta_{\rm e}\,[1+6\,\theta_{\rm e}^2]\,K_1(1/\theta_{\rm e})}{K_2(1/\theta_{\rm e})}\,, \end{aligned} \tag{4.40a}$$

with $E_0 = \gamma_0 m_{\rm e}$, $p_0 = \gamma_0 m_{\rm e}\,\beta_0$ and $\gamma_0 = 1/\sqrt{1-\beta_0^2}$. Here $K_i(1/\theta_{\rm e})$ denotes a modified Bessel function of kind $i$. For small temperatures one can find the approximation

$$G_{\rm m,nr}(\theta_{\rm e}) \overset{\theta_{\rm e}\ll 1}{\approx} 1+6\,\theta_{\rm e}+15\,\theta_{\rm e}^2+\frac{45}{4}\,\theta_{\rm e}^3-\frac{45}{4}\,\theta_{\rm e}^4 \tag{4.40b}$$

Figure 4.10 shows the numerical result for $G_{\rm m,nr}$ in comparison with the analytic approximations (4.40). The low frequency DC emission strongly increases with temperature. One can

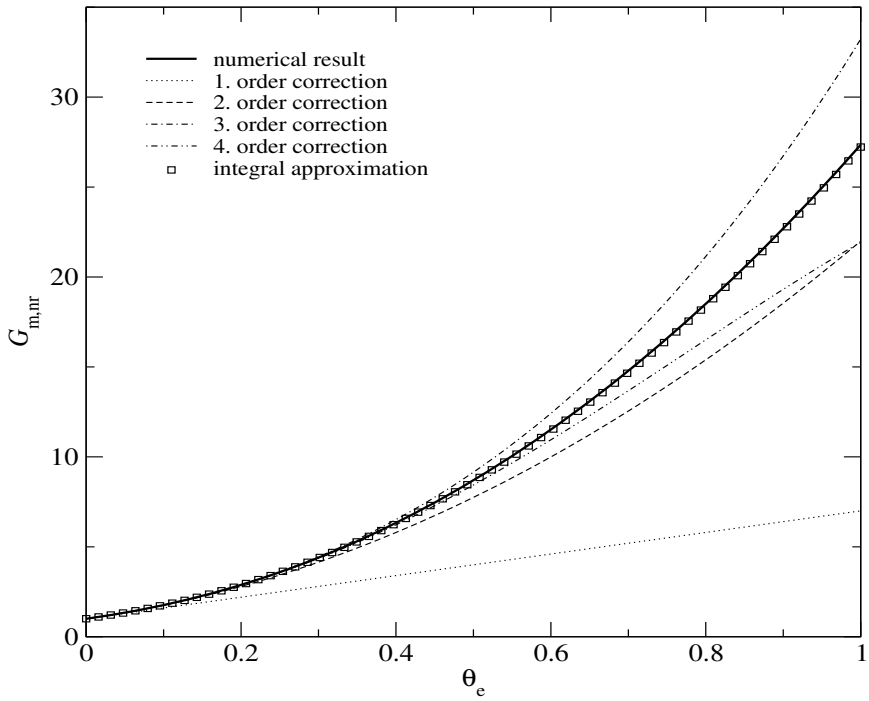


**Figure 4.10:** DC correction factor $G_{\rm m,nr}$ for soft initial photons ($\omega_0 = 10^{-4}$) as a function of the electron temperature $\theta_{\rm e}$. Also shown is the full integral approximation (4.40a) and the expansion (4.40b), taking into account the corrections up to different orders in $\theta_{\rm e}$, as indicated respectively.

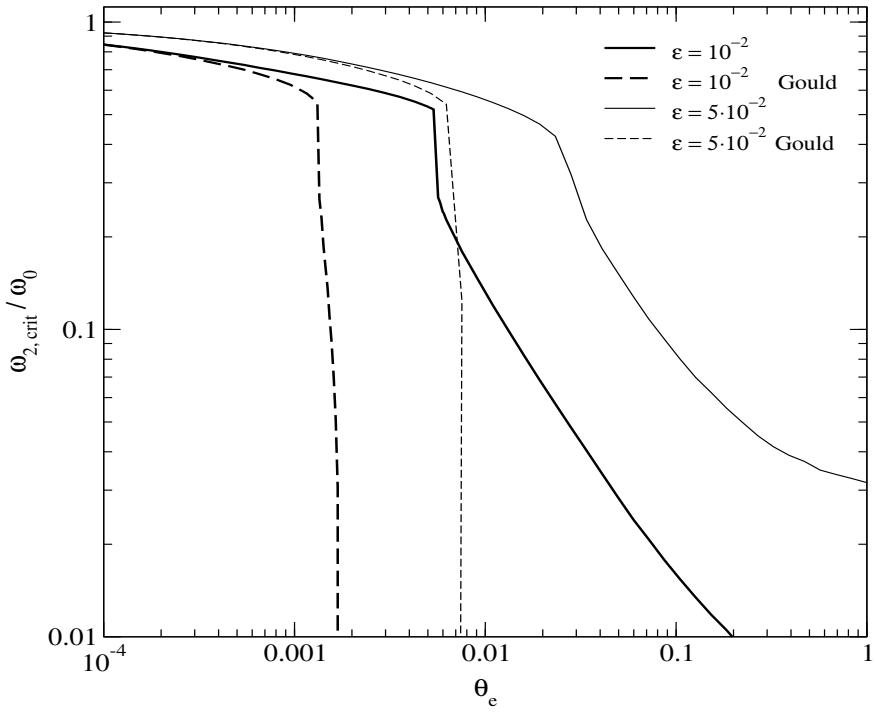


**Figure 4.11:** Critical frequency $\omega_{2,\rm crit}$ above which the analytic approximation $H_{\rm em}^{\rm nr}$ as given by equation (4.41) in combination with (4.40a) deviates more than $\epsilon$ percent from the full numerical result for $H$. Also shown are the results for the Gould-formula (4.27). All the curves were calculated for soft initial photons ($\omega_0 = 10^{-4}$) and a fixed lower energy cutoff $w_{\rm min} = 10^{-4}$.

gain a factor of a few for $\theta_e \leq 0.5$ and even a factor $\sim 30$ for $\theta_e \sim 1$. The expansion (4.40b) provides an excellent description of the numerical results up to very high temperatures ($\theta_e \sim 0.5$), but for higher temperatures the integral approximation (4.40a) should be used. Again one may combine (4.40) with the Gould-factor to obtain the approximation

$$H_{em}^{nr}(\omega_0, \omega_2, \theta_e) = H_G(w) \times G_{m,nr}(\theta_e) \tag{4.41}$$

for the function $H$ as defined by equation (4.28). In Fig. 4.11 we presented the numerical results for the critical frequency at which the approximation (4.41) breaks down. In the considered limit the approximation (4.41) with (4.40a) always dominates over the Gould-formula. The approximation (4.40b) is expected to have a similar performances as (4.40a) but with a sharp drop in the temperature range $\theta_e \sim 0.5 - 0.6$.

### Change of the number density due to DC emission

Fig. 4.12 shows the numerical results for the total photon production rate, $\frac{1}{2}\,\partial N_2/\partial t|_{em}^{m}$, in the case of low energy initial photons ($\omega_0 = 10^{-4}$) as a function of $\theta_e$ in comparison with the Gould-formula (4.30) and the approximation following from equation (4.41). The Gould-formula strongly underestimates the number of created photons for $\theta_e \gtrsim 0.01$, whereas the approximation following from equation (4.41) performs reasonably well (within a few percent) up to high temperatures. Comparing with Fig. 4.8 shows that the photon production rate depends more strongly on the temperature than on the energy of the initial photon.

The mismatch between the full numerical result and the analytic approximation is due to the fact that the width of the DC kernel is increasing much faster with temperature than with the energy of the initial photon. This implies that the asymmetry of the emission spectrum becomes important much faster and therefore the photon production rate is not completely controlled by the low frequency part. This also explains why the mismatch is larger for higher values of the low frequency cutoff.

## 4.4.4 Thermal electrons and arbitrary initial photons

We now vary both the energy of the initial photon and the temperature. As we have seen in Sect. 4.4.2 and 4.4.3 the DC emissivity decreases/increases with increasing energy of the initial photon/electron. Now, in the general case these two effects compete with each other.

As an example, in Fig. 4.13 the numerical results for the DC emission spectrum of initial photons with $\omega_0 = 0.05$ and electrons with different temperatures are presented. At low frequencies the transition between suppression and enhancement can be clearly seen. For $\theta_e = 0.05$ the low frequency DC emission is already enhanced as compared with the Gould limit. This shows that in the considered case the enhancement of emission for increasing temperature is stronger than the suppression due to larger $\omega_0$.

Moreover, at high frequencies the *recoil* and *Doppler* effect influence the shape of the spectrum. As we have seen above the transition from the recoil to Doppler dominated DC kernels is very fast (Sect. 4.3.3). Therefore the full DC emission spectrum within as narrow range of temperatures becomes Doppler dominated and very similar to the spectra presented in the preceeding Section.

### Analytic approximations for the DC emission spectrum

To improve the analytic description of the DC emission we again return to the soft photon limit, expanding the DC differential cross section (4.8) in the lowest orders of $\nu_2 \ll m_e$. To include higher order corrections we also expand this expression up to 4. order in $\omega_0$. Then we carry out all the angular integrations of the Boltzmann emission integral (4.22) again for

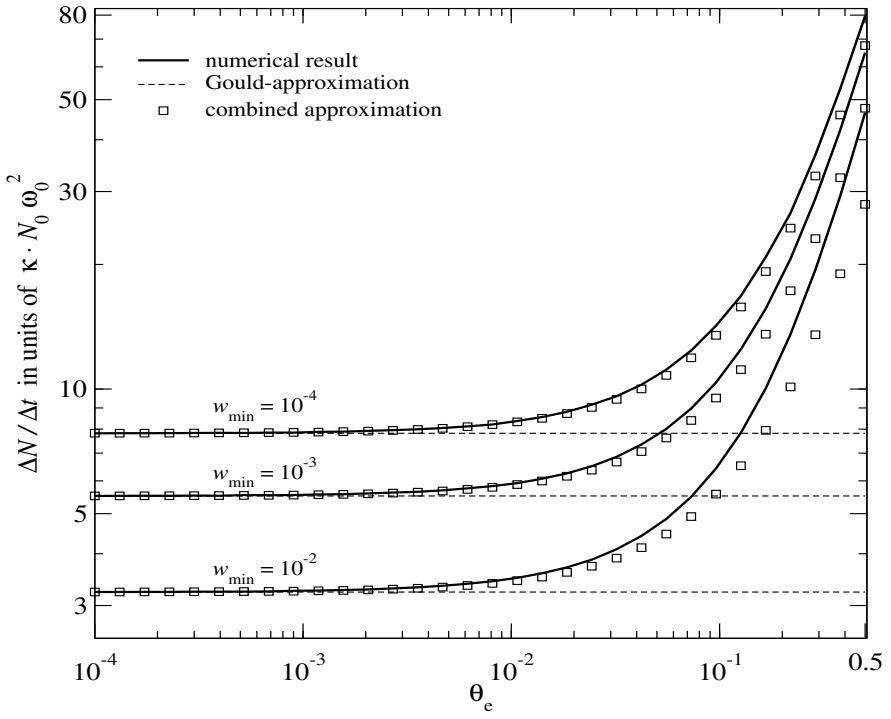


**Figure 4.12:** Total photon production rate, $\frac{1}{2}\,\partial N_2/\partial t|^{\rm m}_{\rm em}$, for soft initial photons ($\omega_0 = 10^{-4}$) as a function of $\theta_{\rm e}$ in comparison with the Gould-formula (4.30) and the approximation following from equation (4.41). All the curves are given in units of $\kappa\, N_0\, \omega_0^2$, with $\kappa = \frac{4\alpha}{3\pi}\, N_{\rm e}\, \sigma_{\rm T}$, and have been calculated for a fixed lower energy cutoff, $w_{\rm min}$, as labeled respectively.

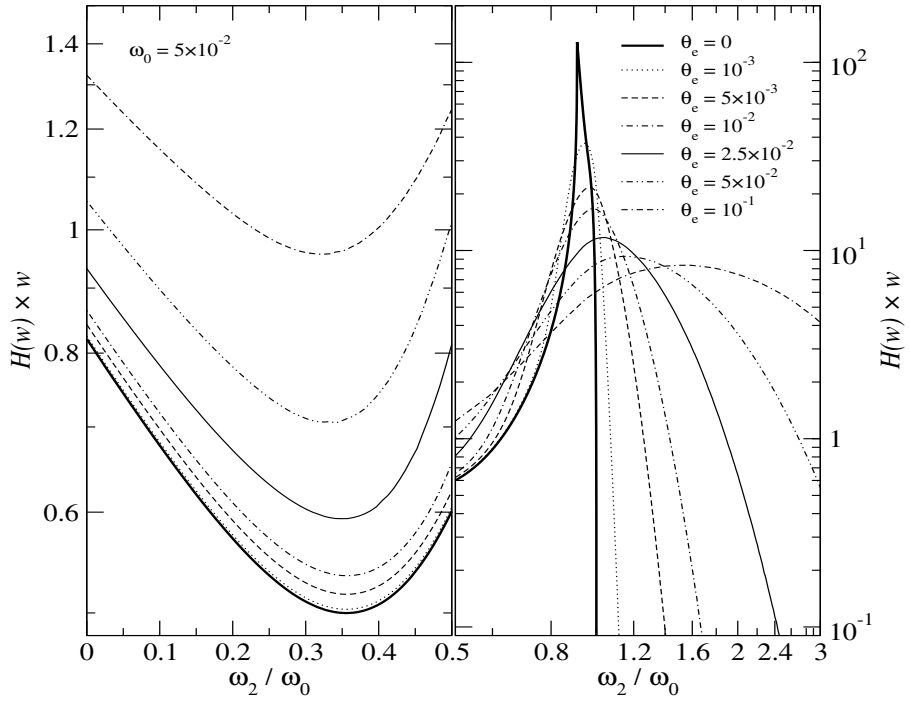


**Figure 4.13:** Two-photon DC emission spectrum for intermediate initial photons ($\omega_0 = 5 \times 10^{-2}$) and electrons with different temperatures. Note that here only the divergency at $w = 0$ has been separated out. All the spectra are given for a fixed lower energy cutoff $w_{\rm min} = 10^{-4}$.

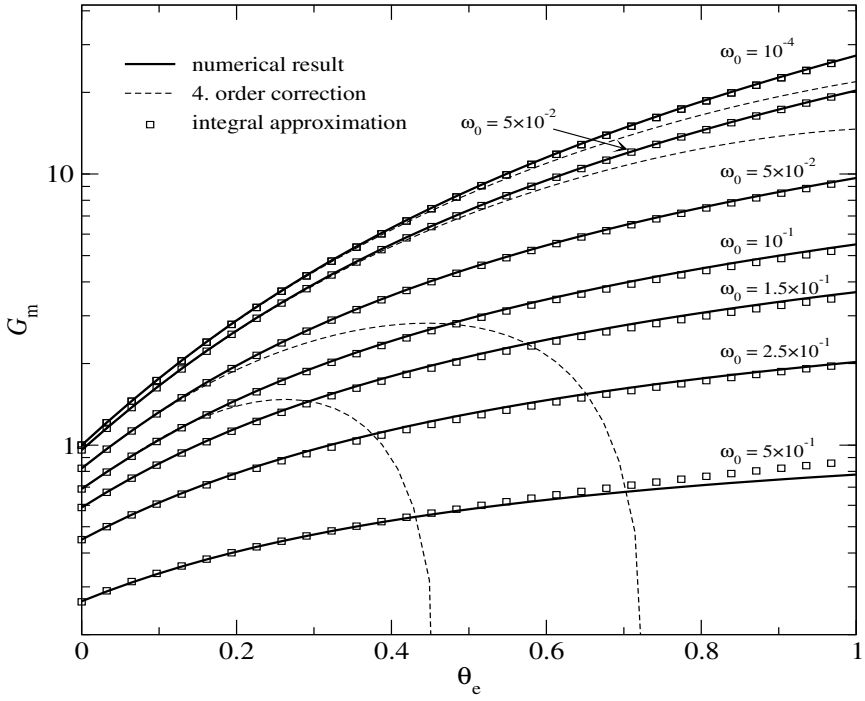


**Figure 4.14:** DC correction factor $G_\mathrm{m}$ for different energy of the initial photons as a function of the electron temperature $\theta_\mathrm{e}$. Also shown is the full integral approximation (4.43) in combination with the inverse factor (4.45a) and, for some cases, the expansion (4.44) taking into account correction terms up to fourth order, as indicated respectively.

monoenergetic electrons, with velocity $\beta_0$. This leads to

$$G_\mathrm{m}(\omega_0,\beta_0) = \gamma_0^2\left[1+\beta_0^2-\frac{21}{5}\left(1+2\beta_0^2+\frac{1}{5}\beta_0^4\right)\gamma_0\omega_0+\frac{357}{25}\left(1+\frac{10}{3}\beta_0^2+\beta_0^4\right)\gamma_0^2\omega_0^2\right.$$
$$\left.-\frac{7618}{175}\left(1+5\beta_0^2+3\beta_0^4+\frac{1}{7}\beta_0^6\right)\gamma_0^3\omega_0^3+\frac{21498}{175}\left(1+7\beta_0^2+7\beta_0^4+\beta_0^6\right)\gamma_0^4\omega_0^4\right]. \qquad (4.42)$$

Like in the previous case the correction factor for thermal electrons with temperature $\theta_\mathrm{e}$ can be found by performing the 1 - dimensional integral

$$G_\mathrm{m}(\omega_0,\theta_\mathrm{e}) = \int_0^\infty G_\mathrm{m}(\omega_0,\beta_0)\, f(E_0)\, p_0^2\,\mathrm{d}p_0\,. \qquad (4.43)$$

Unfortunately here no full analytic solution can be given, but the integral can be easily evaluated numerically. In the limit of low temperatures one can find the approximation

$$G_\mathrm{m}(\omega_0,\theta_\mathrm{e}) \approx 1-\frac{21}{5}\,\omega_0+\frac{357}{25}\,\omega_0^2-\frac{7618}{175}\,\omega_0^3+\frac{21498}{175}\,\omega_0^4+\left[6-\frac{441}{10}\,\omega_0+\frac{5712}{25}\,\omega_0^2\right.$$
$$\left.-\frac{34281}{35}\,\omega_0^3\right]\theta_\mathrm{e}+\left[15-\frac{8379}{40}\,\omega_0+\frac{8568}{5}\,\omega_0^2\right]\theta_\mathrm{e}^2+\left[\frac{45}{4}-\frac{3969}{8}\,\omega_0\right]\theta_\mathrm{e}^3-\frac{45}{4}\,\theta_\mathrm{e}^4 \qquad (4.44)$$

for (4.43), which clearly shows the connection with the two limits, equations (4.34) and (4.40b), discussed above.

As was shown in Sect. 4.4.2 an *inverse* Ansatz for $G_\mathrm{m}$ has lead to an excellent approximation for the full numerical result in the cold plasma case. In order the improve the performance of the obtained analytic approximation for $G_\mathrm{m}(\omega_0,\beta_0)$ again we tried many different functional

forms, always comparing with the direct expansion (4.42). After many attempts we found that

$$G_{\rm m}^{\rm inv}(\omega_0,\beta_0) = \frac{\gamma_0^2\,(1+\beta_0^2)}{1+\sum_{k=1}^{4} f_k(\beta_0)\,\gamma_0^k\omega_0^k}\,, \tag{4.45a}$$

with the functions $f_k(\beta_0)$

$$f_1(\beta_0) = \frac{1}{1+\beta_0^2}\left[\frac{21}{5}+\frac{42}{5}\beta_0^2+\frac{21}{25}\beta_0^4\right] \tag{4.45b}$$

$$f_2(\beta_0) = \frac{1}{(1+\beta_0^2)^2}\left[\frac{84}{25}+\frac{217}{25}\beta_0^2+\frac{1967}{125}\beta_0^4\right] \tag{4.45c}$$

$$f_3(\beta_0) = -\frac{1}{(1+\beta_0^2)^3}\left[\frac{2041}{25}+\frac{1306}{125}\beta_0^2\right] \tag{4.45d}$$

$$f_4(\beta_0) = \frac{1}{(1+\beta_0^2)^4}\,\frac{9663}{4375} \tag{4.45e}$$

provided the best description of the full numerical results.

Figure 4.14 shows the numerical results for $G_{\rm m}(\omega_0,\theta_{\rm e})$ in comparison with the integral approximation (4.43) in combination with the inverse factor (4.45a) and the direct expansion (4.44) taking into account correction terms up to fourth order. Clearly the performance of the integral approximation is excellent in the full range of considered cases, but the direct expansion breaks down at lower and lower temperatures once the initial photon frequency increases. For $\omega_0 \leq 0.1$ the direct expansion should be applicable within a few percent accuracy up to temperatures of $\theta_{\rm e} \sim 0.2$.

Figure 4.14 shows the numerical results for $G_{\rm m}(\omega_0,\theta_{\rm e})$ in comparison with the integral approximation (4.43) in combination with the inverse factor (4.45a) and the direct expansion (4.44) taking into account correction terms up to fourth order. Clearly the performance of the integral approximation is excellent in the full range of considered cases, but the direct expansion breaks down at lower and lower temperatures once the initial photon frequency increases. For $\omega_0 \leq 0.1$ the direct expansion should be applicable within a few percent accuracy up to temperatures of $\theta_{\rm e} \sim 0.2$.

### Aspects of the low frequency DC emission spectrum

At low frequencies the DC emission on one hand is suppressed for increasing initial photon energy and on the other is enhanced for larger electron temperature. This may lead to the question, when the emission coefficient, $w\,H$, at some low frequency $w_{\rm min} = \omega_2/\omega_0 \ll 1$ is equal to unity, such that the Lightman-approximation in principle is applicable. Combining the Gould-factor (4.27) with the expansion (4.44) and keeping terms up to second order in $\theta_{\rm e}$, one may obtain the simple approximation

$$\theta_{\rm e,1} = \sqrt{a^2+b\,\omega_0}-a\,, \tag{4.46a}$$

with

$$a = \frac{1-\frac{147}{20}\,\omega_0+\frac{952}{25}\,\omega_0^2-\frac{11427}{70}\,\omega_0^3}{5-\frac{2793}{40}\,\omega_0+\frac{2856}{5}\,\omega_0^2} \tag{4.46b}$$

$$b = \frac{\frac{7}{5}-\frac{119}{25}\,\omega_0+\frac{7618}{525}\,\omega_0^2-\frac{7166}{175}\,\omega_0^3+\frac{2}{3}\,\frac{w_{\rm min}}{\omega_0}}{5-\frac{2793}{40}\,\omega_0+\frac{2856}{5}\,\omega_0^2}\,, \tag{4.46c}$$

for the temperature at which the emission coefficient fulfills the condition $w_{\rm min}\,H(w_{\rm min}) \equiv 1$. In this definition of $b$ the term $\propto w_{\rm min}$ arises due to the small deviation of the Gould-factor, $w_{\rm min}\,H_{\rm G} \approx 1-2\,w_{\rm min}$, from unity. In the limit of low energy initial photons (4.46a) simplifies to $\theta_{\rm e,1} \approx \frac{7}{10}\,\omega_0+\frac{1}{3}\,w_{\rm min}$. Therefore this deviation becomes important especially when $\omega_0 \lesssim 5\,w_{\rm min}$.

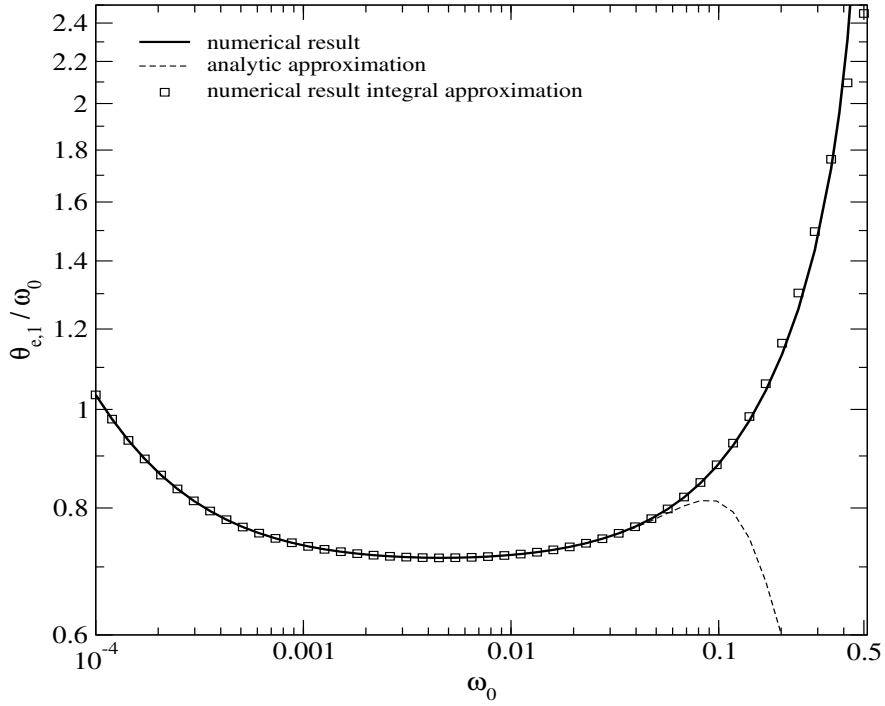


**Figure 4.15:** The numerical results for the temperature, $\theta_{\mathrm{e},1}$, at which the low frequency emission coefficient fulfills the condition $w_{\min} H(w_{\min}) \equiv 1$. In comparison also the approximation (4.46a) and the numerical results obtained using the Gould-factor (4.27) in combination with the integral approximation (4.43) and (4.45a) are presented. All the curves have been calculated for $w_{\min} = 10^{-4}$.

In Figure 4.15 we show the numerical results for the temperature, $\theta_{\mathrm{e},1}$ as a function of the initial photon energy in comparison with the approximation (4.46a). It agrees very well with the full numerical result for $\omega_0 \lesssim 0.1$. In the shown case this temperature is directly proportional to the initial photon energy, $\theta_{\mathrm{e},1} = \frac{7}{10}\,\omega_0$, around $\omega_0 \sim 5 \times 10^{-3}$, but at lower frequencies the term connected with $w_{\min}$ becomes significant. One may also conclude that for monochromatic initial photons below $\omega_0 \sim 0.15$ the electrons can easily compensate the suppression of the DC emission due to the increasing initial photon energy, but for $\omega_0 \gtrsim 0.15$ they have to be several times hotter. We also presented the numerical results obtained using the Gould-factor (4.27) in combination with the integral-approximation (4.43) and (4.45a). Here again the excellent performance of this combined approximation at low frequencies is evident.

### Change of the number density due to DC emission

Even though the integral approximation (4.43) for the low frequency emission performs very well in a broad range of temperatures and initial photon frequencies, it is expected that the number of produced photons is less accurately described. This is mainly due to the fact that the importance of the high frequency part of the DC emission spectrum is not modeled appropriately.

In Fig. 4.16 as an example we present some numerical results for the number of produced photons in comparison with the analytic approximations. The Gould approximation over estimated the number of created photon significantly. For very small values of $w_{\min}$ the integral approximation works fine but for $w_{\min} = 10^{-2}$ deviations start to arise already for $\theta_{\mathrm{e}} \gtrsim 5\times10^{-2}$.

## 4.4.5 The DC infrared divergence and the role of the low frequency cutoff

As mentioned above, like in the case of Bremsstrahlung DC scattering exhibits a *infrared* divergence at low frequencies. This behavior is typical for first order radiative corrections to

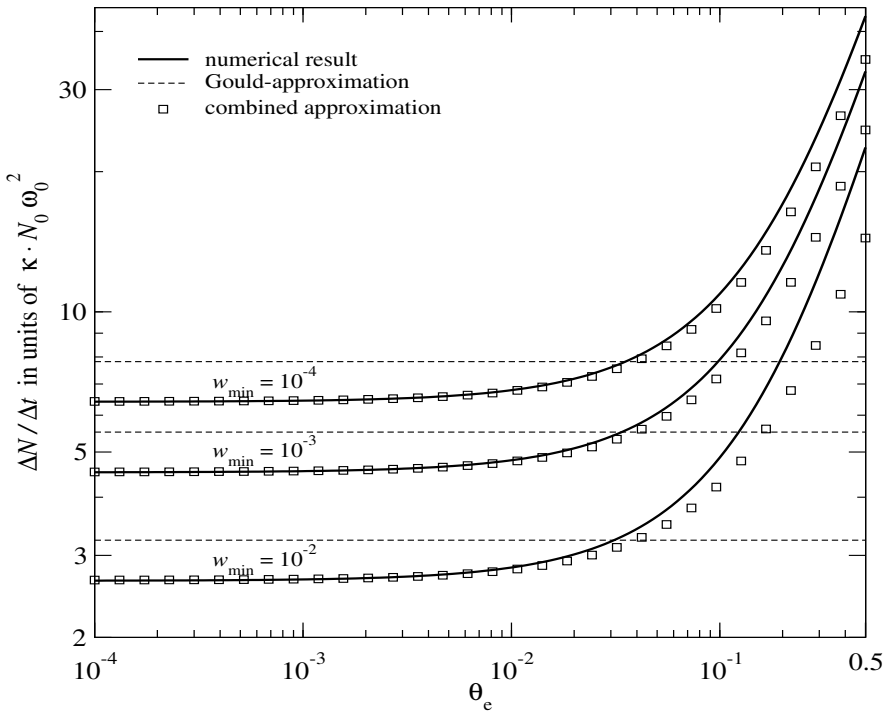


**Figure 4.16:** Total photon production rate, $\frac{1}{2}\,\partial N_2/\partial t|^{\rm m}_{\rm em}$, for intermediate initial photons ($\omega_0 = 5 \times 10^{-2}$) as a function of $\theta_{\rm e}$ in comparison with the Gould-formula (4.30) and the approximation following from equation (4.41) and (4.45). All the curves are given in units of $\kappa\, N_0\, \omega_0^2$, with $\kappa = \frac{4\alpha}{3\pi}\, N_{\rm e}\, \sigma_{\rm T}$, and have been calculated for a fixed lower energy cutoff, $w_{\rm min}$, as labeled respectively.

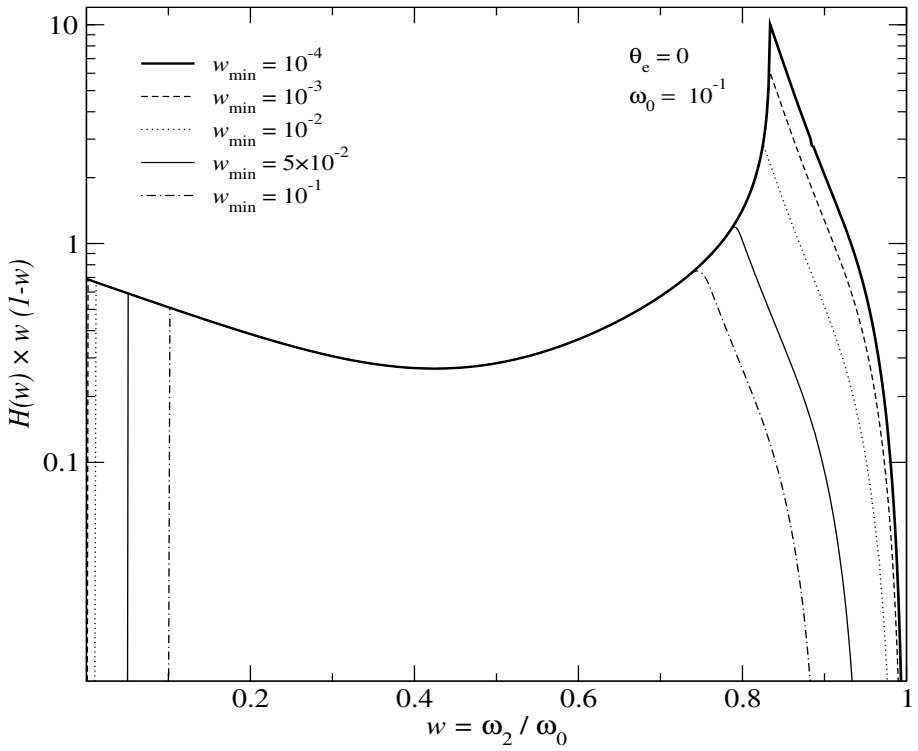


**Figure 4.17:** Role of the low frequency cutoff $w_{\rm min}$ on the shape of the two-photon DC emission spectrum for cold electrons. Shown is the ratio $H(w)$ as given by (4.28) for fixed initial photon energy ($\omega_0 = 10^{-1}$) and different values of $w_{\rm min}$, as indicated respectively. The divergencies at $w = 0$ and $w = 1$ have been separated out.

quantumelectrodynamical processes. Mathematically this divergence can be obtained by series expansion of the invariant matrix element $X$ for DC scattering into lowest order of $\nu_2 \ll m_\mathrm{e}$, showing that $X \propto 1/\nu_2^2$ and therefore the corresponding cross sections diverge like $\mathrm{d}\sigma \propto 1/\nu_2$.

Albeit this similarity to Bremsstrahlung DC scattering in addition exhibits a divergence at high frequencies. If one considers the case of cold electrons and low energy initial photons the conditional DC kernel is very close to a $\delta$-function (cf. Sect. 4.3.1). Therefore a photon emitted at a very low frequency directly implies a scattered photon at frequencies very close to $\nu_0$ and hence the divergence at $w = 1$ simply is a consequence of the *infrared* divergence at $w = 0$.

It is worth mentioning that in the Gould-approximation a lower energy cutoff, $\nu_{2,\mathrm{min}} = \nu_0\, w_\mathrm{min}$, directly implies a high frequency cutoff at $\nu_{2,\mathrm{max}} = \nu_0\,(1 - w_\mathrm{min})$. This is due to the fact that a DC scattered photon with energy $\nu_1 > \nu_{2,\mathrm{max}}$ corresponds to an emitted photon with energy $\nu_2 < \nu_{2,\mathrm{min}}$. Since photons emitted below $\nu_{2,\mathrm{min}}$ are assumed to be efficiently absorbed, the inverse process at high frequencies will also immediately absorb any photons above $\nu_{2,\mathrm{max}}$. Note that energetically DC scattered photons with $\nu_0 > \nu_1 > \nu_{2,\mathrm{max}}$ are *not* principally forbidden.

In order to illustrate the effects of the low energy cutoff, $w_\mathrm{min}$, on the DC emission spectrum in Fig. 4.17 we present some numerical results for cold electrons and initial photons with energy $\omega_0 = 10^{-1}$. The shape of the low frequency DC emission spectrum does not depend on the lower energy cutoff (of course except for the position of the abrupt drop to zero at $\nu_{2,\mathrm{min}}$ itself). Increasing $w_\mathrm{min}$ shifts the position of the cusp, which for $w_\mathrm{min} \ll 1$ is close to $\nu_2 \sim \nu_0/(1{+}2\,\omega_0)$, towards lower frequencies. At frequencies higher than $\nu_{2,\mathrm{max}}$ the DC emission vanishes, with a gradual transition between $\nu_\mathrm{cusp}$ and $\nu_{2,\mathrm{max}}$.

One can understand that the number of photons at the highest frequencies is determined by the superposition of the conditional DC kernels for scattered photons with energies very close to $\nu_1 \gtrsim \nu_0\, w_\mathrm{min}$ (see Fig. 4.1). For non-zero electron temperature the shape of the DC emission spectrum at high frequencies depends in a very similar manner on the low frequency cutoff. But in this case due to *inverse* DC scattering the high frequency cutoff is no more given by $\nu_{2,\mathrm{max}}$ as in the case of cold electrons.

### 4.4.6 Electron heating and cooling due to DC emission

As mentioned above in the Lightman and Gould approach due to the neglect of recoil no *heating* or *cooling* of the electrons or photons due to DC scattering occurs. We have seen in Sect. 4.2.3 that the increase and decrease of the mean photon energy and dispersion in the high frequency part of the emission spectrum scales similar to the case of Compton scattering. Therefore one can expect that the additional energy exchange due to the redistribution of high frequency photons via DC scattering may lead to a small correction of the Compton energy exchange. This correction will depend on the shape of the low energy spectrum, e.g. the low energy cutoff and the 'sea' of soft photons, especially when induced effects are important. However, since the calculation of the energy exchange due to DC scattering is rather demanding and the effects in comparison to Compton cooling and heating are expected to be small, we did not present any numerical results here.

## 4.5 Analytical treatment of the full kinetic equation for DC scattering

In this Section we now discuss the full kinetic equation for the time evolution of the photon phase space distribution under DC scattering. We will first use the analytic results obtained in the preceeding Sections to derive an approximation of the *effective DC Gaunt factor* analytically and then compare it with some full numerical calculations. This shall show that in situations close to full thermodynamic equilibrium the redistribution of high frequency photons

by DC scattering is much less important than the production of new photons a low frequencies. Therefore we then focus on the discussion of the DC kinetic equation at low frequencies, where only the processes (4.1a) and (4.1b) are important. For this we first rewrite the collision integral analytically and then present results for the limit of low electron temperatures and photon energies using the *soft photon approximation*.

### 4.5.1 Analytic approximation for the effective DC Gaunt factor

We have seen in Section 4.3 that in general the DC emission term for monochromatic initial photons and thermal electrons can be given in the form (4.29a), where an excellent approximation to the function $H$ can be obtained combining the Gould-factor (Eq. (4.27)) and the analytic approximations derived for the low frequency part of the DC emission spectrum (in the most general situation by thermally averaging Eq. (4.45a)):

$$H_{\rm app}(\omega_0,\omega_2,\theta_{\rm e}) = H_{\rm G}(\omega_2/\omega_0)\times G(\omega_0,\theta_{\rm e})\,. \tag{4.47}$$

It was shown that the total number of produced photons is represented very well in a wide range of temperatures and initial photon frequencies.

In the Gould approximation it is assumed that neither *recoil* nor *Doppler boosting* are important, implying that $\omega_0\equiv\omega_1+\omega_2$. We have seen that the conditional DC emission kernel in this limit is very close to a $\delta$-function (see Sect. 4.4.1). Therefore one may try to approximate the conditional DC emission kernel by the simple expression

$$\mathcal{P}_{\rm app}(\nu_i\rightarrow\nu_j\,|\,\nu_1) = \kappa_{\rm dc}\,\frac{\omega_i^2}{\nu_j}\,\left[\frac{\omega_j}{\omega_i}\,H_{\rm app}(\omega_i,\omega_j,\theta_{\rm e})\right]\times\delta(\nu_i-\nu_1-\nu_j)\,, \tag{4.48}$$

where $\kappa_{\rm dc}=\frac{4\alpha}{3\pi}\,N_{\rm e}\,\sigma_{\rm T}$. In full thermodynamic equilibrium DC emission is completely balanced by DC absorption. Therefore, at least close to equilibrium, the full collision integral for DC scattering should have the form

$$\left.\frac{\partial n_2}{\partial t}\right|_{\rm DC} = \kappa_{\rm dc}\,\frac{\theta_\gamma^2}{x_2^3}\cdot\Big[1-n_2(e^{x_{\rm e,2}}-1)\Big]\cdot g_{\rm dc}(x_2,\theta_\gamma,\theta_{\rm e})\,, \tag{4.49}$$

where here we introduced the *effective double Compton Gaunt factor*, $g_{\rm dc}$, and defined the dimensionless frequencies $x_i=\omega_i/\theta_\gamma$ and $x_{{\rm e},i}=\omega_i/\theta_{\rm e}$, where the photon temperature $\theta_\gamma$ should be regarded as a parameter describing the *energy density* of the photon field. In the case of Planckian photons it is identical to the *thermodynamic* temperature (see Appendix B). In the form (4.49) one can directly see that the DC collision integral vanishes when the photons are Planckian with the thermodynamic temperature $\theta_\gamma\equiv\theta_{\rm e}$. In order to derive the effective Gaunt factor, we now consider the reactions (4.1a) and (4.1c) and their contributions to (4.49) separately.

#### Reactions $\gamma_0+e\rightarrow\gamma_1+\gamma_2+e'$

Inserting the approximation (4.48) for the DC kernel into the Boltzmann equation (4.9) and only considering the first integral one may find

$$\left.\frac{\partial n_2}{\partial t}\right|_{\rm DC,a} = \kappa_{\rm dc}\,\frac{\theta_\gamma^2}{x_2^3}\,[1+n_2]\int\limits_{x_2+x_{\rm min}}^{\infty} x_0^4\,n(x_0)\,[1+n(x_0-x_2)]\left[\frac{x_2}{x_0}\,H_{\rm app}(\omega_0,\omega_2,\theta_{\rm e})\right]{\rm d}x_0 \tag{4.50a}$$

$$= \kappa_{\rm dc}\,\frac{\theta_\gamma^2}{x_2^3}\,[1+n_2]\times g_{\rm dc,a}(x_2,\theta_\gamma,\theta_{\rm e})\,. \tag{4.50b}$$

Here we introduced the lower energy cutoff $x_{\rm min}$ making the assumption that for $x<x_{\rm min}$ the photon distribution is Planckian with temperature $\theta_\gamma=\theta_{\rm e}$, such that the emission is

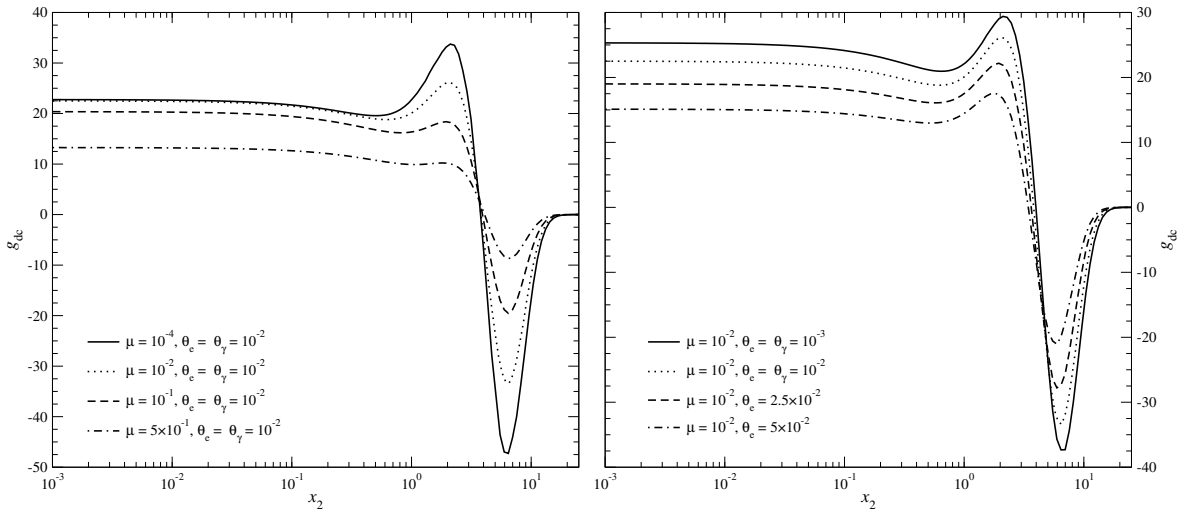


**Figure 4.18:** Numerical results for the effective Gaunt factor as defined by equation (4.49) with different values of the chemical potential $\mu$ and temperatures, as indicated respectively. In all the calculations we assumed a lower frequency cutoff $x_{\rm min} = 10^{-3}$.

completely balanced by absorption. In the case of cold electrons only photons with $x_2 + x_{\rm min} \leq x_0$ contribute to the emission at $x_2$ (see the range of integration in (4.50)). At low frequencies $1 + n(x_0 - x_2) \approx 1 + n(x_0)$ and $w H_{\rm G}(w) \approx 1$. Since for situations close to equilibrium the main contributions to the integral come from $x_0 \sim 4 - 5$ induced effects at $x_2 \ll 1$ are of the order of a few percent. However at high frequencies $x_2 \gtrsim 1$ induced effects are significant and $g_{\rm dc,a}$ becomes very sensitive to the lower frequency cutoff.

### Reactions $\gamma_2 + e \rightarrow \gamma_0 + \gamma_1 + e'$

For this channel we proceed in the same way as in the previous paragraph now considering the third integral in equation (4.9). This then leads to

$$\left.\frac{\partial n_2}{\partial t}\right|_{\rm DC,c} = -\frac{\kappa_{\rm dc}}{2}\, x_2^2\, \theta_\gamma^2\, n_2\, [1+n_2] \int\limits_{x_{\rm min}}^{x_2 - x_{\rm min}} \frac{1+n(x_0)}{x_0}\, \frac{1+n(x_2-x_0)}{1+n_2} \left[\frac{x_0}{x_2}\, H_{\rm app}(\omega_2, \omega_0, \theta_{\rm e})\right] {\rm d}x_0 \tag{4.51a}$$

$$= -\frac{\kappa_{\rm dc}}{2}\, x_2^2\, \theta_\gamma^2\, n_2\, [1+n_2] \times g_{\rm dc,c}(x_2, \theta_\gamma, \theta_{\rm e}) \tag{4.51b}$$

This reactions can be considered as *scattering* of photons *out* of the phase space volume at $x = x_2$. For cold electrons only photon with $x_{\rm min} \leq x_0 \leq x_2 - x_{\rm min}$ can be produced (see the range of integrations). When induced terms are not important $g_{\rm dc,c}(x_2, \theta_\gamma, \theta_{\rm e})$ is proportional to the total number of photons emitted into the range $x_{\rm min} \leq x_0 \leq x_2 - x_{\rm min}$ for an initial photon energy $x_2$. At low frequencies $g_{\rm dc,c} \approx 0$ since the allowed range of integration becomes small. In any case $\partial_t n_2|_{\rm DC,c} \ll \partial_t n_2|_{\rm DC,a}$ for $x_2 \ll 1$ (relative factor of $\sim x_2^5\, n_2$ and $n_2 \sim 1/x_2$). At high frequencies again induced terms become very important.

### Final result for $g_{\rm dc}(x_2, \theta_\gamma, \theta_{\rm e})$

The effective Gaunt factor as defined by equation (4.49) is now given as the sum of $g_{\rm dc,a}$ and $g_{\rm dc,a}$ with appropriate scalings determined by (4.50) and (4.51). One can easily find

$$g_{\rm dc}(x_2, \theta_\gamma, \theta_{\rm e}) = g_{\rm dc,a}(x_2, \theta_\gamma, \theta_{\rm e}) - \frac{1}{2}\, x_2^5\, n_2\, g_{\rm dc,c}(x_2, \theta_\gamma, \theta_{\rm e})\,. \tag{4.52}$$

The basic properties of this result for the DC Gaunt factor can be summarized as follows:

(i) At low frequencies the contribution arising due to the reaction (4.1c) is negligible. Here mainly DC emission and absorption are occurring and the redistribution of photons is tiny. Induced effects are not very important for the effective Gaunt factor.

(ii) At high frequencies the term proportional to $g_{\rm dc,c}$ becomes very important. In fact it partially cancels the large positive contribution arising from $g_{\rm dc,a}$ resulting in a much smaller effective Gaunt factor. Here the redistribution of photons is much more important than emission and induced effects are strong.

We shall now present some full numerical results for the effective Gaunt. In some cases we have compared the numerical results with those obtained by equation (4.52) and found very good agreement. A detailed discussion will be presented in some future work.

### Comparing with full numerical results

In this paragraph we will present some numerical results for the effective DC Gaunt factor. We will restrict ourselves to situations close to full thermodynamic equilibrium, which are the most relevant in the context of the thermalization of CMB spectral distortions. Therefore we shall consider photons, which follow a Bose-Einstein distribution, $n_{\rm BE}(x) = 1/(e^{x+\mu} - 1)$, with dimensionless chemical potential $\mu = \text{const}$ and temperature $\theta_\gamma = \theta_{\rm e}$.

In Fig. 4.18 we show the effective Gaunt factor for some combinations of the chemical potential and different temperatures of the electrons, as indicated respectively. In the left panel one can see the decrease of the importance of induced scattering at high frequencies with larger $\mu$. The right panel illustrates the decrease of the DC emissivity at low frequencies with increasing temperature. It can be seen that photons at high frequencies due to DC scattering cool. As mentioned above in cases $\theta_{\rm e} > \theta_\gamma$ one would expect that also heating can occur, but a more detailed discussion shall be presented elsewhere.

### Comparing with Compton scattering

In the particular cases discussed above *no* redistribution of photons by Compton scattering is occurring and principally DC *emission* and *redistribution* dominate in the full range of frequencies. Of course in the more general situation Compton scattering will redistribute photons much faster than DC scattering. Although competing with the lowest order Compton effect (as described by the Kompaneets equation [75]) in most cases is impossible, it is still fair to ask, when the redistribution of high energy photons due to DC scattering will become comparable with the contribution due to the first order temperature correction to the kinetic equation of Compton scattering.

Even though the effective DC Gaunt factor at high frequencies is of the order of a few $\times\, 10$, using the generalized Kompaneets equation [67] we have estimated that for situations close to equilibrium effective Gaunt factors of the order of few $\times\, 10^3$ would be necessary to make DC scattering comparable with the first order temperature correction to the Kompaneets equation. Therefore we conclude that at least in situations close to thermodynamic equilibrium the redistribution of photons by DC scattering is negligible. However, it may be still possible that the redistribution of photons by DC scattering can become important for cases far away from equilibrium, e.g. when the temperatures differ strongly, but this is beyond the scope of this work and shall not be discussed here.

## 4.5.2 Derivation of the effective DC Gaunt factor in the soft photon limit

In Section 4.5.1 we have obtained an analytical approximation for the effective Gaunt factor using the results derived for the DC emission by monochromatic initial photons and convolving these with more general distributions of photons. The inclusion of induced effects was only possible under the assumption that $\nu_0 = \nu_1 + \nu_2$. Furthermore we have seen that the contributions

of DC scattering to the evolution of high frequency photons (at least for cases we are interested in here) is not very important, since Compton scattering is orders of magnitudes faster and will wipe out any disturbance of the spectrum at high frequencies within a very short time.

We shall now derive similar expression, as presented above, for the effective Gaunt factor at *low* frequencies, where only the reactions (4.1a) and (4.1b) contribute to the collision integral, including all induced effects self-consistently. For this we start from the Boltzmann equation (4.7) and consider only the first term in the integrand. We then go to the soft photon limit and perform Taylor series expansions in the photon frequency $\nu_0$ and the energy of the initial electron. In this Section we shall present some details of this derivation.

### Rewriting the collision integral for DC scattering

Starting from the Boltzmann equation in the form (4.7) and considering only the first term in the integrand, by Taylor expansion the statistical factor $F_{\gamma_0\gamma_1\gamma_2}$ may be cast into the form

$$F_{\gamma_0\gamma_1\gamma_2} = f\,n(n+1)\cdot\Big[1-n_2(e^{x_{\rm e,2}}-1)\Big] + f\sum_{k=1}^{\infty}\frac{\Delta x_{\rm e}^k}{k!}\left\{(1+n_2)\cdot\,n\,\frac{\partial^k n}{\partial x_{\rm e}^k} - n_2\,e^{x_{\rm e,2}}\cdot(1+n)\left[1+\frac{\partial}{\partial x_{\rm e}}\right]^k n\right\}, \quad (4.53)$$

where the definitions of Sect. 4.2 were used and we introduced the dimensionless variables $x_{\rm e}=\nu/T_{\rm e}$ and $\Delta x_{\rm e}=(\nu_1-\nu)/T_{\rm e}$. Note that here and below we omit the index '0' for the initial photon. Now, with (4.53) the Boltzmann equation for DC scattering at low frequencies can be rewritten as

$$\left.\frac{\partial n_2}{\partial t}\right|_{\rm DC}^{\rm soft} = \kappa_{\rm dc}\,\frac{\theta_{\rm e}^2}{x_{\rm e,2}^3}\Big[1-n_2(e^{x_{\rm e,2}}-1)\Big]\cdot J_0 + \kappa_{\rm dc}\,\frac{\theta_{\rm e}^2}{x_{\rm e,2}^3}\Big[\,(1+n_2)\cdot J_1 - n_2\,e^{x_{\rm e,2}}\cdot J_2\Big], \quad (4.54)$$

where we introduced the integrals

$$J_0 = \int x_{\rm e}^2\,{\rm d}x_{\rm e}\Big[n(n+1)\Big]\cdot I_0 \quad (4.55a)$$

$$J_1 = \sum_{k=1}^{\infty}\int x_{\rm e}^2\,{\rm d}x_{\rm e}\left[n\,\frac{\partial^k n}{\partial x_{\rm e}^k}\right]\cdot I_k \quad (4.55b)$$

$$J_2 = \sum_{k=1}^{\infty}\int x_{\rm e}^2\,{\rm d}x_{\rm e}\left[(1+n)\left[1+\frac{\partial}{\partial x_{\rm e}}\right]^k n\right]\cdot I_k \quad (4.55c)$$

$$I_k = \frac{1}{k!}\,\frac{1}{\kappa_{\rm dc}\,\theta_{\rm e}^2}\,\frac{x_{\rm e,2}^2}{x_{\rm e}}\int d\Omega\int\frac{p^2\,{\rm d}p}{\gamma}\,{\rm d}\Omega_{\rm e}\,{\rm d}\Omega_1\,f\,\Delta x_{\rm e}^k\,X(K_0,K_1,K_2)\,. \quad (4.55d)$$

Note that the differential operator $\partial_{x_{\rm e}}$ only affects the photon distribution $n\equiv n(\nu)$.

### Calculation of the $I_k$'s

All the further calculations are very lengthy and where performed with the computer algebra program Mathematica. We assumed that the secondary photon $K_2$ is *soft* ($\nu_2\ll\nu_1$, $\nu_2\ll m_{\rm e}$ and also that equivalent relations in the rest frame of the scattering electron hold). Therefore we took only contributions to the integrals $I_k$'s in lowest order of $\nu_2$ into account, i.e. $\propto\nu_2^{-2}$. Furthermore, we expanded the integrand of $I_k$, assuming soft initial photons and low electron temperature, in orders of $\omega/m_{\rm e}$ and $\eta=p/m_{\rm e}$. Afterwards all the integrals $I_k$ could be solved analytically and their results are given in the Appendix D.3. As one can see $I_0$ is equivalent to the result (4.44), which was obtained for monochromatic initial photons. All the integrals $I_k$ for $k>0$ arise due to induced effects.

Inserting the results (D.13) for the lowest order in $x_{\rm e,2}$ into equations (4.55b) and (4.55c), up to the forth order corrections in the electron temperature one can show that $J_1 \equiv J_2$ for all photon distributions which vanish sufficiently fast in the limit $x_{\rm e} \rightarrow \infty$. This is a rather tedious calculation and will not be presented here. With $J_1 = J_2$ the Boltzmann-equation for the phase space evolution of the photons under DC scattering in lowest order of $x_{\rm e,2}$ can be expressed as

$$\left.\frac{\partial n_2}{\partial t}\right|_{\rm DC}^{\rm soft} = \kappa_{\rm dc}\,\frac{\theta_{\rm e}^2}{x_{\rm e,2}^3}\cdot\Big[1-n_2(e^{x_{\rm e,2}}-1)\Big]\cdot G(\theta_{\rm e})\,. \tag{4.56}$$

Here the DC emission coefficient $G(\theta_{\rm e})$ is given by the *direct* expansion

$$G(\theta_{\rm e}) = \sum_{k=0}^{4} G_k\cdot\theta_{\rm e}^k \tag{4.57}$$

where the definitions of the integrals $G_i$ may be found in the Appendix (D.15). The first integral $G_0$ corresponds to the non-relativistic result obtained earlier by Lightman [80].

### 4.5.3 Beyond the limit $\theta_{\rm e} \ll 1$

The procedure described above results in an asymptotic expansion of the effective DC Gaunt factor in the soft photon limit. This expansion in most of the cases is expected to converge very slowly. Therefore, using the *direct* expansion (4.57) we again tried to 'guess' the correct functional form of the DC emission coefficient $G(\theta_{\rm e})$ and thereby to extend the applicability of our analytic expressions. Examining the general behavior of the results obtained in our numerical integrations (Sect. 4.5.6) for Planckian initial spectra showed that for $\theta_{\rm e} \lesssim \theta_\gamma$ in general the ratio between the relativistic and non-relativistic DC emission coefficient, $G/G_0$, is dropping towards higher electron temperatures. After several attempts we found that this behavior is best represented by the functional form

$$G^{\rm inv}(\theta_{\rm e}) = \frac{G_0}{1+a\,\theta_{\rm e}}\,. \tag{4.58a}$$

Now, comparing the Taylor expansion of (4.58a) for small temperature with equation (4.57) one can immediately deduce

$$a = -\tilde{G}_1\,. \tag{4.58b}$$

Here $\tilde{G}_i = G_i/G_0$ was defined. As will be shown below, equation (4.58a) together with (4.58b) and (D.15) provides a description of the low frequency DC emission coefficient, which for photon distributions close to equilibrium is better than 5 % for temperatures up to $\sim 25$ keV in the range $0.2 \leq \rho \leq 50$. Here we defined the ratio of the electron to photon temperature as $\rho = \theta_{\rm e}/\theta_\gamma$. For a detailed discussion we refer the reader to Sect. 4.5.6.

### 4.5.4 Results for different incoming photon spectra

In this Section, we give the analytic results for the integrals $G_i$ in the definition of the DC emission coefficient (4.57) for different incoming photon spectra, which in astrophysical situations may represent the most interesting cases. Utilizing equation (4.58a) some useful approximations are derived, which, as will be shown below, are valid in a very broad range of temperatures. In Sect. 4.5.6 we give a detailed discussion of the results summarized here.

#### Planck spectrum

The kinetic equation for DC scattering in the form (4.56) shows that for Planckian photons of temperature $\theta_\gamma \equiv \theta_{\rm e}$ DC emission is completely balanced by DC absorption. However, in more

general situations, i.e. $\theta_\gamma \neq \theta_\mathrm{e}$, also for Planckian initial photons DC emission arises. With a Planck spectrum $n_\mathrm{Pl}(x_\mathrm{e}) = 1/\left(e^{\rho\, x_\mathrm{e}} - 1\right)$ of temperature $\theta_\gamma$ the integrals $G_i$ can be evaluated analytically. Since the analytic expressions are rather lengthy and not very illuminating, in the results given below the numerical coefficients were evaluated.

$$G_{0,\mathrm{Pl}} = \frac{4\pi^4}{15\,\rho^5} \approx 25.976\,\rho^{-5} \tag{4.59a}$$

$$G_{1,\mathrm{Pl}} = -G_{0,\mathrm{Pl}}\big[19.739 - 5.5797\,\rho\big]/\rho \tag{4.59b}$$

$$G_{2,\mathrm{Pl}} = G_{0,\mathrm{Pl}}\big[398.91 - 207.26\,\rho + 15.041\,\rho^2\big]/\rho^2 \tag{4.59c}$$

$$G_{3,\mathrm{Pl}} = -G_{0,\mathrm{Pl}}\big[8480.7 - 6390.2\,\rho + 984.49\,\rho^2 - 7.7023\,\rho^3\big]/\rho^3 \tag{4.59d}$$

$$G_{4,\mathrm{Pl}} = G_{0,\mathrm{Pl}}\big[191071 - 190816\,\rho + 47842\,\rho^2 - 2331.7\,\rho^3 + 6.0652\,\rho^4\big]/\rho^4\,. \tag{4.59e}$$

Making use of (4.58a) and (4.58b) one obtains:

$$G_\mathrm{Pl}^\mathrm{inv} = \frac{25.976/\rho^5}{1 + [19.739 - 5.5797\,\rho]\cdot\theta_\gamma}\,. \tag{4.60}$$

To estimate the effects of induced scattering, which are important for the formation of a Planckian photon distribution, we neglect the corresponding terms in the integrals (D.15a) and (D.15b), i.e. drop $\bar{\mathcal{H}}_{6,1}$ and replace $\bar{\mathcal{I}}_i \rightarrow \bar{\mathcal{G}}_{i,1}$. We then find:

$$G_\mathrm{Pl,noind}^\mathrm{inv} = \frac{24.886/\rho^5}{1 + [20.603 - 6\,\rho]\cdot\theta_\gamma}\,. \tag{4.61}$$

This result shows that the differences connected with induced emission are of the order of a few percent. Note that in the above equation we replaced the electron temperature by $\theta_\mathrm{e} \rightarrow \rho\,\theta_\gamma$.

### Bose-Einstein spectra

In contrast to Compton scattering DC scattering still affects the photon field in the case of Bose-Einstein equilibrium, producing photons at low frequencies and redistributing the photons at high frequencies. For Bose-Einstein spectra $n_\mathrm{BE}(x_\mathrm{e}) = 1/(e^{\rho\, x_\mathrm{e}+\mu} - 1)$ with the dimensionless chemical potential $\mu$, it is possible to obtain analytic expressions in the limits $|\mu| \ll 1$ and $\mu \gg 1$. In the case $\mu \gg 1$ one may write $n_\mathrm{BE}(x_\mathrm{e}) \approx e^{-\mu}\cdot e^{-\rho\, x_\mathrm{e}}$. Therefore this case is described by a Wien spectrum with $N_0 = e^{-\mu}$, for which the results will be given in the next paragraph. In the limit $|\mu| \ll 1$ it is possible to use the first order expansion of the photon occupation number in the chemical potential, $n_\mathrm{BE} \approx n_\mathrm{Pl}(x_\mathrm{e}) + \mu\cdot\partial_x n_\mathrm{Pl}$. Here we only give the approximate expressions up to the first order temperature correction.

$$G_{0,\mathrm{BE}} \approx G_{0,\mathrm{Pl}}\,\big[1 - 1.1106\cdot\mu\big] \tag{4.62a}$$

$$G_{1,\mathrm{BE}} \approx G_{1,\mathrm{Pl}}\,\left[1 - \frac{20.119 - 5.5958\,\rho}{19.739 - 5.5797\,\rho}\cdot\mu\right] \tag{4.62b}$$

Equation (4.62a) suggests that $G_{0,\mathrm{BE}}$ may have the functional form $\propto e^{-\beta\mu}$. We found that

$$G_{0,\mathrm{BE}} \approx G_{0,\mathrm{Pl}}\cdot e^{-1.055\,\mu} \tag{4.63}$$

provides a fit to $G_{0,\mathrm{BE}}$, which is better than 1% for $0 \leq \mu \leq 1$.

A numerical calculation of the coefficient $a$ as given by equation (4.58b) has shown that for $0 \leq \mu \leq 1$ the relativistic corrections are roughly independent of the value of the chemical potential. We found that

$$a_\mathrm{BE} \approx \frac{19.739 - 5.5797\,\rho}{\rho}\cdot\left[1 + 0.0293\ln(1 + 3.06\cdot\mu)\right] \tag{4.64}$$

reproduces the coefficient $a$ to better than 0.5% for $0 \leq \mu \leq 1$ and $0.2 < \rho < 1.5$ and that for $\mu > 1$ one may use the formulae obtained for Wien spectra.

### Wien spectrum

For a Wien spectrum $n_{\rm W}(x_{\rm e}) = N_0\,e^{-\rho\,x_{\rm e}}$ of temperature $\theta_\gamma$, making the assumption $N_0 \ll 1$, which implies that induced terms may be neglected, the functions $G_i$ are given as

$$G_{0,\rm W} = \;\; 24\,N_0\,\rho^{-5} \tag{4.65a}$$
$$G_{1,\rm W} = -G_{0,\rm W}[21 - 6\,\rho]/\rho \tag{4.65b}$$
$$G_{2,\rm W} = \;\; G_{0,\rm W}[428.4 - 220.5\,\rho + 15\,\rho^2]/\rho^2 \tag{4.65c}$$
$$G_{3,\rm W} = -G_{0,\rm W}[9141.6 - 6854.4\,\rho + 1047.375\,\rho^2 - 11.25\,\rho^3]/\rho^3 \tag{4.65d}$$
$$G_{4,\rm W} = \;\; G_{0,\rm W}[206380.8 - 205686\,\rho + 51408\,\rho^2 - 2480.625\,\rho^3 - 11.25\,\rho^4]/\rho^4\,. \tag{4.65e}$$

Making use of (4.58a) and (4.58b) one finds:

$$G_{\rm W}^{\rm inv} = \frac{24\,N_0/\rho^5}{1 + [21 - 6\,\rho]\cdot\theta_\gamma}\,. \tag{4.66}$$

Note that here we again replaced the electron temperature by $\theta_{\rm e} \rightarrow \rho\,\theta_\gamma$.

### 4.5.5 Beyond the soft photon limit

Strictly speaking equation (4.56) is only valid for the very low frequency part of the DC emission spectrum. We have already seen that in general the effective DC Gaunt factor is a function of the electron temperature, $\theta_{\rm e}$, the exact shape of the spectrum of the initial photons, $n(\nu)$, and the frequency of the emitted photon, $\nu_2$. If we are not interested in the redistribution of photons at high frequencies it is possible to neglect $g_{\rm dc,c}$ in the definition of $g_{\rm dc}$ as given by equation (4.52) and replace $g_{\rm dc,a}$ by

$$\tilde{g}_{\rm dc,a}(x_2) = \int\limits_{2x_2}^{\infty} x_0^4\,n(x_0)\,[1 + n(x_0 - x_2)]\left[\frac{x_2}{x_0}\,H(x_2/x_0)\right]\,{\rm d}x_0\,, \tag{4.67}$$

Here it was assumed that all the photon above $\nu_2/\nu_0 = 1/2$ can be considered as *scattered* photons and therefore are not taken into account in the integral over the emission spectrum (see lower boundary). The effective Gaunt factor in a similar form (with $H = H_{\rm G}$, where $H_{\rm G}$ is the Gould factor (4.27)) was also used by Bond [20] and Burigana, Danese & de Zotti [25]. As Burigana, Danese & de Zotti [25] claim, for Bose-Einstein spectra a good approximation of $\tilde{g}_{\rm dc,a}$ can be given as $\tilde{g}_{\rm dc,a}(x_2, \theta_\gamma) \approx \rho^5 G_0\,e^{-x_2/2}$. Therefore one simple way to extend the applicability of the results given here in the soft photon limit is to use

$$\tilde{g}_{\rm dc,a}(x_2, \theta_\gamma, \theta_{\rm e}) \approx \rho^5 G^{\rm inv}(\theta_\gamma, \theta_{\rm e}) \times e^{-x_2/2}\,, \tag{4.68}$$

where $G^{\rm inv}$ is defined by (4.58a). Note that the factor of $\rho^5$ arises due to the different definitions of integration variables $x \leftrightarrow x_{\rm e}$. Comparison with full numerical results has shown that the approximation (4.68) works very well for photon distributions close to equilibrium. We now concentrate on the discussion of the low frequency part of the DC emission, where most of the photons are produced.

### 4.5.6 Discussion of the results for Planck, Bose-Einstein and Wien spectra

For Planckian photons DC scattering only changes the number of photons if $\theta_\gamma \neq \theta_{\rm e}$. Despite this fact, for order of magnitude estimates even the case $\rho \equiv 1$ is still quite useful, since in situations close to full thermodynamic equilibrium, i.e. for $|\mu| \ll 1$, deviations of the DC emissivity from the case of Planckian photons are in second order of $\mu$.

Fixing the temperature of the electrons one can see from equation (4.59a) that the non-relativistic DC emission coefficient $G_0$ increases for $\rho < 1$ and decreases for $\rho > 1$ with the fifth

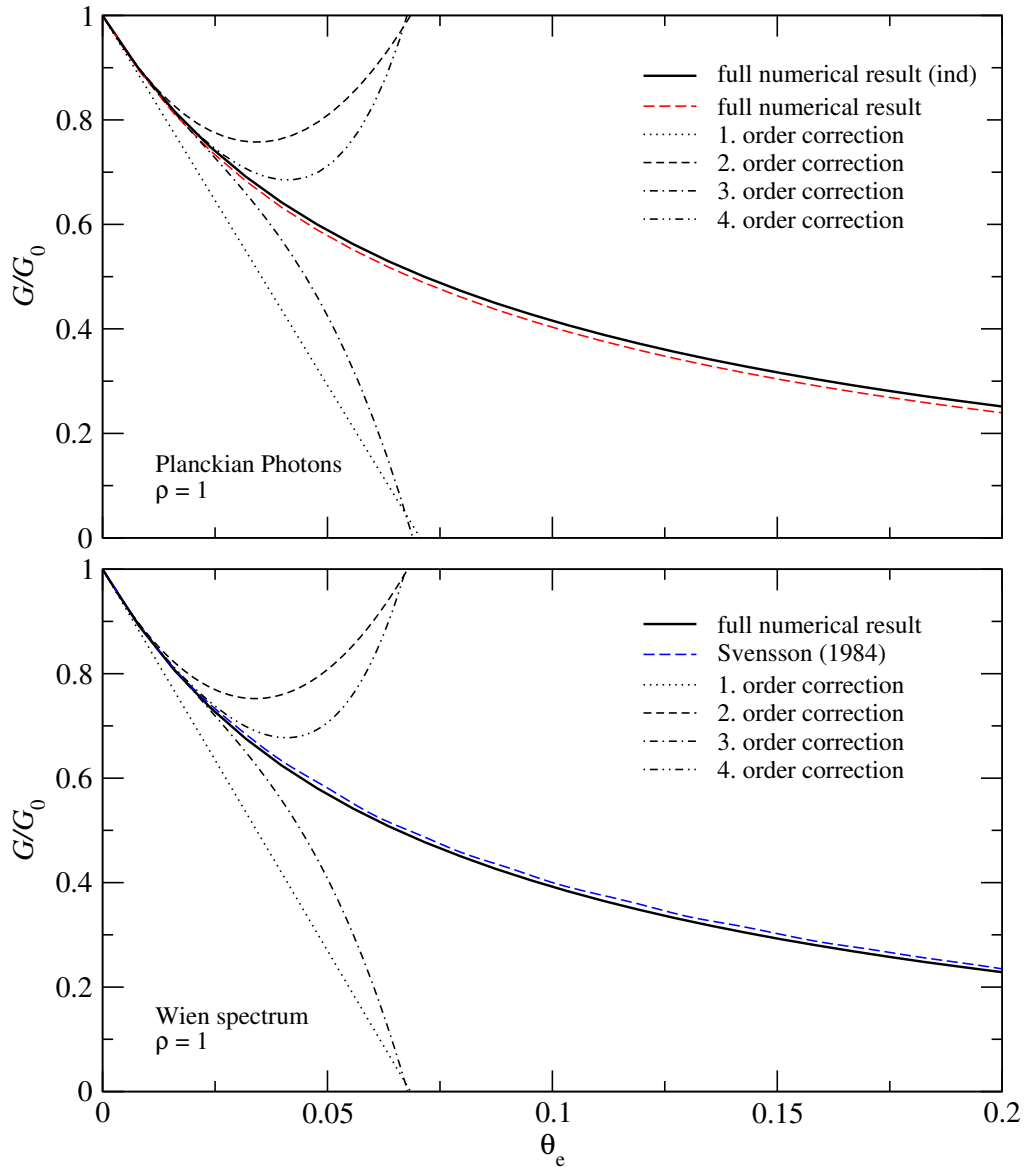


**Figure 4.19:** Production rate of soft photons by double Compton scattering relative to the non-relativistic result $G_0$ as a function of $\theta_e$: **Top**: Full numerical results for Planckian photons, with allowance made for induced scattering, in comparison with the *direct* expansion as given by equations (4.59) including temperature corrections up to different orders, as indicated respectively. Also the numerical result neglecting induced effects is shown (red/long-dashed). — **Bottom**: Same as a) but for a Wien spectrum. Only spontaneous scattering is taken into account ($N_0 \ll 1$). The analytic approximation is given by equations (4.65). In addition, the approximation formula (4.69) as given by Svensson [132] is shown (blue/long-dashed). The *inverse* formula (4.66) shows a similarly good performance but for the sake of clarity is not presented here. For further discussion about the performance of the *inverse* formula for Planckian photons see Fig. 4.20 and Sect. 4.5.6.

power of $\rho$. Therefore even a 10% difference in the electron and photon temperature results in a factor of $\sim 1.6$ increase or decrease of the DC photon production rate. Below we now first discuss the case $\rho = 1$ and then the more general case $\rho \neq 1$ in detail. For this we compare the ratio, $G/G_0$, of the DC emission coefficient $G$ in the soft photon limit including all temperature corrections and the non-relativistic coefficient $G_0$ with the full numerical results. Since Bose-Einstein spectra lie between a Planck spectrum ($\mu = 0$) and Wien spectra, with small number density $N_0 \ll 1$, and the differences between the results for Planck and Wien spectra are of the order of a few percent (of course after rescaling $G$ by $G_0$, see below), here we do not discuss Bose-Einstein spectra in more detail.

### Case $\rho = 1$

In Fig. 4.19 the results for incoming Planck and Wien spectra with temperature $\theta_\gamma = \theta_\mathrm{e}$ are shown. With increasing temperature the ratio, $G/G_0$, of the relativistic and non-relativistic DC photon production rate decreases strongly, implying that the main contribution to $G_0$ comes from photons with energies $\omega_0 \geq \frac{10}{7}\,\theta_\mathrm{e}$ (see equation (4.46a)). This suggests that for higher temperatures the efficiency of DC emission is significantly overestimated by the non-relativistic result as obtained by Lightman [80]. For example, even for rather low temperatures $T_\mathrm{e} \sim 4\,\mathrm{keV}$ there is a 10% negative correction due to relativistic effects.

In the considered case the direct formulae (4.57) with (4.59) for a Planckian and (4.65) for a Wien spectrum are valid up to $\theta_\mathrm{e} \sim 0.05$, within reasonable accuracy. As will be discussed below, the inverse formula (4.58a) and the corresponding coefficients $a$ for $\rho \sim 1$ provides an approximation which is better than 5 % up to $\theta_\mathrm{e} \sim 0.2$. This case is most interesting for the thermalization of spectral distortions in the early universe.

In general our numerical results have shown, that for an incoming Planck spectrum the contributions due to induced scattering are of the order of a few percent. Only in extreme cases ($\rho \ll 1$) the contribution of induced terms was significant. In comparison to a Wien spectrum the difference in general was also of the order of a few percent. Therefore we will not discuss induced effects in more detail below. Comparing the result for an incoming Wien spectrum with the approximation given by Svensson [132],

$$G_\mathrm{S}(\theta_\mathrm{e}) \approx \frac{G_{0,\mathrm{W}}}{1 + 13.91\,\theta_\mathrm{e} + 11.05\,\theta_\mathrm{e}^2 + 19.92\,\theta_\mathrm{e}^3} \tag{4.69}$$

shows that in the considered case, i.e. $\rho = 1$, it provides a very good fit to the numerical result. The *inverse* formula (4.66) shows a similarly good performance. In the more general case, i.e. $\rho \neq 1$, the approximation given by Svensson [132] can not reproduce the numerical results, since the strong dependence of the relativistic corrections on the ratio of the electron to the photon temperature was not taken into account.

### Case $\rho \neq 1$

Figure 4.20 illustrates the dependence of the DC emission on the ratio of the electron to the photon temperature $\rho = \theta_\mathrm{e}/\theta_\gamma$ for a incoming Planck spectrum. Since the general behavior of the numerical results for Bose-Einstein and Wien spectra are the same as for a Planck spectrum, it is sufficient to consider this case only. We expect the main conclusions to hold also for Bose-Einstein and Wien spectra.

In general the characteristics of the ratio $G/G_0$ can be summarized as follows: If we define the critical ratio $\rho_\mathrm{c} = 3/(1 - \frac{3}{2\pi^2}) \sim 3.538$ of electron to photon temperatures, for which the first order correction to $G$ vanishes (cf. Eq. (4.59b)), then two regimes can be distinguished: (i) for $\rho < \rho_\mathrm{c}$ the ratio $G/G_0$ is monotonically dropping with increasing electron temperature, whereas (ii) for $\rho \geq \rho_\mathrm{c}$ it is first increasing and then turning into a decrease at some high temperature. This suggests that $\rho_\mathrm{c}$ separates the regions where Doppler boosting is compensating the suppression of DC emission due to higher photon energy. Estimating the mean photon

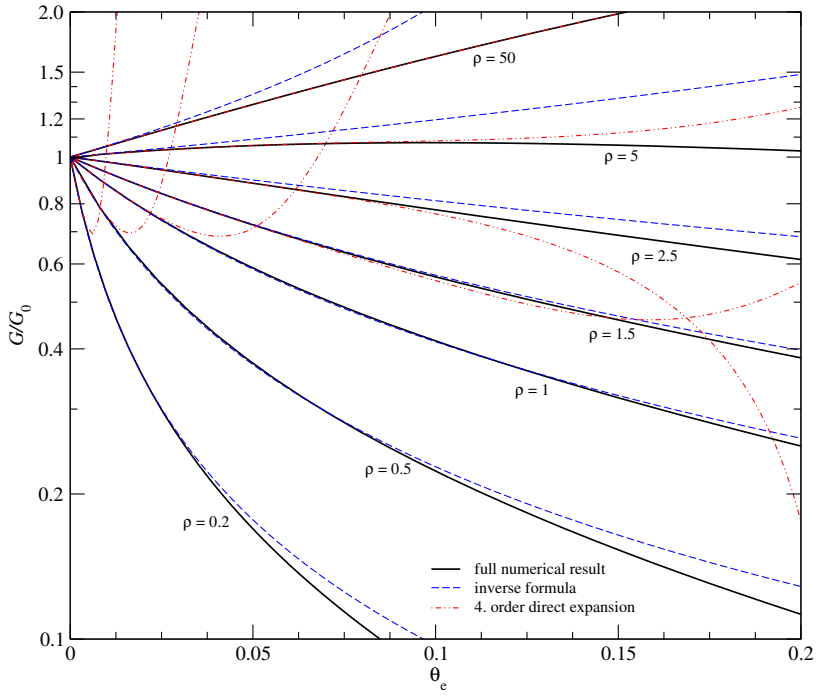


**Figure 4.20:** Production rate of soft photons by double Compton scattering relative to the non-relativistic result $G_0$ for Planckian photons as function of the electron temperature and different values of $\rho = \theta_e/\theta_\gamma$. Presented are the full numerical result, the 4. order direct formula as given by equation (4.59) and the inverse formula (Eq. (4.60)).

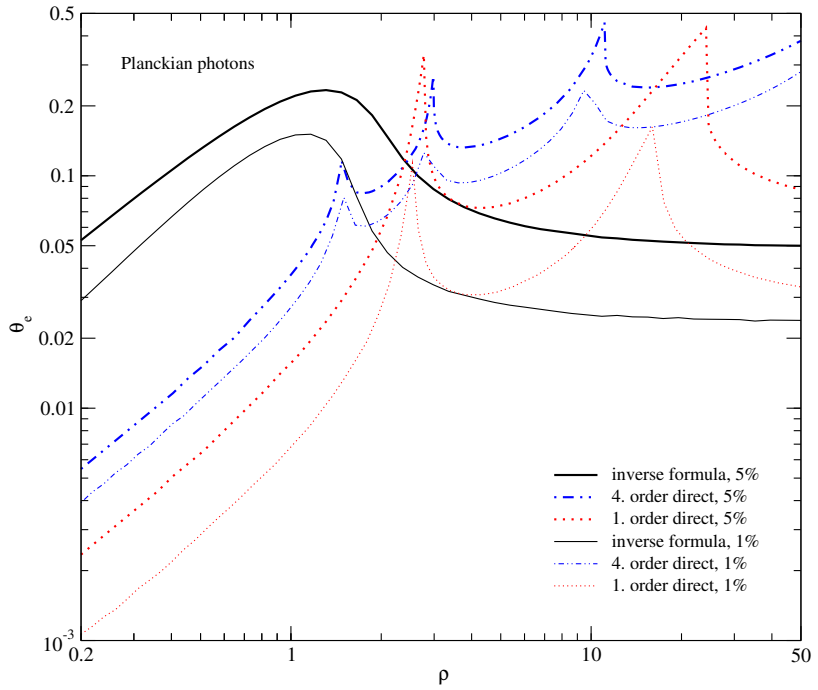


**Figure 4.21:** Range of applicability for a Planck spectrum with different $\rho = \theta_e/\theta_\gamma$: Shown is electron temperature $\theta_e$ above which the relative difference between the analytic predictions and the numerical results becomes bigger than $\epsilon$ percent. The numerical results were compared with the *inverse* formula, equation (4.60), and the *direct* expansion (4.59) up to first order and fourth order in temperature, as indicated respectively.

energy weighted by $G_0$, i.e. $\langle\omega_0\rangle = \int x^5 n[1+n]\,\mathrm{d}x / \int x^4 n[1+n]\,\mathrm{d}x \approx 4.8\,\theta_\gamma$, and using the approximation $\omega_0 = \frac{10}{7}\,\theta_\mathrm{e}$ for the condition $G_\mathrm{m}(\omega_0, \theta_\mathrm{e}) = 1$ (see Eq. (4.46a)) yields $\rho_\mathrm{c} \approx 3.35$, which further supports this conclusion.

In general one finds (see Figs. 4.20 and 4.21) that for $\rho < \rho_\mathrm{c}$ the *inverse* approximation (4.58a) has a better performance than the *direct* expansion formula (4.57) and vice versa for the case $\rho \geq \rho_\mathrm{c}$. It is worth mentioning that the direct formula performs very well for $\rho \geq \rho_\mathrm{c}$ even in lower orders of the temperature corrections. Combining these two approximations an accuracy of better than $\sim 5\%$ can be achieved in a very broad range of temperatures. If the photons and electrons have similar temperatures then the inverse formula (4.58a) is valid even up to $k\,T \sim 100\,\mathrm{keV}$.

One obvious advantage of the inverse formula (4.58a) over the direct expansion (4.57), is that only the first order corrections are needed to obtain an excellent approximation up to high temperatures. Especially for numerical applications this is important, since higher order derivatives of the spectrum may introduce significant difficulties. We have also compared the full numerical results with the approximation as given by (4.52), which involves a 2-dimensional integral over the spectrum and the electron distribution. It turned out that this approximation performed similarly well as the inverse formula, but without any improvements. This is mainly due to the fact, that the main contributions to the DC emissivity arise from photons of energy $\langle\omega_0\rangle \sim 4 - 5 \times \theta_\gamma$. Therefore in the case $\rho = 1$ at temperatures $\theta_\mathrm{e} \sim 0.2$ it follows that $\langle\omega_0\rangle \sim 1$, such that the approximations given for monochromatic photon start to break down.

## 4.6 Summary and outlook

In this Chapter we have studied the full kinetic equation for the time evolution of the photon phase space density under DC scattering. We included both the *creation* of new photons at low frequencies and the *redistribution* of photons at high frequencies. We have shown that the DC emissivity strongly decreases with higher mean energy of the initial photons leading to a suppression of the total number of newly created photons as compared to the non-relativistic limit. On the other hand boosting leads to an enhancement of the DC emissivity the higher the electron temperature becomes.

Furthermore, an expression for the *effective DC Gaunt factor* has been derived and shortly discussed in comparison with the full numerical results (Sect. 4.5.1). We have argued that at least in situations close to thermodynamic equilibrium the evolution of the high frequency photons is not significantly affected by DC scattering, but a more detailed study should be undertaken to include cases far from equilibrium.

Simple and accurate analytic expressions for the low frequency DC scattering emission coefficient of monochromatic initial photons (Sect. 4.4; in the most general situation see Eq. (4.45)) and in the case of Planck, Bose-Einstein and Wien spectra were given (see Sect. 4.5.4). We discussed in detail the DC emission for monochromatic initial photons and in the soft photon limit for an incoming Planck spectrum, but expect that our main conclusions also hold for Bose-Einstein, Wien and more general photon distributions. For more general incoming photon distributions two analytic approximations for the low frequency DC emission coefficient, equation (4.57) as a *direct* expansion up to fourth order in temperature and (4.58a) as a *inverse* approximation, were deduced, which in combination should describe the full numerical results to better than 5 % in a very broad range of temperatures and involve only 1-dimensional integrals over the photon distribution and its derivatives (see Fig. 4.21 and Sec. 4.5.6 for discussion).

If the photons and the electrons have similar temperatures, which is the case in most physical situations close to equilibrium, especially in the context of the thermalization of CMB spectral distortions, then the inverse formula (4.58a) may be applicable up to $k\,T \sim 100\,\mathrm{keV}$ with an accuracy of better than a few percent. Since only first order corrections are necessary for this inverse formula (4.58a), it it generally more suitable for numerical applications. For photon distributions close to equilibrium our discussion has shown that at high temperatures

the DC emission for $T_\mathrm{e} \leq 3.538\,T_\gamma$ is less efficient than in the non-relativistic limit. Negative corrections can be as big as 90 % for electron temperatures around $k\,T \sim 100\,\mathrm{keV}$. On the other hand in the case $T_\mathrm{e} \geq 3.538\,T_\gamma$ DC emission turns out to be more efficient by a factor of a few up to very high temperatures.

In the following Chapter we will discuss some attempts to apply the approximations derived here in the context of the thermalization of CMB spectral distortions. One can expect that at redshifts $z \gtrsim 10^6 - 10^7$ relativistic corrections to DC emission become important. As we have seen, at higher temperatures DC emission is less efficient. This may slow down the thermalization of chemical potential distortion at high redshift and potentially allow to place tighter constraints on the amount of released energy, which is still compatible with the Cobe/Firas limits.

# Chapter 5

# Thermalization of CMB spectral distortions

In this Chapter we want to discuss the effects of relativistic corrections to the physical processes at work in the thermalization of CMB spectral distortions after energy injection. As a first step toward the full solution of this problem we have derived accurate analytic approximations for DC emission in a hot thermal plasma (see. Chapt. 4). He we want to provide two more steps: (i) we reexamine the *formulation* of the full problem and attempt to point out relevant changes with respect to the non-relativistic calculation and (ii) we discuss the thermalization of *small* spectral distortions at high redshifts with inclusion of all the necessary corrections.

## 5.1 General formulation of the thermalization problem

A solution of the full thermalization problem for the isotropic Universe in general can only be done numerically, especially for large energy injections at high redshifts. Currently we are developing a code for this purpose but a general discussion and solution is still on the way. Nevertheless, we obtained some additional insights, which go beyond the standard calculation.

At redshifts $z \gtrsim 10^8 - 10^9$ electrons and positrons are very abundant and electron-positron, electron-electron and positron-positron Bremsstrahlung will be many orders of magnitude more efficient in producing soft photons than double Compton scattering (DC) or normal electron-ion Bremsstrahlung (BS). Hence thermalization of CMB spectral distortions will be extremely rapid. Therefore we shall restrict ourselves to redshifts below $z \lesssim 10^8$. Here electrons and positrons have fallen out of equilibrium with the photons and only insignificant amounts of positrons are left from the era of electron-positron annihilation. During the subsequent evolution of the Universe the main interactions between the photons and matter are governed by Compton scattering (CS), double Compton scattering and Bremsstrahlung. Furthermore due to the expansion of the Universe the photons suffer from redshifting.

The photons do not interact directly with the baryonic matter (hydrogen, helium and the nuclei of other light elements), but only mediated by electrons, which themselves are strongly coupled to the baryons via Coulomb scattering. The time scale, on which the electrons and baryons adjust their energy distributions is much shorter than any other time scale of importance here (see Appendix E.3). Therefore it can be assumed that the electrons and baryons always follow a relativistic Maxwell Boltzmann distribution with temperature $T_{\rm e}$. In this case the problem can be formulated with the Boltzmann equations for the evolution of the photon phase space distribution function and a coupled equation describing the time evolution of the electron (and baryon) temperature. Below we shall now write down the photon Boltzmann equation in the expanding Universe and the evolution equation for the electron temperature with inclusion of heating and relevant relativistic corrections.

### 5.1.1 The Boltzmann equation in the expanding Universe

The time evolution of the phase space distribution function $f(\boldsymbol{x}, \boldsymbol{p})$ of a particle is described by the Boltzmann equation

$$\hat{\mathbf{L}}[f] = \hat{\mathbf{C}}[f] \tag{5.1}$$

where $\hat{\mathbf{C}}$ is the collision operator and $\hat{\mathbf{L}}$ is the Liouville operator. In an isotropic, homogeneous Friedmann-Robertson-Walker (FRW) Universe $f(\boldsymbol{x}, \boldsymbol{p}) \equiv f(t, E)$, where $E$ and $p = |\boldsymbol{p}|$ are the relativistic energy and momentum of the particle, respectively. In this case the Liouville operator is given as

$$\hat{\mathbf{L}} = E\frac{\partial}{\partial t} - \frac{\dot{a}}{a}\, p^2 \frac{\partial}{\partial E}\,, \tag{5.2}$$

where $\dot{a}/a =: H$ is the expansion rate of the Universe. With $\partial_E = E/p \cdot \partial_p$ the Boltzmann Equation can be cast into the form

$$\frac{\partial f}{\partial t} - H\, p\, \frac{\partial f}{\partial p} = \frac{\hat{\mathbf{C}}[f]}{E} = I_{\rm coll}\,. \tag{5.3}$$

The right hand side of this equation shall henceforth be called the Boltzmann *collision term*. In general the collision term is a sum of all the terms describing the different interactions of the particles. To describe the evolution of a system with different gas species, in general one has to solve a coupled set of Boltzmann equations for each considered species. Without any simplifying assumptions this is a highly complex problem. For more details about the formulation of the relativistic Boltzmann equation see Cercignani & Kremer [29].

### 5.1.2 Evolution of the number and energy density

If the phase space distribution $f_{\rm i}$ of a particle of species i is given for every time $t$, instead of following the evolution with the full Boltzmann equation (5.3) one can use integrated quantities, like the number and energy density. Therefore, with the definition (A.1) for the number density, integration of equation (5.3) over $\mathrm{d}^3p$ making use of integration by parts yields

$$\frac{\mathrm{d}N_{\rm i}}{\mathrm{d}t} + 3H\, N_{\rm i} = \frac{g_{\rm i}}{(2\pi\hbar)^3}\int 4\pi\, p^2 I_{\rm coll,i}\,\mathrm{d}p\,. \tag{5.4}$$

The left hand side of this equation can be rewritten as

$$\frac{\mathrm{d}N_{\rm i}}{\mathrm{d}t} + 3H\, N_{\rm i} = \frac{1}{a^3}\frac{\mathrm{d}a^3 N_{\rm i}}{\mathrm{d}t}\,. \tag{5.5}$$

If no particles are produced or destroyed the integral over the collision term $I_{\rm coll,i}$ vanishes. Therefore equations (5.4) and (5.5) then simply reflects the conservation of the number of particles in the Universe and their dilution due to the expansion.

In a similar way, using the definition (A.4a) for the energy density with equation (5.3), for relativistic particles ($E = p\,c \gg m_{\rm i}c^2$) one can find

$$\left.\frac{1}{a^4}\frac{\mathrm{d}a^4\rho_{\rm i}}{\mathrm{d}t}\right|_{\rm rel} = \frac{g_{\rm i}}{(2\pi\hbar)^3}\int 4\pi\, E\, p^2 I_{\rm coll,i}\,\mathrm{d}p\,. \tag{5.6}$$

Here the fact that the energy of the particle is redshifted is reflected in the additional factor of $1/a$. Thus, if there are no collisions, the particle phase space density undergo adiabatic expansion and redshifting of the energy ($\rho_{\rm i} \propto a^{-4}$).

For non-relativistic massive particles ($m_{\rm i}c \gg p$) it follows:

$$\left.\frac{1}{a^3}\frac{\mathrm{d}a^3\rho_{\rm i}}{\mathrm{d}t}\right|_{\rm nr} = \frac{g_{\rm i}}{(2\pi\hbar)^3}\int 4\pi\, E\, p^2 I_{\rm coll,i}\,\mathrm{d}p\,, \tag{5.7}$$

where here $\rho_{\rm i} = m_{\rm i}\, c^2\, N_{\rm i}$. If there are no collisions, non-relativistic particle species do not suffer from redshifting of their energy but only from the dilution due to the expansion ($\rho_{\rm i} \propto a^{-3}$).

## 5.2 Evolution of the photons in the expanding Universe

In the early Universe the photons undergo many interactions with the matter (mainly with the electrons) in the Universe. As mentioned earlier, the most important processes are Compton scattering, double Compton scattering, Bremsstrahlung and the adiabatic expansion of the Universe. Among these processes for most of the times Compton scattering is the fastest. Therefore it is convenient to express all the involved time scales in units of the Compton scattering time, $t_{\rm C} = 1/\sigma_{\rm T}\, N_{\rm e}\, c$ (see Appendix E.3).

The Boltzmann equation for the evolution of the photon phase space density in the expanding Universe then can be written as:

$$\frac{\partial n_\gamma}{\partial \tau} - H\, t_{\rm C}\, p\, \frac{\partial n_\gamma}{\partial p} = \left.\frac{{\rm d}n_\gamma}{{\rm d}\tau}\right|_{\rm C} + \left.\frac{{\rm d}n_\gamma}{{\rm d}\tau}\right|_{\rm DC} + \left.\frac{{\rm d}n_\gamma}{{\rm d}\tau}\right|_{\rm BS}, \tag{5.8}$$

where we introduced the optical depth $d\tau = dt/t_{\rm C}$ to Compton scattering as the dimensionless time variable. Note that here and in the following $n_\gamma$ is the phase space density of the photons and not their number density $N_\gamma$.

In equation (5.8) the seconds term on the left hand side is due to the expansion of the Universe and the right hand side terms correspond to the physical processes listed above. Below we now first give the collision terms with lowest order relativistic corrections and then discuss the expansion term.

### 5.2.1 Compton scattering

The contribution of Compton scattering to the right hand side of the photon Boltzmann equation (5.8) in the non-relativistic limit can be treated by the Kompaneets equation [75]:

$$\left.\frac{{\rm d}n_\gamma}{{\rm d}\tau}\right|_{\rm C,nr} = \frac{\theta_{\rm e}}{x^2}\,\frac{\partial}{\partial x}\, x^4 \left[\frac{\partial n_\gamma}{\partial x} + \phi\, n_\gamma (n_\gamma + 1)\right] \quad . \tag{5.9}$$

Here we used the abbreviations $x = h\nu/k\,T_\gamma$ and $\phi = T_\gamma/T_{\rm e}$. The Kompaneets equation was found by lowest order Fokker-Planck expansion of the collision term for Compton scattering. Maintaining the next order terms in electron temperature one can derive first order relativistic correction to the Kompaneets equation [30, 67, 114]:

$$\left.\frac{{\rm d}n_\gamma}{{\rm d}\tau}\right|_{\rm C,rel} = \frac{\theta_{\rm e}}{x^2}\frac{\partial}{\partial x}\, x^4 \left[F + \theta_{\rm e}\cdot\left\{\frac{5}{2}\,F + \frac{21}{5}\,x\,\frac{\partial F}{\partial x} + \frac{7}{10}\,x^2\left[\phi\, F_-\,(\phi - 6\,F_-) + \frac{\partial^2 F_+}{\partial x^2}\right]\right\}\right] \tag{5.10}$$

where we have defined $F(x) = \partial n_\gamma/\partial x + \phi\, n_\gamma(n_\gamma + 1)$ and $F_\pm(x) = F \pm \phi\, n_\gamma(n_\gamma + 1)$.

One can easily verify, that the number of photons is conserved under Compton scattering in both the non-relativistic and relativistic case by multiplying (5.10) with $x^2$ and integrating over frequency using integration by parts and the fact that the photon distribution vanishes sufficiently fast for $x \to 0$ and $x \to \infty$. Furthermore one can also easily check that for photons, which follow a Bose-Einstein distribution, $n_{\rm BE}(x) = 1/[e^{x+\mu} - 1]$, with constant chemical potential $\mu$, equation (5.10) vanishes identically.

In equation (5.10) only first order corrections in the electron temperature have been included. In this order it should be applicable up to $\theta_{\rm e} \sim 0.01$ for $x \lesssim 5$. Since the main emission due to DC scattering and Bremsstrahlung is coming from regions $x \lesssim 10^{-3} - 10^{-2}$, we expect that (5.10) represents the Compton scattering corrections at low frequencies up to even higher temperatures ($\theta_{\rm e} \sim 10^{-1}$ for $x \lesssim 1$), but it is not obvious how to treat the high frequency part.

### 5.2.2 Double Compton scattering and Bremsstrahlung

The contribution of double Compton scattering and Bremsstrahlung to the right hand side of the photon Boltzmann equation (5.8) can be written in the form [108, 80]:

$$\left.\frac{\mathrm{d}n_\gamma}{\mathrm{d}\tau}\right|_{\mathrm{DC+BS}} = \frac{e^{-x}}{x^3}\cdot\left[1-n_\gamma\,(e^{\phi\,x}-1)\right]\times K(x,\theta_\gamma,\theta_\mathrm{e}) \tag{5.11}$$

where the emission coefficient $K$ is given by the sum of the contribution due to double Compton scattering and Bremsstrahlung, $K = K_\mathrm{DC} + K_\mathrm{BS}$. We now discuss each of them separately.

#### Double Compton scattering

Due to the large entropy of the Universe at high redshifts ($z \gtrsim$ few $\times\, 10^5$) DC emission dominates over BS by many orders of magnitude. The DC scattering emission coefficient can be given as

$$K_\mathrm{DC}(x,\theta_\mathrm{e}) \;=\; \frac{4\alpha}{3\pi}\,\theta_\gamma^2\,e^x\times g_\mathrm{dc}(x,\theta_\gamma,\theta_\mathrm{e})\,, \tag{5.12}$$

where $\alpha$ is the fine structure constant and $g_\mathrm{dc}(x,\theta_\gamma,\theta_\mathrm{e})$ is the effective DC Gaunt factor.

In Chapter 4 we have discussed the contribution of DC scattering in a hot isotropic thermal plasma to the kinetic equation in great detail. There we derived different approximations for the effective DC Gaunt factor $g_\mathrm{dc}(x,\theta_\gamma,\theta_\mathrm{e})$. In the most general case, i.e. when DC emission at low frequencies and the redistribution of photons at high frequencies are taken into account, we obtained the approximation (4.52). Until now we only checked the applicability of this result for cases when the temperature difference between the photons and electrons is small and found excellent agreement. A more general exploration of parameters is still one the way, but as we have argued in Sect. 4.5.1 at least in cases fairly close to equilibrium the DC energy redistribution of photons at high frequencies is many orders of magnitude less important than the first order relativistic corrections to Compton scattering as included in equation (5.10). Therefore in a more conservative approach we may neglect terms arising due to the redistribution of photon by DC scattering and only include effects due to DC emission. This then leads to the approximation for the DC Gaunt factor as given by equation (4.67).

#### Bremsstrahlung

At low redshifts ($z \lesssim$ few $\times\, 10^5$) Bremsstrahlung starts to become the main source of soft photons. One can define the Bremsstrahlung emission coefficient as

$$K_\mathrm{BS}(x,\theta_\mathrm{e}) \;=\; \frac{\alpha\,\lambda_\mathrm{e}^3}{2\pi\,\sqrt{6\pi}}\,\frac{\theta_\mathrm{e}^{-7/2}\,e^{x[1-\phi]}}{\phi^3}\cdot\sum_\mathrm{i} Z_\mathrm{i}^2\,N_\mathrm{i}\cdot g_\mathrm{ff}(Z_\mathrm{i},x,\theta_\mathrm{e})\,. \tag{5.13}$$

Here $\lambda_\mathrm{e} = h/m_\mathrm{e}\,c$ is the Compton wavelength of the electron, $Z_\mathrm{i}$, $N_\mathrm{i}$ and $g_\mathrm{ff}(Z_\mathrm{i},x,\theta_\mathrm{e})$ are the charge, the number density and the BS Gaunt factor for a nucleus of species i, respectively. Various simple analytical approximations exists [108], but nowadays more accurate fitting formulae may be found in Nozawa et al. [90] and Itoh et al. [68].

In the early Universe hydrogen and helium contribute most to the BS Gaunt factor. In the non-relativistic case the hydrogen and helium Gaunt factors are approximately equal, $g_\mathrm{H,ff} \approx g_\mathrm{He,ff}$, down to a few percent. Therefore at low redshifts the sum in (5.13) may be simplified to $\sum \approx g_\mathrm{H,ff}\,N_\mathrm{b}$, where $N_\mathrm{b}$ is the baryon number density as given by (E.1a). However, for percent accuracies one should take the full expressions for $g_\mathrm{H,ff}$ and $g_\mathrm{He,ff}$ into account.

### 5.2.3 Expansion term

The left hand side of the photon Boltzmann equation (5.8) may be simplified using different variables. Transforming from $p \equiv h\nu/c$ to $\xi(t,\nu) = h\nu/kT$ starting from (5.3) one finds

$$\begin{aligned}\left.\frac{\partial n_\gamma}{\partial t}\right|_p - H\,p\,\left.\frac{\partial n_\gamma}{\partial p}\right|_t &= \left.\frac{\partial n_\gamma}{\partial t}\right|_\xi + \left.\frac{\partial n_\gamma}{\partial \xi}\right|_t \cdot \left[\left.\frac{\partial \xi}{\partial t}\right|_\nu - H\,\xi\right] \\ &= \left.\frac{\partial n_\gamma}{\partial t}\right|_\xi - \xi\,\left.\frac{\partial n_\gamma}{\partial \xi}\right|_t \cdot \left[\frac{\dot{T}}{T} + H\right]. \end{aligned} \tag{5.14}$$

Until now we have not specified the choice for $T_\gamma(t)$, which can be regarded as a *free* parameter to describe the energy density of the photon field (see Appendix B.2). The two natural possibilities are the electron temperature $T_\mathrm{e}$ and the effective temperature $T_z = T_0\,(1+z)$ of an undisturbed blackbody with energy density as given today for the CMB.

The effects of the expansion on the evolution of CMB spectral distortions become only important if the temperature of the electrons and the photons differ significantly. Nevertheless, here we are interested in percent accuracy and therefore should include this term. On this level it is also important to include the change of the expansion rate during heating, especially when one is considering the evolution of initially large distortions.

## 5.3 Evolution of the electrons and baryons in the Universe

Interactions between the electrons and the baryons in the Universe are extremely rapid. Thus, it can be safely assumed that the phase space densities for these particles at any time of interest to us are very close to relativistic Maxwell-Boltzmann distributions (see Appendix A for definitions) with the same temperature $T_\mathrm{i} \equiv T_\mathrm{e}$.

Unlike the baryons the electrons in addition are strongly coupled to the photons via Compton scattering. Below we shall assume that only insignificant amounts of electrons or baryons are created in the process leading to the injection of energy. Then the number densities for e, H, He and other light elements are given by $N_\mathrm{i} \approx N_{\mathrm{i},0}(1+z)^3$, where $N_{\mathrm{i},0}$ is the present day value. Therefore instead of following the evolution of the phase space distribution it is sufficient to consider only the evolution of the electron temperature. Below we now derive the equation governing this evolution including relativistic corrections.

### 5.3.1 Evolution of the electron temperature

In order to describe the evolution of the electron temperature we consider the first law of thermodynamics for each species i ($\gamma$, e, H, He and other light elements):

$$\mathrm{d}Q_\mathrm{i} = \mathrm{d}(a^3\rho_\mathrm{i}) + P_\mathrm{i}\,\mathrm{d}a^3\,, \tag{5.15}$$

where the external source of heating is represented by $\mathrm{d}Q_\mathrm{i}$ and $\rho_\mathrm{i}$ and $P_\mathrm{i}$ are the energy density and pressure of the particle i, respectively. Then the total, comoving heating rate is

$$\frac{1}{a^3}\,\frac{\mathrm{d}Q}{\mathrm{d}t} = \sum_i \left\{\frac{1}{a^3}\,\frac{\mathrm{d}a^3\rho_\mathrm{i}}{\mathrm{d}t} + \frac{1}{a^3}\,\frac{\mathrm{d}a^3}{\mathrm{d}t}\,P_\mathrm{i}\right\}. \tag{5.16}$$

For photons the pressure is given by $P_\gamma = \rho_\gamma/3$ (see Appendix B). Thus, with the identity $a^{-3}\,\mathrm{d}a^3/\,\mathrm{d}t = 3H$ the contribution of the photons to (5.16) reduces to

$$\frac{1}{a^3}\,\frac{\mathrm{d}Q_\gamma}{\mathrm{d}t} = \frac{1}{a^4}\frac{\mathrm{d}a^4\rho_\gamma}{\mathrm{d}t}\,. \tag{5.17}$$

This is directly related to the collision integral of the Boltzmann equation describing the photon phase space density evolution (cf. Eq. (5.6)). We will discuss this term in Section 5.3.2.

To find the contributions due to e, H, He, etc. for each of them we substitute $\rho_\mathrm{i}$ and $P_\mathrm{i}$ from equations (A.5a) and (A.5b) into (5.16). This then leads to

$$\frac{1}{a^3}\frac{\mathrm{d}Q}{\mathrm{d}t} = \frac{1}{a^4}\frac{\mathrm{d}a^4\rho_\gamma}{\mathrm{d}t} + \sum_{i\neq\gamma} m_\mathrm{i}\, c^2 \left\{ F(\theta_\mathrm{i})\,\frac{1}{a^3}\frac{\mathrm{d}a^3 N_\mathrm{i}}{\mathrm{d}t} + N_\mathrm{i}\,\frac{\mathrm{d}F(\theta_\mathrm{i})}{\mathrm{d}t} + 3H\,N_\mathrm{i}\,\theta_\mathrm{i} \right\}, \tag{5.18}$$

where $\theta_\mathrm{i} = k\,T_\mathrm{i}/m_\mathrm{i}\,c^2$ and $F(x)$ is given by (A.6). Since we assume that no e or H, He and other nuclei are destroyed or created the first term in the sum vanishes. To simplify the second term in the sum we can use the definition of the specific heat capacities, $c_{V,\mathrm{i}}$, as given in the Appendix A.4. With this one can write

$$m_\mathrm{i}\,c^2\,N_\mathrm{i}\frac{\mathrm{d}F(\theta_\mathrm{i})}{\mathrm{d}t} = k\,N_\mathrm{i}\,\frac{\mathrm{d}T_\mathrm{i}}{\mathrm{d}t}\frac{\mathrm{d}F(\theta_\mathrm{i})}{\mathrm{d}\theta_\mathrm{i}} = N_\mathrm{i}\,c_{V,\mathrm{i}}\,\frac{\mathrm{d}T_\mathrm{i}}{\mathrm{d}t}\,. \tag{5.19}$$

Since due to Coloumb interactions the temperatures of all particles are $T_\mathrm{i} \equiv T_\mathrm{e}$ and because the masses of the nuclei of H, He and the other light elements are orders of magnitude larger than the electron rest mass, for these we neglect relativistic corrections, i.e. $c_{V,\mathrm{i}} \approx 3k\,/2$. Now, one can reformulate equation (5.18) in the following way:

$$\frac{1}{a^3}\,\frac{\mathrm{d}\tilde{Q}}{\mathrm{d}t} = \frac{1}{a^4}\,\frac{\mathrm{d}a^4\tilde{\rho}_\gamma}{\mathrm{d}t} + \alpha^*\,\frac{\mathrm{d}\theta_\mathrm{e}}{\mathrm{d}t} + 2H\alpha\,\theta_\mathrm{e} \tag{5.20a}$$

where tilde denotes that the quantity is expressed in units of the electron rest mass and we introduced the definitions

$$\alpha = \sum_{i\neq\gamma}\frac{3}{2}\,N_\mathrm{i} \tag{5.20b}$$

$$\alpha^* = \alpha + N_\mathrm{e}\left[\frac{\mathrm{d}F(\theta_\mathrm{e})}{\mathrm{d}\theta_\mathrm{e}} - \frac{3}{2}\right]. \tag{5.20c}$$

The second term of (5.20c) arises only due to relativistic corrections of the electron heat capacity. For $\theta_\mathrm{e} \ll 1$ it directly follows that $\alpha \equiv \alpha^*$. If we only consider electrons, hydrogen and helium, using the definitions (E.3) one can write

$$\alpha = \frac{3}{2}\left[\chi_\mathrm{e}\left(1-\frac{Y_\mathrm{p}}{2}\right) + \left(1-\frac{3}{4}\,Y_\mathrm{p}\right)\right] N_\mathrm{b} \tag{5.21a}$$

$$\alpha^* \approx \alpha + \chi_\mathrm{e}\left(1-\frac{Y_\mathrm{p}}{2}\right)\left[\frac{15}{4}\,\theta_\mathrm{e} - \frac{45}{8}\,\theta_\mathrm{e}^2 + \frac{135}{32}\,\theta_\mathrm{e}^3\right] N_\mathrm{b} + \mathcal{O}(\theta_\mathrm{e}^4) \tag{5.21b}$$

The characteristic time scale in equation (5.20) is determined by the interaction of electrons and photons and hence is given by the Compton time $t_\mathrm{C} = 1/\sigma_\mathrm{T}\,N_\mathrm{e}\,c$. Again it is convenient to express the time derivative in terms of optical depth to Compton scattering $\mathrm{d}\tau = \mathrm{d}t/t_\mathrm{C}$. With this one finds the equation describing the evolution of the electron temperature

$$\frac{\mathrm{d}\theta_\mathrm{e}}{\mathrm{d}\tau} = \frac{1}{\alpha^*}\left[q - \frac{1}{a^4}\frac{\mathrm{d}a^4\tilde{\rho}_\gamma}{\mathrm{d}\tau} - 2H\,t_\mathrm{C}\,\alpha\,\theta_\mathrm{e}\right] \tag{5.22}$$

where we introduced $q = \frac{1}{a^3}\frac{d\tilde{Q}}{d\tau}$. Due to Compton scattering the temperature of the electrons is always very close to the Compton scattering equilibrium temperature $\theta_\mathrm{eq}$, which will be discussed in Section 5.3.2. For small spectral distortions this temperature is nearly equal to the effective CMB temperature. Thus it is convenient to rewrite equation (5.22) in terms of the relative difference between the photon and electron temperature, $[\theta_\mathrm{e} - \theta_\gamma]/\theta_\gamma$. This leads to

$$\frac{\mathrm{d}}{\mathrm{d}\tau}\frac{\Delta\theta_\mathrm{e}}{\theta_\gamma} = \frac{1}{\alpha^*\theta_\gamma}\left[q - \frac{1}{a^4}\frac{\mathrm{d}a^4\tilde{\rho}_\gamma}{\mathrm{d}\tau} - H\,t_\mathrm{C}\,[2\alpha-\alpha^*]\,\theta_\mathrm{e}\right], \tag{5.23}$$

where we defined $\Delta\theta_\mathrm{e} = \theta_\mathrm{e} - \theta_\gamma$. For numerical applications this form is more suitable, since even in cases with rather big CMB spectral distortions the relative difference $\Delta\theta_\mathrm{e}/\theta_\gamma$ is small.

### Some simple considerations

If we consider the case when the Universe is only filled with matter and no heating by dissipation of energy or decay of unstable particles is occurring, then, if we neglect relativistic corrections, equation (5.22) reduces to

$$\frac{\mathrm{d}\theta_\mathrm{e}}{\mathrm{d}t} = -2H\,\theta_\mathrm{e} = \frac{\mathrm{d}\ln a^{-2}}{\mathrm{d}t}\,\theta_\mathrm{e}\,, \tag{5.24}$$

which has the simple solution $T_\mathrm{e} = T_{\mathrm{e},0}(1+z)^2$. Here $T_{\mathrm{e},0}$ is the present day temperature of the electrons. This solution shows that without any photons, due to the expansion the electrons would cool down faster than $T_z = T_0(1+z)$.

If one now includes undistorted photons and assumes that due to Compton scattering $T_\mathrm{e} = T_\gamma \equiv T_z$ for all times (since there are no initial spectral distortions this should be true), then it follows that the photons have to continously heat the matter to keep it close to the temperature $T_z$. It is easy to find a solution also in this case. Using (5.23) it follows that

$$\frac{1}{a^4}\frac{\mathrm{d}a^4\tilde{\rho}_\gamma}{\mathrm{d}t} = -H\alpha\,\theta_\gamma\,, \tag{5.25}$$

which has the simple solution $\rho_\gamma = \rho_{\gamma,0}\,[1+\lambda\ln(1+z)]\;(1+z)^4$, where the subscript '0' indicates present day values and $\lambda \approx 3[1-5Y_\mathrm{p}/8]\,N_{\mathrm{b},0}\theta_{\gamma,0}/\rho_{\gamma,0} \approx 6\times10^{-10}$. Luckily due to the large entropy the heat capacity of the electrons and all the baryonic matter is tiny as compared to the huge energy reservoir of the photons. Let us now examine the term arising due to the interactions with the photons.

## 5.3.2 Interactions with the photons

The heating and cooling of the electrons due to interactions with the photons can be split up into the contributions due to Compton scattering and due to the emission of low frequency photons by DC scattering and Bremsstrahlung ($\mathrm{d}\tilde{\rho}_\mathrm{e}/\,\mathrm{d}\tau \;=\; -\,\mathrm{d}\tilde{\rho}_\gamma/\,\mathrm{d}\tau$):

$$-\frac{1}{a^4}\,\frac{\mathrm{d}a^4\tilde{\rho}_\gamma}{\mathrm{d}\tau} = \left.\frac{\mathrm{d}\tilde{\rho}_\mathrm{e}}{\mathrm{d}\tau}\right|_\mathrm{C} + \left.\frac{\mathrm{d}\tilde{\rho}_\mathrm{e}}{\mathrm{d}\tau}\right|_\mathrm{DC+BS}\,. \tag{5.26}$$

Typically the energy transfer due to Compton scattering is much more important than cooling due to emission of soft photons. We now shall examine each of these contributions separately.

### Compton heating and cooling

To derive the term describing the energy transfer due to Compton scattering one can use the generalized Kompaneets equation including first order relativistic corrections (see Eq. (5.10)). Multiply by $E = pc$ and integrating over $\mathrm{d}^3p$, making use of integration by parts, one may obtain (see also Sazonov & Sunyaev [114] for similar expressions):

$$\left.\frac{\mathrm{d}\tilde{\rho}_\mathrm{e}}{\mathrm{d}\tau}\right|_\mathrm{C} = \tilde{\rho}_\gamma\left[\frac{\mathcal{I}_4}{\mathcal{G}_{3,1}}\,\theta_\gamma - 4\,\theta_\mathrm{e} - \frac{21}{5}\,\frac{\mathcal{G}_{5,1}}{\mathcal{G}_{3,1}}\,\theta_\gamma^2 + \frac{\mathcal{I}_4}{\mathcal{G}_{3,1}}\left(\frac{47}{2} - \frac{21}{5}\,\frac{\mathcal{H}_{6,1}}{\mathcal{I}_4}\right)\theta_\mathrm{e}\,\theta_\gamma - 10\,\theta_\mathrm{e}^2\right]\,, \tag{5.27}$$

where $\tilde{\rho}_\gamma = \rho_\gamma/m_\mathrm{e}c^2$ is the energy density of the photons in units of the electron rest mass, with $\rho_\gamma$ as given by (B.3b). The integrals $\mathcal{I}_i$, $\mathcal{G}_{i,j}$ and $\mathcal{H}_{i,j}$ are defined in the Appendix (D.4).

### Compton equilibrium temperature

The Compton cooling term can be conveniently written in terms of the Compton scattering *equilibrium temperature* $\theta_\mathrm{eq}$. This temperature is reached when the energy transfer by Compton scattering vanishes, i.e. when Compton heating and cooling are balanced. Therefore one can

find $\theta_{\rm eq}$ by solving the quadratic equation $\mathrm{d}\tilde{\rho}_{\rm e}/\,\mathrm{d}\tau = 0$ for $\theta_{\rm e}$. Expanding in terms of small photon temperature ($\theta_\gamma \ll 1$) this then leads to

$$\theta_{\rm eq} = \theta_{\rm eq,0}\left[1 - \frac{21}{5}\,\theta_\gamma\left\{\frac{\mathcal{G}_{5,1}}{\mathcal{I}_4} + \frac{\theta_{\rm eq,0}}{\theta_\gamma}\left[\frac{\mathcal{H}_{6,1}}{\mathcal{I}_4} - 5\right]\right\}\right] \tag{5.28}$$

where $\theta_{\rm eq,0} = \theta_\gamma\,\mathcal{I}_4/4\,\mathcal{G}_{3,1}$ corresponds to the result obtained by using the Kompaneets equation in lowest order of the electron temperature. The other terms arise due to first order relativistic corrections to the kinetic equation for Compton scattering. For photons, which follow a Bose-Einstein distribution, one can verify $\theta_{\rm eq} \equiv \theta_\gamma$.

With (5.28) it is possible to rewrite equation (5.27) as

$$\left.\frac{\mathrm{d}\tilde{\rho}_{\rm e}}{\mathrm{d}\tau}\right|_{\rm C} = 4\,\tilde{\rho}_\gamma\cdot(\theta_{\rm eq} - \theta_{\rm e})\cdot\left[1 - \frac{\theta_\gamma}{4}\left\{\frac{\mathcal{I}_4}{\mathcal{G}_{3,1}}\left(\frac{47}{2} - \frac{21}{5}\,\frac{\mathcal{H}_{6,1}}{\mathcal{I}_4}\right) - 10\cdot\frac{\theta_{\rm eq}+\theta_{\rm e}}{\theta_\gamma}\right\}\right] \tag{5.29}$$

Here again the first term in brackets can be found using the Kompaneets equation, whereas the other terms follow from first order relativistic corrections.

Inserting this result into (5.22) one can derive the time scale, on which the electrons adjust their temperature in a given photon field, i.e. $t_{\gamma\rm e} = \alpha^*\,t_{\rm C}/4\,\tilde{\rho}_\gamma$ (see Appendix (E.3)). Due to the large entropy of the Universe this time scale is much shorter than the time needed to transfer energy from the electrons to the photons, i.e. $t_{\rm K} = t_{\rm C}/4\,\theta_{\rm e}$ (see Appendix (E.3)), because a given electron has many more photons to collide with than a given photon.

### Heating and cooling due to photon production

Since during the thermalization process photons have to be produced also cooling and heating due to emission occurs. One may obtain the corresponding term in a similar way as given above using equation (5.11). This then leads to

$$\left.\frac{\mathrm{d}\tilde{\rho}_{\rm e}}{\mathrm{d}\tau}\right|_{\rm DC+BS} = -\kappa_\gamma\cdot\int_0^\infty e^{-x}\Big[1 - n_\gamma\,(e^{\phi\,x}-1)\Big]\times K(x,\theta_\gamma,\theta_{\rm e})\,\mathrm{d}x\,, \tag{5.30}$$

where the emission coefficient $K(x,\theta_\gamma,\theta_{\rm e})$ was defined in Section 5.2.2. Since most of the photons are produced at low frequencies usually this term is very small as compared to energy transfer due to Compton scattering.

## 5.4 Towards a numerical solution of the problem

Above we have given a detailed formulation of the thermalization problem including relevant relativistic corrections. The most significant correction arises due to the decrease of the DC emissivity for higher temperatures. The general problem consists of a system of two coupled equations, one for the time evolution of the photon phase space distribution, the other for the time evolution of the electron (and baryon) temperature. Here we want to further point out some numerical issues, which may be of use.

### 5.4.1 Representation of the photon spectrum

In equilibrium the photons follow a Planckian distribution, which varies over many orders of magnitude in the full range of frequencies. Therefore we decided that it is better to describe the photon distribution as a Bose-Einstein spectrum, with frequency dependent chemical potential $\mu(t,x)$. In this representation equilibrium with respect to Compton scattering is reached, when the derivative of $\mu$ vanishes at all frequencies. This should allow for much higher accuracy with smaller computational efforts (e.g a smaller number of grid points in frequency). In the

Appendix B we have given several relations between the photon phase space distribution and quantities like its derivatives and frequency dependent chemical potential, which have been very useful in rewriting all the equations given above.

For a complete representation of the photons one also has to *choose* the temperature $\theta_\gamma$. It turns out, that for $T \equiv T_\gamma = T_0\,(1+z)$ the term in the brackets of equation (5.14) vanishes, since then $\dot{T}_\gamma/T_\gamma = -H$, so that one has $\xi \equiv x$. This simplifies the computations significantly, because the expansion term was found to be liable for numerical instabilities [25]. However, it still appears in the equation governing the electron temperature evolution (see Sect. 5.3).

### 5.4.2 Compton scattering relativistic corrections

The contribution of Compton scattering to the collision integral including the first order relativistic corrections was formulated as a forth order partial differential equation (see Eq. (5.10)). For numerical applications this is not simple to solve and including higher order corrections in the Fokker-Planck series is hopeless. Therefore instead we studied an approach combining the Kompaneets equation and the relativistic Compton kernel. For this we split the evolution up in to the *fast* part, which is represented by the Kompaneet equation, and modeled the *slow* part resulting from the relativistic corrections by the Compton kernel. Unfortunately, the final implementation and discussion of results are still not completed.

### 5.4.3 Double Compton and Bremsstrahlung

The calculation of the contributions due to DC scattering involve 1-dimensional integrals over the photon spectrum. Neglecting the redistribution of photons by DC scattering, it is sufficient to update the values of these integrals on much longer time scales than required for Compton scattering, since these change only when the photon distribution a high frequencies is modified significantly (the main contribution to the integrals comes form $x \sim 5$).

Using the fits to the Gaunt factors for Bremsstrahlung as provided by Nozawa et al. [90] and Itoh et al. [68] involves sums over many coefficients ($\sim 100$), which turns out to be very time consuming. The Bremsstrahlungs Gaunt factors only change significantly when the electron temperature has evolved. It is possible to analytically derive derivatives of the fitting functions with respect to $x$ and $\theta_\mathrm{e}$ and to calculate these up to some specified order. Given the Gaunt factor and its derivatives at some temperature in the full frequency range, one can estimate when the next updating of these coefficients is necessary. This saves a lot of time and the required accuracy can be controlled easily.

### 5.4.4 Electron temperature

In general one has to couple equation (5.23) to the photon Boltzmann-equation. This leads to a very *stiff* system and a solution is slow. After heating has ceased it is possible to assume that the electron temperature is always given by the Compton equilibrium temperature $\theta_\mathrm{eq}$ as defined by (5.28). This significantly eases the numerical solution of the problem, but for high accuracy this may not be adequate, since the energy required for the production of low frequency photons has to be taken into account properly.

## 5.5 Thermalization of small spectral distortions

In the previous Section we have given a formulation of the thermalization problem including all the relevant relativistic corrections. In this Section we want to examine the effects of relativistic corrections on the thermalization of *small* spectral distortions analytically using suitable additional assumptions.

From the discussion in Chapter 4 it can be expected that relativistic corrections to Compton and DC scattering of CMB photons are of the order of a few $\times\, 1-10$ percent at redshifts

$z \gtrsim$ few $\times 10^6$. At lower redshifts relativistic corrections become negligible at least if one is not considering the details of the heating mechanisms, which may involve electromagnetic cascades with very hard photons and relativistic particles. Since at these early epochs Bremsstrahlung is orders of magnitude less efficient than DC emission we shall completely neglect it here. Furthermore any energy injection at $z \gtrsim$ few $\times 10^5$ leads to a $\mu$-type spectral distortion [126, 65, 46, 59], with frequency dependent chemical potential $\mu(t, x)$. Therefore we now focus the discussion on the evolution of small chemical potential distortions, arising after energy injection in the high-$z$ Universe including relativistic correction.

### 5.5.1 Time evolution of small chemical potential distortions

Starting with the equations given in Sections (5.2) and (5.3) we now introduce the following additional simplification: (i) we assume that the photon and electron temperatures are identical, $T_\mathrm{e} = T_\gamma$. For small spectral distortions this is certainly true, since the Compton equilibrium temperature is very close to the effective photon temperature. (ii) We use $T_\gamma = T_z = T_0(1+z)$, such that the expansion term in the photon Boltzmann equation transforms away. This fixes the energy density of the photons to be close to the CMB energy density. (iii) We assume that the photons evolve along a sequence of equilibrium spectra. Therefore the left hand side of the photon Boltzmann equation (5.8) may be set to zero. At high redshifts Compton and DC scattering are extremely efficient, which justifies this assumption.

With all these comments the solution of the problem can be obtained in two steps: first one may solve the equilibrium Boltzmann equation

$$0 = \left.\frac{\mathrm{d}n_\gamma}{\mathrm{d}\tau}\right|_\mathrm{C} + \left.\frac{\mathrm{d}n_\gamma}{\mathrm{d}\tau}\right|_\mathrm{DC}, \tag{5.31}$$

where $\mathrm{d}n_\gamma/\mathrm{d}\tau|_\mathrm{C}$ is given by (5.10) with $\phi = 1$ and $\mathrm{d}n_\gamma/\mathrm{d}\tau|_\mathrm{DC}$ has the form (5.11) with appropriate emission coefficient $K = K_\mathrm{DC}$ as discussed below. This reduces the problem to a fourth order non-linear ordinary differential equation in $x_\mathrm{e} \equiv x = h\nu/k\,T_\gamma$. After obtaining the frequency dependence of the chemical potential at a fixed time it can be used to solve the time dependence of its high frequency amplitude. A similar procedure was first introduced by Sunyaev & Zeldovich [126] to solve the evolution of CMB chemical potential distortions under Compton scattering and Bremsstrahlung in the non-relativistic limit (the importance of DC emission in this context was realized later by Lightman [80]).

#### Equilibrium spectrum in the limit of small chemical potential

For small chemical potential $|\mu(t, x_\mathrm{e})| \ll 1$ one can approximate the photon phase space distribution by $n(t, x_\mathrm{e}) = 1/[e^{x_\mathrm{e}+\mu(t,x_\mathrm{e})} - 1] \approx n_\mathrm{Pl} + \mu(t, x_\mathrm{e}) \cdot \partial_{x_\mathrm{e}} n_\mathrm{Pl}$, where $n_\mathrm{Pl}$ is a Planck spectrum. Using this and the relations (B.3) equation (5.31) can be linearized keeping only the lowest orders in $\mu$ and its derivatives. This then leads to

$$\frac{4\,\hat{x}_\mathrm{c}^2\,e^{x_\mathrm{e}/2}}{x_\mathrm{e}\,(e^{x_\mathrm{e}}-1)}\,\mu - \frac{\partial}{\partial x_\mathrm{e}} x_\mathrm{e}^4\,n_1\Bigg[\mu' + \theta_\mathrm{e}\left\{\left[\frac{5}{2} - \frac{21}{5}\,x_\mathrm{e}\,n_2 + \frac{21}{5}\,x_\mathrm{e}^2\,n_1\right]\mu' + \frac{7}{10}\,[6 - x_\mathrm{e}\,n_2]\,x_\mathrm{e}\,\mu'' + \frac{7}{10}\,x_\mathrm{e}^2\,\mu'''\right\}\Bigg] = 0 \tag{5.32}$$

where prime denotes derivative with respect to $x_\mathrm{e}$ and the abbreviations $n_1 = n_\mathrm{Pl}(n_\mathrm{Pl}+1)$ and $n_2 = 2n_\mathrm{Pl}+1$ were used. To define the critical frequency $\hat{x}_\mathrm{c}$ we have to specify the DC emission coefficient $K_\mathrm{DC}$. Here we shall use the approximation $g_\mathrm{dc}(x_\mathrm{e}, \theta_\mathrm{e}) \approx e^{-x_\mathrm{e}/2}\,G(\theta_\mathrm{e})$ for the effective DC Gaunt factor, as given in Section 4.5.5. We mentioned earlier (Sect. 4.5.4) that relativistic corrections to DC emission depend only weakly on the value of the chemical potential. Since we also assumed that spectral distortions are small we may use the results

obtained for the case of Planckian photons, i.e. Eq. (4.60). This yields $G(\theta_\mathrm{e}) \approx G_0^\mathrm{Pl}/[1{+}14.16\,\theta_\mathrm{e}]$, where $G_0^\mathrm{Pl} = 4\pi^4/15 \approx 25.976$. Therefore the critical frequency is given by

$$\hat{x}_\mathrm{c} = \left[\frac{\alpha}{3\pi}\,\theta_\mathrm{e}\,e^{x_\mathrm{e}/2} g_\mathrm{dc}(x_\mathrm{e},\theta_\mathrm{e})\right]^{1/2} \approx 3.03\times10^{-6}\,\Theta_{2.7}^{1/2}\,(1+z)^{1/2}\,[1+14.16\cdot\theta_\mathrm{e}]^{-1/2}\,, \tag{5.33}$$

which in the non-relativistic limit becomes

$$\hat{x}_\mathrm{c}^\mathrm{nr} = 3.03\times10^{-6}\,\Theta_{2.7}^{1/2}\,(1+z)^{1/2}\,. \tag{5.34}$$

The critical frequency strongly depends on the temperature and changes significantly with redshift. Comparing $\hat{x}_\mathrm{c}$ and $\hat{x}_\mathrm{c}^\mathrm{nr}$ shows that due to relativistic correction to DC scattering the critical frequency shifts toward smaller values.

Now, following Sunyaev & Zeldovich [126], we go to the limit $x_\mathrm{e} \ll 1$. Therefore one may further simplify equation (5.32) with the substitutions $n_1 \rightarrow 1/x_\mathrm{e}^2$ and $2n_2 \rightarrow 2/x_\mathrm{e}$:

$$\frac{4\,\hat{x}_\mathrm{c}^2}{x_\mathrm{e}^2}\,\mu - \frac{\partial}{\partial x_\mathrm{e}}\,x_\mathrm{e}^2\left[\mu' - \theta_\mathrm{e}\cdot\left\{\frac{17}{10}\,\mu' - \frac{14}{5}\,x_\mathrm{e}\,\mu'' - \frac{7}{10}\,x_\mathrm{e}^2\,\mu'''\right\}\right] = 0\,. \tag{5.35}$$

With the assumption that relativistic corrections are small, it is possible to use a perturbative approach. Inserting $\mu = \mu^{(0)} + \theta_\mathrm{e}\,\mu^{(1)}$ into (5.35) and collecting terms according to their orders in $\theta_\mathrm{e}$ one may obtain the following system of two 2. order linear differential equations:

$$\frac{4\hat{x}_\mathrm{c}^2}{x_\mathrm{e}^2}\,\mu^{(0)} - \frac{\partial}{\partial x_\mathrm{e}}\,x_\mathrm{e}^2\,\frac{\partial\mu^{(0)}}{\partial x_\mathrm{e}} = 0 \tag{5.36a}$$

$$\frac{4\hat{x}_\mathrm{c}^2}{x_\mathrm{e}^2}\,\mu^{(1)} - \frac{\partial}{\partial x_\mathrm{e}}\,x_\mathrm{e}^2\,\frac{\partial\mu^{(1)}}{\partial x_\mathrm{e}} = S(x_\mathrm{e},\mu^{(0)})\,. \tag{5.36b}$$

Here the source term $S(x_\mathrm{e},\mu^{(0)})$ may be written as

$$S(x_\mathrm{e},\mu^{(0)}) = -\frac{\partial}{\partial x_\mathrm{e}}\,x_\mathrm{e}^2\left[\frac{17}{10}\,\frac{\partial\mu^{(0)}}{\partial x_\mathrm{e}} - \frac{14}{5}\,x_\mathrm{e}\,\frac{\partial^2\mu^{(0)}}{\partial x_\mathrm{e}^2} - \frac{7}{10}\,x_\mathrm{e}^2\,\frac{\partial^3\mu^{(0)}}{\partial x_\mathrm{e}^3}\right]. \tag{5.36c}$$

The 0. order equation was already derived and solved by Sunyaev & Zeldovich [126]:

$$\mu^{(0)} = \mu_0\,e^{-2\xi}\,, \tag{5.37}$$

with $\xi(t,x_\mathrm{e}) = \hat{x}_\mathrm{c}/x_\mathrm{e}$. At large frequencies ($x_\mathrm{e} \gg \hat{x}_\mathrm{c}$) $\mu^{(0)} \rightarrow \mu_0$ and for $x_\mathrm{e} \ll \hat{x}_\mathrm{c}$ it vanishes. Inserting $\mu^{(0)}$ into equation (5.36b) one may find the solution for the first order correction

$$\mu^{(1)} = -\mu^{(0)}\left[C + \xi\cdot\left\{\frac{11}{4} + \frac{21}{10}\,\xi - \frac{14}{15}\,\xi^2\right\}\right]. \tag{5.38}$$

Since the chemical potential should approach $\mu_0$ for $x_\mathrm{e} \rightarrow \infty$, the integration constant $C$ is set to zero. Then the approximate solution for the equilibrium chemical potential at a fixed time $t$ is given by

$$\mu(t,x_\mathrm{e}) = \mu_0(t)\,e^{-2\xi}\left[1 - \theta_\mathrm{e}\,\xi\cdot\left\{\frac{11}{4} + \frac{21}{10}\,\xi - \frac{14}{15}\,\xi^2\right\}\right]. \tag{5.39}$$

With this the brightness temperature $\theta_*(x_\mathrm{e})$ can be given by $\theta_*(x_\mathrm{e}) = \theta_\mathrm{e}/[1+\mu(x_\mathrm{e})/x_\mathrm{e}]$ (see Eq. (B.2b) in the Appendix). In the non-relativistic case the maximum of $|\theta_*(x_\mathrm{e})|$ is at the frequency $x_\mathrm{e,max}^\mathrm{nr} = 2\,\hat{x}_\mathrm{c}^\mathrm{nr}$. Including first order relativistic corrections to both Compton and DC scattering, this frequency shifts towards lower values

$$x_\mathrm{e,max} \approx 2\hat{x}_\mathrm{c}\left[1 + \frac{83}{40}\,\theta_\mathrm{e}\right] \approx 2\hat{x}_\mathrm{c}^\mathrm{nr}[1 - 5\,\theta_\mathrm{e}]\,. \tag{5.40}$$

In Figure 5.1 the comparison between the equilibrium solution in the non-relativistic and relativistic limit are shown as functions of $x_\mathrm{e}$ for $z = 5\times10^7$ and $\mu_0 = 2\times10^{-3}$. Relativistic corrections lead to a few % differences. Due to relativistic corrections the effective value of the critical frequency $\hat{x}_\mathrm{c}$ is shifted towards lower values. Also the position of the maximum difference in brightness temperature decreases as compared to the non-relativistic case.

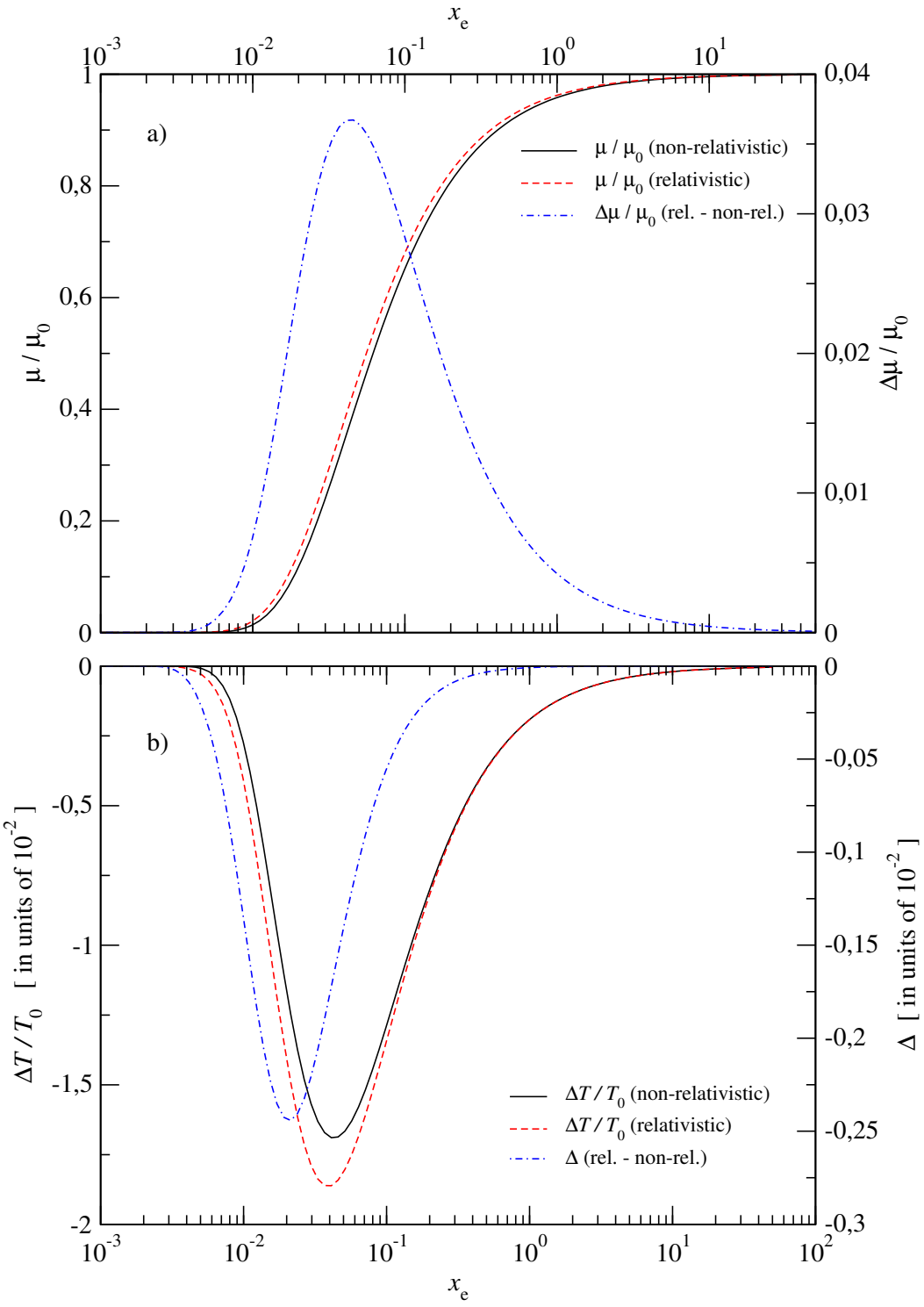


**Figure 5.1:** Comparison between the equilibrium solution in the non-relativistic and relativistic limit for $\mu_0 = 2\times10^{-3}$ at redshift $z = 5\times10^7$. **a)** Chemical potential: non-relativistic result $\mu^{(0)}/\mu_0$ (solid), with relativistic corrections to CS and DC scattering (dashed) and the difference between the relativistic and non-relativistic equilibrium chemical potentials, $\Delta\mu/\mu_0$ (dashed-dotted). **b)** Brightness temperature: non-relativistic result $\Delta T/T_0 = (T-T_0)/T_0$ (solid), with relativistic corrections to CS and DC scattering (dashed) and the difference between these two, $\Delta = (T^{\rm rel} - T^{\rm nr})/T_0$ (dashed-dotted).

### 5.5.2 Solving the time evolution in the limit of small chemical potential

In the previous paragraph we have given the equilibrium solution of the chemical potential at a fixed time. With this one can calculate the number, $N_\gamma(t) = N_{\rm Pl} \cdot \phi_\mu$, and energy density, $\rho_\gamma(t) = \rho_{\rm Pl} \cdot f_\mu$, of the photons using the definitions (B.5). The main contributions to the number and energy density of the photons come from the region $x \geq 1$. At these frequencies $\mu \approx \mu_0$ is roughly constant. It follows

$$\frac{1}{\rho_\gamma}\frac{\mathrm{d}\rho_\gamma}{\mathrm{d}t} = 4\,\frac{\mathrm{d}\ln T_\gamma}{\mathrm{d}t} + \frac{\mathrm{d}\ln f_\mu}{\mathrm{d}\mu_0}\cdot\frac{\mathrm{d}\mu_0}{\mathrm{d}t} \tag{5.41a}$$

$$\frac{1}{N_\gamma}\frac{\mathrm{d}N_\gamma}{\mathrm{d}t} = 3\,\frac{\mathrm{d}\ln T_\gamma}{\mathrm{d}t} + \frac{\mathrm{d}\ln \phi_\mu}{\mathrm{d}\mu_0}\cdot\frac{\mathrm{d}\mu_0}{\mathrm{d}t} \tag{5.41b}$$

for the time derivatives of $N_\gamma$ and $\rho_\gamma$. Combining these equations it is possible to eliminate the time derivative of the temperature:

$$\frac{\mathrm{d}\mu_0(\tau)}{\mathrm{d}\tau} = \frac{1}{B_\mu}\left[3\,\frac{1}{\rho_\gamma}\frac{\mathrm{d}\rho_\gamma}{\mathrm{d}\tau} - 4\,\frac{1}{N_\gamma}\frac{\mathrm{d}N_\gamma}{\mathrm{d}\tau}\right], \tag{5.42}$$

with $B_\mu = 3\,\frac{\mathrm{d}\ln f_\mu}{\mathrm{d}\mu_0} - 4\,\frac{\mathrm{d}\ln \phi_\mu}{\mathrm{d}\mu_0} = \frac{8I_1}{I_2} - \frac{9I_2}{I_3} \approx 2.143$ and the integrals $I_i = \int_0^\infty x^i\, n_{\rm Pl}\,\mathrm{d}x$, $I_1 \approx 1.645$, $I_2 \approx 2.404$ and $I_3 \approx 6.494$. Moreover we have already linearized in $\mu_0$ and transformed to the variable $\tau$. This equation was first formulated by Sunyaev & Zeldovich [126].

#### Change of the number density

The change of the number density of the photons is only due to DC emission, since Compton scattering conserves the number of photons. Therefore using equation (5.11), in the limit $|\mu| \ll 1$ one may find:

$$\frac{1}{N_\gamma}\frac{\mathrm{d}N_\gamma}{\mathrm{d}\tau} == \frac{4\,\hat{x}_{\rm c}^2\,\theta_{\rm e}}{I_2}\,\mu_0 \int_0^\infty \frac{e^{y/2}\,\hat{\mu}(t,y)}{y(e^y-1)}\,\mathrm{d}y\,, \tag{5.43}$$

with $\hat{\mu} = \mu/\mu_0$. The remaining integral can be solved approximately by splitting the integration region up into $\xi < 1$ and $\xi \geq 1$:

$$I_\mu = \int_0^\infty \frac{e^{y/2}\,\hat{\mu}(t,y)}{y(e^y-1)}\,\mathrm{d}y \approx \int_0^{\hat{x}_{\rm c}/2} e^{-\hat{x}_{\rm c}/2\xi}\,\hat{\mu}_{\rm appr}(t,\xi)\,\frac{d\xi}{\xi} + \frac{1}{\hat{x}_{\rm c}}\int_{\hat{x}_{\rm c}/2}^\infty \hat{\mu}(t,\xi)\,\mathrm{d}\xi\,, \tag{5.44}$$

with

$$\hat{\mu}_{\rm appr} = 1 - \left[2 + \frac{11}{4}\,\theta_{\rm e}\right]\xi + \left[2 + \frac{17}{4}\,\theta_{\rm e}\right]\xi^2 - \left[\frac{4}{3} + \frac{11}{30}\,\theta_{\rm e}\right]\xi^3\,. \tag{5.45}$$

Since for redshifts $z \leq 10^8$ it follows $\hat{x}_{\rm c} \sim$ few $\times\, 10^{-2} \ll 1$ consistent up to $\mathcal{O}(\theta_{\rm e})$ Eq. (5.44) may be written as:

$$\begin{aligned} I_\mu &= \frac{1}{2\hat{x}_{\rm c}}\left[1 - \frac{69}{40}\,\theta_{\rm e} - (1+2\sigma)\,\hat{x}_{\rm c} + \left\{\frac{1}{2} - \frac{2}{e} - 2\,\sigma\right\}\hat{x}_{\rm c}^2\right] \\ &\approx \frac{1 - 1.725\,\theta_{\rm e} - 0.5612\,\hat{x}_{\rm c} + 0.2030\,\hat{x}_{\rm c}^2}{2\hat{x}_{\rm c}}\,, \end{aligned} \tag{5.46}$$

where $\sigma = \mathrm{Ei}(-1) = -\int_1^\infty e^{-t}/t\,\mathrm{d}t \approx -0.2194$. The approximation to $I_\mu$ given here is accurate up to better than 0.15% in the range $\theta_{\rm e} < 0.05$ and $\hat{x}_{\rm c} < 0.01$.

It is important to note, that in the integral $I_\mu$ the term proportional to the electron temperature is due to the relativistic corrections to CS only. The terms proportional to $\hat{x}_{\rm c}$ arise as corrections to the non-relativistic result, with the modifications of the critical frequency due to DC relativistic correction taken into account. We neglected terms $\propto \theta_{\rm e}\,\hat{x}_{\rm c}$ and higher since they are already of $\mathcal{O}(\theta_{\rm e}^{3/2})$.

### Final evolution equation

Now, using (5.43), (5.44) and (5.46) one may rewrite equation (5.42) as:

$$\frac{\mathrm{d}\mu_0}{\mathrm{d}t} = -\frac{\mu_0}{t_{\mu,\mathrm{DC}}} + a\,Q(t)\,, \tag{5.47}$$

where $a = 3/B_\mu \approx 1.399$ and $Q(t) = \dot{\rho}_\gamma/\rho_\gamma$ is the energy injection rate relative to the CMB energy density. Here $t_{\mu,\mathrm{dc}}$ is given by

$$\begin{aligned} t_{\mu,\mathrm{dc}} &= t_\mathrm{C}\,\frac{B_\mu\,I_2}{8\,\theta_\mathrm{e}\,\hat{x}_\mathrm{c}^\mathrm{nr}}\cdot f^{-1}(z) \\ &= 2.09\times10^{33}\,(1-Y_\mathrm{p}/2)^{-1}(\Omega_\mathrm{b}h^2)^{-1}\times\Theta_{2.7}^{-3/2}\cdot(1+z)^{-9/2}f^{-1}(z)\;\mathrm{s}\,, \end{aligned} \tag{5.48}$$

where we used $\Theta_{2.7} = T_0/2.7\,\mathrm{K}$ and

$$f(z) = 2\hat{x}_\mathrm{c} I_\mu\,[1+14.16\,\theta_\mathrm{e}]^{-1/2}\,. \tag{5.49}$$

For the the WMAP concordance model [11] (the parameters are given in the Appendix E) one finds $t_{\mu,\mathrm{DC}} \approx 1.05\times10^{35}\,(1+z)^{-9/2}f^{-1}(z)$ s .

Up to $z \lesssim 10^8$ relativistic corrections to CS and DC scattering are only of the order of a few percent. Therefore, keeping only terms up to $\mathcal{O}(\theta_\mathrm{e})$, we may approximate $f(z)$ in the integrand of $F(z)$ including all other corrections by

$$f(z) \approx 1 - A_{1/2}\,\lambda^{1/2}\,(1+z)^{1/2} - A_1\,\lambda\,(1+z)\,, \tag{5.50}$$

where $\lambda = k\,T_0/m_\mathrm{e}c^2 \approx 4.55\times10^{-10}\,\Theta_{2.7}$ and the coefficients $A_{1/2}$ and $A_1$ for different types of corrections are given in Table 5.1.

### General solution

Assuming radiation domination the expansion time is given as $t_\mathrm{exp} = t_*/(1+z)^2$, with the abbreviation $t_* = 4.88\times10^{19}\,\Theta_{2.7}^{-2}\,\mathrm{s}$ (see Appendix E.3). Now, the general solution of equation (5.47) can be written as

$$\mu(z,z_0) = \mu(z_0)\cdot H_+(z)\cdot H_-(z_0) + \tilde{\kappa}\,H_+(z)\cdot\mathcal{L}(z,z_0)\,, \tag{5.51}$$

with $\tilde{\kappa} = a\,t_*$ and where we defined the functions

$$H_\pm(z) = \exp\left[\pm F(z)\right] \tag{5.52a}$$

$$F(z) = \frac{5}{2}\int_{-1}^{z}\frac{(1+z')^{3/2}}{(1+z_\mu)^{5/2}}\,f(z')\,\mathrm{d}z' \tag{5.52b}$$

$$\mathcal{L}(z,z_0) = \int_z^{z_0}\frac{Q(z')}{(1+z')^3}\,H_-(z')\,\mathrm{d}z'\,. \tag{5.52c}$$

Here the *thermalization* redshift $z_\mu$ for DC scattering is given by

$$\begin{aligned} 1+z_\mu &= \left[\frac{5\,t_{\mu,\mathrm{dc}}\,(1+z)^{9/2}\,f(z)}{2\,t_*}\right]^{2/5} \\ &= 4.09\times10^5\,(1-Y_\mathrm{p}/2)^{-2/5}(\Omega_\mathrm{b}h^2)^{-2/5}\Theta_{2.7}^{1/5} \end{aligned} \tag{5.53}$$

and has the value $z_\mu \approx 1.97\times10^6$ for the WMAP concordance model. Distortions arising from redshifts $z_0$ much before the critical redshift, i.e. $z_0 \gg z_\mu$, can be completely thermalized, whereas distortions arising afterwards, i.e. $z_0 \ll z_\mu$, can survive. In the following we assume

**Table 5.1:** Coefficients $A_{1/2}$, $A_1$, $\tilde{A}_{1/2}\times10^3$ and $\tilde{A}_1\times10^3$ for different types of corrections: $\hat{x}_{\rm c}^{\rm nr}$ corrections to the non-relativistic result, DC double Compton temperature correction, CS Compton scattering temperature corrections, DC & CS temperature corrections.

| | $\hat{x}_{\rm c}^{\rm nr}$ | DC | CS | DC & CS |
|---|---|---|---|---|
| $A_{1/2}$ | 0.080 | 0 | 0 | 0 |
| $A_1$ | -0.004 | 7.080 | 1.725 | 8.805 |
| $\tilde{A}_{1/2}$ | 1.994 | 0 | 0 | 0 |
| $\tilde{A}_1$ | $-0.002$ | 4.526 | 1.103 | 5.629 |

that $z_0 \gg z_\mu$ and therefore set $\mu(z_0) = 0$. The time where heating sets in will be called $z_{\rm h}$ and obeys $z_{\rm h} < z_0$.

Substituting the approximation (5.50) into equation (5.52b), the integral $F(z)$ can be solved and is given by

$$F(z) \approx w^{5/2}\left[1 - \tilde{A}_{1/2}\, w^{1/2} - \tilde{A}_1\, w\right]. \tag{5.54}$$

Here the variable $w = [1+z]/[1+z_\mu]$ and the coefficients $\tilde{A}_{1/2} = \frac{5}{6}\,A_{1/2}\,\theta_\mu^{1/2}$ and $\tilde{A}_1 = \frac{5}{7}\,A_1\,\theta_\mu$ (see Table 5.1), with the temperature at the thermalization redshift, $\theta_\mu = \lambda\,(1+z_\mu) \approx 8.95\times 10^{-4}$, were introduced.

In (5.54) the term $\propto w^{5/2}$ corresponds to the non-relativistic limit and was obtained earlier by Danese & de Zotti [46]. The term $\propto w^3$ arises only from the $\hat{x}_{\rm c}^{\rm nr}$ correction to the integral $I_\mu$ and is of the same order as the CS and DC scattering temperature corrections. It changes the non-relativistic result by a few percent. The term $\propto w^{7/2}$ mainly corresponds to temperature corrections to CS and to the DC emission coefficient with a very small contribution from the $(x_{\rm c}^{\rm nr})^2$ correction to $I_\mu$. In the following we will neglect the $(x_{\rm c}^{\rm nr})^2$ correction. The effects of relativistic corrections only enter through the temperature corrections to DC and CS.

## 5.6 Energy injection by different physical mechanisms

In this Section we will discuss the solution (5.51) of the high frequency time evolution of the chemical potential for different energy release mechanisms and estimate the residual distortion at redshift $z = 0$. We shall assume that energy is injected well before Compton scattering is able to bring the spectrum into quasi-equilibrium, which roughly happens at $z \sim 4\sqrt{2}\,z_{\rm K}$ [25]. Here $z_{\rm K}$ is determined by the condition $t_{\rm exp}/t_{\rm K} \sim 1$, i.e. where the expansion rate and the rate of energy transfer from the electrons to the photons become equal. With the relations in the Appendix E.3 one can find

$$z_{\rm K} = 7.09\times10^3\,\Theta_{2.7}^{1/2}(1-Y_{\rm p}/2)^{-1/2}\,(\Omega_{\rm b}h^2)^{-1/2}, \tag{5.55}$$

which is $z_{\rm K} = 5.09\times10^4$ for the WMAP concordance model. For $z \lesssim 4\sqrt{2}\,z_{\rm K} \sim 2.88\times10^5 \ll z_\mu$ CS can no longer efficiently up-scatter photons from low frequencies and hence the number of photons (and the residual chemical potential) at high frequencies *freeze out*. On the other hand at low frequencies DC and (at some point) BS still produce photons, but relativistic corrections are already negligible. Therefore the low frequency spectrum will subsequently evolve like in the non-relativistic limit, which has been discussed in Hu & Silk [59].

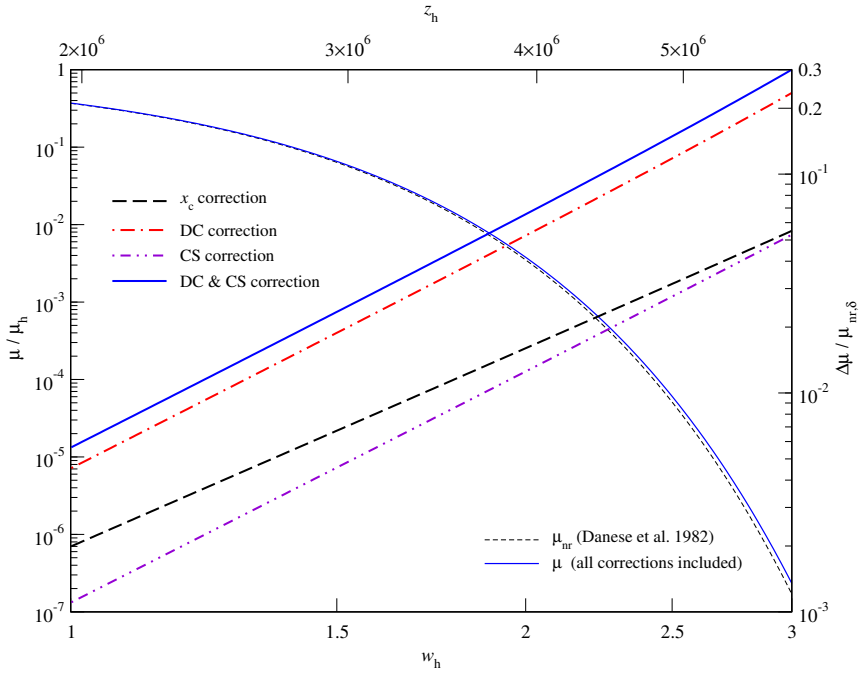


**Figure 5.2:** Remaining high frequency chemical potential $\mu/\mu_\mathrm{h}$ with $\mu_\mathrm{h} = \mu(z_\mathrm{h})$ for a single energy injection at heating redshift $w_\mathrm{h} = [1 + z_\mathrm{h}]/[1 + z_\mu]$: The thin dashed line shows the non-relativistic result as given by (5.58), whereas the thin solid line shows the result with relativistic corrections to CS and DC included (Eq. (5.57)). — The heavy lines show the relative difference between the remaining chemical potential $\mu$ and $\mu_{\mathrm{nr},\delta}$ (right ordinate) including CS relativistic correction (dash-dot-dotted), DC scattering relativistic correction (dash-dotted) and both relativistic corrections (solid). Also shown is the $\hat{x}_\mathrm{c}$ correction to the non-relativistic result (dashed).

### 5.6.1 Single energy injection at $z_\mathrm{h}$

For a single energy injection the heating rate is given by $Q(z) = Q_0\,\delta(z - z_\mathrm{h})/\,|\,\mathrm{d}t/\,\mathrm{d}z|$, where $Q_0 = \delta\rho_\gamma/\rho_\gamma$ is the fractional change of the photon energy density and $\mathrm{d}t/\,\mathrm{d}z = -t_\mathrm{exp}/(1+z)$. Inserting this into equation (5.52c) yields

$$\mu_\delta(z, z_\mathrm{h}) = a\,Q_0\,H_+(z)\cdot H_-(z_\mathrm{h}) \tag{5.56}$$

Now, setting $z = 0$ and substituting $w_\mathrm{h} = (1 + z_\mathrm{h})/(1 + z_\mu)$ the residual chemical potential after thermalization can be written as:

$$\mu_\delta(0, z_\mathrm{h}) = \mu(w_\mathrm{h}) \times \exp\left[-w_\mathrm{h}^{5/2}\left(1 - \tilde{A}_{1/2}\,w_\mathrm{h}^{1/2} - \tilde{A}_1\,w_\mathrm{h}\right)\right]\,, \tag{5.57}$$

where $\mu_\mathrm{h} = \mu(w_\mathrm{h}) = a\,\delta\rho_\gamma/\rho_\gamma$. The first term in the exponent of equation (5.57) corresponds to the result in the non-relativistic limit [46], where the $\hat{x}_\mathrm{c}^\mathrm{nr}$ correction to the integral $I_\mu$ is neglected. Including this correction one may write:

$$\mu_{\mathrm{nr},\delta}(0, z_\mathrm{h}) = \mu(w_\mathrm{h}) \times \exp\left[-w_\mathrm{h}^{5/2}\left(1 - \beta_\mathrm{nr}\,w_\mathrm{h}^{1/2}\right)\right]\,, \tag{5.58}$$

where $\beta_\mathrm{nr} \equiv \tilde{A}_{1/2} = 1.994 \times 10^{-3}$ (Here we have neglected the small contribution due to the $(x_\mathrm{c}^\mathrm{nr})^2$ correction). Since the temperature $\theta_\mu \approx 8.95\times10^{-4}$ at the thermalization redshift is very small, one may find for the relative difference $\Delta = \mu_\delta/\mu_{\mathrm{nr},\delta} - 1$ between the non-relativistic (5.58) and the relativistic (5.57) result

$$\Delta(z_\mathrm{h}) \approx \tilde{A}_1\,w_\mathrm{h}^{7/2}\,. \tag{5.59}$$

For $w_\mathrm{h} \sim 1$ the temperature corrections to CS and DC are only of the order of $\Delta \sim \text{few} \times 10^{-3}$, but for $w_\mathrm{h} \sim 1.2$ they reach already percent level. At heating redshifts $z \sim 5 \times 10^6$ relativistic

corrections for the Wmap Universe lead to $\sim 15\,\%$ deviations from the non-relativistic result (see Fig. 5.2). It is important to note that CS relativistic corrections are a factor of $\sim 4$ less important than DC relativistic correction.

It is important to note that for $w_{\rm h} \sim 2.22$ a value of $Q_0 = \delta\rho_\gamma/\rho_\gamma \sim 0.1$ is still compatible with the Cobe limit on the residual chemical potential, $|\mu| \lesssim 9 \times 10^{-5}$. In this limiting case it follows that $\mu_{\rm h} \sim 1.4\,\delta\rho_\gamma/\rho_\gamma$ is not much smaller than unity anymore. Therefore one can expect that non-linear effects in the evolution of the chemical potential may already become significant. We will discuss this point again below.

### 5.6.2 Energy injection from annihilating relict particles

After particle freeze-out the number density of relict particles of species X and its anti-particles $\bar{\rm X}$ evolve like $n_{\rm X} \equiv n_{\bar{\rm X}} = n_{\rm X\,0}\,(1+z)^3$, where $n_{\rm X\,0}$ is the present day number density and we assumed symmetry between the particle and its anti-particle. Then the annihilation rate is given as $\Gamma_{\rm X\bar{X}} = \langle\sigma_{\rm X\bar{X}}\,v\rangle\; n_{\rm X}\,n_{\bar{\rm X}}$, where $\langle\sigma_{\rm X\bar{X}}\,v\rangle$ is the thermally averaged annihilation cross section times relative velocity. We assume that this quantity is approximately constant, $\langle\sigma_{\rm X\bar{X}}\,v\rangle = \sigma_0$, i.e. s-wave annihilation. From this it follows that the relative heating rate per unit time is given as $Q(z) = Q_0\,(1+z)^2$, where $Q_0 = 2\,\sigma_0\,m_{\rm X}c^2\,n_{\rm X\,0}^2/\rho_{\gamma\,0}$, $m_{\rm X}$ is the rest mass of the particle and $\rho_{\gamma\,0}$ is the present day energy density of the CMB.

To obtain the chemical potential form continuous energy injection one may use the result (5.57) and integrate $a\,Q(z)\,|\,{\rm d}t/\,{\rm d}z|\,\mu_\delta(0,z)/\mu(w_{\rm h})$ over ${\rm d}z$. If heating starts at redshift $z_{\rm s}$ and ends at $z_{\rm e}$, then one may approximate the resulting chemical potential as follows:

$$\mu_{\rm X\bar{X}}(z_{\rm e}, z_{\rm s}) \approx \Lambda \int_{w_{\rm e}}^{w_{\rm s}} \frac{{\rm d}\xi}{\xi} \times \exp\left[-\xi^{5/2}\left(1 - \tilde{A}_{1/2}\,\xi^{1/2} - \tilde{A}_1\,\xi\right)\right], \tag{5.60}$$

with $\Lambda = \tilde{\kappa}\,Q_0$. In the limit $\theta_\mu \ll 1$ the solution of this integral may be written as

$$\mu_{\rm X\bar{X}}(z_{\rm e}, z_{\rm s}) = \frac{2}{5}\,\Lambda\left[\Gamma\left(0,\,\xi^{5/2}\right) + \tilde{A}_{1/2}\,\Gamma\left(\tfrac{1}{5},\,\xi^{5/2}\right) + \tilde{A}_1\,\Gamma\left(\tfrac{2}{5},\,\xi^{5/2}\right)\right]_{w_{\rm s}}^{w_{\rm e}}. \tag{5.61}$$

Here the convention $[g(x)]_b^a = g(a) - g(b)$ and the definition of incomplete Gamma-Function, $\Gamma(a,\,x) = \int_x^\infty t^{a-1}\,e^{-t}\,{\rm d}t$ were used.

The term $\propto \Gamma\left(0,\,\xi^{5/2}\right)$ corresponds to the exact non-relativistic result. In the limit $w_{\rm e} \ll 1$ and $w_{\rm s} \simeq 1$ it is approximately given by

$$\mu_{\rm X\bar{X},\Theta}(z_{\rm e}) = \Lambda\,\ln\left[\frac{1+z_\mu}{1+z_{\rm e}}\right], \tag{5.62}$$

which was used by [86] to constrain the abundance and cross-sections of annihilating relict particles. Despite a $5-10\%$ difference between the exact non-relativistic result and the approximation (5.62), relativistic corrections to CS and DC scattering are completely negligible in this context. This is due to the fact that the bulk of the energy from any annihilating particle is injected during the non-relativistic regime of the chemical potential evolution.

### 5.6.3 Energy injection by unstable relict particles

For non-relativistic decaying relict particles of type X the energy density at time $t$ is given by

$$\rho_{\rm X}(z) = \rho_{\rm s,X}\,\left[\frac{1+z}{1+z_{\rm s}}\right]^3 \exp[-(t-t_{\rm s})/t_{\rm X}]\,, \tag{5.63}$$

where $\rho_{\rm s,X}$ is the initial energy density of the particle at the time $t_{\rm s}$ at which the heating by decay starts and $t_{\rm X}$ is the mean lifetime of the particle. Apparently we assumed $t_{\rm s} > t_{\rm f}$, i.e. the decay starts at times after the freeze-out of the particle density. Furthermore, assuming that a

fraction $f$ of the released energy is finally heating the photon field, the relative photon heating rate is given by

$$Q(z) = Q_0\, w^{-1}\, \exp[-(t-t_{\rm s})/t_{\rm X}]\,, \tag{5.64}$$

where here $Q_0 = \Gamma_{\rm X}\, r\, w_{\rm s}$, with the decay rate $\Gamma_{\rm X} = 1/t_{\rm X}$ and $r = f\,\rho_{\rm s,X}/\rho_{\rm s,\gamma}$ is the ratio of the energy density of the decaying particle and the photons at time $t_{\rm s}$. In the radiation dominated era the time-redshift relation is given by $t(z) = t_*/2(1+z)^2 \approx 2.44\times 10^{19}\;\Theta_{2.7}^{-2}\,(1+z)^{-2}\,{\rm s}$. Using this relation and inserting (5.64) into (5.52c) the residual chemical potential resulting from particle decay can be cast into the form:

$$\mu_{\rm X}(0,z_{\rm s}) \approx a\,\Lambda \int\limits_0^{w_{\rm s}} \frac{{\rm d}\xi\, e^{-(\xi_{\rm X}/\xi)^2}}{\xi^4/\xi_{\rm X}^2} \times \exp\left[-\xi^{5/2}\left(1-\tilde{A}_{1/2}\,\xi^{1/2}-\tilde{A}_1\,\xi\right)\right]\,, \tag{5.65}$$

where $\Lambda = 2\,r\,w_{\rm s}$ and $\xi_{\rm X} = w_{\rm X} = \sqrt{t_\mu/t_{\rm X}} \equiv [1+z_{\rm X}]/[1+z_\mu]$, with $z_{\rm X} = z(t_{\rm X})$ and $t_\mu = t(z_\mu)$:

$$t_\mu \approx 1.46\times 10^8\;(1-Y_{\rm p}/2)^{4/5}(\Omega_{\rm b}h^2)^{4/5}\,\Theta_{2.7}^{-12/5}\,{\rm s}\,, \tag{5.66}$$

which has the value $t_\mu \approx 6.15\times 10^6$ s for the WMAP concordance model. The parameter $\Lambda$ may be rewritten in the following way:

$$\Lambda \approx 7.79\times 10^6\;(1-Y_{\rm p}/2)^{2/5}(\Omega_{\rm b}h^2)^{2/5}\,\Theta_{2.7}^{-1/5}\cdot\chi\,, \tag{5.67}$$

with $\chi = f\left[\frac{m_{\rm X}c^2}{\rm GeV}\right]\frac{n_{\rm X}(t_{\rm s})}{n_\gamma(t_{\rm s})}$ where $n_{\rm X}(t_{\rm s})$ and $n_\gamma(t_{\rm s})$ are the relict particle and photon number densities at the time $t_{\rm s}$, respectively. $\Lambda \approx 1.61\times 10^6\chi$ for the WMAP concordance model.

The integral (5.65) can be easily solved numerically. For its derivation we have assumed that an negligible amount of photons is injected during the decay. This implies that the number density of the particles has to obey $n_{\rm X} \ll n_\gamma$ at any time and that the possible electromagnetic cascade of particles after the decay will also contain a negligible amount of photons. Calculations of pair-photon cascades show that in the early Universe this assumption is well justified [140].

### Alternative consideration

It is interesting to compare the remaining chemical potential (5.65) to the chemical potential which results if *all* the energy injected during the decay is effectively released at $t = t_{\rm X}$. To do so, we first calculate the total amount of energy released into the CMB

$$\begin{aligned}\frac{\delta\rho_\gamma}{\rho_\gamma} &= \int_{t_{\rm s}}^{\infty} Q\,{\rm d}t \approx \Lambda\int_0^\infty \frac{{\rm d}\xi\, e^{-(\xi_{\rm X}/\xi)^2}}{\xi^4/\xi_{\rm X}^2} = \frac{\sqrt{\pi}}{4}\,\Lambda\,\xi_{\rm X}^{-1}\\ &\approx 2.86\times 10^2\;\Theta_{2.7}\,\sqrt{t_{\rm X}/1{\rm s}}\;\cdot\chi\,.\end{aligned} \tag{5.68}$$

Here for simplicity we have neglected any relativistic corrections. Now, using the results obtained in Sect. 5.6.1 and $z \propto 1/\sqrt{t}$ one may easily find

$$\begin{aligned}\mu(0,z_{\rm h}) &= a\,\frac{\delta\rho_\gamma}{\rho_\gamma}\cdot\exp\left[-\left(t_\mu/t_{\rm X}\right)^{5/4}\right]\\ &\approx 4.00\times 10^2\;\Theta_{2.7}\,\sqrt{t_{\rm X}/1{\rm s}}\cdot\exp\left[-\left(t_\mu/t_{\rm X}\right)^{5/4}\right]\cdot\chi\,.\end{aligned} \tag{5.69}$$

Despite a factor of 2 difference in the numerical coefficient this equation was previously obtained by Hu & Silk [58] and used to constrain the lifetimes and energy density of decaying relict particles. In this estimate the visibility function for chemical potential spectral distortions, $\mathcal{V} \sim \exp[-w^{5/2}]$, in the low baryon density Universe has been neglected. For long lived

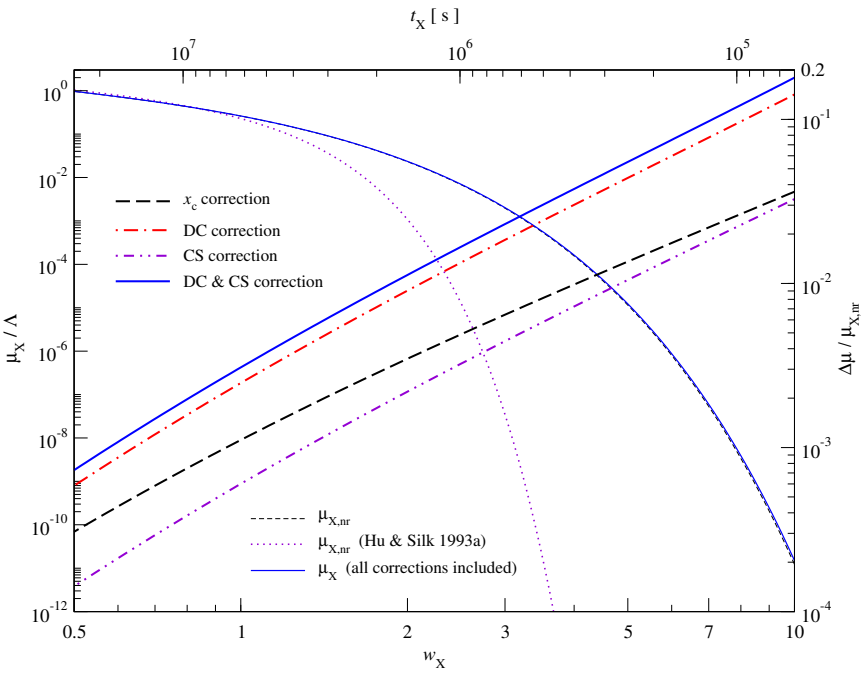


**Figure 5.3:** Remaining high frequency chemical potential $\mu_X/\Lambda$ after energy injection due to unstable particles with different lifetimes $t_X$: In the non-relativistic case (thin/dashed) and with relativistic corrections to CS and DC (thin/solid). Also shown is the estimate as given by Hu & Silk [58], were the effects of the visibility function for DC thermalization has been neglected (thin/dotted) — The heavy lines show the relative difference between the remaining chemical potential $\mu_X$ and $\mu_{X,nr}$ (right ordinate) including CS relativistic correction (dash-dot-dotted), DC scattering relativistic correction (dash-dotted) and both relativistic corrections (solid). Also shown is the $\hat{x}_c$-correction (dashed).

particles ($t_X \gtrsim 10^7$ s) energy injection effectively occurs at late times, where $\mathcal{V} \sim 1$ and thereby justifies this approximation. On the other hand, for particles with lifetimes comparable with the thermalization time $t_\mu$ the effects of the visibility function have to be taken into account. Neglecting the visibility function leads to an underestimation of the remaining chemical potential and therefore weakens the constraint significantly.

In Figure 5.3 the remaining chemical potential $\mu_X$ due to the decay of unstable particles is shown. For short lifetime particles ($\xi_\mu \geq 1$) the relativistic corrections change the results by a few percent. In comparison with the case of single energy injection, relativistic corrections are less important. For long lifetime particles ($\xi_\mu < 1$) relativistic corrections can be completely neglected.

## 5.7 Summary and discussion

In this Chapter we have reexamined the formulation of the thermalization problem including relevant relativistic corrections (such as corrections to CS, DC and the heat capacity of the electrons). Likely, the main corrections arise due to the decrease in the DC photon production efficiency for higher temperatures. This should slow down the process of thermalization at high redshifts ($z \geq$ few $\times 10^6$) and therefore make the CMB spectrum more vulnerable for large distortions even beyond the thermalization redshift $z \sim 2 \times 10^6$. A full numerical solution of the problem was not obtained yet.

Furthermore we have studied the thermalization of small chemical potential distortions at high redshift, where one expects the largest effects due to relativistic corrections. We obtained analytic approximations for the residual high frequency chemical potential in the case of single energy injection and for heating by annihilating and unstable particles, including relativistic

corrections to CS and DC scattering. Our results show that temperature corrections to Compton scattering are less important (roughly a factor of 4) than DC relativistic corrections, but a conclusive examination requires the inclusion of non-linear effects, possible temperature differences between the electrons and photons (especially for large distortions) and deviations from quasi-equilibrium (especially at lower redshifts). Therefore one has to await a full numerical solution of this problem. Let us note that in the limit of small distortions we have already confirmed the results for single energy injections including DC corrections numerically.

### Non-linear effects

In the derivations presented above we have assumed that $|\mu| \ll 1$. Even in the non-relativistic limit deviations due to non-linear effects lead to significant corrections already for $\mu \gtrsim 10^{-3}$. As noted by Burigana, Danese & de Zotti [25] and Hu & Silk [59], for larger initial chemical potential the value of the critical redshift effectively increases. Here one important effect is that for larger chemical potential the transition between the high ($\mu$ =const) and low ($\mu = 0$) frequencies becomes much faster. Therefore the region where most of the DC emission is arising gets more narrow leading to a strong decrease of the photon production rate. As has been noted by Hu & Silk [59] for $\mu_{\rm i} > 10^{-2} - 10^{-1}$ it is not sufficient to use (5.56) with at larger value of the critical redshift $z_\mu$ in order to account for these effects of non-linearity.

Another point is connected with the decrease of the low frequency non-relativistic DC emission coefficient for larger $\mu$. In Section 4.5.6 we have given approximations for the emission coefficient of Bose-Einstein spectra in the form

$$G_{0,\rm BE} \approx \begin{cases} \frac{4\,\pi^4}{15} \cdot e^{-1.055\,\mu} & \text{for} \quad \mu \leq 1 \\ 24 \cdot e^{-\mu} & \text{for} \quad \mu > 1 \end{cases}. \tag{5.70}$$

Here, for $\mu > 1$ the BE spectrum was approximated by a Wien spectrum $n(x_{\rm e}) = n_0 \cdot e^{-x_{\rm e}}$ with number density $n_0 = e^{-\mu}$. This approximation is sufficient within a few percent for $1 < \mu < 3$ and excellent for $\mu \geq 3$.

Using this expression we have estimated that the solution shows the right tendency: for bigger initial chemical potentials the thermalization is slower. But in fact the solution is only significantly different from (5.56) if the initial chemical potential is $\mu_{\rm i} \geq 5 \cdot 10^{-1}$ and even then the difference is only a few ten percent. Therefore the modification of the DC emission coefficient is likely not responsible for the big differences in the thermalization timescales for $\mu_{\rm i} \lesssim 1$ and $z_{\rm h} > 10^6$.

We conclude that relativistic corrections to DC and possibly to CS may significantly slow down the thermalization of spectral distortions at high redshifts. Especially for large energy injections non-linear effects become very important and a full solution of this problem has to be performed numerically. Due to non-linear effects we expect that corrections exceed the 10 percent level. This may significantly tighten the constraints on the allowed amount of energy injected at $z \geq 2 \times 10^6$.

# Conclusions

We derived the changes to the SZ cluster brightness, flux and number counts induced by the motion of the Solar System with respect to the CMB rest frame (Chapt. 2). Since both the amplitude and direction of this motion are known with high precision it is easy to take these changes into account in the analysis and interpretation of future SZ data. The corrections to the SZ cluster brightness and flux have a similar spectral dependence and amplitude as the first order velocity correction to the th-SZ. Since the motion-induced cluster signal can contribute $\sim 10\%$ of the k-SZ it might be necessary to take it into account in future high precision CMB surveys, dedicated to accurately measuring the line of sight component of the cluster peculiar motions. Furthermore, we have shown that the dipolar asymmetry induced in the SZ cluster number counts in contrast to the counts of more conventional sources can change polarity depending on the observational frequency (see Sect. 2.3.3). This behavior is due to the very specific frequency dependence of the SZ effect. Our estimates show that frequencies around the crossover frequency of the $\sim 217$ GHz and in the range $\sim 400 - 500$ GHz are most promising for a detection of this motion-induced number count asymmetry.

We have discussed in detail the spectral distortions arising due to the superposition of blackbodies with different temperatures in the limit of small temperature fluctuations (Chapt. 3). The superposition leads to y-distortion with y-parameter $y_{\rm S} = \left\langle \delta^2 \right\rangle /2$, where $\left\langle \delta^2 \right\rangle$ denotes the second moment of the temperature distribution function, if the difference in temperatures is less than a few percent of the mean Rayleigh-Jeans temperature. We have shown that in this limit even comparing two pure blackbodies leads to a y-distortion. The results of this derivation were then applied to measurements of the CMB temperature anisotropies with finite angular resolution and in particular to the CMB dipole and its associated spectral distortions, but in principle the method developed here can be applied whenever one is dealing with the superposition of blackbodies with similar temperatures. We have shown that taking the difference of the CMB intensities in the direction of the maximum and the minimum of the CMB dipole leads to a y-distortion with y-parameter $y = 3.1 \cdot 10^{-6}$. This value is 12 times higher than the y-type monopole, $y = 2.6 \cdot 10^{-7}$. Since the amplitude of this distortion can be calculated with the same precision as the CMB dipole, i.e. 0.3% today [51], it may open a way to use it for calibration issues and to check the response of the detectors on small level signals. The main obstacle for measuring and utilizing the effects connected with the superposition of blackbodies is the lack of knowledge about both the spectral and spacial distribution of foregrounds, but given the fast progress in experimental technology and the increasing amount of data available there may still be a way to separate all these signals in the future. In any case, for upcoming CMB experiments spectral distortions arising due to the superposition of blackbodies, the effects of foregrounds and correlated noise should be taken into account simultaneously and self-consistently. As we discussed, an alternative source for calibration issues in the future may be clusters of galaxies, especially for experiments covering only small fractions of the sky.

As a first step towards an inclusion of relativistic corrections into the thermalization problem, in Chapter 4 we have studied the full kinetic equation for the time evolution of the photon phase space density under double Compton scattering. We included both the *creation* of new photons at low frequencies and the *redistribution* of photons at high frequencies. We have shown that the double Compton emissivity strongly decreases with higher mean energy

of the initial photons leading to a suppression of the total number of newly created photons as compared to the non-relativistic limit. On the other hand boosting leads to an enhancement of the double Compton emissivity the higher the electron temperature becomes. Furthermore, an expression for the *effective double Compton Gaunt factor* has been derived and shortly discussed in comparison with the full numerical results (Sect. 4.5.1). We have argued that at least in situations close to thermodynamic equilibrium the evolution of the high frequency photons is not significantly affected by double Compton scattering, but a more detailed study should be undertaken to include cases far from equilibrium. Simple and accurate analytic expressions for the low frequency double Compton scattering emission coefficient of monochromatic initial photons (Sect. 4.4; in the most general situation see Eq. (4.45)) and in the case of Planck, Bose-Einstein and Wien spectra were given (see Sect. 4.5.4). We discussed in detail the double Compton emission for monochromatic initial photons and in the soft photon limit for an incoming Planck spectrum, but expect that our main conclusions also hold for Bose-Einstein, Wien and more general photon distributions. For more general incoming photon distributions two analytic approximations for the low frequency double Compton emission coefficient, equation (4.57) as a *direct* expansion up to fourth order in temperature and (4.58a) as a *inverse* approximation, were deduced, which in combination should describe the full numerical results to better than 5 % in a very broad range of temperatures and involve only 1-dimensional integrals over the photon distribution and its derivatives (see Fig. 4.21 and Sec. 4.5.6 for discussion). If the photons and the electrons have similar temperatures, which is the case in most physical situations close to equilibrium, especially in the context of the thermalization of CMB spectral distortions, then the inverse formula (4.58a) may be applicable up to $k\,T \sim 100\,\mathrm{keV}$ with an accuracy of better than a few percent. Since only first order corrections are necessary for this inverse formula (4.58a), it it generally more suitable for numerical applications.

In the last Chapter we have reexamined the formulation of the thermalization problem including relevant relativistic corrections (such as corrections to Compton scattering, double Compton scattering and the heat capacity of the electrons). Likely, the main corrections arise due to the decrease in the double Compton photon production efficiency for higher temperatures. This should slow down the process of thermalization at high redshifts ($z \geq$ few $\times\, 10^6$) and therefore make the CMB spectrum more vulnerable for large distortions even beyond the thermalization redshift $z \sim 2 \times 10^6$. A full numerical solution of the problem was not obtained yet. Furthermore we have studied the thermalization of small chemical potential distortions at high redshift, where one expects the largest effects due to relativistic corrections. We obtained analytic approximations for the residual high frequency chemical potential in the case of single energy injection and for heating by annihilating and unstable particles, including relativistic corrections to Compton and double Compton scattering. Our results show that temperature corrections to Compton scattering are less important (roughly a factor of 4) than double Compton relativistic corrections, but a conclusive examination requires the inclusion of non-linear effects, possible temperature differences between the electrons and photons (especially for large distortions) and deviations from quasi-equilibrium (especially at lower redshifts). Therefore one has to await a full numerical solution of this problem. Let us note that in the limit of small distortions we have already confirmed the results for single energy injections including double Compton corrections numerically. We conclude that relativistic corrections to double Compton and possibly to Compton scattering may significantly slow down the thermalization of spectral distortions at high redshifts. Especially for large energy injections non-linear effects become very important and a full solution of this problem has to be performed numerically. Due to non-linear effects we expect that corrections exceed the 10 percent level. This may significantly tighten the constraints on the allowed amount of energy injected at $z \geq 2 \times 10^6$.

# Appendix A

# Relativistic Maxwell-Boltzmann distribution

In this Chapter we shall summarize some of the most important properties of a relativistic Maxwell-Boltzmann distribution for particles of species i in an isotropic plasma. Although most of the material presented here can be found in standard textbooks, the relations and approximations given here will be of great use in the discussion of the kinetic equation of DC scattering and the thermalization of spectral distortions of the CMB in the early universe.

## A.1 Number and phase space density

The number density $N_{\rm i}$ of a gas of particles of species i is defined by the integral

$$N_{\rm i} = \frac{g_{\rm i}}{(2\pi\hbar)^3}\int_0^\infty 4\pi\, p^2\, f_{\rm i}(p)\,{\rm d}p \tag{A.1}$$

over the phase space density $f_{\rm i}(p)$, where $g_{\rm i}$ gives the number of spin states ($\gamma$, e, H, He: $g=2$; $\nu$: $g=1$). For Fermions the general phase space distribution can be written in the form $f_{\rm i}(g) \propto 1/[e^{(\epsilon+\mu)/\theta_{\rm i}}+1]$, with chemical potential $\mu$. Here $\epsilon = E/m_{\rm i}\,c^2 = \sqrt{1+\eta^2}$ is the relativistic energy $E$ in units of the rest mass, $m_{\rm i}\,c^2$, of the particles with $\eta = p/m_{\rm i}\,c$ and the dimensionless temperature, $\theta_{\rm i} = k\,T_{\rm i}/m_{\rm i}\,c^2$, of the gas.

When the gas in non-degenerate ($N_{\rm i} \ll 1$) Fermi-blocking becomes negligible and thus Maxwell-Boltzmann statistics is applicable. In this case the distribution of the particle momenta $p$ is given by $f_{\rm i}(p) \propto e^{-\epsilon/\theta_{\rm i}}$. Inserting $f_{\rm i}(p) = A\cdot\, e^{-\epsilon/\theta_{\rm i}}$ into (A.1) one can deduce the corresponding normalization $A$ (for some details see Appendix A.5). In a relativistic Maxwell-Boltzmann gas the phase space density then is described by the distribution function

$$f_{\rm i}(p) = \frac{\lambda_{\rm i}^3}{g_{\rm i}}\,\frac{N_{\rm i}}{4\pi\,K_2(1/\theta_{\rm i})\,\theta_{\rm i}}\,e^{-\epsilon/\theta_{\rm i}}\,, \tag{A.2}$$

where $\lambda_{\rm i} = h/m_{\rm i}\,c$ is the *Compton wavelength* of the particle of species i. Furthermore $K_2(x)$ is the modified Bessel function of second kind [1].

## A.2 Low temperature expansion of the relativistic Maxwell-Boltzmann distribution

In the case $\theta_{\rm i} \ll 1$ a Maxwell-Boltzmann gas becomes non-relativistic. For a given species of particles this happens at higher temperatures (i.e. earlier times in the history of the universe) the bigger their mass $m_{\rm i}$ is. Therefore in the history of the expanding universe electrons stay longer relativistic (up to redshift $z \sim 10^8 - 10^9$) than for example protons ($z \sim 10^{11} - 10^{12}$).

The low temperature expansion of (A.2) leads to

$$\begin{aligned} f_{\mathrm{i}}(p) = \frac{N_{\mathrm{i}}\, e^{-\xi}}{(2\pi\, m_{\mathrm{i}}^6\, \theta_{\mathrm{i}})^{3/2}} \Bigg[ & 1 - \theta_{\mathrm{i}} \cdot \left( \frac{15}{8} - \frac{1}{2}\xi^2 \right) + \theta_{\mathrm{i}}^2 \cdot \left( \frac{345}{128} - \frac{15}{16}\xi^2 - \frac{1}{2}\xi^3 + \frac{1}{8}\xi^4 \right) \\ & - \theta_{\mathrm{i}}^3 \cdot \left( \frac{3285}{1024} - \frac{345}{256}\,\xi^2 - \frac{15}{16}\,\xi^3 - \frac{25}{64}\,\xi^4 + \frac{1}{4}\,\xi^5 - \frac{1}{48}\,\xi^6 \right) \\ & + \theta_{\mathrm{i}}^4 \cdot \left( \frac{95355}{32768} - \frac{3285\,\xi^2}{2048} - \frac{345\,\xi^3}{256} - \frac{855\,\xi^4}{1024} - \frac{13\,\xi^5}{32} + \frac{51\,\xi^6}{128} - \frac{\xi^7}{16} + \frac{\xi^8}{384} \right) , \end{aligned} \tag{A.3}$$

with $\xi = \eta^2/2\,\theta_{\mathrm{i}}$ and $\eta = p/m_{\mathrm{i}}\, c$.

## A.3 Energy density and pressure

The energy density $\rho_{\mathrm{i}}$ and pressure $P_{\mathrm{i}}$ of a gas of particles of species i are defined by the integrals

$$\rho_{\mathrm{i}} = \frac{g_{\mathrm{i}}}{(2\pi\hbar)^3} \int_0^\infty 4\pi\, E\, p^2\, f_{\mathrm{i}}(p)\, \mathrm{d}p \tag{A.4a}$$

$$P_{\mathrm{i}} = \frac{g_{\mathrm{i}}}{(2\pi\hbar)^3} \int_0^\infty 4\pi\, \frac{p^2 c^2}{3\, E}\, p^2\, f_{\mathrm{i}}(p)\, \mathrm{d}p\,. \tag{A.4b}$$

Inserting the phase space density (A.2) the results

$$\rho_{\mathrm{i}} = m_{\mathrm{i}}\, c^2\, N_{\mathrm{i}}\, F(\theta_{\mathrm{i}}) \tag{A.5a}$$

$$P_{\mathrm{i}} = N_{\mathrm{i}}\, k\, T_{\mathrm{i}} \tag{A.5b}$$

can be found (for details see Appendix (A.5)). Here the function $F(\theta_{\mathrm{i}})$ is defined by

$$F(\theta_{\mathrm{i}}) = \left[ 3\,\theta_{\mathrm{i}} + \frac{K_1(1/\theta_{\mathrm{i}})}{K_2(1/\theta_{\mathrm{i}})} \right] , \tag{A.6}$$

where $K_1(x)$ is the modified Bessel function of first kind [1]. As equation (A.5b) shows a relativistic Maxwell-Boltzmann gas has the same equation of state as a non-relativistic, ideal gas. For low temperatures ($\theta_{\mathrm{i}} \ll 1$) by expanding (A.6) one finds the expression

$$\rho_{\mathrm{i}} = m_{\mathrm{i}}\, c^2\, N_{\mathrm{i}} + \frac{3}{2}\, N_{\mathrm{i}}\, k\, T_{\mathrm{i}} \left[ 1 + \frac{5}{4}\,\theta_{\mathrm{i}} - \frac{5}{4}\,\theta_{\mathrm{i}}^2 + \frac{45}{64}\,\theta_{\mathrm{i}}^3 + \frac{15}{16}\,\theta_{\mathrm{i}}^4 \right] + \mathcal{O}(\theta_{\mathrm{i}}^6) \tag{A.7}$$

In the non-relativistic case this reduces to $\rho_{\mathrm{i}} = m_{\mathrm{i}}\, c^2\, N_{\mathrm{i}} + \frac{3}{2}\, N_{\mathrm{i}}\, k\, T_{\mathrm{i}}$.

## A.4 Heat capacity

The specific heat capacity for constant volume $c_V$ is defined by $N_{\mathrm{i}}\, c_V = \mathrm{d}\rho_{\mathrm{i}}/\,\mathrm{d}T_{\mathrm{i}}$. Using (A.5a) one may find

$$\begin{aligned} c_V = k\, \frac{\mathrm{d}F(\theta_{\mathrm{i}})}{\mathrm{d}\theta_{\mathrm{i}}} &= k \left[ 3 + \frac{K_2(1/\theta_{\mathrm{i}})\,[K_1(1/\theta_{\mathrm{i}}) + K_2(1/\theta_{\mathrm{i}})] - K_1(1/\theta_{\mathrm{i}})\,[K_1(1/\theta_{\mathrm{i}}) + K_3(1/\theta_{\mathrm{i}})]}{2\,\theta_{\mathrm{i}}\, K_2(1/\theta_{\mathrm{i}})} \right] \\ &\approx \frac{3}{2}\, k \left[ 1 + \frac{5}{2}\,\theta_{\mathrm{i}} - \frac{15}{4}\,\theta_{\mathrm{i}}^2 + \frac{45}{16}\,\theta_{\mathrm{i}}^3 + \frac{75}{16}\,\theta_{\mathrm{i}}^4 \right] + \mathcal{O}(\theta^5)\,. \end{aligned} \tag{A.8}$$

In the non-relativistic limit this reduces to $c_V = \frac{3}{2} k$ for an ideal gas.

## A.5 Solving integrals over the relativistic Maxwell-Boltzmann distribution

To find the normalization of a relativistic Maxwell-Boltzmann distribution one has to solve the integral of the form

$$\frac{A \cdot g_\mathrm{i}}{(2\pi\hbar)^3} \int_0^\infty 4\pi\, p^2\, e^{-\sqrt{1+(p/m_\mathrm{i}\, c)^2}/\theta_\mathrm{i}}\, \mathrm{d}p. \tag{A.9}$$

Here one can use the substitution $p/m_\mathrm{i}\, c = \sinh(x)$. With this integral (A.9) reduces to

$$\frac{A \cdot 4\pi\, g_\mathrm{i}\, (m_\mathrm{i}\, c)^3}{(2\pi\hbar)^3} \int_0^\infty \sinh^2(x) \cosh(x)\, e^{-\cosh(x)/\theta_\mathrm{i}}\, \mathrm{d}x \tag{A.10}$$

The solution of the integral then can be found by comparison with

$$\int_0^\infty \sinh(\gamma\, x)\, \sinh(x)\, e^{-u\, \cosh(x)}\, \mathrm{d}x = \frac{\gamma}{u}\, K_\gamma(1/u) \tag{A.11}$$

From this it follows that the normalization of the relativistic Maxwell-Boltzmann distribution of particles is given as

$$A = \frac{\lambda_\mathrm{i}^3}{g_\mathrm{i}} \frac{N_\mathrm{i}}{4\pi\, K_2(1/\theta_\mathrm{i})\, \theta_\mathrm{i}}, \tag{A.12}$$

where $\lambda_\mathrm{i} = h/m_\mathrm{i}c$ is the Compton wavelength of the particle and $N_\mathrm{i}$ is the number density.

To solve the integrals (A.5a) and (A.5b) for the energy density and the pressure of a relativistic Maxwell-Boltzmann gas one again can use the substitution $p/m_\mathrm{i}\, c = \sinh(x)$. This then leads to integrals of the form

$$\int_0^\infty \sinh(2x)\, \sinh(2x)\, e^{-u\, \cosh(x)}\, \mathrm{d}x \tag{A.13a}$$

$$\int_0^\infty \sinh^4(x)\, e^{-u\, \cosh(x)}\, \mathrm{d}x \tag{A.13b}$$

The first one may be solved by the identity $\cosh(x)\, e^{-u\, \cosh(x)} = -\partial_u\, e^{-u\, \cosh(x)}$ and interchanging the derivation and integration, whereas the second can be solved by the replacement $\sinh^2(x) = 1 + \cosh^2(x)$ and the solution of the first one.

# Appendix B

# Relations for the photon phase space distribution

Any isotropic photon phase space distribution or *occupation number* can be written in the form

$$n(x) = \frac{1}{e^{x+\mu(x)} - 1}\,, \tag{B.1}$$

where $x = h\nu/k\,T_\gamma$ is the dimensionless frequency and $\mu(x)$ is the dimensionless and frequency dependent chemical potential. Here the photon temperature $T_\gamma$ should be regarded as a *parameter* describing the *energy density* of the photon field (see Sect. B.2).

From (B.1) one can immediately write down the value of the chemical potential and the *brightness* temperature

$$\mu(x) = \ln\left(\frac{1+n}{n}\right) - x \tag{B.2a}$$

$$T_*(x) = \frac{T_\gamma}{1+\mu(x)/x} \tag{B.2b}$$

for any kind of spectrum. For $\mu(x) = 0$ one obtains the occupation number for *Planckian* photons and for $\mu(x) = \mu_0 = \text{const}$ equation (B.1) represents a *Bose-Einstein* distribution, which in the limit of $\mu_0 \gg 1$ becomes a *Wien* distribution. We will now summarize some of the most important relations for $n(x)$ and quantities like its number and energy density, pressure and effective temperature.

## B.1 Pressure, energy and number density

In Chapter A we have given the definitions of the number density (A.1), the energy density (A.4a) and pressure (A.4b) of a gas of particles. For photons using $p = E/c = h\nu/c$ and $g_\gamma = 2$ one can easily find

$$N_\gamma = \kappa_\gamma\,\theta_\gamma^3 \cdot \mathcal{G}_{2,1} \tag{B.3a}$$

$$\rho_\gamma = m_\mathrm{e}c^2\,\kappa_\gamma\,\theta_\gamma^4 \cdot \mathcal{G}_{3,1} \tag{B.3b}$$

$$P_\gamma = \rho_\gamma/3\,, \tag{B.3c}$$

with the dimensionless temperature $\theta_\gamma = k\,T_\gamma/m_\mathrm{e}c^2$ and $\kappa_\gamma = 8\,\pi\,\lambda_\mathrm{e}^{-3} \approx 1.7595 \times 10^{30}\,\mathrm{cm}^{-3}$, where $\lambda_\mathrm{e} = h/m_\mathrm{e}c = 2.426 \times 10^{-10}\,\mathrm{cm}$ is the *Compton wavelength* of the electron. We also made use of the definitions (D.14) for $\mathcal{G}_{i,j}$.

In the case of Planckian photons, $n_\mathrm{Pl}(x) = 1/(e^x - 1)$, the integrals $\mathcal{G}_{i,j}$ are given by $\mathcal{G}_{2,1}^\mathrm{Pl} \approx 2.4041$ and $\mathcal{G}_{3,1}^\mathrm{Pl} \approx 6.4939$ and their ratio $\mathcal{G}_{3,1}^\mathrm{Pl}/\mathcal{G}_{2,1}^\mathrm{Pl} \approx 2.7012$. In the more general case

one has to evaluate these numerically. For small chemical potential $|\mu| \ll 1$ one can introduce the approximation

$$n \approx n_{\rm Pl} + \mu(x) \cdot \partial_x n_{\rm Pl} = n_{\rm Pl} - n_{\rm Pl}[1 + n_{\rm Pl}] \cdot \mu(x)\,. \tag{B.4}$$

Now, introducing the number $N_{\rm Pl}$ and energy density $\rho_{\rm Pl}$ for Planckian photons, one can find that the corresponding energy and number density in this limit are given by $\rho_\gamma = \rho_{\rm Pl} \cdot f_\mu$ and $N_\gamma = N_{\rm Pl} \cdot \phi_\mu$, respectively, where the functions $f_\mu$ and $\phi_\mu$ were defined as:

$$f_\mu \;=\; 1 - \frac{3I_2}{I_3} \cdot \left[\frac{I_2^\mu}{I_2} + \frac{1}{3}\,\frac{I_3^{\mu'}}{I_2}\right] \tag{B.5a}$$

$$\phi_\mu \;=\; 1 - \frac{2I_1}{I_2} \cdot \left[\frac{I_1^\mu}{I_1} + \frac{1}{2}\,\frac{I_1^{\mu'}}{I_1}\right]\,, \tag{B.5b}$$

with the integrals $I_i = \int_0^\infty x^i\, n_{\rm Pl}\,{\rm d}x$, $I_i^{g(x)} = \int_0^\infty x^i\, g(x)\, n_{\rm Pl}\,{\rm d}x$ and $\mu' = \partial_x \mu$. Here $3I_2/I_3 \approx 1.111$ and $2I_1/I_2 \approx 1.368$. Similar expression where given by Sunyaev & Zeldovich [126] and Illarionov & Sunyaev [65], assuming constant $\mu$, i.e. $I_i^\mu = \mu\, I_i$ and $I_i^{\mu'} = 0$.

## B.2 Effective temperature

For any photon field with given energy density $\rho_\gamma$ one can define the effective temperature $T_{\rm eff}$:

$$\frac{k\,T_{\rm eff}}{m_{\rm e}c^2} = \left[\frac{\rho_\gamma}{\kappa_\gamma\,\mathcal{G}_{3,1}^{\rm Pl}}\right]^{1/4}\,. \tag{B.6}$$

The effective temperature corresponds to the *thermodynamic* temperature of a blackbody with total energy density $\rho_{\rm Pl} = \rho_\gamma$. In the definitions (B.3) we have used the temperature $T_\gamma$ as a *parameter* to describe the photon field. Inserting (B.3b) into (B.6) one can obtain the relation

$$T_{\rm eff} = T_\gamma \left[\frac{\mathcal{G}_{3,1}}{\mathcal{G}_{3,1}^{\rm Pl}}\right]^{1/4} \tag{B.7}$$

between these two quantities.

Note that in numerical applications one can principally chose any $T_\gamma$ to characterize the photon distribution. Of course in this case the integrals $\mathcal{G}_{i,j}$ change accordingly, since the number and energy densities should not depend on this choice. This usually introduced an artificial frequency dependent chemical potential.

## B.3 Useful relations between $n(x, \mu(x))$ and its derivatives $\partial_x^i n$

Using (B.1) one can easily derive the partial derivatives of the occupation number with respect to $x$. Here we present these relations up to third order derivatives. One may find:

$$\partial_x n = -n(n+1)\,\left[1 + \mu'\right] \tag{B.8a}$$

$$\partial_x^2 n = +n(n+1)\,\left[(2\,n+1)\cdot(1+\mu')^2 - \mu''\right] \tag{B.8b}$$

$$\partial_x^3 n = -n(n+1)\,\left[(6\,n(n+1)+1)\cdot(1+\mu')^3 - 3(2n+1)\cdot(1+\mu')\mu'' - \mu'''\right] \tag{B.8c}$$

where prime denotes the derivative with respect to $x$.

# Appendix C

# Collection of analytic approximations for the Compton scattering kernel

In this Chapter we give some of the analytic approximations which were of great use in the discussion and numerical implementation for the DC emission kernel.

## C.1 Compton kernel for cold electrons

The full expression for the Compton kernel of cold electrons can be derived in a similar way as is presented in Pozdnyakov et al. [100] in lowest order of $\omega_0 = \nu_0/m_\mathrm{e}$. It follows

$$\mathcal{P}_0(\nu_0 \rightarrow \nu_1) = \frac{3}{8}\,\frac{\sigma_\mathrm{T}\,N_\mathrm{e}}{\omega_0^2}\left[2 - \frac{2\Delta}{\omega_0} + \frac{\Delta^2}{1+\Delta} + \frac{\Delta^2}{\omega_0^2}\right] \overset{\omega_0\ll 1}{\underset{\approx}{\downarrow}} \frac{3}{8}\,\frac{\sigma_\mathrm{T}\,N_\mathrm{e}}{\omega_0^2}\left[1 + \left(\frac{\nu_1-\nu_0}{\nu_0}\right)^2\right], \quad \text{(C.1)}$$

with $\Delta = \frac{\nu_0-\nu_1}{\nu_1}$. This expression is valid in the frequency range $\nu_0[1-2\,\nu_0/(1+2\,\nu_0)] \leq \nu_1 \leq \nu_0$.

### C.1.1 Normalization, mean energy and dispersion of the Compton kernel for cold electrons

With (C.1) and similar definitions as (4.21) one may obtain

$$\mathcal{N}_{\mathcal{P}_0,\mathrm{CS}} = \frac{3}{8}\,\frac{\sigma_\mathrm{T}\,N_\mathrm{e}}{\omega_0^2}\left\{\frac{2[2+\omega_0(1+\omega_0)(8+\omega_0)]}{(1+2\omega_0)^2} - \frac{2+\omega_0(2-\omega_0)}{\omega_0}\,\ln(1+2\omega_0)\right\}$$
$$\overset{\omega_0\ll 1}{\underset{\approx}{\downarrow}} \sigma_\mathrm{T}\,N_\mathrm{e}\left[1 - 2\,\omega_0 + \frac{26}{5}\,\omega_0^2\right] \quad \text{(C.2a)}$$

$$\bar{w}_{\mathcal{P}_0,\mathrm{CS}} = \frac{3}{8\mathcal{N}_{\mathcal{P}_0,\mathrm{CS}}}\,\frac{\sigma_\mathrm{T}\,N_\mathrm{e}}{\omega_0^2}\left\{\frac{\ln(1+2\omega_0)}{\omega_0} - \frac{6+2\,\omega_0[15+2\,\omega_0(9-\omega_0[3+8\,\omega_0])]}{3(1+2\omega_0)^3}\right\}$$
$$\overset{\omega_0\ll 1}{\underset{\approx}{\downarrow}} 1 - \omega_0 + \frac{11}{5}\,\omega_0^2 \quad \text{(C.2b)}$$

$$\sigma^2_{\mathcal{P}_0,\mathrm{CS}} = \frac{\sigma_\mathrm{T}\,N_\mathrm{e}}{\mathcal{N}_{\mathcal{P}_0,\mathrm{CS}}}\,\frac{2+\omega_0[8+\omega_0(14+9\,\omega_0)]}{2(1+2\omega_0)^4} - \bar{w}^2_{\mathcal{P}_0,\mathrm{CS}}$$
$$\overset{\omega_0\ll 1}{\underset{\approx}{\downarrow}} \frac{2}{5}\,\omega_0^2\,, \quad \text{(C.2c)}$$

Here it is important to note that the integrations over $\mathrm{d}\nu_1$ were carried out in the range $\nu_0[1-2\,\nu_0/(1+2\,\nu_0)] \leq \nu_1 \leq \nu_0$.

## C.2 Compton kernel for thermal electrons

Sazonov & Sunyaev [113] gave an expression (Eq. 19a in that paper) for the Compton kernel in a hot, isotropic medium, which is applicable in the range $h\nu_0(h\nu_0/m_\mathrm{e}c^2) \lesssim k\,T_\mathrm{e} \lesssim 25\,\mathrm{keV}$ and $h\nu_0 \lesssim 50\,\mathrm{keV}$. More analytic approximations for the Compton kernel in different limits may be also found in Sazonov & Sunyaev [113] and references therein.

### C.2.1 Normalization, mean energy and dispersion of the Compton kernel for thermal electrons

In this case we use the approximations for the moments given by Sazonov & Sunyaev [113] (see Eq. 25 therein) and definition of the mean energy and dispersion similar to (4.21). From this it follows

$$\mathcal{N}_{\mathcal{P},\mathrm{CS}} \approx \sigma_\mathrm{T}\,N_\mathrm{e}\left[1 - 2\,\omega_0 - \frac{44}{5}\,\omega_0\,\theta_\mathrm{e} - \frac{53}{10}\,\theta_\mathrm{e}^2 + \frac{63}{20}\,\omega_0^2\right] \tag{C.3a}$$

$$\bar{w}_{\mathcal{P},\mathrm{CS}} \approx 1 + 4\,\theta_\mathrm{e} + 10\,\theta_\mathrm{e}^2 - \omega_0 - \frac{31}{2}\,\omega_0\,\theta_\mathrm{e} + \frac{11}{5}\,\omega_0^2 \tag{C.3b}$$

$$\sigma^2_{\mathcal{P},\mathrm{CS}} \approx 2\,\theta_\mathrm{e} + 31\,\theta_\mathrm{e}^2 - \frac{66}{5}\,\omega_0\,\theta_\mathrm{e} + \frac{2}{5}\,\omega_0^2\,, \tag{C.3c}$$

In our numerical integrations we used $\sigma^2 \approx [2 + 31\,\theta_\mathrm{e}]\theta_\mathrm{e}$ to estimate the width of the DC kernel and the range of integration for the number and energy densities of the DC emission spectrum.

# Appendix D

# Double Compton scattering

## D.1 Squared matrix element for double Compton scattering

In order to write down the DC differential cross section one has to calculate the squared matrix element $|\mathcal{M}|^2$ describing the DC process. This calculation was first performed by Mandl & Skyrme [81]. In the book of Jauch & Rohrlich [69] one can find the expression for the squared matrix element of the double Compton process (pp. 235):

$$\begin{aligned} X = {} & 2\,(a\,b-c)\left[\,(a+b)\,(2+x)-(a\,b-c)-8\right]-2\,x\left[a^2+b^2\right]-2\,\left[a\,b+c\,(1-x)\right]\rho \\ & -8\,c+\frac{4\,x}{A\,B}\left[(A+B)\,(1+x)+x^2\,(1-z)+2\,z-(a\,A+b\,B)\left(2+\frac{(1-x)\,z}{x}\right)\right], \end{aligned} \tag{D.1}$$

where the following abbreviations have been used

$$a=\frac{1}{\kappa_0}+\frac{1}{\kappa_1}+\frac{1}{\kappa_2} \qquad b=\frac{1}{\kappa_0'}+\frac{1}{\kappa_1'}+\frac{1}{\kappa_2'} \qquad c=\frac{1}{\kappa_0\,\kappa_0'}+\frac{1}{\kappa_1\,\kappa_1'}+\frac{1}{\kappa_2\,\kappa_2'} \tag{D.2a}$$

$$x=\kappa_0+\kappa_1+\kappa_2 \qquad\qquad z=\kappa_0\,\kappa_0'+\kappa_1\,\kappa_1'+\kappa_2\,\kappa_2' \tag{D.2b}$$

$$A=\kappa_0\,\kappa_1\,\kappa_2 \qquad B=\kappa_0'\,\kappa_1'\,\kappa_2' \qquad \rho=\frac{\kappa_0}{\kappa_0'}+\frac{\kappa_0'}{\kappa_0}+\frac{\kappa_1}{\kappa_1'}+\frac{\kappa_1'}{\kappa_1}+\frac{\kappa_2}{\kappa_2'}+\frac{\kappa_2'}{\kappa_2}\,. \tag{D.2c}$$

For the definitions of $\kappa_i$, $\kappa_i'$ we used those of the original paper from Mandl & Skyrme [81]:

$$m_\mathrm{e}^2\,\kappa_0=-P\cdot K_0 \qquad m_\mathrm{e}^2\,\kappa_1=+P\cdot K_1 \qquad m_\mathrm{e}^2\,\kappa_2=+P\cdot K_2 \tag{D.3a}$$

$$m_\mathrm{e}^2\,\kappa_0'=+P'\cdot K_0 \qquad m_\mathrm{e}^2\,\kappa_1'=-P'\cdot K_1 \qquad m_\mathrm{e}^2\,\kappa_2'=-P'\cdot K_2\,, \tag{D.3b}$$

with the standard signature of the Minkowski-metric $(+\,-\,-\,-)$. Assuming that the outgoing photon $K_2$ is *soft* as compared with $K_1$ one can expand $X$ into orders of the frequency $\omega_2$ and keep only the lowest order term, i.e. terms of the order $\mathcal{O}(\omega_2^{-2})$. Similar expansions for the limits $\omega_0 \ll 1$ and $\beta \ll 1$ can be performed. Since the results of these expansions are extremely complex and not very illuminating, we omitted them here.

## D.2 Numerical solution of the Boltzmann integrals

In order to solve the Boltzmann integrals we implemented two different programs, one based on the NAG routine `D01GBF`, which uses an adaptive Monte-Carlo method to solve multidimensional integrals, the other using the VEGAS routine of the CUBA Library[1] [55]. The latter turned out to

[1] Download of the CUBA Library available at: http://www.feynarts.de/cuba/

be much more efficient since it significantly benefitted from importance sampling. The expense and performance of the calculation critically depend on the required accuracy. For most of the calculations presented here we chose a relative error of the order of $\epsilon \sim 10^{-3}$.

Since at high frequencies the DC spectra (especially for the conditional DC kernel) have rather complex structure we also implemented an adaptive mesh refinement scheme to decrease the amount of actually calculated points to a minimum and obtained the rest by polynomial interpolation. Still a couple of tens to hundreds points were typically necessary for an accurate representation of the DC emission spectrum in the full frequency range. The typical time the calculation for one spectrum took was a few hours on a 2.8 GHz processor, for high temperature cases even up to one night. In order to compare the numerical with the analytical results in some cases even accuracies up to $\epsilon \sim 10^{-4}$ were necessary, making the integration extremely hard and time consuming.

### Treatment of the infrared divergence

The calculation was further complicated by the appearance of the *infrared* divergence at low frequencies. Choosing a lower frequency cutoff, $\nu_{2,\mathrm{min}}$, we assumed that in any event the energy of the *scattered* photon $K_1$ had to be larger than this lower cutoff, i.e. $\nu_1 \geq \nu_{2,\mathrm{min}}$. Especially for high frequencies $\nu_2$ of the *emitted* photon, i.e. when it was energetically playing the role of the *scattered* photon, this significantly decreases the accessible phase space volume for $K_1$. In calculations we always made sure that the chosen parameters lay within the allowed phase space volume by checking their consistency with the energy and momentum equation (4.6a) and (4.6b). Here one point is very important. Since $\Sigma_2 = (P + K_0 - K_2) \cdot \hat{K}_1 \equiv P' \cdot \hat{K}_1$ for allowed interactions should always be non-negative also $\Sigma_1 = P \cdot K_0 - P \cdot K_2 - K_0 \cdot K_2$ has to fulfill the same condition. Although for $\Sigma_1 < 0 \ \wedge \ \Sigma_2 < 0$ it still follows that $0 \leq \omega_1$ the 4-vector $P'$ would lie outside the light-cone and therefore violate causality.

### Integration over the electron momenta

In oder to restrict the integration region over the electron momenta for low electron temperature we determined the maximal Lorentz factor, $\gamma_{\mathrm{max}}$, such that the change in the normalization of the electron distribution was less than a fraction of the required accuracy. Furthermore, instead of $p$ we used the variable $\xi = \eta^2/2\,\theta_\mathrm{e}$ with $\eta = p/m_\mathrm{e}$.

For high electron temperature it turned out to be more efficient to use the normalization of the electron distribution itself as a variable. For this we defined

$$N(x) = \int_1^x \gamma\sqrt{\gamma^2-1}\, f(\gamma m_\mathrm{e})\,\mathrm{d}\gamma\,, \tag{D.4}$$

which for $x \to \infty$ becomes $N \equiv N_\mathrm{e}$. For calculations one now had to invert this equation and find the function $x(N)$. This was done numerically before the integrations were performed for a sufficiently large number of points ($n \sim 512$), such that the function $x(N)$ during the integrations could be accurately given by spline interpolation.

### Domains of integration for the photons

Using energetic arguments one can obtain constraints on the allowed range of photon frequencies. Since the energy of the scattered photon should be *non-negative*, the condition $0 \leq \omega_1$ leads to different regions of integration. To obtain these regions one should consider the inequality

$$0 \leq \frac{\gamma\omega_0\lambda_0 - \omega_2[\gamma\lambda_2 + \omega_0\alpha_{02}]}{\gamma\lambda_1 + \omega_0\alpha_{01} - \omega_2\alpha_{12}} \equiv \frac{\Sigma_1}{\Sigma_2}\,, \tag{D.5}$$

where we used the abbreviations $\lambda_i = \hat{P}\cdot\hat{K}_i$ and $\alpha_{ij} = \hat{K}_i\cdot\hat{K}_j$. Since $\Sigma_2 = (P+K_0-K_2)\cdot\hat{K}_1 \equiv P'\cdot\hat{K}_1 \geq 0$ for allowed interactions should always be non-negative the quantities $\Sigma_i$ have to

fulfill $\Sigma_1 > 0 \wedge \Sigma_2 > 0$ in order to satisfy (D.5) and causality. Therefore one can define the frequencies $\omega_{2,\Sigma_i}$

$$\omega_{2,\Sigma_1} = \frac{\gamma\omega_0\lambda_0}{\gamma\lambda_2 + \omega_0\alpha_{02}} \qquad \omega_{2,\Sigma_2} = \frac{\gamma\lambda_1 + \omega_0\alpha_{01}}{\alpha_{12}}\,, \tag{D.6}$$

for which $\Sigma_i|_{\omega_2=\omega_{2,\Sigma_i}} = 0$ is fulfilled. This then lead to the interval

$$0 \le \omega_2 \le \min(\omega_{2,\Sigma_1}, \omega_{2,\Sigma_2}) \tag{D.7}$$

for integrations over $\mathrm{d}\omega_2$. In calculations of moments of the DC kernel this condition significantly reduces the required phase space volume. Note that $\omega_{2,\Sigma_1}$ is equivalent to the energy conservation equation for Compton scattering.

In calculations of the full Boltzmann collision integral for incoming distributions of photons one has to integrate over $\mathrm{d}\omega_0$. For the reaction channels (4.1a) and (4.1b) again one can restrict the range of integrations using (D.5). In this case the frequencies $\omega^{\mathrm{ab}}_{0,\Sigma_i}$, for which the condition $\Sigma_i|_{\omega_0=\omega^{\mathrm{ab}}_{0,\Sigma_i}} = 0$ is fulfilled, can be defined as

$$\omega^{\mathrm{ab}}_{0,\Sigma_1} = \frac{\gamma\omega_2\lambda_2}{\gamma\lambda_0 - \omega_2\alpha_{02}} \qquad \omega^{\mathrm{ab}}_{0,\Sigma_2} = \frac{\omega_2\alpha_{12} - \gamma\lambda_1}{\alpha_{01}}\,. \tag{D.8}$$

If $\omega_2 \ge \gamma\lambda_0/\alpha_{02}$ only $\Sigma_1 < 0$ is possible for all values of $\omega_0$. Therefore one finds

$$\omega_2 \ge \frac{\gamma\lambda_0}{\alpha_{02}} \;\Rightarrow\; \text{no allowed region for } \omega_0 \tag{D.9a}$$

$$\omega_2 < \frac{\gamma\lambda_0}{\alpha_{02}} \;\Rightarrow\; \max(\omega^{\mathrm{ab}}_{0,\Sigma_1}, \omega^{\mathrm{ab}}_{0,\Sigma_2}) \le \omega^{\mathrm{ab}}_0\,. \tag{D.9b}$$

Here one in principle may use the condition $\omega_2 \ge \gamma\lambda_0/\alpha_{02}$ to for example limit the range of possible scattering angles $\theta_{02}$. This then leads to an inequality of the form $a_1\sqrt{1-\mu_{02}^2} \ge a_2\,\mu_{02} + a_3$, which has various solutions for different coefficients $a_i$. In our calculations we did not make use of this restrictions until now. Especially for large electron temperature ($\theta_{\mathrm{e}} \ge 0.01$) and at high frequencies this will lead to a significant increase of efficiency.

For the reaction channels (4.1c) and (4.1d) the inequality

$$0 \le \frac{\gamma\omega_2\lambda_2 - \omega_0[\gamma\lambda_0 + \omega_2\alpha_{02}]}{\gamma\lambda_1 + \omega_2\alpha_{12} - \omega_0\alpha_{01}} \equiv \frac{\tilde{\Sigma}_1}{\tilde{\Sigma}_2}\,, \tag{D.10}$$

in a similar way as described above yields

$$\omega^{\mathrm{cd}}_{0,\Sigma_1} = \frac{\gamma\omega_2\lambda_2}{\gamma\lambda_0 + \omega_2\alpha_{02}} \qquad \omega^{\mathrm{cd}}_{0,\Sigma_2} = \frac{\omega_2\alpha_{12} + \gamma\lambda_1}{\alpha_{01}} \tag{D.11}$$

and

$$0 \le \omega^{\mathrm{cd}}_0 \le \min(\omega^{\mathrm{cd}}_{0,\Sigma_1}, \omega^{\mathrm{cd}}_{0,\Sigma_2})\,. \tag{D.12}$$

In actual integrations one would in addition introduce a lower and upper energy cutoff and modify the equations accordingly. We have checked the correctness of the conditions obtained above setting $\omega_{\min} \le \omega \le \omega_{\max}$, where in the cases of kernel integrations we used the assumed lower energy cutoff as $\omega_{\min}$ and a constant large value for $\omega_{\max}$ (this value was estimated using the mean and dispersion of the Compton kernel and then multiplying it by a factor of 20), of course with significant loss of efficiency, since many evaluations of the functions were done outside the accessible phase space volume. For Planckian photons we typically used $\omega_{\min} = 10^{-6}\,\theta_\gamma$ and $\omega_{\max} = 25\,\theta_\gamma$.

## D.3 Results for the integrals $I_k$'s up to $\mathcal{O}(\theta_\mathrm{e}^4)$

Here the $I_k$ following from (4.55d) are given for the lowest order in frequency $x_{\mathrm{e},2}$.

$$I_0 = \left[1+\theta_\mathrm{e}\left(6-\frac{21}{5}x_\mathrm{e}\right)+\theta_\mathrm{e}^2\left(15-\frac{441}{10}\,x_\mathrm{e}+\frac{357}{25}\,x_\mathrm{e}^2\right)+\theta_\mathrm{e}^3\left(\frac{45}{4}-\frac{8379}{40}\,x_\mathrm{e}+\frac{5712}{25}\,x_\mathrm{e}^2 -\frac{7618}{175}\,x_\mathrm{e}^3\right)+\theta_\mathrm{e}^4\left(-\frac{45}{4}-\frac{3969}{8}\,x_\mathrm{e}+\frac{8568}{5}\,x_\mathrm{e}^2-\frac{34281}{35}\,x_\mathrm{e}^3+\frac{21498}{175}\,x_\mathrm{e}^4\right)\right]x_\mathrm{e}^2 \tag{D.13a}$$

$$I_1 = \frac{7}{5}\,\theta_\mathrm{e}\left[6-x_\mathrm{e}+\theta_\mathrm{e}\left(63-\frac{109}{2}\,x_\mathrm{e}+\frac{44}{7}\,x_\mathrm{e}^2\right)+\theta_\mathrm{e}^2\left(\frac{1197}{4}-\frac{6031}{8}\,x_\mathrm{e}+\frac{78276}{245}\,x_\mathrm{e}^2 -\frac{13409}{490}\,x_\mathrm{e}^3\right)+\theta_\mathrm{e}^3\left(\frac{2835}{4}-\frac{43185}{8}\,x_\mathrm{e}+\frac{278322}{49}\,x_\mathrm{e}^2-\frac{297369}{196}\,x_\mathrm{e}^3+\frac{4908}{49}\,x_\mathrm{e}^4\right)\right]x_\mathrm{e}^3 \tag{D.13b}$$

$$I_2 = \frac{7}{5}\,\theta_\mathrm{e}\left[1+\theta_\mathrm{e}\left(\frac{109}{2}-\frac{132}{7}\,x_\mathrm{e}+\frac{11}{14}\,x_\mathrm{e}^2\right)+\theta_\mathrm{e}^2\left(\frac{6031}{8}-\frac{37824}{49}\,x_\mathrm{e}+\frac{77169}{490}\,x_\mathrm{e}^2 -\frac{320}{49}\,x_\mathrm{e}^3\right)+\theta_\mathrm{e}^3\left(\frac{43185}{8}-\frac{629280}{49}\,x_\mathrm{e}+\frac{181407}{28}\,x_\mathrm{e}^2-\frac{46124}{49}\,x_\mathrm{e}^3+\frac{8504}{245}\,x_\mathrm{e}^4\right)\right]x_\mathrm{e}^4 \tag{D.13c}$$

$$I_3 = \frac{11}{5}\,\theta_\mathrm{e}^2\left[8-x_\mathrm{e}+\theta_\mathrm{e}\left(\frac{25216}{77}-\frac{12752}{77}\,x_\mathrm{e}+\frac{1280}{77}\,x_\mathrm{e}^2-\frac{64}{231}\,x_\mathrm{e}^3\right) +\theta_\mathrm{e}^2\left(\frac{419520}{77}-\frac{486240}{77}\,x_\mathrm{e}+\frac{135416}{77}\,x_\mathrm{e}^2-\frac{55708}{385}\,x_\mathrm{e}^3+\frac{20}{7}\,x_\mathrm{e}^4\right)\right]x_\mathrm{e}^5 \tag{D.13d}$$

$$I_4 = \frac{11}{10}\,\theta_\mathrm{e}^2\left[1+\theta_\mathrm{e}\left(\frac{12752}{77}-\frac{3200}{77}\,x_\mathrm{e}+\frac{128}{77}\,x_\mathrm{e}^2\right) +\theta_\mathrm{e}^2\left(\frac{486240}{77}-\frac{314000}{77}\,x_\mathrm{e}+\frac{249208}{385}\,x_\mathrm{e}^2-\frac{200}{7}\,x_\mathrm{e}^3+\frac{5}{21}\,x_\mathrm{e}^4\right)\right]x_\mathrm{e}^6 \tag{D.13e}$$

$$I_5 = \frac{64}{35}\,\theta_\mathrm{e}^3\left[10-x_\mathrm{e}+\theta_\mathrm{e}\left(\frac{3925}{4}-\frac{5805}{16}\,x_\mathrm{e}+\frac{495}{16}\,x_\mathrm{e}^2-\frac{55}{96}\,x_\mathrm{e}^3\right)\right]x_\mathrm{e}^7 \tag{D.13f}$$

$$I_6 = \frac{64}{105}\,\theta_\mathrm{e}^3\left[1+\theta_\mathrm{e}\left(\frac{5805}{16}-\frac{1155}{16}\,x_\mathrm{e}+\frac{165}{64}\,x_\mathrm{e}^2\right)\right]x_\mathrm{e}^9 \tag{D.13g}$$

$$I_7 = \frac{22}{21}\,\theta_\mathrm{e}^4\,[12-x_\mathrm{e}]\,x_\mathrm{e}^8 \tag{D.13h}$$

$$I_8 = \frac{11}{42}\,\theta_\mathrm{e}^4 x_\mathrm{e}^{10}\,. \tag{D.13i}$$

The $I_k$ are fifth-order or higher in $\theta_\mathrm{e}$ for $k > 8$.

## D.4 Integration over the frequency of the incoming photons

The integrals $J_1$ and $J_2$ can be reduced analytically using integration by parts, assuming that the incoming photon distribution and all its derivatives up to sixth order in $x$ vanish faster than $x^{-12}$ for very high frequencies. The calculation is rather lengthy and is therefore not presented here. The integrals $J_i$ can be expressed in terms of the following functions:

$$\bar{\mathcal{I}}_i = \int x_\mathrm{e}^i\, n(n+1)\,\mathrm{d}x_\mathrm{e} = \phi^{i+1}\int x^i\, n(n+1)\,\mathrm{d}x = \phi^{i+1}\,\mathcal{I}_i \tag{D.14a}$$

$$\bar{\mathcal{G}}_{i,j} = \int x_\mathrm{e}^i\, n^j\,\mathrm{d}x_\mathrm{e} = \phi^{i+1}\int x^i\, n^j\,\mathrm{d}x = \phi^{i+1}\,\mathcal{G}_{i,j} \tag{D.14b}$$

$$\bar{\mathcal{H}}_{i,j} = \int x_\mathrm{e}^i\left[\frac{\partial^j n}{\partial\, x_\mathrm{e}^j}\right]^2\mathrm{d}x_\mathrm{e} = \phi^{i+1-2\,j}\int x^i\left[\frac{\partial^j n}{\partial\, x^j}\right]^2\mathrm{d}x = \phi^{i+1-2\,j}\,\mathcal{H}_{i,j} \tag{D.14c}$$

where $n(x)$ is the photon phase space distribution and $x = h\nu/k\;T_\gamma$, $x_\mathrm{e} = \phi x$ and $\phi = \theta_\gamma/\theta_\mathrm{e}$.

With equation (4.54), collecting the different orders in $\theta_\mathrm{e}$, one can define the functions $G_i$ in equation (4.56) as

$$G_0 = \bar{\mathcal{I}}_4 \tag{D.15a}$$

$$G_1 = 6\,\bar{\mathcal{I}}_4 - \frac{21}{5}\,\bar{\mathcal{G}}_{5,1} - \frac{7}{5}\bar{\mathcal{H}}_{6,1} \tag{D.15b}$$

$$G_2 = 15\,\bar{\mathcal{I}}_4 - \frac{441}{10}\,\bar{\mathcal{G}}_{5,1} + \frac{357}{25}\,\bar{\mathcal{I}}_6 - \frac{147}{10}\,\bar{\mathcal{H}}_{6,1} + \frac{11}{10}\left[\bar{\mathcal{H}}_{8,2} - \bar{\mathcal{H}}_{8,1}\right] \tag{D.15c}$$

$$\begin{aligned} G_3 = {} & \frac{45}{4}\,\bar{\mathcal{I}}_4 - \frac{8379}{40}\,\bar{\mathcal{G}}_{5,1} + \frac{5712}{25}\,\bar{\mathcal{I}}_6 - \frac{7618}{175}\,\bar{\mathcal{G}}_{7,1} - \frac{2793}{40}\,\bar{\mathcal{H}}_{6,1} \\ & + \frac{11}{350}\left[560\,\bar{\mathcal{H}}_{8,2} - 1779\,\bar{\mathcal{H}}_{8,1}\right] - \frac{64}{105}\left[\bar{\mathcal{H}}_{10,3} - 3\,\bar{\mathcal{H}}_{10,2}\right] \end{aligned} \tag{D.15d}$$

$$\begin{aligned} G_4 = {} & -\frac{45}{4}\,\bar{\mathcal{I}}_4 - \frac{3969}{8}\,\bar{\mathcal{G}}_{5,1} + \frac{8568}{5}\,\bar{\mathcal{I}}_6 - \frac{34281}{35}\,\bar{\mathcal{G}}_{7,1} + \frac{21498}{175}\,\bar{\mathcal{I}}_8 - \frac{1323}{8}\,\bar{\mathcal{H}}_{6,1} - \frac{139161}{140}\,\bar{\mathcal{H}}_{8,1} \\ & + 132\,\bar{\mathcal{H}}_{8,2} - \frac{2454}{175}\bar{\mathcal{H}}_{10,1} + \frac{15704}{175}\,\bar{\mathcal{H}}_{10,2} - \frac{96}{7}\,\bar{\mathcal{H}}_{10,3} + \frac{11}{42}\bar{\mathcal{H}}_{12,2} - \frac{11}{7}\,\bar{\mathcal{H}}_{12,3} + \frac{11}{42}\,\bar{\mathcal{H}}_{12,4}\,. \end{aligned} \tag{D.15e}$$

If induced scattering is negligible one has to drop the integrals $\bar{\mathcal{H}}_{i,j}$ and replace $\bar{\mathcal{I}}_i \to \bar{\mathcal{G}}_{i,1}$. This is equivalent to setting $J_1 = J_2 = 0$ and in addition replacing $n(n+1) \to n$ in the definition of the integral $J_0$.

In the derivation of the $G_i$ the following relations between the photon phase space distribution $n$ and the integrals $\mathcal{I}_i$, $\mathcal{G}_{i,j}$ and $\mathcal{H}_{i,j}$ have been very useful:

$$\int x^i\,\partial_x^j\,n\,\mathrm{d}x = \frac{(-)^j\,i!}{(i-j)!}\,\mathcal{G}_{i-j,1} \tag{D.16a}$$

$$\int x^m\,n\,\partial_x n\,\mathrm{d}x = -\frac{1}{2}\,\frac{m!}{(m-1)!}\,\mathcal{G}_{m-1,2} \tag{D.16b}$$

$$\int x^m\,n\,\partial_x^2 n\,\mathrm{d}x = +\frac{1}{2}\,\frac{m!}{(m-2)!}\mathcal{G}_{m-2,2} - \mathcal{H}_{m,1} \tag{D.16c}$$

$$\int x^m\,n\,\partial_x^3 n\,\mathrm{d}x = -\frac{1}{2}\,\frac{m!}{(m-3)!}\mathcal{G}_{m-3,2} + \frac{3}{2}\,\frac{m!}{(m-1)!}\mathcal{H}_{m-1,1} \tag{D.16d}$$

$$\int x^m\,n\,\partial_x^4 n\,\mathrm{d}x = +\frac{1}{2}\,\frac{m!}{(m-4)!}\mathcal{G}_{m-4,2} - 2\,\frac{m!}{(m-2)!}\mathcal{H}_{m-2,1} + \mathcal{H}_{m,2} \tag{D.16e}$$

$$\int x^m\,n\,\partial_x^5 n\,\mathrm{d}x = -\frac{1}{2}\,\frac{m!}{(m-5)!}\mathcal{G}_{m-5,2} + \frac{5}{2}\,\frac{m!}{(m-3)!}\mathcal{H}_{m-3,1} - \frac{5}{2}\,\frac{m!}{(m-1)!}\mathcal{H}_{m-1,2} \tag{D.16f}$$

$$\int x^m\,n\,\partial_x^6 n\,\mathrm{d}x = +\frac{1}{2}\,\frac{m!}{(m-6)!}\mathcal{G}_{m-6,2} - 3\,\frac{m!}{(m-4)!}\mathcal{H}_{m-4,1} + \frac{9}{2}\,\frac{m!}{(m-2)!}\mathcal{H}_{m-2,2} - \mathcal{H}_{m,3} \tag{D.16g}$$

# Appendix E

# Summary of useful relations in the cosmological context

In this Chapter we summarize some of the equations and relations, which have been used in the derivations of the thermalization of small chemical potential distortions in the cosmological context. Most of these equations can be found in standard textbooks [108, 94, 93] and have only been given here to clarify the notation and to guide the reader.

Here we also explicitly give the expressions for the values of the WMAP concordance model (a more complete list of parameters including error bars can be found in Bennett et al. [11]): $Y_{\rm p} = 0.2485$ (this value was taken from Cyburt [41]), $\Omega_{\rm m} h^2 = 0.135$, $\Omega_{\rm b} h^2 = 0.0224$, $h = 0.71$ and $T_0 = 2.725\,{\rm K}$, where $Y_{\rm p}$ is the primordial mass fraction of helium, $\Omega_{\rm m} h^2$ and $\Omega_{\rm b} h^2$ are the total matter density and baryon density of the universe, respectively, and $T_0$ is the temperature of the CMB today. We use the definition $h = H_0/100\,{\rm km\ s^{-1}\ Mpc^{-1}}$, where $H_0$ is the Hubble-parameter at redshift $z = 0$.

## E.1 Electron, hydrogen and helium number densities

The electron, hydrogen and helium number densities, due to the fact that the universe as a whole is neutral, can all be related to the baryon density $N_{\rm b}$, which is defined as

$$\begin{aligned} N_{\rm b} &= \Omega_{\rm b} h^2 \frac{\rho_{\rm c}/h^2\,(1+z)^3}{[m_{\rm e}\,(1-Y_{\rm p}/2) + m_{\rm p}\,(1-Y_{\rm p}/2) + m_{\rm n}\,(Y_{\rm p}/2)]} \\ &\approx 1.1225\cdot 10^{-5}\,\Omega_{\rm b} h^2\,(1+z)^3\,{\rm cm^{-3}} \\ &\overset{\rm WMAP}{\approx} 2.5144\cdot 10^{-7}\,(1+z)^3\,{\rm cm^{-3}}\,. \end{aligned} \tag{E.1a}$$

Here $m_{\rm e}$, $m_{\rm p}$ and $m_{\rm n}$ are the electron, proton and neutron rest mass, respectively, and the critical density of the universe is given by

$$\rho_{\rm c} = \frac{3\,H_0^2}{8\pi\,G} \approx 1.8788\times 10^{-29} h^2 {\rm g\ cm^{-3}}\,. \tag{E.2}$$

With this one can write down the electron, $N_{\rm e}$, hydrogen, $N_{\rm H}$, and helium, $N_{\rm H}$, number densities using the Helium mass fraction, $Y_{\rm p}$:

$$N_{\rm e} = (1-Y_{\rm p}/2)\,\chi_{\rm e}\,N_{\rm b} \tag{E.3a}$$

$$N_{\rm H} = (1-Y_{\rm p})\,N_{\rm b} \tag{E.3b}$$

$$N_{\rm He} = (Y_{\rm p}/4)\,N_{\rm b} \tag{E.3c}$$

where $\chi_{\rm e}$ is the ionization fraction of the hydrogen and helium atoms. At high redshifts ($z \gtrsim 10^4$) the ionization fraction is $\chi_{\rm e} \equiv 1$, but as helium and hydrogen *recombination* at low redshifts ($800 \lesssim z \lesssim 10^4$) proceeds it drops very fast toward zero and only increases again at low redshifts ($z \leq 20 - 100$) when *reionization* by the first sources occurs.

## E.2 Photon energy and number density

The photons in the universe are very close to Planckian and therefore the energy and number densities are completely fixed by the temperature $T_\gamma$. With (B.3) and $T_\gamma = T_0(1+z)$ for the photon energy density it follows

$$\begin{aligned}\rho_\gamma &\approx 4.911\times10^{-7}\;\Theta_{2.7}^4\, m_\mathrm{e}c^2\,(1+z)^4\,\mathrm{cm}^{-3} \\ &\approx 4.474\times10^{-34}\;\Theta_{2.7}^4\, c^2\,(1+z)^4\,\mathrm{g\,cm}^{-3}\,,\end{aligned} \tag{E.4}$$

where we defined $\Theta_{2.7} = T_\gamma/2.7\,\mathrm{K}$. Similarly for the photon number density one obtains

$$N_\gamma \approx 399.3\times\Theta_{2.7}^3\,(1+z)^3\,\mathrm{cm}^{-3}\,. \tag{E.5}$$

With equation (E.1a) one finds

$$\frac{N_\mathrm{b}}{N_\gamma} = 2.811\times10^{-8}\,\Omega_\mathrm{b}h^2\,\Theta_{2.7}^{-3} \tag{E.6}$$

for the baryon to photon ratio. In the WMAP concordance model $N_\mathrm{b}/N_\gamma \approx 6.125\times10^{-10}$. This huge difference in the number of photons and baryons is normally referred to as the large entropy of the universe.

## E.3 Time scales

In this Section we shall give some of the most important timescales and their scaling with redshift and the adopted parameters of the underlying universe, which are involved in the description of the thermalization of CMB spectral distortions. Similar expressions can be found in Hu [62].

**Expansion time** $t_\mathrm{exp} = 1/H$

The expansion rate of the universe is determined by the Hubble parameter $H$, which depends on the energy densities of the photons, neutrino species, matter and dark energy. Assuming spatial flatness and neglecting the $\Lambda$-term (which only becomes important very low redshifts) one can write

$$\begin{aligned} t_\mathrm{exp} \quad &= \quad 6.32\times10^{19}\,\kappa^{-1/2}\,\Theta_{2.7}^{-2}\,[1+(1+z_\mathrm{eq})/(1+z)]^{-1/2}\,(1+z)^{-2}\,\mathrm{s} \\ &\overset{z\gg z_\mathrm{eq}}{\downarrow} \\ &= \quad 4.88\times10^{19}\,\Theta_{2.7}^{-2}\,(1+z)^{-2}\,\mathrm{s} \\ &\overset{z\ll z_\mathrm{eq}}{\downarrow} \\ &= \quad 3.08\times10^{17}\,(\Omega_\mathrm{m}h^2)^{-1/2}\,(1+z)^{-3/2}\,\mathrm{s}\,, \end{aligned} \tag{E.7}$$

where $\kappa = 1 + N_\nu\,(7/8)\,(4/11)^{4/3} \approx 1.68$ is effective number of spin states, with $N_\nu$ being the number of relativistic neutrino species. Here the redshift of matter and radiation equality is

$$z_\mathrm{eq} = 4.20\times10^4\;\Theta_{2.7}^{-4}\,\kappa^{-1}\,\Omega_\mathrm{m}h^2\,. \tag{E.8}$$

For the standard WMAP concordance model one obtains $z_\mathrm{eq} \approx 3.25\times10^3$ and in the limit $z \ll z_\mathrm{eq}$ the expansion time $t_\mathrm{exp} \approx 8.38\times10^{17}\,(1+z)^{-3/2}\,\mathrm{s}$.

**Compton scattering time** $t_\mathrm{C} = 1/\sigma_\mathrm{T}\,N_\mathrm{e}\,c$

Using the expression (E.1a) for the baryon number density one finds

$$t_\mathrm{C} \quad\approx\quad 4.46\times10^{18}\,\chi_\mathrm{e}^{-1}\,(1-Y_\mathrm{p}/2)^{-1}\,(\Omega_\mathrm{b}h^2)^{-1}\,(1+z)^{-3}\,\mathrm{s}\,, \tag{E.9}$$

which for the standard WMAP concordance model is $t_\mathrm{C} \approx 2.27\times10^{20}\,\chi_\mathrm{e}^{-1}\,(1+z)^{-3}\,\mathrm{s}$.

**Comptonisation time** $t_{\rm K} = t_{\rm C}/4\,\theta_{\rm e} \equiv t_{\rm e\gamma}$

The time scale for energy being transfered form the electrons to the photons is given by

$$t_{\rm K} \;\approx\; 2.45\times10^{27}\,\Theta_{2.7}^{-1}\,\phi\,\chi_{\rm e}^{-1}\,(1-Y_{\rm p}/2)^{-1}\,(\Omega_{\rm b}h^2)^{-1}\,(1+z)^{-4}\,{\rm s}\,, \tag{E.10}$$

where we used $\Theta_{2.7} = T_0/2.7\,{\rm K}$ and $\phi = T_\gamma/T_{\rm e}$. For the standard WMAP concordance model we have: $t_{\rm K} \approx 1.24\times10^{29}\,\phi\,\chi_{\rm e}^{-1}\,(1+z)^{-4}\,{\rm s}$.

**Cooling time for Electrons** $t_{\gamma{\rm e}} = \alpha^*\,t_{\rm C}/4\,\tilde{\rho}_\gamma$

The time scale, on which the electrons (and baryons due to Coulomb interactions with the electrons) adjust their temperature in a given photon field is given by

$$t_{\gamma{\rm e}} \;\approx\; 7.65\times10^{19}\,\Theta_{2.7}^{-4}\,\xi_{\rm cool}\,(1+z)^{-4}\,{\rm s}\,, \tag{E.11}$$

where we defined $\xi_{\rm cool} = \alpha^*/3\,N_{\rm e}$. If one assumes $Y_{\rm p} = 1/4$ and $\chi_{\rm e} = 1$ then in the non-relativistic case $\xi_{\rm cool} = 27/28$. For the standard WMAP concordance model we have ($\chi_{\rm e} \equiv 1$): $t_{\rm e\gamma} \approx 7.11\times10^{19}\,(1+z)^{-4}\,{\rm s}$. Due to the large entropy of the universe $t_{\gamma{\rm e}} \ll t_{\rm e\gamma}$. For $Y_{\rm p} = 0$ it follows that $t_{\gamma{\rm e}} \equiv 3\chi_{\rm e}m_{\rm e}c/8\,\sigma_{\rm T}\,\rho_\gamma$.

**Coulomb cooling time** $t_{\rm pe}$

The time needed for protons to transfer energy to the electrons is determined by [122, 124]

$$\begin{aligned} t_{\rm pe} &= \frac{t_{\rm C}}{\ln\Lambda}\sqrt{\frac{\pi}{2}}\,\frac{m_{\rm p}}{m_{\rm e}}\times\theta_{\rm e}^{3/2} \\ &\approx 4.98\times10^{6}\,\phi^{3/2}\chi_{\rm e}^{-1}\,(1-Y_{\rm p}/2)^{-1}\,(\Omega_{\rm b}h^2)^{-1}\Theta_{2.7}^{3/2}\,(1+z)^{-3/2}\,{\rm s}\,, \end{aligned} \tag{E.12}$$

for $\theta_{\rm e} \ll m_{\rm p}/m_{\rm e}$. Here $\ln\Lambda \approx 20$ is the *Coulomb logarithm*, which results from shielding of the Coulomb force for large distances of the interacting particles. This time scale is always many orders of magnitude shorter than any other time scale discussed here.

# Bibliography


[1] Abramovitz, M., & Stegun, I.A., 1965, *Handbook of Mathematical Functions*, Dover Publications, Inc. New York

[2] ACBAR Homepage at http://cosmology.berkeley.edu/group/swlh/acbar/

[3] Aghanim, N., Hansen, S.H., Pastor, S., & Semikoz, D.V., 2003, *Journal of Cosmology and Astro-Particle Physics*, 5, 7

[4] AMI Homepage at http://www.mrao.cam.ac.uk/telescopes/ami/

[5] ARCADE Homepage at http://arcade.gsfc.nasa.gov/arcade/science_mu.html

[6] ARCHEOPS Homepage at http://www.archeops.org/

[7] APEX Homepage at http://bolo.berkeley.edu/apexsz/

[8] Baleisis, A., Lahav, O., Loan, A.J., & Wall, J.V., 1998, *Mon. Not. Roy. Astron. Soc.*, Vol. 297, pp. 545-558

[9] Basu, K., Hernández-Monteagudo, C., & Sunyaev, R.A., 2004, *Astron. & Astrophys.*, 416, pp. 447

[10] Bennett et al., 1996, *Astrophys. Journ.*, 464, p.L1

[11] Bennett et al., 2003, *Astrophysical Journal Supplement*, 148, 1-27

[12] de Bernardis et al., 1990, *Astrophys. Journ.*, 353, 145

[13] de Bernardis et al., 2000, *Nature*, 404, 955

[14] Birkinshaw, M., Hughes, J.P., & Arnaud, K.A. 1991, *Astrophys. Journ.*, 379, 466

[15] Birkinshaw, M., *Physics Reports*, 1999, Vol. 310, Issue 2-3, p. 97-195

[16] Birkinshaw, M., & Lancaster, K., 2004, Varenna Summer School review, available at: http://www.star.bris.ac.uk/~mb1/export.html

[17] Blake, Ch., & Wall, J., 2002, *Nature*, 416, 150-152

[18] Blain, A.W., Smail, I., Ivison, R.J., Kneib, J.P., & Frayer, D.T., 2002, *Physics Reports*, 369, 111-176

[19] Boekelheide, PhD thesis, State University of Iowa, 1952 (unpublished)

[20] Bond, J.R., 1988, *The early Universe*, eds W.G. Unruh, G.W. Semenoff, Reidel, Dordrecht, p. 283

[21] Bono, G., Balbi, A., Cassisi, S., Vittorio, N. & Buonanno, R., 2002, *Astrophys. Journ.*, 568, p. 463-469

[22] BOOMERANG Homepage at http://cmb.phys.cwru.edu/boomerang/

[23] Bottani, S., de Bernardis, P., & Melchiorri, F., 1992, *Astrophys. Journ.*, 384, p. L1-L3

[24] Bryan, G.L., & Norman, M.L., 1998, 495, 80-99

[25] Burigana, C. Danese, L., & de Zotti, G., 1991, *Astron. & Astrophys.*, 246, 49-58

[26] Burigana, C., & Salvaterra, R., 2003, *Mon. Not. Roy. Astron. Soc.*, 342, 543-556

[27] Cavanagh, P.E., 1952, Phys. Rev., 87, p. 1131

[28] CBI Homepage at http://www.astro.caltech.edu/ tjp/CBI/

[29] Cercignani, C., & Kremer, G.M., 2002, *The Relativistic Boltzmann Equation*, Birkhäuser Verlag, Berlin

[30] Challinor, A., & Lasenby, A., 1998, *Astrophys. Journ.*, 499, 1-6

[31] Challinor, A., & van Leeuwen, F., 2002, *Physical Review D*, 65, 103001, pp. 1-13

[32] Carlstrom, J.E., Holder, G.P., Reese, E.D., 2002, *Annual Reviews in Astronomy & Astrophysics*, 40, 643-680

[33] Chluba, J., & Mannheim, K., 2002, *Astron. & Astrophys.*, 396, 419-427

[34] Chluba, J., & Sunyaev, R.A., 2004, *Astron. & Astrophys.*, 424, 389-408

[35] Chluba, J., Hütsi, G., & Sunyaev, R.A., astro-ph/0409058

[36] Chluba, J., Sazonov, S.Y., & Sunyaev, R.A., in preparation

[37] Church, S. 2002, technical report, scripts for talk available from: http://ophelia.princeton.edu/~page/cmbpol-technology-v2.ppt

[38] COBE Homepage at http://lambda.gsfc.nasa.gov/product/cobe/

[39] Compton, A.H., & Getting, I.A., 1935, *Physical Review*, 47, 817-821

[40] Croft, R.A.C., et al., 2002, *Astrophys. Journ.*, 581, 20

[41] Cyburt, R.H., 2004, *Physical Review D*, 70, 023505

[42] DASI Homepage at http://astro.uchicago.edu/dasi/

[43] Dicke, R.H., Peebles, P.J.E., Roll, P,G.,& Wilkinson, D.T., 1965, *Astrophys. Journ.*, 142, 414-419

[44] DIMES Homepage at http://map.gsfc.nasa.gov/DIMES/dimes_cosmology.html

[45] Daly, R.A., 1991, *Astrophys. Journ.*, 371, 14-28

[46] Danese, L., & de Zotti, G., 1982, *Astron. & Astrophys.*, 107, 39-42

[47] Eliezer, C.J., 1946, *Proc. Roy. Soc. A*, 187, 210

[48] Ellis, G.F.R., & Baldwin, J.E., 1984, *Mon. Not. Roy. Astron. Soc.*, 206, 377-381

[49] Enßlin, T.A., & Kaiser, C.R., 2000, *Astron. & Astrophys.*, 360, 417

[50] Fixsen, D.J., et al., 1996, *Astrophys. Journ.*, 473, 576-587

[51] Fixsen, D.J., & Mather, J.C., 2002, *Astrophys. Journ.*, 581, 817-822

[52] Freedman, W.L., et al., 2001, *Astrophys. Journ.*, 553, 47

[53] Gorski, K.M., Hivon, E., Wandelt, B.D., 1999, Proceedings of the MPA/ESO Cosmology Conference, pp. 37-42 (also astro-ph/9812350)

[54] Gould, R.J., 1984, *Astrophys. Journ.*, 285, 275-278

[55] Hahn, T., 2004, hep-ph/0404043, download of the Cuba Library available from: http://www.feynarts.de/cuba/

[56] Heitler & Nordheim, 1934, *Physics*, 1059

[57] Hu, J., & Lou, Y., 2004, *Astrophysical Journal Letters*, 606, L1

[58] Hu, W., & Silk, J., 1993a, *Physical Review Letters*, 18, 2661-2664

[59] Hu, W., & Silk, J., 1993b, *Physical Review D*, 48, 485-502

[60] Hu, W., Scott, D., & Silk, J., 1994a, *Astrophys. Journ.*, 43, L5-L8

[61] Hu, W., Scott, D., & Silk, J., 1994b, *Physical Review D*, 49, 648-670

[62] Hu, W., 1995, PhD Thesis, University of California at Berkeley

[63] Hu, W., 2000, *Physical Review D*, 62, id.043007

[64] Hu, W., & Dodelson, S., 2002, *Annual Reviews in Astronomy & Astrophysics*, 40, p. 171-216

[65] Illarionov, A.F., & Sunyaev, R.A., 1975a, *Soviet Astronomy*, 18, 413-419

[66] Illarionov, A. F., & Sunyaev, R. A., 1975b, *Soviet Astronomy*, 18, p. 691-699

[67] Itoh, N., Kohyama, Y., & Nozawa, S., 1998, *Astrophys. Journ.*, 502, 7-15

[68] Itoh, N. et al., 2000, *Astrophysical Journal Supplement*, 128, 125-135

[69] Jauch, J.M., & Rohrlich, F., 1976, *The Theory of Photons and Electrons*, Springer-Verlag

[70] Kamionkowski, M., & Knox, L., 2003 *Physical Review D*, 67, Issue 6, id. 063001

[71] Kamionkowski, M., & Kosowsky, A., 1999 *Annu. Rev. Nucl. Part. Sci.*, 49, 77-123

[72] Kogut, A., 1996, astro-ph/9607100

[73] Kogut et al, 2003 *Astrophysical Journal Supplement*, 148, 1, 161-173

[74] Kogut, A., Fixsen, D.J., Levin, S., Limon, M., Lubin, P.M., Mirel, P., Seiffert, M., & Wollack, E, 2004, *Astrophysical Journal Supplement*, 154, 493

[75] Kompaneets, A.S., 1956, *Soviet Physics JETP*, 31, p. 876

[76] Korolev, V.A., Syunyaev, R.A., & Yakubtsev, L.A., 1986, *Soviet Astronomy Letters*, 12, 141

[77] Kosowsky, A., 2003, *New Astronomy Reviews*, 47, 939-943

[78] Kovac, J.M., 2002, *Nature*, 420, 772-786

[79] Leitch, E.M., 2002, *Nature*, 420, 763-771

[80] Lightman, A.P., 1981, *Astrophys. Journ.*, 244, 392-405

[81] Mandl, F., & Skyrme, T.H.R., 1952, *Proc. Roy. Soc.*, A215, 497

[82] Maoz, E, 1994, *Astrophys. Journ.*, vol. 428, p. 454-457

[83] Markevitch, M., Blumenthal, G. R., Forman, W., Jones, C., Sunyaev, R. A, 1991, *Astrophysical Journal Letters*, 378, p. L33-L36.

[84] Mather, J.C., et al., 1994, *Astrophysical Journal Letters*, 420, pp. 439

[85] MAXIMA Homepage at http://cosmology.berkeley.edu/group/cmb/

[86] McDonald, P., Scherrer, R.J., & Walker, T.P., 2000, *Physical Review D*, 63, 023001

[87] McGie, M.R., Brady, F.P., & Knox, W.J., 1966, *Physical Review*, 152, pp. 1190-1194

[88] Mohr, J.J., Mathiesen, B., & Evrard, A.E., 1999, *Astrophys. Journ.*, 517, 627-649

[89] Mork, K.J., 1971, *Physical Review A*, 4, pp. 917-927

[90] Nozawa, S., Itoh, N., & Kohyama, Y., 1998a, *Astrophys. Journ.*, 507, 530-557

[91] Nozawa, S., Itoh, N., & Kohyama, Y., 1998b, *Astrophys. Journ.*, 508, 17-24

[92] Oh, S.P., Cooray, A., & Kamionkowski, M., 2003, *Mon. Not. Roy. Astron. Soc.*, 342, L20-L24

[93] Padmanabhan, T., 2002, *Theoretical Astrophysics, Volumes I-III*, Cambrige University Press

[94] Peebles, P. J. E., 1993, *Principles of Physical Cosmology*, Princeton Series in Physics

[95] Peebles, P. J. E., & Yu, J. T., 1970, *Astrophys. Journ.*, p.815

[96] Penzias, A.A. & Wilson, R.W., 1965, *Astrophys. Journ.*, 142, pp. 419

[97] PLANCK Homepage at http://www.rssd.esa.int/planck

[98] Press, W.H., & Schechter, P., 1974, *Astrophys. Journ.*, 187, 425-438

[99] Pfrommer, C., Enßlin, T. A., Sarazin, C. L., 2005, *Astron. & Astrophys.*, 430, p.799-810

[100] Pozdnyakov, L.A., Sobol, I.M., Sunyaev R.A., 1979, *Astron. & Astrophys.*, 75, p.214-222

[101] Pozdnyakov, L.A., Sobol, I.M., Sunyaev R.A., 1983, *Astrophysics and Space Physics Review*, ed. R.A. Sunyaev, Harwood Academic Publishers, Chur, vol. 2, 189

[102] Ram, M., & Wang, P.Y., 1971, *Physical Review Letters*, 26, 476-479

[103] Reese, E.D., et al., 2002, *Astrophys. Journ.*, 581, 53-85

[104] Rephaeli, Y., 1995a, *Annual Reviews in Astronomy & Astrophysics*, 33, p. 541-580

[105] Rephaeli, Y., 1995b, *Astrophys. Journ.*, 445, p. 33-36

[106] Rosati, P., et al., 2002, *Astrophys. Journ.*, 566, 667-674

[107] Rubiño-Martín, J.A., & Sunyaev, R.A., 2003, *Mon. Not. Roy. Astron. Soc.*, 344, Issue 4, 1155-1174

[108] Rybicki, G.B., & Lightman, A.P., 1979, John Wiley & Sons, Inc.

[109] Sachs, R.K., & Wolfe, A.M, 1967, *Astrophys. Journ.*, 147, 73

[110] Santos, M.G., Cooray, A., Haiman, Z., Knox, L., Ma, C., 2003, *Astrophys. Journ.*, 598, pp. 756-766

[111] Sazonov, S.Y., & Sunyaev, R.A., 1998, *Astrophys. Journ.*, 508, 1-5

[112] Sazonov, S.Y., & Sunyaev, R.A., 1999, *Mon. Not. Roy. Astron. Soc.*, 310, 765-772

[113] Sazonov, S. Y., & Sunyaev, R.A., 2000, *Astrophys. Journ.*, 543, 23-55

[114] Sazonov, S. Y., & Sunyaev, R.A., 2001, *Astronomy Letters*, 27, 481-492

[115] Scharf, C.A., Jahoda, K., & Boldt, E., 1995, *Astrophys. Journ.*, 454, 573-579

[116] Schuecker, P., Finoguenov, A., Miniati, F., Böhringer, H., & Briel, U.G, 2004, *Astron. & Astrophys.*, 426, 387

[117] Sheth, R.K., Mo, H., & Tormen, G., 2001, *Mon. Not. Roy. Astron. Soc.*, 323, 1-12

[118] Silk, J., 1968, *Astrophys. Journ.*, 151, 459

[119] Smoot, G.F., Gorenstein, M.V.,& Muller, R.A., 1977, *Physical Review Letters*, 39, 898-901

[120] Smoot, G.F., et al., 1992, *Astrophysical Journal Letters*, 396, L1

[121] Spergel, D.N. et al., 2003, *Astrophysical Journal Supplement*, 148, 175-194

[122] Spitzer, L., 1956, *Physics of Fully Ionized Gases*, Wiley, New York

[123] Springel, V., White, M., & Hernquist, L., 2001, *Astrophys. Journ.*, 549, 681-687 (erratum 562, 1086)

[124] Stepney, S. 1983, *Mon. Not. Roy. Astron. Soc.*, 202, p. 467-418

[125] Sunyaev, R.A., & Zeldovich, Ya. B., 1970a, *Astrophysics and Space Science*, 7, 3-19

[126] Sunyaev, R.A., & Zeldovich, Ya. B., 1970b, *Astrophysics and Space Science*, 7, 20-30

[127] Sunyaev, R.A., & Zeldovich, Ya. B., 1972, *Comments on Astrophysics and Space Physics*, 4, p.173

[128] Sunyaev, R.A., & Zeldovich, Ya. B., 1980a, *Annual Reviews in Astronomy & Astrophysics*, 18, p. 537-560

[129] Sunyaev, R.A., & Zeldovich, Ya. B., 1980, *Mon. Not. Roy. Astron. Soc.*, 190, 413-420

[130] Sunyaev, R.A., & Zeldovich, Ya. B., 1981, *Astrophysics and Space Physics Reviews*, 1, p. 1-60

[131] Strukov, I.A., Skulachev, D.P., Boyarskii, M.N., Tkachev, A.N., 1987, *Soviet Astronomy Letters*, 13, p. 65

[132] Svensson, R., 1984, *Mon. Not. Roy. Astron. Soc.*, 209, 175-208

[133] Thorne, K.S., 1981, *Mon. Not. Roy. Astron. Soc.*, 194, 439-473

[134] Theus, R.B., & Beach, L.A., 1957, *Phys. Rev.*, 106, pp. 1249-1252

[135] White, M., Scott, D., & Silk, J., 1994, *Annual Reviews in Astronomy & Astrophysics*, 32, 319-370

[136] White, M., Hernquist, L., & Springel, V., 2002, *Astrophys. Journ.*, 579, 16-22

[137] WMAP Homepage at http://lambda.gsfc.nasa.gov/product/map/

[138] VSA Homepage at http://www.mrao.cam.ac.uk/telescopes/vsa/

[139] Zaldarriaga, M., & Seljak, U., 1997, *Physical Review D*, 55, pp.1830-1840

[140] Zdziarski, A.A., 1988, *Astrophys. Journ.*, 335, 786-802

[141] Zeldovich, Ya. B., & Sunyaev, R.A., 1969, *Astrophysics and Space Science*, 4, 301-316

[142] Zeldovich, Ya. B., Illarionov, A. F., & Sunyaev, R.A., 1972, *Soviet Physics JETP*, 35, 643-830

# Acronyms

| | |
|---|---|
| ACBAR | Arcminute Cosmology Bolometer Array Receiver [2] |
| ACT | Atacama Cosmology Telescope |
| AMI | Arcminute MicroKelvin Imager [4] |
| APEX | Atacama Pathfinder EXperiment [7] |
| ARCADE | Absolute Radiometer for Cosmology, Astrophysics, and Diffuse Emission [5] |
| BOOMERANG | Balloon Observation of Millimetric Extragalactic Radiation and Geophysics [22] |
| BS | Bremsstrahlung |
| CBI | Cosmic Background Imager [28] |
| CHANDRA | Satellite Mission of NASA |
| CMB | Cosmic Microwave Background |
| COBE | Cosmic Background Explorer [38] |
| CS | Compton Scattering |
| DASI | Degree Angular Scale Interferometer [42] |
| DIMES | Diffuse Microwave Emission Survey [44] |
| DC | Double Compton |
| DMR | Differential Microwave Radiometer (COBE instrument) |
| FIRAS | Far Infrared Absolute Spectrophotometer (COBE instrument) |
| k-SZ | kinetic Sunyaev Zeldovich (effect) |
| LSS | Last Scattering Surface |
| MAXIMA | Millimeter Anisotropy eXperiment IMaging Array [85] |
| PLANCK | Satellite mission of the European Space Agency [97] |
| RJ | Rayleigh-Jeans |
| SPT | South Pole Teloscope |
| SZ | Sunyaev Zeldovich (effect) |
| th-SZ | thermal Sunyaev-Zeldovich (effect) |
| WMAP | Wilkinson Microwave Anisotropy Probe [137] |
| VSA | Very Small Array [138] |

## Acknowlegdements

First of all I would like to thank my supervisor Prof. Dr. Rashid Sunyaev for his guidance throughout my PhD. He never lost hope in me and always found some time and way to motivate me or just bring me back onto the right path. I am also very grateful to Dr. Sergey Sazonov, who never lost patience and always had an open ear for any of my questions. It was a pleasure to work with him and I am thankful for all his help and advice. Furthermore I wish to thank my Diploma-Thesis supervisor Prof. Dr. Karl Mannheim, who encouraged and helped me to go to the MPA after I graduated and supported me in my search for the first Post-Doc.

Ein besonderer Dank gilt meinem ehemaligen Zimmergenossen Dr. Petar Mimica, der es die ganze Zeit am MPA mit mir ausgehalten hat. Er ist einer der wenigen Menschen, mit denen ich meine Begeisterung für Helge Schneider ausleben konnte. Mit ihm wurde es nie langweilig und er fand immer wieder neue Wege, mich auf den Boden der Tatsachen zurückzubringen.

I also wish to thank my colleague and friend Gert Hütsi, who beyond doubt is the best life-windshield and collaborator one can think of. I really enjoyed all the scientific discussion with him and will certainly not forget our visits in the Shamrocks. In addition I want to thank Dr. Serena Bertone and Dr. Corina Vogt. They both always found some ways to cheer me up and gave me a lot of opportunities to enjoy their excellent cooking abilities.

Ein grosser Dank auch an meinen Freund und Kollegen Dr. Carlos Hernández-Monteagudo, der mir stets mit Rat und Tat beistand und einer der ausgefallensten Sänger ist, die ich kenne. Also a big zthank you to Dr. Señor Rubiño-Martín. We always had a lot of fun playing the guitarra together and practicing our special language skills.

Thanks also to my friend, colleague and flatmate Dr. Dimitrios Giannios, who is my great Greek supporter, chess grandmaster and still did not look for another place to live. I am also grateful to Dr. Kaustuv moni Basu, Jorge Cuadra, Patricia Arévalo, Rasmus Voss, Stefanie Walch, Dr. Jonathan Braithwaite and Maximilian Stritzinger. You all made me enjoy the last years in Munich much more.

Einen Dank auch an meine ehemaligen Kommilitonen Martin Feix und Gernot Krause, die mich all die Jahre immer wieder unterstützt haben. Ich freue mich sehr, dass unsere Freundschaft auch über das Studium hinaus gehalten hat. Ebenfalls einen herzlichen Dank an Ai Morita für ihre ruhespendende Gesellschaft beim Zusammenschreiben.

Einen lieben Dank an Daniela Fischer und Marco Lindemeier, meine Brüder Lars, Nils und Jörg sowie meine kleinen Geschwister Jan und Julia. Wann ich auch in die Heimat gekommen bin, ich konnte mich immer darauf freuen, Euch zu sehen. Ausserdem einen grossen Dank an meine ganze Familie, aber insbesondere an meinem Vater, meine Mutter und meine Oma. Ihr alle habt immer an mich geglaubt, mich wo es ging unterstützt und immer wieder einen Goldapfel für mich übrig gehabt.